amU
Aix Marseille Université

NNT : 2025AIXM0035

THÈSE DE DOCTORAT

Soutenue à AMU — Aix-Marseille Université
le 6 Février 2025 à 10h00 par

Anass NAJLAOUI

Advancing the modeling of high-beta tokamak plasmas

Discipline
Physique et Sciences de la Matière

Spécialité
Energie, Rayonnement et Plasma

École doctorale
ED 352

Laboratoire/Partenaires de recherche
Physique des Intéractions Ioniques et Moléculaires (PIIM) AMU, CNRS, UMR7345

IRFM - CEA Cadarache, 13108 Saint-Paul-Lez-Durance, France

ITER Organization, Route de Vinon-sur-Verdon, 13067 St-Paul-Lez-Durance, France

Composition du jury

Pär STRAND Chalmers University of Technology	Rapporteur et Président du jury
Josefine PROLL Max Planck Institute for Plasma Physics	Rapporteur
Maurizio GIACOMIN University of Padova	Examinateur
Alberto LOARTE ITER Organization	Membre invité
Clarisse BOURDELLE IRFM, CEA	Co-Directrice de thèse
Yann CAMENEN CNRS, Aix Marseille University	Directeur de thèse

Affidavit

I, undersigned, Anass Najlaoui, hereby declare that the work presented in this manuscript is my own work, carried out under the scientific supervision of Yann Camenen and Clarisse Bourdelle, in accordance with the principles of honesty, integrity and responsibility inherent to the research mission. The research work and the writing of this manuscript have been carried out in compliance with both the french national charter for Research Integrity and AMU charter on the fight against plagiarism.

This work has not been submitted previously either in this country or in another country in the same or in a similar version to any other examination body.

Marseille 11/12/2025



This work is licensed under Creative Commons Attribution-NonCommercial-NoDerivatives 4.0 International Public License

Liste de publications et participation aux conférences

Liste des publications et/ou brevets réalisées dans le cadre du projet de thèse :

1. **A. Najlaoui**, Y. Camenen, C. Bourdelle and A. Loarte. *Verifying turbulence model reduction in high beta tokamak plasmas. Plasma Phys. Control. Fusion* **67**, 045016 (2025). 10.1088/1361-6587/adbc1d
2. M. Marin, Y. Camenen, C. Bourdelle, F.J. Casson, R. Coosemans, L. Garzotti, P. Maget, P. Manas, **A. Najlaoui**, O. Sauter and the TCV Team. *Full radius integrated modelling of ohmic ramp-up at TCV including self consistent density prediction. Nuclear Fusion* **65**, 036015 (2025). 10.1088/1741-4326/adb169

Participation aux conférences et écoles d'été au cours de la période de thèse :

1. **50th EPS Conference on Plasma Physics 2024**, qui s'est tenue du 8 au 12 juillet 2024 à Salamanque, en Espagne. (Un poster a été présenté)
2. **27th Joint EU-US Transport Task Force Meeting (TTF 2023)**, qui s'est tenue du 12 au 15 septembre 2023 à Nancy, en France. (Un poster a été présenté)
3. **59th Culham Plasma Physics Summer School**, qui s'est tenue du 18 au 28 juillet 2022 à Oxfordshire, au Royaume-Uni.

Résumé

Dans les tokamaks, les forces magnétiques doivent équilibrer la pression exercée par le plasma pour maintenir sa stabilité, assurant ainsi un confinement efficace du plasma magnétisé. L'efficacité de ce confinement est essentielle pour maintenir un plasma à haute pression, condition nécessaire aux réactions de fusion. Le paramètre sans dimension β, défini comme le rapport entre la pression cinétique du plasma et la pression magnétique, mesure cette efficacité. Des valeurs élevées de β permettent une puissance de fusion accrue, cette puissance étant proportionnelle à β^2. Cependant, à mesure que β augmente, le plasma devient plus sensible aux instabilités électromagnétiques, qui peuvent le déstabiliser et compromettre son confinement. Étant donné que les futurs réacteurs de fusion devraient fonctionner dans des régimes à haut-β, il est crucial de développer des modèles précis capables de simuler ces conditions. La modélisation intégrée, utilisée pour simuler le plasma, combine plusieurs codes et nécessite des évaluations rapides des flux turbulents sur plusieurs positions radiales et pas de temps. Les simulations gyrocinétiques non linéaires, bien qu'elles fournissent des informations détaillées sur la turbulence, sont trop coûteuses en calcul pour être utilisées dans la modélisation intégrée. Les modèles quasi-linéaires, tels que le modèle gyrofluide TGLF [1, 2], simplifient les aspects non linéaires de la turbulence, permettant de prédire le transport turbulent sur des échelles de temps de calcul bien plus rapides. Cependant, les simplifications inhérentes aux modèles quasi-linéaires, notamment dans leur traitement des mécanismes de saturation non linéaires, limitent leur fiabilité dans des régimes de paramètres peu explorés. Pour les plasmas à haut-β, où les effets électromagnétiques dominent, ces modèles n'ont pas été vérifiés de manière approfondie, laissant des incertitudes significatives dans leurs prédictions. La vérification de ces modèles dans de tels régimes est indispensable avant leur application fiable dans des études de modélisation intégrées. Cette thèse aborde ces incertitudes en vérifiant le modèle de turbulence quasi-linéaire TGLF à l'aide de simulations gyrocinétiques non linéaires réalisées avec le code GKW [3]. La vérification de la réponse linéaire de TGLF a commencé pour un cas de référence et a ensuite été étendue à une décharge expérimentale du tokamak JET à haut-β. Les résultats ont montré que, dans l'ensemble, TGLF pouvait raisonnablement capturer les taux de croissance linéaires et la structure des modes, mais des écarts sont apparus aux échelles de turbulence plus élevées, essentielles pour prédire avec précision les flux quasi-linéaires. Pour remédier à ces limitations, un nouveau mécanisme de filtrage a été développé et intégré dans TGLF. Les prévisions de flux de TGLF ont ensuite été comparées aux simulations non linéaires de GKW, révélant des erreurs moyennes de 67,0 % et 45,6 % pour les flux de particules d'ions et d'électrons, respectivement, et de 75,9 % et 64,7 % pour les flux de chaleur d'ions et d'électrons, respectivement.

Cette étude a permis d'évaluer les forces et les limites du modèle de transport réduit TGLF pour la modélisation du transport turbulent dans les plasmas à haut-β, tout en posant des bases solides pour des recherches futures dans ce régime.

Mots-clés : Tokamak, plasma, fusion magnétique, gyrocinétique, transport turbulent, plasmas à haut β, simulations gyrocinétiques non linéaires, prédictions quasi-linéaires des flux.

Abstract

In tokamaks, magnetic forces must balance the pressure exerted by the plasma to maintain stability, thereby ensuring an effective confinement of the magnetized plasma. The efficiency of this confinement is essential to sustaining a high-pressure plasma, a condition required for fusion reactions. The dimensionless parameter β, defined as the ratio of the plasma kinetic pressure to the magnetic pressure, measures this efficiency. Achieving high values of β allows for increased fusion power, as fusion power scales with β^2. However, as β increases, the plasma becomes more susceptible to electromagnetic instabilities, which can destabilize it and compromise its confinement. Since future fusion reactors are expected to operate in high-β regimes, it is crucial to develop accurate models capable of simulating these conditions. The integrated modeling approach, used to simulate plasma discharges, combines multiple codes and requires fast evaluations of turbulent fluxes across several positions and time steps. Nonlinear gyrokinetic simulations, although they provide detailed insights into turbulence, are computationally too expensive for integrated modeling. Quasi-linear models, such as the gyrofluid model TGLF [1, 2], simplify the nonlinear aspects of turbulence, allowing for predictions of turbulent transport on computational timescales that are significantly faster. However, the inherent simplifications in quasi-linear models, particularly in their treatment of the non-linear saturation mechanisms, limit their reliability when applied to less-explored parameter regimes. For high-β plasmas, where electromagnetic effects dominate, these models have not been extensively verified, leaving significant uncertainties in their predictions. Verifying these models in such regimes is indispensable before they can be confidently applied in integrated modeling studies. This thesis addresses these uncertainties by verifying the quasi-linear turbulence model TGLF using nonlinear gyrokinetic simulations performed with the GKW code [3]. The verification of TGLF's linear response began with a reference case and was then extended to an experimental high-β JET discharge. Results showed that, overall, TGLF could reasonably capture the linear growth rates and mode structures, but discrepancies arose at the low-binormal wavevector region, corresponding to higher scales of turbulence, which are critical for accurately predicting quasi-linear fluxes. To address these limitations, a new filtering mechanism was developed and implemented within TGLF. TGLF's flux predictions were then compared to nonlinear GKW simulations, revealing Root Mean Square errors of 67.0 % and 45.6 % for ion and electron particle fluxes, respectively, and 75.9 % and 64.7 % for ion and electron heat fluxes, respectively. This study evaluated the strengths and limitations of the reduced transport model TGLF for modeling turbulent transport in high-β plasmas, laying a foundation for future research in this regime.

Keywords: Tokamak, plasma, magnetic fusion, gyrokinetic, turbulence transport, High-β Plasmas, Nonlinear Gyrokinetic Simulations, Quasi-Linear Flux Predictions.

Résumé étendu

Dans les tokamaks, les forces magnétiques doivent équilibrer la pression exercée par le plasma pour maintenir sa stabilité, assurant ainsi un confinement efficace du plasma magnétisé. L'efficacité de ce confinement est essentielle pour maintenir un plasma à haute pression, condition nécessaire aux réactions de fusion. Le paramètre sans dimension β, défini comme le rapport entre la pression cinétique du plasma et la pression magnétique, mesure cette efficacité. Des valeurs élevées de β permettent une puissance de fusion accrue, cette puissance étant proportionnelle à β^2. Cependant, à mesure que β augmente, le plasma devient plus sensible aux instabilités électromagnétiques, qui peuvent le déstabiliser et compromettre son confinement. Étant donné que les futurs réacteurs de fusion devraient fonctionner dans des régimes à haut-β, il est crucial de développer des modèles précis capables de simuler ces conditions. La modélisation intégrée, utilisée pour simuler le plasma, combine plusieurs codes et nécessite des évaluations rapides des flux turbulents sur plusieurs positions radiales et pas de temps. Les simulations gyrocinétiques non linéaires, bien qu'elles fournissent des informations détaillées sur la turbulence, sont trop coûteuses en calcul pour être utilisées dans la modélisation intégrée. Les modèles quasi-linéaires, tels que le modèle gyrofluide TGLF [1, 2], simplifient les aspects non linéaires de la turbulence, permettant de prédire le transport turbulent sur des échelles de temps de calcul bien plus rapides. Cependant, les simplifications inhérentes aux modèles quasi-linéaires, notamment dans leur traitement des mécanismes de saturation non linéaires, limitent leur fiabilité dans des régimes de paramètres peu explorés. Pour les plasmas à haut-β, où les effets électromagnétiques dominent, ces modèles n'ont pas été vérifiés de manière approfondie, laissant des incertitudes significatives dans leurs prédictions. La vérification de ces modèles dans de tels régimes est indispensable avant leur application fiable dans des études de modélisation intégrées. Cette thèse aborde ces incertitudes en vérifiant le modèle de turbulence quasi-linéaire TGLF à l'aide de simulations gyrocinétiques non linéaires réalisées avec le code GKW [3].
Les objectifs incluent :

- **Intégration et Benchmarking :** Intégration de TGLF dans le cadre IMAS (*Integrated Modelling and Analysis Suite*) [4] afin de simplifier les échanges de données et d'assurer un benchmarking cohérent Entre TGLF et d'autres codes gyrocinétiques.
- **Vérification de la Réponse Linéaire :** La réponse linéaire de TGLF dans les plasmas à haut-β a été comparée aux simulations obtenues avec GKW.
  - Initialement, la validation a porté sur un cas standard de référence, pour évaluer la capacité de TGLF à reproduire la transition entre une turbulence dominée par les instabilités de type ITG et des régimes dominés par les

instabilités de type KBM. TGLF a réussi à reproduire les taux de croissance linéaires et les structures des modes dans des conditions de cisaillement magnétique ($\hat{s}$) standard, mais a montré des écarts significatifs pour de très faibles cisaillements magnétiques, en particulier près de la transition ITG-KBM.
  - La validation a été étendue ensuite pour une décharge expérimentale à haut-β du tokamak JET [5], caractérisée par un faible cisaillement magnétique et un β élevé. Dans ce cas, des écarts sont apparus aux échelles de turbulence plus élevées, essentielles pour prédire avec précision les flux quasi-linéaires, révélant des limites dans le mécanisme de filtrage de modes présent dans TGLF.
- **Développement d'un Filtre pour la Modélisation des KBM :** Pour résoudre les limitations identifiées, un nouveau mécanisme de filtrage a été développé et intégré à TGLF. Ce filtre, basé sur la fréquence des modes et leur parité, distingue les KBM des modes parasites, améliorant considérablement la modélisation des KBM par TGLF dans les plasmas à haut-β, notamment dans des conditions de faible cisaillement magnétique. Ce développement a été soumis pour publication dans la revue *Plasma Physics and Controlled Fusion*.
- **Vérification des Flux Quasi-Linéaires :** Les prédictions des flux quasi-linéaires de TGLF ont ensuite été vérifiées par rapport aux flux non linéaires issus des simulations GKW.
  - En se concentrant sur une décharge expérimentale du tokamak JET à la position radiale $\rho = 0.15$, cette étude a exploré 14 cas avec différents gradients de température (R/L_{T_i}, R/L_{T_e}), gradients de densité (R/L_{N_e}) et taux de cisaillement ($E \times B$) ($\gamma_{E\times B}$). Les résultats ont montré un accord modeste pour les flux de chaleur et de particules ioniques. Il a été observé que TGLF sous-estime fortement les contributions éléctromagnétiques au flux de chaleur électronique.
  - Des scans variant les différents gradients de températures R/L_{T_i} et R/L_{T_e} ont montré que TGLF reproduit les tendances observées dans les simulations non linéaires réalisées avec le code GKW.

Intégration et Benchmarking

Le code *Trapped Gyro-Landau Fluid* (TGLF) [1, 2] est un modèle gyrofluide quasi-linéaire utilisé pour prédire le transport turbulent dans les plasmas de tokamak. En tant que code quasi-linéaire, TGLF résout les équations gyrocinétiques linéaires sur un spectre de nombres d'onde, en prédisant le transport turbulent résultant à l'aide de modèles semi-empiriques pour décrire la saturation de ces instabilités. Cette approche rend TGLF nettement plus efficace que les codes gyrocinétiques non linéaires, tout en conservant une précision suffisante pour de nombreuses applications pratiques [6]. TGLF fournit des estimations rapides et raisonnablement précises des flux turbulents, avec un temps de calcul moyen d'environ 10 secondes CPU par simulation.

Ces court temps de calculs sont essentiels pour simuler le comportement global du plasma dans un tokamak. En revanche, les codes gyrocinétiques non linéaires, tels que GKW [7], offrent une représentation détaillée de la dynamique non linéaire de la turbulence dans le plasma, mais à un coût computationnel nettement plus élevé, nécessitant plus de 10^5 heures CPU pour une seule simulation à une position radiale et un seul pas de temps. Cela fait de GKW un outil mieux adapté aux études détaillées de phénomènes spécifiques de turbulence, tandis que TGLF est idéal pour la modélisation intégrée, où des prédictions rapides et efficaces des flux sont requises. Cependant, les prédictions de TGLF doivent faire l'objet d'une vérification rigoureuse avant de pouvoir être utilisées de manière fiable dans les cadres de modélisation intégrée, en particulier pour des régimes exigeants comme les plasmas à haut beta, où des instabilités électromagnétiques telles que les *Kinetic Ballooning Modes* (KBM) sont prévalentes. TGLF n'a pas encore été vérifié de manière approfondie pour ces conditions, et son benchmarking par rapport à un code gyrocinétique non linéaire comme GKW est essentiel pour évaluer sa fiabilité.

Dans les simulations gyrocinétiques, faire une comparaison entre différents codes est une tâche complexe en raison des incohérences dans la manière dont les principaux paramètres physiques sont définis et normalisés. Chaque code utilise sa propre méthode pour définir et normaliser des grandeurs physiques identiques, telles que les gradients de densité et de température ou encore la pression du plasma. Ces différences peuvent entraîner des erreurs qui se traduisent par des écarts significatifs lors de la comparaison des résultats, car de petites variations dans les normalisations peuvent entraîner des grandes déviations dans les flux prédits. Ce manque de standardisation complique le processus de vérification entre différents codes, pourtant essentiel pour garantir la fiabilité des modèles réduits. Pour faciliter les vérifications croisées, un cadre commun est nécessaire afin de s'assurer que chaque code fonctionne sur une base unifiée pour le traitement des données d'entrée et de sortie. Sans un tel cadre, le benchmarking reste sujet aux erreurs et inefficace. **Integrated Modelling and Analysis Suite (IMAS)** apporte une solution à ce problème. IMAS est une infrastructure complète développée pour soutenir tous les aspects de la modélisation et de l'analyse des plasmas pour ITER, englobant un large éventail de modèles physiques et de workflows, allant de l'intégration des données expérimentales à la modélisation complexe de scénarios [4]. De plus, IMAS est conçu avec une grande flexibilité : sa structure modulaire permet le développement, l'extension et l'intégration de composants individuels selon les besoins. Bien qu'IMAS soit conçu comme une infrastructure générale pour la gestion des données et l'intégration des modèles, dans ce travail, nous nous concentrons spécifiquement sur son application aux simulations gyrocinétiques de tube de flux (*flux-tube*) via l'utilisation de la structure de données d'interface gyrocinétique (IDS) [8]. Un ensemble unifié de conventions et de normalisations pour les entrées et les sorties des simulations gyrocinétiques dans la limite δf a été développé au sein d'IMAS pour faciliter le benchmarking cohérent et l'intégration de divers codes gyrocinétiques, tels que TGLF et GKW. En utilisant un format commun et des normalisations standardisées pour les données, le cadre IMAS crée efficacement un "langage commun" pour ces codes, leur permettant de communiquer de manière

fluide. Les **Gyrokinetic-local Interface Data Structure (IDS)** d'IMAS sont au cœur de cet effort. Les IDS fournissent des entités standardisées pour le stockage et l'accès aux données expérimentales et de simulation. Pour les simulations de tube de flux, les IDS gyrocinétiques définissent la structure permettant de stocker des paramètres tels que les profils de plasma, les grandeurs d'équilibre et les flux prédits. En adoptant cette norme, les codes n'ont plus besoin de scripts de conversion personnalisés pour comparer leurs résultats. Au lieu de cela, les IDS d'IMAS offrent un cadre où les données issues de différentes simulations gyrocinétiques peuvent être directement comparées entre elles. Le cadre IDS ne soutient pas seulement la cohérence des simulations, mais améliore également la transparence et la reproductibilité. Chaque IDS contient des métadonnées détaillées qui retracent la provenance des données, incluant la version du code utilisé, les paramètres spécifiques et les effets physiques inclus dans les simulations. Ce niveau de détail garantit que les résultats sont entièrement traçables et que les exercices de benchmarking peuvent être reproduits avec précision. En fournissant une plateforme commune que chaque groupe de recherche peut utiliser, IMAS, lorsqu'il est intégré à une base de données centralisée de cas, réduit encore davantage les redondances, permettant aux chercheurs de se concentrer sur l'avancement des connaissances physiques plutôt que sur la gestion des différences de format de données. Le modèle de données d'IMAS est indépendant des machines, ce qui signifie que le cadre de benchmarking est extensible au-delà des machines ou modèles individuels. Le rôle d'IMAS va au-delà de la standardisation des données de simulation : il intègre également les données expérimentales dans le même modèle de données. Cette intégration permet des comparaisons directes entre les simulations et les mesures expérimentales, renforçant la capacité à valider les prédictions théoriques à partir des données empiriques [9].

Vérification de la Réponse Linéaire et Développement d'un Filtre pour la Modélisation des KBM

Dans le chapitre 3, nous comparerons la réponse linéaire de TGLF avec celle de GKW. Notre analyse commence par le cas de référence dit *Waltz standard* [10], dont les paramètres plasma sont détaillés dans le tableau 3.1. Nous avons choisi ce cas en raison de la précision démontrée précédemment de TGLF dans la modélisation des régimes dominés par le gradient de température ionique (ITG) [11]. Notre méthodologie implique des scans en β afin d'explorer la transition du régime ITG aux modes KBM. Ces scans sont réalisés pour deux valeurs différentes du cisaillement magnétique : $\hat{s} = 1.0$, afin d'examiner TGLF dans des conditions standards, et $\hat{s} = 0.05$, pour évaluer son comportement dans des conditions de faible cisaillement, typiques des régions proches de l'axe magnétique d'un tokamak. Ensuite, l'analyse se concentre sur la décharge hybride H-mode de JET #75225, afin d'évaluer la précision de la réponse linéaire de TGLF dans la région centrale des plasmas à haut β et faible cisaillement

magnétique, où les KBM sont prédits comme instables [5, 12].

Cas de référence Waltz Standard

Pour évaluer la capacité de TGLF à capturer la transition ITG-KBM, un scan en β plasma est réalisé. La figure 1 présente les variations du taux de croissance (γ), de la fréquence (ω_r), et des poids quasi-linéaires en fonction de β pour le cas Waltz Standard à $k_\theta \rho_s = 0.4$. Ces calculs sont effectués avec un gradient de pression constant $\beta' = 0$, pour deux valeurs de cisaillement magnétique, $\hat{s} = 1.0$ et $\hat{s} = 0.05$.

TGLF modélise efficacement la réponse linéaire des KBM dans le cas de référence Waltz Standard, mais des défis subsistent dans des conditions de très faible cisaillement magnétique et près de la transition ITG-KBM, où des écarts persistent malgré des ajustements des paramètres d'entrée de TGLF.

Décharge hybride H-mode de JET #75225

Après avoir évalué la capacité de TGLF à modéliser les KBM dans un scénario idéalisé représenté par le cas de référence Waltz Standard, cette section étend le benchmark en comparant les résultats de TGLF et de GKW pour la décharge hybride H-mode de JET #75225. Cette décharge hybride H-mode, réalisée lorsque le tokamak JET était équipé de parois en carbone, a fait l'objet d'une analyse détaillée dans une étude précédente [12]. Les simulations incluent trois espèces : ions deutérium, électrons et carbone.

Table 1. – Paramètres plasma normalisés IMAS pour la décharge JET #75225

ρ	R/L_{Ti}	R/L_{Te}	R/L_{Tc}	R/L_{ni}	R/L_{ne}	R/L_{nc}
0.15	4.2	2	4.2	1.67	1.5	-0.7
0.33	7.6	4.03	7.6	3.08	2.7	-1.49
ρ	T_i/T_e	T_c/T_e	n_i/n_e	n_c/n_e	$\beta(\%)$	u
0.15	1.43	1.43	0.93	0.01	3.2	0.38
0.33	1.19	1.19	0.92	0.01	2.5	0.34
ρ	u'	ν	q	r_N	p'_N	$\hat{s}$
0.15	0.59	0.015	1.1	0.05	0.37	0.05
0.33	1.31	0.020	1.12	0.12	0.42	0.2

ρ	κ	$R_0 \frac{\partial \kappa}{\partial r}$	$\frac{\partial R_c}{\partial r}$	$\frac{\partial Z_c}{\partial r}$	c_n	s_n	$R_0 \frac{\partial c_n}{\partial r}$	$R_0 \frac{\partial s_n}{\partial r}$
0.15	1.35	-0.13	-0.08	-0.005	[0,0]	[0,0.02]	[0,0]	[0,0.19]
0.33	1.30	-0.002	-0.13	-0.01	[0,0]	[0,0.036]	[0,0]	[0,0.26]

Par défaut, TGLF configure le paramètre `FILTER` à 2, ce qui élimine automatiquement tous les modes ayant des fréquences dépassant deux fois la fréquence des ondes

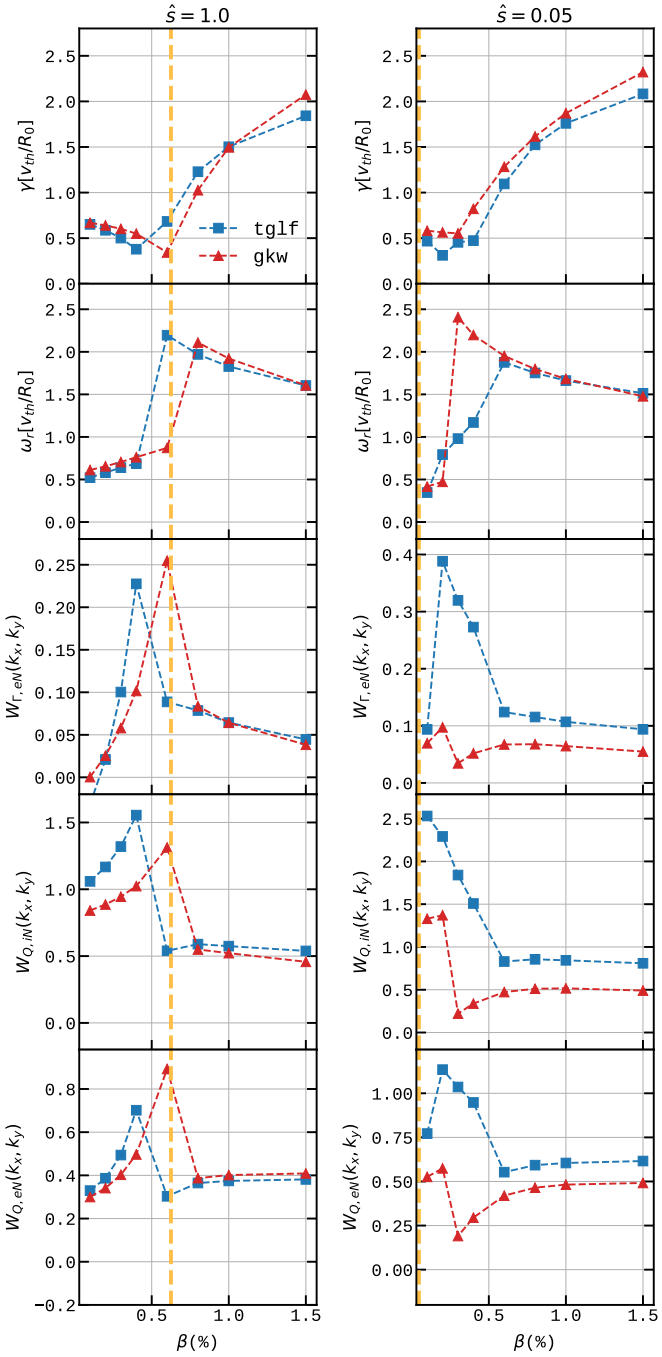


Figure 1. – Taux de croissance (γ), fréquence (ω_r) et variations des poids linéaires des modes pour le cas de référence Waltz Standard en fonction de β plasma, à $k_\theta \rho_s = 0.4$, avec un gradient de pression fixé à $\beta' = 0$, pour deux valeurs différentes du cisaillement magnétique, $\hat{s} = \{1.0, 0.05\}$.

de dérive (*drift waves*). Bien que cette configuration permette de supprimer efficacement les modes non physiques indésirables, elle exclut également les modes à haute

fréquence légitimes, tels que les KBM. Ce paramètre était donc désactivé jusqu'à présent en réglant `FILTER` à 0. Cependant, cette désactivation augmente significativement le risque que des modes parasites incorrects soient pris en compte, entraînant des prédictions erronées et excessivement élevées des flux quasi-linéaires.

Pour résoudre ce problème, nous avons développé un nouveau filtre qui supprime les modes à haute fréquence, sauf si ces derniers présentent une structure paire dans la partie réelle du potentiel électrostatique. Cette modification permet d'éliminer efficacement les modes parasites (qui ont généralement des fonctions propres de parité impaire) tout en conservant les KBM. Cette nouvelle option est activée en attribuant une valeur négative au paramètre `FILTER`.

La figure 2 présente un arbre de décision décrivant les étapes suivies par le nouveau filtre pour déterminer si un mode doit être conservé ou supprimé.

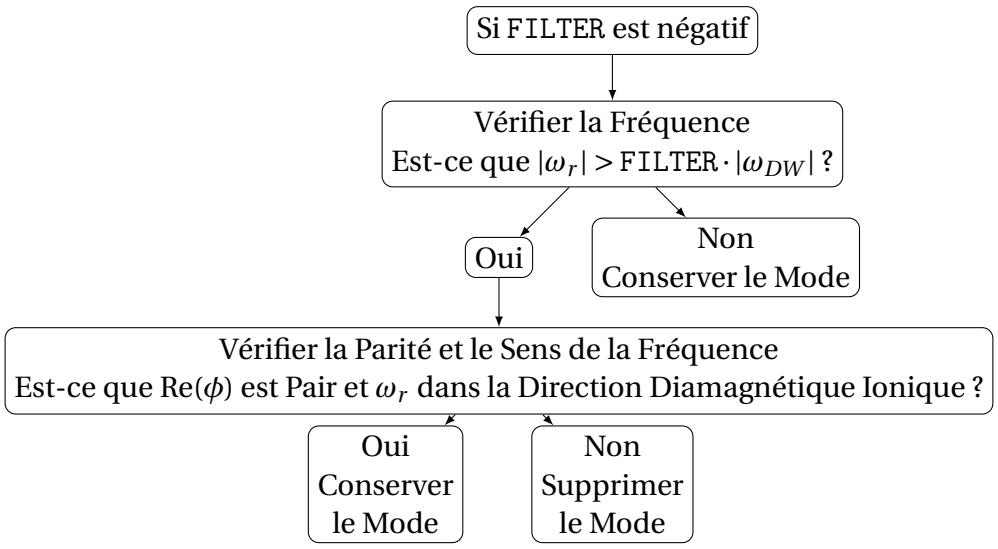


Figure 2. – Arbre de décision pour le nouveau filtre

La figure 3 illustre les taux de croissance et les fréquences en fonction du vecteur d'onde binormal $k_\theta \rho_s$ pour la décharge JET #75225 à $\rho = 0.15$.

La réponse linéaire de TGLF pour les KBM, en utilisant le cas Waltz Standard et la décharge JET #75225, est proche de la référence fournie par GKW, à condition que les modes parasites soient filtrés à l'aide de la méthode nouvellement développée.

Vérification des Flux Quasi-Linéaires

Dans cette section, nous comparons les prédictions des flux quasi-linéaires de TGLF avec celles obtenues à partir de simulations non linéaires réalisées à l'aide du code gyrocinétique GKW. Cette comparaison se concentre sur la modélisation de la région centrale de la décharge JET #75225 à la position radiale $\rho = 0.15$, un cas examiné précédemment dans les simulations linéaires de la section précédente.

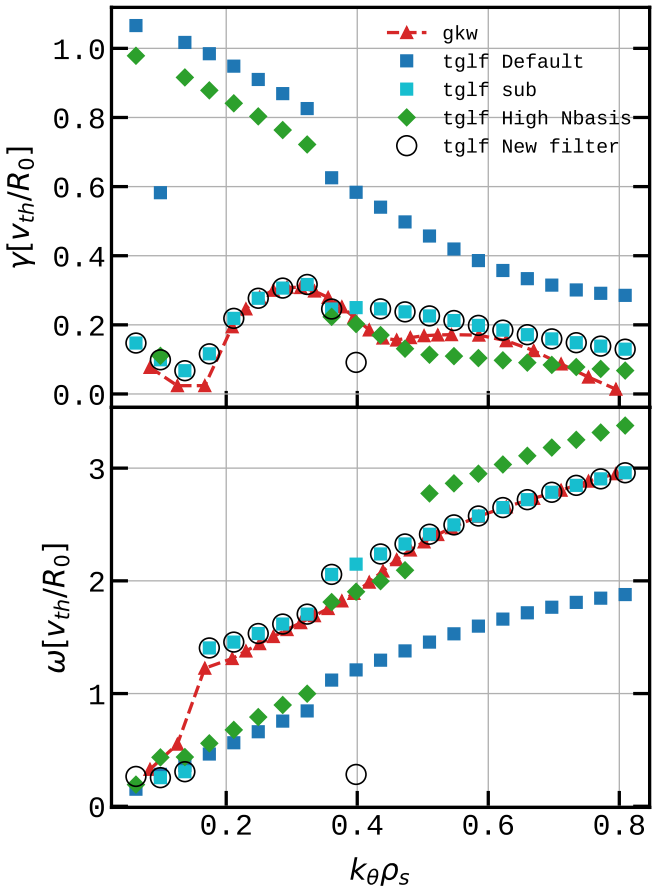


Figure 3. – Spectres des taux de croissance linéaires et des fréquences réelles en fonction du vecteur d'onde binormal $k_\theta\rho_s$ pour la décharge JET #75225 à $\rho = 0.15$. Les spectres sont présentés pour les configurations TGLF avec le filtre par défaut, une valeur élevée de `Nbasis`, et les réglages du nouveau filtre.

Pour évaluer les performances de TGLF dans la modélisation de la turbulence KBM, nous avons effectué une série de 14 simulations non linéaires avec le code GKW. Les paramètres variés dans ces simulations incluent R/L_{Ti}, R/L_{Te}, R/L_n et le taux de cisaillement γ_{E_N}. Le tableau 2 résume les caractéristiques de chaque simulation. Près de l'axe magnétique, le gradient de rotation toroïdale est relativement faible, et le taux de cisaillement associé est modéré par rapport au taux de croissance linéaire maximal, avec un impact limité sur le niveau de saturation observé dans les simulations non linéaires.

Pour évaluer les performances de TGLF dans la prédiction du potentiel saturé, nous comparons les spectres binormaux du potentiel électrique $\langle|\delta\phi|^2\rangle$ issus des simulations non linéaires de GKW avec ceux obtenus à partir des simulations quasi-linéaires de TGLF pour divers réglages. Ici, $\langle|\delta\phi|^2\rangle$ représente le potentiel saturé au carré, moyenné temporellement et sur la surface de flux, sommé sur tous les $k_r\rho_s$ et normal-

Indice	R/L_{Ti}	R/L_{Te}	R/L_{Ne}	γ_{E_N}
1	4.2	2	1.5	0
2	**3.15**	2	1.5	0
3	4.2	**1.5**	1.5	0
4	4.2	**2.5**	1.5	0
5	4.2	2	**1.2**	0
6	4.2	2	**0.9**	0
7	**3.15**	2	**1.2**	0
8	4.2	2	1.5	**0.05**
9	4.2	**1.5**	1.5	**0.05**
10	4.2	2	**0.9**	**0.05**
11	**3.15**	2	1.5	**0.05**
12	4.2	**2.5**	1.5	**0.05**
13	4.2	2	**1.2**	**0.05**
14	**3.15**	2	**1.2**	**0.05**

Table 2. – Résumé des paramètres plasma variés dans les 14 simulations non linéaires avec GKW. Le cas 1 correspond au cas de référence. Les valeurs en gras indiquent les écarts par rapport au cas de référence.

isé par $\Delta k_\theta \rho_s$ pour tenir compte des grilles binormales potentiellement différentes dans TGLF et GKW. Les paramètres optimisés de TGLF, qui offrent la meilleure correspondance avec les résultats de GKW pour les cas analysés, sont résumés dans le tableau 3. Ces réglages servent de base pour nos comparaisons et analyses.

Paramètre	Valeur Optimisée
`FILTER`	-1.5
`WIDTH`	3
`KYGRID_MODEL`	1
`ALPHA_ZF`	-1

Table 3. – Réglages optimisés des paramètres de TGLF pour la modélisation de la turbulence KBM.

À partir de ces réglages optimisés, nous explorons les variations suivantes :
— `FILTER` : Modification de -1.5 (optimisé) à 2 (valeur par défaut).
— `WIDTH` : Modification de 3 (optimisé) à 1.65 (valeur par défaut).
— `KYGRID_MODEL` : Modification de 1 (optimisé) à 4.
— `ALPHA_ZF` : Modification de -1 (optimisé) à 1 (valeur par défaut).

La figure 4 illustre les spectres de $\langle|\phi|^2\rangle$ en fonction du vecteur d'onde binormal $k_\theta \rho_s$ pour six cas différents référencés dans le tableau 2. Les courbes rouges représentent les résultats des simulations GKW, servant de référence. Les résultats des simulations TGLF sont présentés pour cinq configurations différentes : optimisée (bleu), `WIDTH` = 1.65 (orange), `ALPHA_ZF` = 1 (vert), `KYGRID_MODEL` = 4 (violet, avec des cercles ouverts)

et FILTER = 2 (marron).

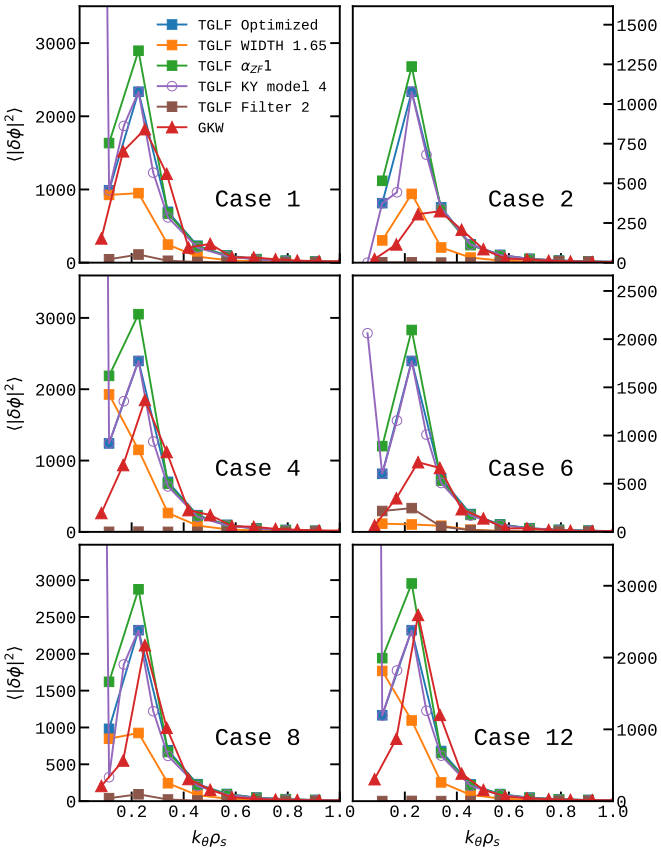


Figure 4. – Profils de $\langle|\delta\phi|^2\rangle$ issus des simulations GKW (rouge) et TGLF pour cinq configurations différentes. Les numéros des cas sont indiqués en référence au tableau 2.

Nous comparons ici les prédictions des flux quasi-linéaires de TGLF, en utilisant les réglages optimisés du tableau 3, avec les flux non linéaires obtenus à partir des simulations GKW. La figure 5 présente une analyse comparative des flux de chaleur et de particules pour les ions et les électrons. Chaque point des graphiques représente l'une des 14 simulations différentes répertoriées dans le tableau 2. La ligne pointillée indique une correspondance parfaite entre les prédictions de TGLF et les résultats de GKW. Dans l'ensemble, pour les flux de particules d'ions et d'électrons, l'accord entre TGLF et GKW est bon, bien qu'il existe quelques exceptions où TGLF prédit un flux de particules d'ions avec un signe incorrect. Pour le flux de chaleur ionique, TGLF a tendance à légèrement surestimer les flux par rapport à GKW. Cependant, pour le flux de chaleur électronique, TGLF sous-estime les flux, en particulier dans les cas où ces flux sont élevés.

La figure 6 illustre les flux de chaleur pour les ions et les électrons ainsi que les flux de particules électroniques en fonction de R/L_{Te} et R/L_{Ti} pour TGLF et GKW. Nous observons que TGLF a tendance à surestimer les flux par rapport à GKW, à l'exception

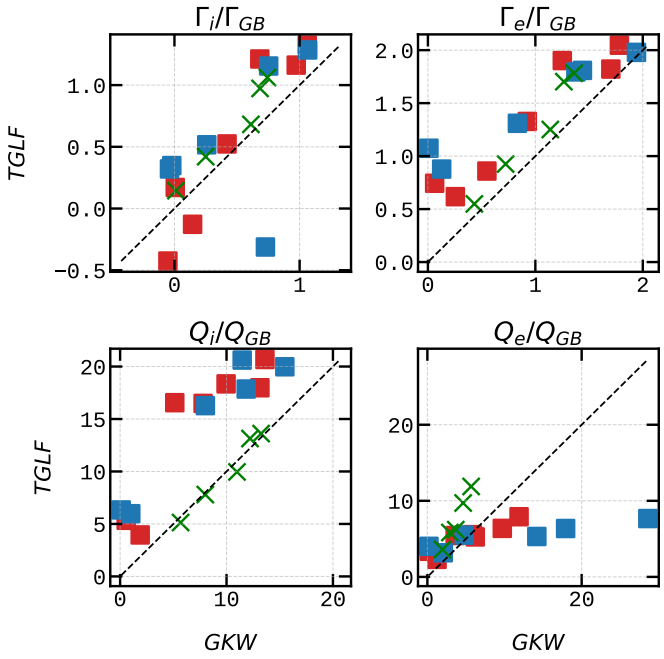


Figure 5. – Comparaison des flux de chaleur et de particules pour les ions et les électrons entre TGLF et GKW. Les points rouges représentent les simulations sans taux de cisaillement, les points bleus incluent ce taux. La ligne pointillée indique un accord parfait.

du flux de chaleur électronique. Malgré cette surestimation, TGLF suit la tendance générale observée dans les simulations GKW, ce qui indique sa capacité à reproduire le comportement global des flux avec l'augmentation des gradients de température.

Conclusion

Cette étude met en évidence les forces et les limites de TGLF dans la modélisation du transport turbulent dans les plasmas à haut β. La comparaison des flux quasi-linéaires prédits par TGLF avec ceux obtenus à partir de simulations gyrocinétiques non linéaires a permis de vérifier les performances de TGLF dans la région centrale de la décharge JET #75225. Bien que les prédictions globales soient cohérentes avec les tendances observées, des écarts subsistent. Le développement d'un nouveau mécanisme de filtrage et l'identification de réglages optimisés ont permis d'améliorer la modélisation des KBMs avec TGLF, tout en maintenant un équilibre entre précision et efficacité computationnelle. Cependant, cette étude a également révélé des limites dans le traitement des effets électromagnétique de TGLF. Ces résultats, limités à un cas expérimental spécifique, mettent en lumière l'importance d'étendre la vérification de TGLF à d'autres scénarios expérimentaux à haut β. Une validation dans des cadres de modélisation intégrée est également cruciale. En posant les bases pour des recherches futures, cette étude ouvre la voie à une amélioration continue des modèles de trans-

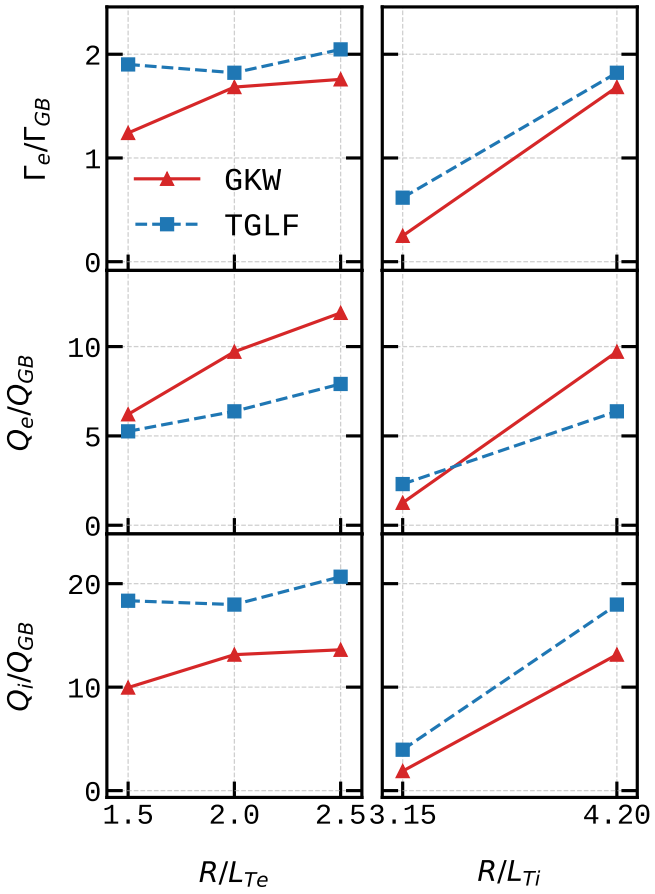


Figure 6. – Comparaison des flux entre TGLF et GKW en fonction de R/L_{Te} et R/L_{Ti}.

port turbulent réduits, comme TGLF, pour modéliser avec précision les plasmas de fusion à haut-β.

Acknowledgments

I would like to start by expressing my deepest gratitude to the members of my jury for their time and effort in evaluating my work. A special thanks to my supervisors, Yann Camenen and Clarisse Bourdelle for their invaluable guidance throughout these years. Their constant support, patience, and encouragement have been fundamental to my growth, and I am truly grateful for everything they shared with me.

A heartfelt thank you to my office mates, Alodie and Mattia, who have been by my side since the very beginning. Through the highs and the lows, they were always there, offering their support, laughter, and friendship. I owe them all so much.

To all my brothers, Aghiles, Benjamin, Exaucé, Salah, Walid, Aziz, Ioaquin, Thomas, and Guillaume, thank you for your support, your presence, and your friendship throughout this journey. T.E.F.

I am grateful to all the members of the PIIM laboratory. The supportive atmosphere they created has played a key role in my work and made this experience all the more enriching. A special thank to the friends I have made in the lab: Emanuele, Daniel, Romeo, Tom, Emil, Enzo, Matheus, Mouna, Federica, Martino, Julien, Akbar, Daniele, Surabhi, Matisse, Yosvany, Vassili, Silvia, David, Matthieu, Aleksandr and Mun. Your kindness and camaraderie have made the journey much more enjoyable.

I also want to express my gratitude to all the People who have supported me in different ways: Coach Fouad and Coach Johan, Yanis, Chris and Nissa. Their encouragement has meant a lot to me.

Finally, I want to thank my family, who have always been a source of strength, love, and support. To my sister Asma Myriam, thank you for always checking in on me, for your messages, and for your support no matter what. Your presence has meant more than words can say. To my sister Soumaya, thank you for your endless kindness, your care, and for always being there when I needed it. To my brother Hassan, thank you for your courage, your strength, and all our shared moments during training, you've inspired me more than you know. To my little sister Assia, thank you for those late-night gaming sessions, for your joyful spirit, and the precious time we shared. And to my mother, the most incredible mom one could ever hope for, thank you for your love, your patience, and the light you always bring into my life.

Contents

Affidavit 2

Liste de publications et participation aux conférences 3

Résumé 4

Abstract 6

Résumé étendu 8

Acknowledgments 20

Contents 21

List of Figures 23

List of Tables 27

1. Introduction 28
- 1.1. Fusion energy . . . 28
  - 1.1.1. Current Global Energy Landscape . . . 28
  - 1.1.2. Nuclear Fusion . . . 31
  - 1.1.3. Tokamak Configuration and Magnetic Confinement . . . 33
  - 1.1.4. Importance of the Beta (β) Parameter in Fusion . . . 37
- 1.2. Plasma Confinement and transport . . . 39
  - 1.2.1. Operational Limits in Tokamaks . . . 39
  - 1.2.2. Classical, Neoclassical and Turbulent Transport in Tokamaks . . . 42
  - 1.2.3. Integrated Modeling Frameworks for Tokamak Simulations . . . 45
- 1.3. Turbulent transport modelling . . . 47
  - 1.3.1. Gyrokinetic Theory . . . 47
  - 1.3.2. Derivation of Turbulent Radial Fluxes . . . 52
  - 1.3.3. Quasi-Linear Theory . . . 57
- 1.4. Thesis Motivation and Outline . . . 60

2. The TGLF Code and Its Integration in IMAS 62
- 2.1. TGLF Model Overview . . . 63
  - 2.1.1. Turbulence Saturation Models . . . 64
  - 2.1.2. Key Improvements in TGLF Over GLF23 . . . 64
  - 2.1.3. Hermite Basis Function Expansion for Eigenmode Calculations 65

2.2. Simulation Workflow of the TGLF Code . . . 66
2.2.1. TGLF Simulation Setup . . . 66
2.2.2. TGLF simulation workflow in single-k_y linear stability . . . 67
2.2.3. Transport Model in TGLF . . . 69
2.3. Unified standard for Gyrokinetic simulations . . . 75
2.3.1. Scripts for IMAS-TGLF Integration . . . 76
2.3.2. Structure and Functionalities of the Conversion . . . 76
2.3.3. Parameter Enforcement and Technical Choices for TGLF Input Conversion . . . 90
2.3.4. Tests Overview . . . 93
2.3.5. Conclusions . . . 101

3. Verification of TGLF Linear Response in High-Beta Plasmas 104
3.1. Simplified Linear Fluid and Kinetic Models for the Toroidal ITG Instability 104
3.1.1. The reference delta-f gyrokinetic equation . . . 105
3.1.2. Coordinate System . . . 106
3.1.3. Magnetic Geometry . . . 106
3.1.4. Perturbed Quantities and Gyro-Average . . . 106
3.1.5. Linearized One-Point Gyrokinetic Equation . . . 107
3.1.6. Quasi-Neutrality and Adiabatic Electron Approximation . . . 108
3.1.7. Kinetic Model . . . 109
3.1.8. Fluid Model . . . 110
3.1.9. Comparison between the Fluid and Kinetic Models . . . 114
3.2. Kinetic Ballooning Modes . . . 116
3.3. Comparison of TGLF linear response against gyrokinetic simulations (GKW) . . . 119
3.3.1. Practical Steps in Benchmarking . . . 120
3.3.2. Codes setup . . . 121
3.3.3. Waltz Standard Case linear analysis . . . 122
3.3.4. Jet hybrid H-mode #75225 . . . 129

4. Comparison of TGLF Quasi-linear Fluxes Against Gyrokinetic Nonlinear Simulations for KBM turbulence 137
4.1. Codes Setup . . . 138
4.2. Nonlinear Simulations with GKW . . . 139
4.2.1. Comparing the Saturated Potential: Nonlinear GKW vs. Quasilinear TGLF . . . 139
4.3. Comparison of TGLF Quasi-linear Fluxes and GKW Nonlinear Fluxes . 144

5. Conclusions and Future Perspectives 150

ANNEXES 154

A. Integrals For Moment of fluid model derivation 155

List of Figures

1. Taux de croissance (γ), fréquence (ω_r) et variations des poids linéaires des modes pour le cas de référence Waltz Standard en fonction de β plasma, à $k_\theta \rho_s = 0.4$, avec un gradient de pression fixé à $\beta' = 0$, pour deux valeurs différentes du cisaillement magnétique, $\hat{s} = \{1.0, 0.05\}$. . . 13
2. Arbre de décision pour le nouveau filtre 14
3. Spectres des taux de croissance linéaires et des fréquences réelles en fonction du vecteur d'onde binormal $k_\theta \rho_s$ pour la décharge JET #75225 à $\rho = 0.15$. Les spectres sont présentés pour les configurations TGLF avec le filtre par défaut, une valeur élevée de `Nbasis`, et les réglages du nouveau filtre. 15
4. Profils de $\langle|\delta\phi|^2\rangle$ issus des simulations GKW (rouge) et TGLF pour cinq configurations différentes. Les numéros des cas sont indiqués en référence au tableau 2. 17
5. Comparaison des flux de chaleur et de particules pour les ions et les électrons entre TGLF et GKW. Les points rouges représentent les simulations sans taux de cisaillement, les points bleus incluent ce taux. La ligne pointillée indique un accord parfait. 18
6. Comparaison des flux entre TGLF et GKW en fonction de R/L_{Te} et R/L_{Ti}. 19

1.4. Evolution of the triple product ($nT\tau_E$) achieved by fusion devices over time. Data from: ITER [13], JT-60U [14, 15], TFTR [16], JET ([17], Alcator-C [18], PLT [19], TFR [20], ST [21], T-3 [22], ZETA [23]. 34
1.5. Schematic diagram of a tokamak, illustrating the key components of magnetic confinement. (Credit : [24]) 35
1.6. Volume-averaged β versus I_p/aB_T for data from various high-β tokamak experiments. The dotted line represents the scaling $\langle\beta\rangle = 3.5\frac{I}{aB_T}$, showing the strong correlation with the Troyon limit. Reproduced from : [25] 41

2.1. Cylindrical coordinate systems used in TGLF and IMAS. The system is right-handed with R as the major radius, Z as the elevation, and φ as the toroidal angle. 77
2.2. Linear growth rate and frequency as a function of $k_\theta \rho_s$, comparing TGLF and GKW results. Both axes use logarithmic scales, except for the frequency plot near zero. 94
2.3. Real part of the electrostatic potential as a function of θ for $k_\theta \rho_s = 0.1$ and $k_\theta \rho_s = 0.2$, comparing TGLF and GKW. 95

2.4. Linear growth rate and frequency as a function of ion charge (Z), comparing TGLF and GKW results. 96
2.5. Linear growth rate and frequency as a function of ion mass (m_i), comparing TGLF and GKW results. 96
2.6. Linear growth rate and frequency as a function of ion to electron temperature ratio $T_{iN} = T_i/T_e$, comparing TGLF and GKW results. 97
2.7. Linear growth rate and frequency as a function of R/L_N, comparing GKW and TGLF results. 97
2.8. Linear growth rate and frequency as a function of R/L_T, comparing GKW and TGLF results. 98
2.9. Comparison of TGLF and GKW linear growth rate and frequency as a function of magnetic shear ($\hat{s}$) in IMAS units. 98
2.10. Comparison of TGLF and GKW linear growth rate and frequency as a function of pressure gradient (p'_N) in IMAS units. 99
2.11. Comparison of TGLF and GKW linear growth rate and frequency as a function of $\frac{\partial R}{\partial r}$, in IMAS units. 99
2.12. Comparison of linear growth rate and frequency as a function of elongation (κ) between GKW and TGLF in IMAS units. 100
2.13. Comparison of TGLF and GKW linear growth rate and frequency as a function of $\partial\kappa/\partial r$, expressed in IMAS units. 100
2.14. Linear growth rate and frequency as a function of inverse aspect ratio (r_N), comparing GKW and TGLF results. 101
2.15. Linear growth rate and frequency as a function of safety factor (q), comparing GKW and TGLF results. 101
2.16. Linear growth rate and frequency as a function of electron-ion collision frequency. Results from GKW and TGLF are compared, with both curves expressed in IMAS units. 102
2.17. Linear growth rate and frequency as a function of plasma β. The results from GKW and TGLF are plotted for comparison, with both curves expressed in IMAS units. 102
2.18. Real part of the electrostatic potential as a function of the parallel coordinate, θ, for $\beta = 0.2\%$ (ITG regime) and , for $\beta = 1\%$ (KBM regime). . . 103

3.1. Growth rate γ as a function of the temperature gradient R/L_T and density gradient R/L_n using the fluid model with $\hat{k_z} = 0$ and $\rho_0 k_y = 0.5$ . . 113
3.2. Comparison of growth rate γ as a function of R/L_T for $R/L_n = 3$, $k_y\rho = 0.4$, and $\hat{k_z} = 0$. The results from the simplified fluid model, kinetic model, and GKW are shown. For GKW, linear simulations were performed with a magnetic shear $\hat{s} = 1$ and a safety factor $q = 2$, at $k_y\rho = 0.4$, using adiabatic electrons and evaluating a single point at $\theta = 0$. 114
3.3. Growth rate γ as a function of $k_y\rho$ for $R/L_n = 3$ and $\hat{k_z} = 0$, comparing the kinetic model with GKW for $R/L_T = 9$. 115
3.4. Benchmarking workflow for comparing TGLF against GKW using IMAS IDS for standardized normalization. 120

3.5. Growth rate (γ), frequency (ω_r), and linear mode weights variations for the Waltz Standard case as a function of plasma β, for the Waltz Standard case at $k_\theta \rho_s = 0.4$, at a fixed pressure gradient $\beta' = 0$, for two different values of the magnetic shear, $\hat{s} = 1.0, 0.05$. 123
3.6. Real part of the normalized perturbed electrostatic potential ϕ_N for different values of $\hat{s}$ and β as a function of the poloidal angle θ. 124
3.7. Comparison of the real part of the perturbed electrostatic potential ϕ_N as a function of the parallel direction θ, obtained from GKW and TGLF for `NBASIS_MAX` values of 6 and 26 in the Waltz STD case at $k_\theta \rho_s = 0.4$, $\beta = 0.4\%$, and $\hat{s} = 0.05$. 124
3.8. Relative errors in the linear response parameters ($\alpha_{\gamma,\omega,\Gamma,Q}$) between TGLF and GKW as a function of `NBASIS_MAX` for the Waltz STD case at $k_\theta \rho_s = 0.4$, $\beta = 0.4\%$, and $\hat{s} = 0.05$. 125
3.9. Relative errors in the linear response parameters ($\alpha_{\gamma,\omega,\Gamma,Q}$) between TGLF and GKW for the JET 75225 discharge as a function of `NBASIS_MAX`, at $\rho = 0.15$, $\beta = 3.2\%$, and $\hat{s} = 0.05$. 126
3.10. Linear growth rate and frequency as a function of β for the JET 75225 discharge at $\rho = 0.15$. Comparison between GKW and TGLF with `WIDTH` values of 1.65 and 3.0 and `FILTER=-1.5`. 127
3.11. Parallel mode structure of the real part of the normalized electric potential ϕ for the Jet 75225 simulation at $\rho = 0.15$, for $\beta = 4.2\%$ with `WIDTH` values of 1.65 and 3.0 127
3.12. Effect of β' on growth rates for (a) ITG regime at $\beta = 0.1\%$ and (b) KBM regime at $\beta = 1.5\%$, for the Waltz Standard case with $k_\theta \rho_s = 0.15$ and $\hat{s} = 1.0$. 128
3.13. Growth rates and frequencies as a function of β for the Waltz Standard case with β' proportional to β, at $\hat{s} = 1.0$. 128
3.14. Relative differences between TGLF and GKW for the growth rate (α_γ), frequency (α_ω), and linear mode weights (α_{Γ_e}, α_{Q_i}, α_{Q_e}) in the Waltz Standard case at $k_\theta \rho_s = 0.4$. 129
3.15. Spectra of linear growth rates and real frequencies as a function of the binormal wavevector $k_\theta \rho_s$ for the JET 75225 discharge at $\rho = 0.15$. The spectra are shown for TGLF configurations with the default filter, high `Nbasis`, and the new filter settings. 131
3.16. Growth rate and frequency as a function of $k_\theta \rho_s$ for the JET 75225 discharge. Comparison of GKW with TGLF `Filter` = 0, 1.5 and -1.5. 133
3.17. Decision Tree for New Filter 134
3.18. Parallel mode structure of the real part of the normalized electric potential ϕ_N for the JET 75225 simulation at $\rho = 0.15$ for different values of $k_\theta \rho_s$ and TGLF settings. 134
3.19. Growth rate (γ), frequency (ω_r), and linear mode weights variations for Jet #75225 case as a function of plasma β, at two different radial positions, $\rho = 0.15$ ($k_\theta \rho_s = 0.29$) and $\rho = 0.33$ ($k_\theta \rho_s = 0.32$). 136

4.1. Time evolution of turbulent fluxes for varying ion and electron temperature gradients in nonlinear GKW simulations. Cases 1,2,3 and 4 are shown. The reference case corresponds to $R/L_{Ti} = 4.2$ and $R/L_{Te} = 2$. . 141
4.2. $\langle|\delta\phi|^2\rangle$ profiles from GKW (red) and TGLF simulations for five different settings. Case numbers are indicated referring to Table 4.1. 142
4.3. Comparison of ion and electron heat and particle fluxes between TGLF and GKW. Red points represent simulations without shearing rate, blue points include it, and green markers show results from the hybrid GKW-QL approach. The dashed line indicates perfect agreement. 145
4.4. Comparison of electrostatic (ϕ) and magnetic flutter ($A_\parallel$) contributions to ion and electron heat fluxes between TGLF and GKW. 146
4.5. Spectrum decomposition of ion heat flux (Q_i) for TGLF and GKW, showing electrostatic (ϕ) and magnetic flutter ($A_\parallel$) contributions for cases 3 ($R/L_{T_e} = 1.5$), 1 ($R/L_{T_e} = 2$), 4 ($R/L_{T_e} = 2.5$), and 12 ($R/L_{T_e} = 2.5$ and ExB shearing). 147
4.6. Spectrum decomposition of electron heat flux (Q_e) for TGLF and GKW, showing electrostatic (ϕ) and magnetic flutter ($A_\parallel$) contributions for cases 3 ($R/L_{T_e} = 1.5$), 1 ($R/L_{T_e} = 2$), 4 ($R/L_{T_e} = 2.5$), and 12 ($R/L_{T_e} = 2.5$ and ExB shearing). 148
4.7. Comparison of TGLF and GKW fluxes as a function of R/L_{Te} and R/L_{Ti}. 149

List of Tables

1. Paramètres plasma normalisés IMAS pour la décharge JET #75225 . . . 12
2. Résumé des paramètres plasma variés dans les 14 simulations non linéaires avec GKW. Le cas 1 correspond au cas de référence. Les valeurs en gras indiquent les écarts par rapport au cas de référence. 16
3. Réglages optimisés des paramètres de TGLF pour la modélisation de la turbulence KBM. 16

2.1. Mapping of magnetic equilibrium parameters from Miller parameterization to TGLF input file notations. 78
2.2. TGLF Normalizations 80
2.3. IMAS Normalizations 80
2.4. IMAS normalized plasma parameters of the Waltz Standard case 94

3.1. IMAS normalized plasma parameters of the Waltz Standard case 122
3.2. IMAS normalized plasma parameters of the JET 75225 discharge 130

4.1. Summary of the plasma parameters varied in the 14 nonlinear GKW simulations. Case 1 corresponds to the reference case. Bold values indicate deviations from the reference case. 140
4.2. Optimized TGLF parameter settings for modeling KBM turbulence . . 140
4.3. $k_\theta \rho_s$ spectra for `KYGRID_MODEL` = 1 and 4 (IMAS normalizations) 143

1. Introduction

In this introduction, we will present concepts that are central to understanding and modeling turbulent transport in tokamak plasmas, which is a key focus of this PhD research. Specifically, we will introduce two approaches for simulating plasma turbulence: reduced quasi-linear models and non-linear gyrokinetic codes. The primary objective of this thesis is to assess the accuracy of a reduced fluid quasi-linear model by comparing its predictions with those from a higher fidelity gyrokinetic model, particularly in high-beta tokamak plasmas where electromagnetic effects play a significant role.

1.1. Fusion energy

1.1.1. Current Global Energy Landscape

The global demand for energy has been steadily increasing, with an annual growth rate of about 1% between 2019 and 2023 [26]. Historically, energy transitions have involved the addition of new sources rather than the replacement of existing ones. For instance, coal, followed by oil and later gas, was added to the energy mix, without fully replacing earlier sources [26]. Figure 1.1 illustrates this trend, showing that despite the adoption of renewable energy sources like wind, solar, and nuclear, fossil fuels continue to dominate the global energy supply, currently accounting for approximately 80% of it [27]. This reliance on fossil fuels poses two major challenges: first, fossil fuel reserves are finite, making their continued exploitation unsustainable in the long term; second, the use of fossil fuels significantly contributes to carbon emissions, which must be rapidly reduced to mitigate climate change.

Global energy-related CO2 emissions increased by 5% between 2015 and 2022 [28]. In 2022 alone, emissions grew by 0.9% [29], and by 1.1% in 2023, reaching a record high of 37.4 billion tonnes (Gt) [30]. Without rapid intervention, this trajectory threatens to exhaust the carbon budget estimated by the Intergovernmental Panel on Climate Change (IPCC), which is aligned with limiting global temperature rise to 2°C by the early 2040s [26]. Today's energy transition must focus on substituting fossil fuels with low-carbon alternatives to mitigate their environmental impact and ensure long-term sustainability. The goal is to accelerate the growth of low-carbon energy sources, such as wind, solar, and nuclear, to reduce the global reliance on fossil fuels. While fossil fuel consumption remains high, there are signs of progress. Low-carbon renewable energy, particularly from wind and solar, has grown rapidly, more than doubling since 2018, as shown in Figure 1.1 [26]. This expansion has helped slow the pace of emissions

growth. However, the energy transition is still largely in a phase of addition rather than substitution. The deployment of low-carbon energy technologies, including solar, wind, and electric vehicles, has played a crucial role in reducing the rate of emissions growth. Between 2019 and 2023, energy-related emissions increased by around 900 Mt, but this rise would have been three times greater without the expanded use of low-carbon technologies such as solar PV, wind, nuclear energy, heat pumps, and electric vehicles [30]. Despite these efforts, coal remains a significant contributor to emissions, accounting for 70% of the increase in emissions from energy combustion in 2023 [30]. While technologies like electric vehicles reduce emissions during operation, their production, recycling, and potential reliance on fossil-fuel-generated electricity can still contribute significantly to CO2 emissions. The rise in low-carbon energy sources has helped mitigated emissions growth, but their adoption has not kept pace with growing global energy demand and has only slowed, rather than reversed, the overall trend.

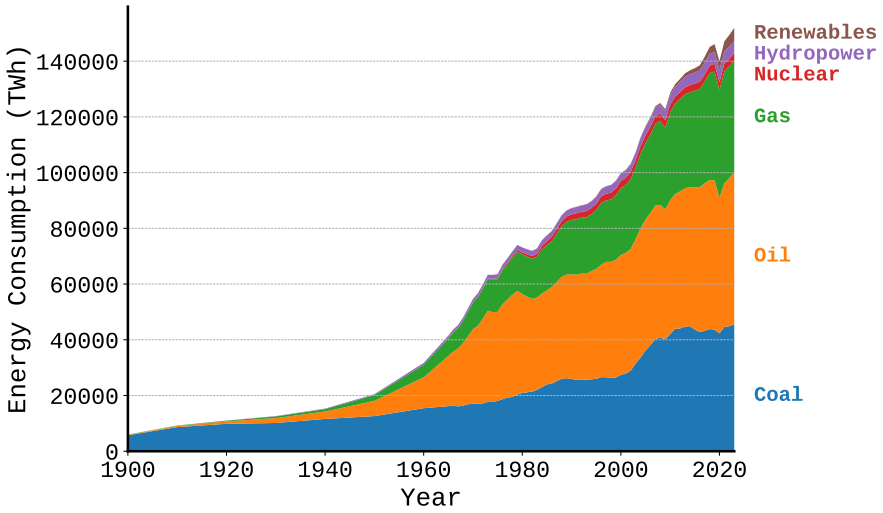


Figure 1.1. – **Global Direct Primary Energy Consumption Over Time.** Energy consumption is measured in terawatt-hours (TWh) [1]. The energy presented represents *direct primary energy*, which refers to energy available in its raw form, such as the fuels burnt in power plants, before it has been converted to secondary energy, like electricity. The data sources are from: *Energy Institute - Statistical Review of World Energy (2024); Smil (2017)*, with major processing by Our World in Data: https://ourworldindata.org/energy

A critical need exists for new energy solutions that can meet global demand while significantly reducing emissions. Decarbonizing electricity generation and enhancing energy efficiency are fundamental strategies. According to the International Energy Agency (IEA) Credible Pathways to 1.5°C report [29], by 2030, the annual addition of

1. A watt-hour is the amount of energy delivered by one watt of power over the span of one hour; since one watt is equivalent to one joule per second, a watt-hour equals 3600 joules of energy.

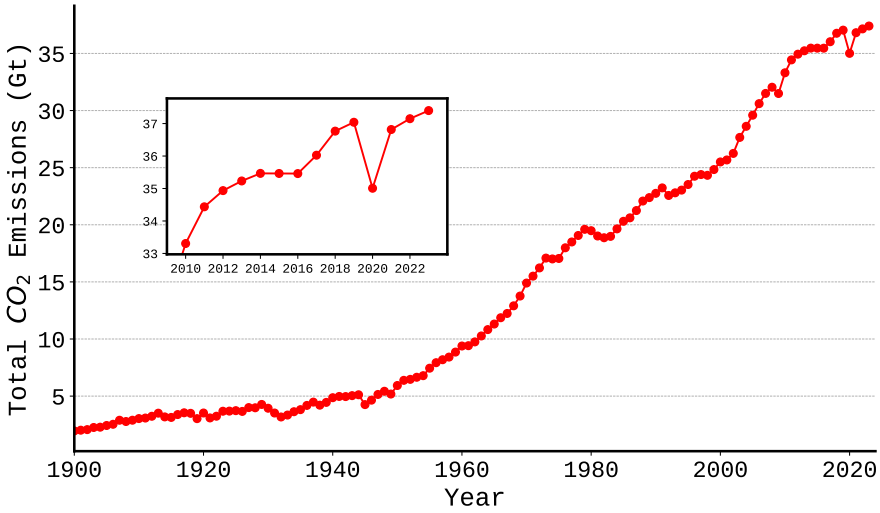


Figure 1.2. – **World CO_2 Emissions Over Time.** Total CO_2 emissions are measured in gigatonnes (Gt). The data includes all major sources of emissions, such as from coal, oil, gas, cement, flaring, and other industries. The zoomed inset focuses on the period from 2010 to 2023, showing more recent trends in global emissions. The data source is from: *Global Carbon Budget (2023)*, with major processing by Our World in Data: https://ourworldindata.org/co2-emissions.

renewable energy capacity must triple compared to 2022 levels, with 90% of all new capacity coming from clean energy sources. The report also states that: "There is no credible pathway to limiting warming to 1.5°C without steep and immediate reductions in energy-related CO2 emissions" [29]. This urgency highlights the necessity for a rapid scale-up in the development of sustainable energy technologies. Momentum toward decarbonization is growing. The IEA's Net Zero Roadmap [28] confirms that although achieving the 1.5°C target is difficult, it remains possible with substantial investment in low-carbon technologies. Since 2020, investments in low-carbon energy have increased by 40% (World Energy Outlook 2023). The IEA identifies nuclear fission as a pivotal low-carbon energy source in the transition to a sustainable energy future. As one of the few scalable technologies capable of delivering consistent baseload electricity, nuclear fission energy is uniquely positioned to complement the intermittency of renewables like wind and solar. Its ability to provide reliable energy makes it indispensable in achieving deep emissions reductions, particularly as countries seek to phase out fossil fuels and scale up renewable capacity. In the IEA's Net Zero Emissions by 2050 Scenario, expanding nuclear fission capacity is seen as critical to balancing growing energy demands while ensuring grid stability and lowering global carbon emissions [28]. Among the promising long-term solutions is nuclear fusion, which could provide a reliable low-carbon energy source. Despite its potential, nuclear fusion was not included in any IEA reports, as it still remains in the research phase and could only become a viable energy source in the long term. Fusion energy offers

several promising benefits in terms of sustainability and CO2 emissions.

1.1.2. Nuclear Fusion

Nuclear fusion has long been recognized for its potential to provide vast amounts of energy, though early research was primarily driven by military applications, such as the development of the hydrogen bomb. Theoretical studies on fusion reactions date back to the 1920s and 1930s, when researchers explored nuclear processes occurring in the cores of stars [31, 32, 33]. Fusion research became more organized and collaborative following its public revelation at the Second United Nations Conference on the Peaceful Uses of Atomic Energy in 1958 [34], which marked the end of nearly a decade of secret studies. This event laid the foundation for international collaborations, such as the ITER project [35]. A very great and complete overwiew of the history of nuclear fusion particurally on the events that have produced fusion's global signature partnership can be found in [34]. Since the energy sector is a major contributor to global greenhouse gas emissions, the introduction of a high-density, low-carbon energy source like nuclear fusion could play a pivotal role in achieving climate action goals. While nuclear fission has successfully generated energy without CO2 or pollutant emissions, it still faces challenges like the creation of long lasting nuclear waste and reliance on non-renewable uranium. [2]

The Sun's energy, which originates primarily from nuclear fusion reactions, motivated humanity to explore and replicates thoses reactions. Despite the complexity of controlling fusion reactions, nuclear fusion has remained appealing due to several key advantages. It generates extremely high power densities, could potentially use a very large sufficient fuel supply (Future fusion reactors are expected to face significant challenges in securing a reliable supply of tritium. [36]), has a minimal carbon footprint [37], lacks chain reactions and compared to nuclear fission, it produces much less long lived radioactive wastes (only to fusion device materials by indirect activation).

Fusion reactions involve the combination of light atomic nuclei under extremely high temperatures. At these temperatures, matter exists in the plasma state, where nuclei move freely, and fusion can occur if the temperature is sufficiently high to enable the nuclei to collide with enough energy to overcome their electrostatic repulsion. The primary challenge in fusion by magnetic confinement research is to sustain these conditions long enough for significant energy production, which necessitates advanced magnetic confinement techniques. The most researched fuels for nuclear fusion involve hydrogen isotopes (deuterium and tritium), helium-3, or boron-11 [38]. The fusion cross section for different reactions are reported in Figure 1.3 .

Among the fusion reactions, the deuterium-tritium (D-T) reaction is favored due to its high fusion reaction rate $\langle \sigma v \rangle$ at relatively low temperatures, making it the primary focus of current fusion research and development efforts. The deuterium–tritium

2. While nuclear fission relies on non-renewable uranium, fast neutron reactors can significantly extend the available fuel supply, delaying concerns about uranium scarcity. In contrast, nuclear fusion requires materials like lithium-6, tungsten, helium, and tritium, the latter of which is particularly rare and difficult to produce in large quantities.

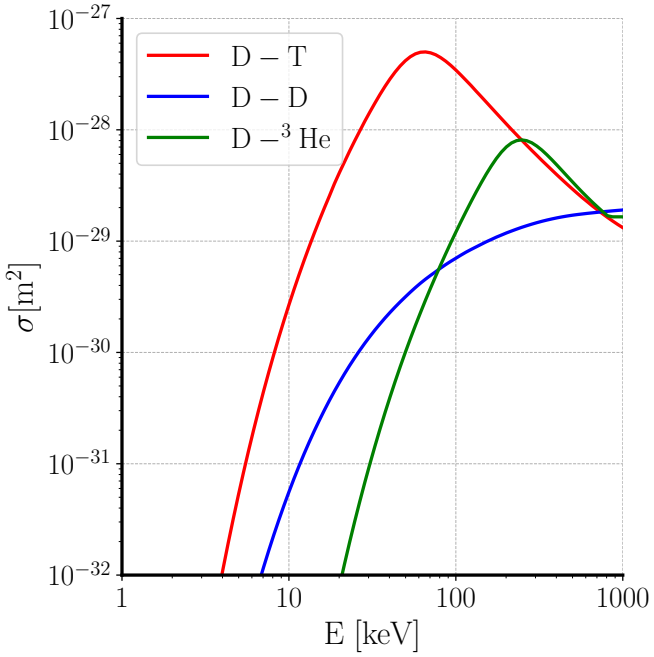


Figure 1.3. – Experimental cross sections (σ) for the D-T, D-D, and D-^{3}He fusion reactions. The x-axis represents the energy in the laboratory frame. Data are derived from the ENDF/B-VIII.0 library [39].

reaction is :

$$^2\mathrm{D} + {}^3\mathrm{T} \rightarrow {}^4\mathrm{He} + n + 17.6\,\mathrm{MeV} \tag{1.1}$$

In this reaction, deuterium (^{2}D) and tritium (^{3}T) nuclei fuse to form a helium nucleus (^{4}He) and a neutron, releasing 17.6 MeV of energy. The majority of this energy, 14.1 MeV, is carried by the neutron, which escapes the plasma and can be absorbed by a blanket surrounding the plasma to breed new Tritium and convert its kinetic energy into heat for electricity generation. The helium nucleus retains the remaining 3.5 MeV of energy, which helps sustain the plasma temperature.

For a fusion reactor to achieve net energy gain, the power produced by fusion must exceed the total power required to operate not just the plasma, but also all auxiliary systems such as the heating systems, magnetic confinement, and cooling of components like the divertor and blankets. The energy gain factor, Q, is defined as the ratio of the fusion power generated, P_{fusion}, to the power input required to sustain the plasma, P_{input}:

$$Q = \frac{P_{\mathrm{fusion}}}{P_{\mathrm{input}}}.$$

In a practical reactor, Q needs to be significantly greater than 1 to ensure energy efficiency, with a target of approximately $Q \gtrsim 40$. The Lawson criterion, often used to describe the conditions for fusion breakeven in the plasma itself, defines the point where the power produced by fusion equals the power required to maintain the plasma, which corresponds to $Q = 1$ [40]. An extension of the Lawson criterion, introducing

the triple product $nT\tau_E$ for D-T fusion in the 10–20 keV range, can be formulated as [41]:

$$nT\tau_E > 3 \times 10^{21}\,\mathrm{m}^{-3}\,\mathrm{keVs} \tag{1.2}$$

where n is the plasma density, T the plasma temperature, and τ_E the energy confinement time. This triple product can be used as a metric for comparing nuclear fusion devices that use different confinement methods and their performance in achieving energy breakeven. Figure 1.4 shows the evolution of the triple product ($nT\tau_E$) across several decades of research. Early devices like ZETA and T-3 achieved modest values, marking the beginning of experimental fusion efforts. Over time, significant advancements were made in machines like JET, JT-60U, and TFTR, where the triple product increased substantially, approaching the critical threshold necessary for breakeven conditions. The progress seen in these experimental results highlights the continuous improvement in plasma performance, ultimately leading to ITER, which is projected to achieve even higher values, moving closer to the goal of sustained fusion energy.

ITER, currently under construction, is designed to operate in a region where Q is predicted to range between 6 and 30 [13], depending on plasma conditions and auxiliary heating power requirements. According to empirical and theory-based transport models [13, 42], ITER aims to achieve $Q = 10$ in its standard operation mode, meaning that the fusion power output will be ten times greater than the heating power coupled to the plasma. In addition to reaching high Q values, ITER also aims to achieve self-sustained fusion, where the power generated by the alpha particles from fusion reactions (P_α) is sufficient to sustain the plasma without external power input (P_{ext}). For self-sustained conditions, Q must be greater than 5, as P_α accounts for one-fifth of the total fusion power output (P_{fus}), with the remaining power carried by neutrons. When $Q > 5$, the energy provided by alpha particles becomes sufficient to maintain the plasma without additional external heating. This scenario corresponds to what is known as a burning plasma, in which the majority of the heating is provided internally by the fusion reactions themselves, thus minimizing the need for auxiliary heating [42].

Achieving controlled nuclear fusion remains an immense technical challenge. The extreme conditions required for fusion make it necessary to use advanced confinement techniques to control the plasma. Among the different approaches proposed for energy production [43, 44, 45, 46, 47], magnetic confinement has emerged as the most promising approach for energy production, and it is the central focus of this thesis. Specifically, the tokamak design, which has demonstrated the highest potential for sustained plasma confinement, will be examined in details in the following sections.

1.1.3. Tokamak Configuration and Magnetic Confinement

A **Tokamak** is a device designed to confine a plasma using magnetic fields in a toroidal (doughnut-shaped) configuration. The word "tokamak" is derived from the Russian acronym for "toroidal chamber with magnetic coils" (TOroïdalnaïa KAmera MAgnitnymi Katushkami). The plasma in a tokamak consists of charged particles,

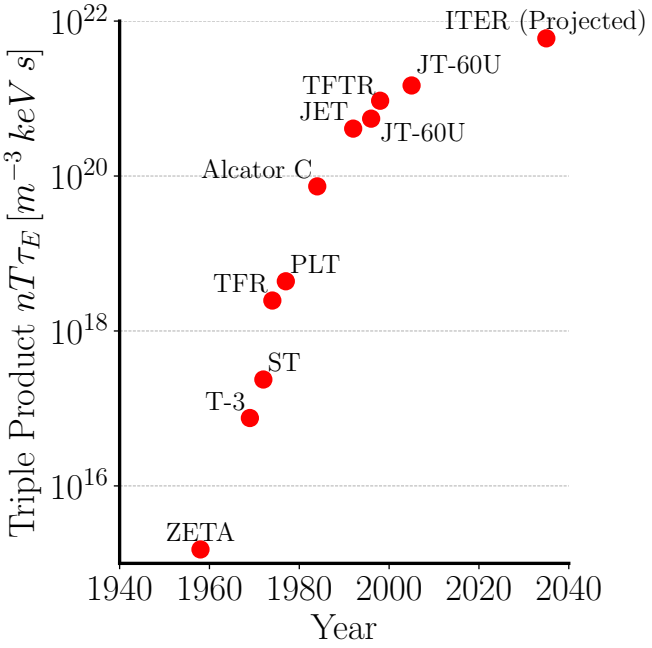


Figure 1.4. – Evolution of the triple product ($nT\tau_E$) achieved by fusion devices over time. Data from: ITER [13], JT-60U [14, 15], TFTR [16], JET ([17], Alcator-C [18], PLT [19], TFR [20], ST [21], T-3 [22], ZETA [23].

electrons and ions sensitive to magnetic fields. By using these fields, the tokamak controls the motion of these particles, preventing them from escaping and allowing the plasma to remain confined at the high temperatures necessary for fusion reactions to occur.

Within the tokamak, charged particles undergo **gyro-motion** as they spiral around the magnetic field lines. This motion is characterized by the **gyrofrequency** ($\Omega = \frac{eB}{m}$), where e is the particle's charge, B is the magnetic field strength, and m is the particle's mass. Typical values for the electron and ion gyrofrequencies in a tokamak are $\Omega_e \approx 10^9$ Hz for electrons and $\Omega_i \approx 10^7$ Hz for ions. The radius of this circular motion, called the **gyro-radius** or Larmor radius ($\rho = \frac{v_\perp}{\Omega}$), depends on the velocity ($v_\perp$) of the particle perpendicular to the magnetic field. The Larmor radius for electrons is smaller than that of ions by a factor of $\sqrt{\frac{m_i}{m_e}}$, where m_e and m_i are the electron and ions masses, respectively. Typical values for the Larmor radius are $\rho_e \approx 0.02 - 0.1$ mm for electrons and $\rho_i \approx 1 - 6$ mm for ions. This behavior ensures that charged particles remain confined within the magnetic field structure, reducing the likelihood of particle loss and allowing for effective plasma confinement.

The basic principle behind plasma confinement in a tokamak relies on both toroidal and poloidal magnetic fields. This configuration is illustrated in Figure 1.5. The toroidal field is produced by external magnetic coils arranged in a circular pattern around the tokamak. This field wraps around the plasma in the toroidal direction (the long way around the doughnut). However, the toroidal magnetic field alone is

insufficient for confinement, as it creates gradients (∇B) and curvature effects that cause charged particles to drift vertically. These drifts, which are opposite for ions and electrons, result in electric fields that drive particles radially outwards, out of the confinement region. To counteract this, a poloidal magnetic field is introduced, generated by inducing an electric current through the plasma itself. This current is driven by a central solenoid, which acts like a transformer, inducing the necessary plasma current to create the poloidal field. The combination of the toroidal and poloidal magnetic fields creates helicoidal magnetic field lines, which wrap around the plasma in a helical pattern. This twisting of the magnetic field lines helps counteract the undesirable effects, preventing the vertical charge separation induced by the ∇B and curvature drifts. In addition to the central solenoid, additional poloidal field coils are employed to control and shape the magnetic equilibrium of the plasma in greater detail. These shaping coils help form specific configurations, such as an "X-point" near the divertor or to maximize plasma elongation to improve confinement. External shaping coils also ensure the stability of the plasma, ensuring that it remains confined and does not come into contact with the walls of the tokamak. The magnetic field lines define nested flux surfaces within the plasma, where each surface represents a region of constant magnetic flux in what can be described as a layered onion-like configuration.

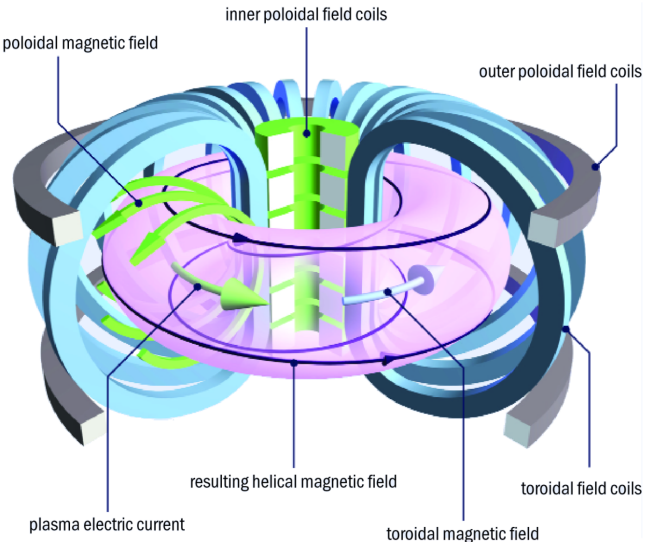


Figure 1.5. – Schematic diagram of a tokamak, illustrating the key components of magnetic confinement. (Credit : [24])

In tokamaks, the toroidal plasma current (I_P) is initially driven inductively by the central solenoid, which is crucial for initiating and ramping up the current during the startup phase. However, inductive operation generates a pulsed plasma, limiting the duration of confinement. For continuous, steady-state operation, a combination of inductive and non-inductive methods is required to sustain the plasma current [48, 49]. Even in steady-state scenarios, the central solenoid remains necessary for initiating the plasma current, while non-inductive currents, such as the bootstrap current,

maintain it. The bootstrap current arises naturally from pressure gradients in the plasma and is supplemented by external heating methods, such as Electron Cyclotron Resonance Heating (ECRH) and lower hybrid waves. ECRH launches microwave beams at frequencies that match the motion of electrons along the magnetic field lines, heating the plasma and helping sustain the non-inductive current necessary for steady-state operation.

Tokamaks are one of the two main method to magnetically confine fusion plasmas. Alternative designs, such as the stellarator, offer different magnetic confinement strategies. Unlike the tokamak, the stellarator does not rely on a plasma current to generate the poloidal field. Instead, the complex geometry of the stellarator's magnetic coils is designed to provide all necessary magnetic fields, making it inherently more stable by avoiding current-driven instabilities that can occur in tokamaks. While stellarators offer the advantage of continuous operation and greater stability, their complex magnetic coil designs make them more challenging to construct, which has so far limited their practical application towards a fusion power plant As a large-scale international collaboration, ITER's primary goal is to demonstrate key steps toward achieving controlled nuclear fusion. Conceived during the height of the Cold War in 1985 and formally launched in 2007, ITER is now supported by seven major partners: the European Union, India, Japan, China, Russia, South Korea, and the United States. Located in Cadarache, France, ITER will be the largest and most advanced tokamak ever constructed. The ITER Tokamak will be the largest ever built, with a plasma volume of 830 cubic metres. ITER is designed to be an experimental tool capable of generating long-duration plasmas and improved confinement. The machine's objectives include:

1. **Sustaining Fusion Conditions**: ITER aims to achieve a deuterium-tritium plasma in which the fusion reactions are sustained primarily by internal fusion heating. This will allow researchers to explore the behavior of a *burning plasma*, where the majority of heating comes from the fusion reactions themselves. ITER is designed to produce 500 MW of fusion power for long pulses, achieving a power gain factor of $Q = 10$. While ITER will not generate electricity, this achievement will demonstrate that fusion can produce net energy gain within the plasma, laying the groundwork for future reactors that aim to convert fusion power into electricity.
2. **Testing Fusion Power Plant Technologies**: ITER will be used to test critical technologies for fusion power plants, such as plasma heating, control, diagnostics, cryogenics, and remote maintenance.
3. **Tritium Breeding**: ITER will explore the feasibility of producing tritium, the fuel for fusion, within the reactor using lithium. This is essential because the global supply of tritium is not sufficient for future large-scale fusion power plants. Also, ITER will not be able to achieve more than 1 dpa (displacements per atom), which is insufficient to test the long-term aging and durability of reactor components under fusion-relevant conditions.

While ITER is an experimental device, it is expected to provide essential experimental

data to study burning plasmas and validate models needed for designing future fusion reactors capable of generating power on a commercial scale.

1.1.4. Importance of the Beta (β) Parameter in Fusion

In the domain of magnetically confined plasmas, the dimensionless parameter β is a fundamental quantity that is defined as the ratio of plasma kinetic pressure ($p_{\text{plasma}} = 2nk_BT$) [3] to magnetic pressure ($p_{\text{magnetic}} = B^2/2\mu_0$). This relationship is expressed as:

$$\beta = \frac{p_{\text{plasma}}}{p_{\text{magnetic}}} = \frac{4\mu_0 nk_BT}{B^2} \tag{1.3}$$

where μ_0 denotes the permeability of free space, n is the plasma density, T is the temperature, and B is the magnetic field strength. This parameter is crucial because it directly measures how effectively the magnetic field confines the plasma, which is key to sustaining the high-pressure environment required for fusion reactions. Initially, it was thought that the beta parameter would be severely restricted by equilibrium constraints [50, 51, 52]. However, further equilibrium modeling demonstrated that much higher beta values could be achieved, resolving earlier concerns and opening new avenues for advanced tokamak designs [53].

The paper [54] presents a detailed analytical derivation showing that when operational limits, such as the density limit and the β limit (see section 1.2.1), are taken into account, the triple product of Eq. 1.2 becomes primarily dependent on the fusion power P_{fus}, and only weakly dependent on the size of the tokamak. This is an important finding, as it suggests that achieving high fusion power is more reliant on optimizing plasma parameters rather than increasing the physical size of the device. Therefore, β governs the maximal achievable power in a fusion reactor. The results indicate that higher values of β allow for greater fusion power without requiring a larger device, making the optimization of β critical for both performance and cost-efficiency in fusion reactor design. Furthermore, the paper also demonstrates that the minimum power required to reach fusion reactor conditions is determined mainly by physics, specifically, energy confinement, while the smallest possible size of the reactor is constrained by engineering and technological factors. This highlights the importance of β not only for maximizing power output but also for enabling more compact reactor designs. In [55], scaling laws are applied to study the impact of these operational constraints on tokamak dimensioning. It is found that fusion power scales as β^2. This reinforces the conclusion that maximizing β is essential for improving the power output and overall efficiency of future fusion reactors. The relation can be understood from the fundamental expression of fusion power P_{fus}, which is proportional to the product of the deuterium (n_D) and tritium (n_T) densities and the reaction cross-section $\sigma_{D,T}$:

$$P_{\text{fus}} \propto n_D n_T \langle \sigma_{D,T} \rangle.$$

3. The factor of 2 arises from the combined contributions of electrons and ions, assumed to share the same temperature.

At typical plasma temperatures ($T \sim 10\,\text{keV}$) [4], the reaction cross-section for deuterium-tritium fusion behaves approximately as $\sigma_{D,T} \propto T^2$. Therefore, the fusion power P_{fus} scales as:

$$P_{\text{fus}} \propto n^2 T^2.$$

Given that the plasma β is defined as the ratio of plasma pressure to magnetic pressure, $\beta \propto \frac{nT}{B^2}$, it follows that [5]:

$$P_{\text{fus}} \propto \beta^2 B^4.$$

ITER's design aims to operate in a high-β regime to maximize energy efficiency and fusion power output. To better understand the behavior of high-β plasmas, advanced tokamak scenarios are being explored in present-day experimental tokamaks, with a specific focus on optimizing plasma performance under high-β conditions. Notably, a significant portion of the Joint European Torus (JET) research has focused on achieving transient high-performance plasmas [56]. In particular, JET has been instrumental in developing and testing so-called hybrid scenarios, which are designed to achieve higher normalized β values while maintaining stable plasma performance. For ITER, these hybrid scenarios are expected to enable operation at lower plasma currents ($I_p < 15,\text{MA}$), facilitating longer discharges. These discharges will allow ITER to operate at higher β with enhanced pulse duration and stability. The hybrid scenario provides an operational advantage by minimizing MHD instabilities and optimizing confinement in high-β regimes. The value of β is often normalized to account for different plasma sizes and magnetic field strengths. The normalized beta, β_N, is defined as:

$$\beta_N = \langle\beta\rangle \frac{a B_T}{I_p} \tag{1.4}$$

where $\langle\beta\rangle$ is the volume-averaged plasma beta, a is the plasma's minor radius, B_T is the toroidal magnetic field at the plasma center, and I_p is the plasma current. The normalized β value, β_N, allows comparisons of plasma performance across different tokamaks by accounting for differences in size and magnetic field strength. A higher β_N indicates better plasma performance relative to the size of the device and the strength of the magnetic field.

Hybrid scenarios represent an advanced operational regime proposed for ITER. The key feature of this regime is the flattened q-profile in the plasma core, which helps to prevent the onset of MHD sawtooth modes. Sawtooth oscillations can trigger large Neoclassical Tearing Modes (NTMs), significantly limiting the performance of the discharge. By suppressing these modes, hybrid scenarios offer the potential for longer pulse durations and reduced disruptivity [57]. Since 2003, JET has conducted extensive research into hybrid H-mode scenarios and high-β operations, providing valuable data for the design of future fusion reactors such as ITER [56]. Early experiments

4. When considering the role of the plasma pressure parameter β in determining the maximum achievable power that maximize $P_{\text{fus}} \propto \beta^2 \langle\sigma_{D,T}\rangle / T^2$, the optimal temperature for maximizing fusion power is $T \approx 13\,\text{keV}$ [55].

5. Note that operating at high magnetic field B reduces the need to maximize β, enabling the plasma to remain in an electrostatic turbulence regime.

at JET [58] and DIII-D [59] observed reduced MHD activity, particularly in sawtooth instabilities, even at elevated β_N . Similarly, the ASDEX Upgrade tokamak has achieved good confinement at very high plasma β_N values, with discharges characterized by a triangularity of $\delta = 0.42$, an edge safety factor q_{95} between 3.6 and 4.1 (the notation q95 denotes the safety factor evaluated at 95% poloidal magnetic flux), and operation at 80–90% of the Greenwald density limit. Under these conditions, β_N values as high as 3.5 were obtained [60]. A comprehensive description of the development of advanced tokamak scenarios at JET, including high-β experiments and hybrid scenarios, can be found in the review by [57]. This work summarizes the progress made in exploring these operational modes up until 2008, offering valuable insights into high-β operation and its implications for ITER. Additional insights into the performance of hybrid scenarios, particularly with respect to high-β regimes, can be found in recent experiments such as [61]. These studies further demonstrate the potential of hybrid scenarios for improving plasma confinement and operational stability in large-scale tokamaks.

Spherical tokamaks, characterized by very small aspect ratio ($R/a \sim 1.5$) compared to typical standard tokamak ($R/a \geq 2.5$) presents many theoretical advantages, including notably their ability to achieve very high β values, making them particularly attractive for exploring high-performance plasma regimes [62, 63]. The National Spherical Torus Experiment (NSTX) was specifically designed to explore high-β regimes. One of its key goals was to achieve high β values while maintaining plasma stability. The results from NSTX not only validated theoretical predictions regarding MHD stability at high β, but also demonstrated the feasibility of achieving sustained high-performance plasmas in spherical tokamaks. [64, 65]. Despite their advantages, the higher sensitivity of large β_N plasmas to MHD instabilities poses a challenge for spherical tokamaks. As stated in [55], in the conclusion on the impact of scaling laws on tokamak reactor dimensioning: *"the relevance of these large β_N plasmas for a reactor may be questioned due to their inherent larger sensitivity to MHD instabilities, and the consequent higher risk of disruptions"*. Furthermore, large β_N plasmas typically require higher plasma current (I_P), which raises concerns regarding runaway electrons. Managing both MHD instabilities and the risks associated with runaway electrons becomes critical in the operation of tokamaks at high β_N.

1.2. Plasma Confinement and transport

1.2.1. Operational Limits in Tokamaks

In tokamaks, magnetic forces must balance the pressure exerted by the plasma to maintain stability. The maximum achievable β is constrained by a variety of Magnetohydrodynamic (MHD) instabilities, which include kink, tearing, and ballooning modes. These instabilities are destabilized when the pressure gradient or plasma current exceeds specific thresholds, leading to a loss of confinement. Two key operational limits affect the performance of tokamak plasmas: the Greenwald density limit [66]

and the Troyon β limit [67, 68].

The Greenwald density limit is an empirical upper bound on the plasma density, traditionally expressed as $n \sim I_P/a^2$ where I_p is the plasma current and a the minor radius of the plasma. When this limit is exceeded, the plasma becomes susceptible to density-driven instabilities, potentially leading to disruptions. However, recent research [69] has shown that the Greenwald limit, while useful, does not capture all the underlying physics. A more nuanced understanding has emerged based on the role of edge turbulent transport and edge collisionality. As detailed in [69], the density limit is not solely a function of plasma current, but also depends on factors such as heating power and edge turbulence. In particular, as the edge collisionality increases at higher densities, turbulent transport in the edge region becomes more intense, which leads to cooling, a collapse in the edge pressure gradient, and eventually disruption. This mechanism helps explain why exceeding the density limit can result in sudden loss of confinement. A new scaling law, based on first-principles physics, incorporates these effects and predicts a higher density limit for future devices like ITER. Unlike the Greenwald limit, this model accounts for the heating power applied to the plasma, providing a more accurate estimate of the maximum achievable density. Importantly, this research suggests that ITER can safely operate at higher densities than previously anticipated, expanding the operational window for future fusion reactors.

In MHD theory, the behavior of plasma can be described in two different frameworks:

— In **Ideal MHD**, the plasma is considered a perfect conductor with no resistivity, meaning the magnetic field lines are "frozen" into the plasma and move with it. This assumption simplifies the analysis of plasma stability and is useful for understanding fundamental stability limits.

— **Non-Ideal MHD** accounts for finite resistivity, allowing for phenomena like magnetic reconnection and resistive instabilities, which are critical for understanding disruptions in real plasmas.

The Troyon β limit defines the maximum β, that can be achieved before ideal MHD instabilities occur. This limit is expressed as $\beta_{\text{Troyon}} \sim \frac{I_P}{aB_T}$, where I_P is the plasma current, a is the minor radius of the plasma, and B_T is the toroidal magnetic field at the plasma center. Ideal MHD stability limits have been shown to accurately predict the scaling of the maximum β value as described by Troyon, yielding a normalized beta limit: $\beta_{N,\text{max}} \approx 3.5$ with $\beta_N = \beta(\%)\frac{aB}{I_P}$. Empirical observations from various tokamak experiments, where non-ideal MHD effects are minimal or do not develop into significant amplitudes, confirm that this limit is consistent with the maximum β_N achieved in earlier tokamak operations [70].

As illustrated in Figure 1.6, data from various tokamak devices show that the maximum β increases with I_p/aB_T, following a coefficient of approximately 3.5. This strong correlation supports the validity of the Troyon scaling limit in pseudo-ideal MHD regimes. The study by [70] extends the Troyon limit, proposing that the maximum achievable β can be more accurately described by:

$$\beta_{N,max} \approx 4 l_i \tag{1.5}$$

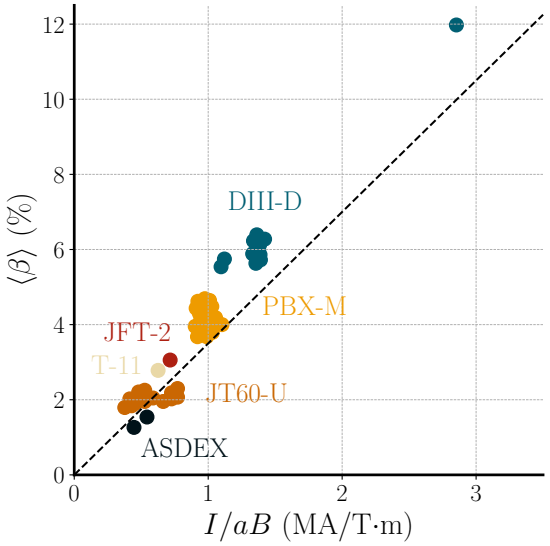


Figure 1.6. – Volume-averaged β versus I_p/aB_T for data from various high-β tokamak experiments. The dotted line represents the scaling $\langle\beta\rangle = 3.5\frac{I}{aB_T}$, showing the strong correlation with the Troyon limit. Reproduced from : [25]

where l_i is the internal inductance of the plasma. This internal inductance depends on the current distribution within the plasma and provides a more refined measure of β stability. In plasmas with a more peaked plasma current density $j(r)$-profile (hence higher l_i), this extension yields results that are more accurate than the Troyon limit. However, in typical plasma conditions, both limits yield comparable values for the maximum β.

While the ideal MHD limits provide a fundamental framework for understanding the constraints on β, non-ideal MHD effects also play a critical role in determining the maximum β achievable in long-duration tokamak experiments. These effects become particularly significant at higher β values, where pressure gradients and current profiles increase susceptibility to instabilities. A key phenomena linked to β-limiting behavior in non-ideal MHD regimes is the formation of neoclassical bootstrap current-driven islands, which has a direct impact on the stability of high-β plasmas: As β increases, the bootstrap current, a component of the plasma current driven by pressure gradients, becomes more significant. The formation of neoclassical bootstrap current-driven islands, often associated with NTMs, poses a major limitation on the achievable β in reactor-grade plasmas. NTMs are triggered by large pressure gradients or sawtooth crashes [6], which create magnetic islands that degrade plasma confinement. These islands can grow to a size where they significantly lower the achievable β_N, sometimes to values well below the Troyon limit. These non-ideal MHD effects impose additional constraints on the maximum β attainable in tokamak experiments and must be carefully managed to achieve stable high-β operation. More insights into the operational limits, derived from both ideal and non-ideal resistive

6. Periodic collapses in the core temperature and density

and kinetic MHD effects, can be found in the detailed reference [25] .

To achieve high fusion power, maximizing β is essential, as fusion power scales directly with it. However, ensuring MHD stability remains equally important. The precise limit of β is difficult to define, given the wide range of discharge scenarios and the nonlinear effects of various instability modes. Despite these complexities, the ongoing objective in fusion research is to increase β while maintaining the plasma in an MHD-stable state, balancing the competing demands of higher pressure and stability to push the performance limits of future reactors. While achieving high β is crucial for increasing fusion power, in practice, the plasma pressure in tokamaks often falls short of the ideal MHD stability limits. This is primarily due to transport mechanisms, particularly turbulent transport, which leads to the loss of energy and particles from the plasma before reaching those limits. Understanding and controlling these transport processes is key to further improving the confinement and performance of future fusion reactors.

1.2.2. Classical, Neoclassical and Turbulent Transport in Tokamaks

Plasma transport processes in tokamaks are typically divided into three categories: classical, neoclassical, and turbulent transport, depending on the mechanism responsible for it and on the associated temporal and spatial scales.

Classical Transport

Classical transport, first described by Braginskii [71], occurs in collisional plasmas where the particle mean free path is short compared to the size of the device. This type of transport arises due to random Coulomb collisions between charged particles and can be modeled as a diffusive process. In a magnetized plasma, charged particles follow helical orbits around magnetic field lines, known as gyro-motion. The radius of this cyclotronic motion is the Larmor radius, ρ_L. In classical transport, it is assumed that after completing one or several gyro-motions, a particle undergoes a collision, which changes its direction and causes it to move by a step size of the order of the Larmor radius. This process repeats itself, forming a random-walk pattern that characterizes the diffusive nature of classical transport. The frequency of these collisions in hot magnetized plasmas is typically around 10^3Hz [7], and therefore, the step size in this diffusive process can be approximated as $\Delta x = \rho_L$. The diffusion coefficient for classical transport can be estimated as:

$$D_{\text{classical}} \sim \frac{\Delta x^2}{\Delta t} \sim \rho_L^2 \nu_{\text{col}},$$

7. For typical conditions in the JET tokamak, the electron-ion collision frequency $\nu_{\text{coll}}^{e/i}$ varies between $10^2 - 10^5$ Hz.

where ν_{col} is the collision frequency. Under typical tokamak conditions, this results in a classical diffusion coefficient for ions of:

$$D_{\text{classical}} \sim 0.001\,\text{m}^2/\text{s}.$$

with even lower values for electrons. Although classical transport provides a fundamental understanding of collisional transport, in most cases, it is relatively weak compared to other transport mechanisms. As a result, in tokamaks, classical transport is often overshadowed by neoclassical and turbulent transport.

Neoclassical Transport

In classical theory, transport is determined locally and is only weakly influenced by the macroscopic field structure. Neoclassical theory focuses on the influence of the magnetic field structure on particle trajectories and the resulting collisional transport. The primary distinction between classical and neoclassical transport lies in the radial displacement (Δx) after each collision. In classical transport, this displacement is on the order of the Larmor radius, $\Delta x_{\text{classical}} \sim \rho_L$. However, in neoclassical transport, particles may become confined to specific trajectories, such as *banana orbits*, leading to greater radial displacements. Banana orbits are elongated, loop-like trajectories that occur in regions of weaker magnetic field. The radial displacement for particles in banana orbits scales with the radial width of the orbit, given by:

$$\delta r_b \sim 2\rho_L\, q \sqrt{\frac{2R_0}{r}},$$

where q is the safety factor, R_0 is the major radius of the tokamak, and r is the minor radius of the flux surface. For typical tokamak conditions, that width can reach scales on the order of tens of Larmor radius, $\Delta x_{\text{neoclassical}} \sim \delta r_b \sim 10\rho_L$, enhancing radial transport compared to classical predictions.

A critical factor in neoclassical transport is the normalized collisionality, which represents the relative magnitude of the collision frequency ν compared to the transit frequency ω_t. The transit frequency describes the rate at which a particle completes a full orbit around a magnetic flux surface, and it is given by:

$$\omega_t = \frac{v_{\text{th}}}{qR}$$

Here, v_{th} is the particle thermal speed, q is the safety factor, which represents the number of poloidal turns a magnetic field line makes for each toroidal loop, and R is the major radius of the tokamak. In high-temperature fusion plasmas, the transit frequency is typically on the order of $10^3 - 10^4$ Hz for ions and $10^6 - 10^7$ Hz for electrons. Depending on the collisionality, neoclassical transport occurs in distinct regimes:

— **Pfirsch-Schlüter Regime**: In plasmas with high collisionality, where $\nu/\omega_t \gg 1$ (i.e., the particle orbit length is much longer than the mean free path), particle

orbits are frequently interrupted by collisions before completing a full transit around the magnetic flux surface. This regime is known as the Pfirsch-Schlüter regime, where collisions dominate the behavior of particle motion.

— **Banana Regime**: In low-collisionality plasmas, where $\nu/\omega_t \ll 1$ (i.e., the mean free path is much longer than the orbit length), particles are able to complete their orbits. In this regime, a significant fraction of particles become "trapped" in the magnetic wells of the toroidal field, following elongated orbits that resemble the shape of a banana. As discussed earlier, these trapped particles lead to a larger diffusion coefficient:

$$D_{\text{neo}} \sim \frac{\Delta x^2}{\Delta t} \sim (10\rho_L)^2 \nu_{\text{col}} \sim 0.1\,\text{m}^2/\text{s}.$$

Neoclassical transport, is much larger than classical transport and can have a significant impact on plasma confinement. This is especially true for impurities with high charge and mass, where neoclassical effects can dominate the transport, leading to central peaking of impurity density profiles, as reviewed in [72]. The neoclassical physics also gives rise to the bootstrap current, which is driven by pressure gradients and plays a crucial role in maintaining plasma confinement without relying solely on external current drives.

For a detailed and comprehensive explanation of classical and neoclassical transport, one can refer to [73] and the review [74].

Turbulent Transport

Turbulent transport in tokamaks is driven by small-scale fluctuations in the plasma, which arise from a variety of microinstabilities. These instabilities are fueled by free energy stored in gradients of density, temperature, and magnetic fields. Among the most significant of these microinstabilities are drift waves, which play a central role in generating turbulence. Drift waves occur due to the collective oscillations of plasma particles in the presence of a magnetic field, where differences in the dynamics of electrons and ions, result in phase-shifted responses. These waves are driven by the pressure gradients and propagate at speeds between the drifts velocities of ions and electrons. In maintaining plasma quasineutrality, drift waves lead to fluctuations in the electric potential. These fluctuations, in turn, drive turbulent transport of both particles and energy throughout the plasma. Turbulence, however, is not solely caused by drift waves. Another key source of turbulence in tokamaks is interchange instabilities, which occur when the pressure gradient (∇P) and magnetic field curvature (∇B) act together to destabilize the plasma, particularly on the low-field side of the tokamak, allowing the outward pressure forces to displace plasma. In Section 3.1, we will derive two simplified linear dispersion relations to model the Ion Temperature Gradient (ITG) mode instability, which exhibits a combined "drift-interchange" nature.

Due to the nonlinear interactions between different instabilities and the multiscale nature of turbulence, turbulent transport is challenging to predict. The turbulent diffusion coefficient, D_{turb}, is closely linked to the small-scale fluctuations in the

plasma, with typical values on the order of:

$$D_{\text{turb}} \sim 1\,\text{m}^2/\text{s}.$$

This is substantially larger than both classical and neoclassical transport, making turbulent transport the dominant mechanism responsible for energy and particle losses in fusion plasmas. In fact, in most operating tokamaks, turbulent transport can account for the majority of transport losses, significantly surpassing neoclassical predictions (except for impurity transport), often preventing the plasma pressure to reach the MHD limits. Turbulent transport is not only more intense but also more complex than neoclassical transport due to its nonlinear nature. In turbulent systems, small fluctuations in density, and temperature interact with each other in a highly dynamic way, leading to transports that impact the density and temperature again. These nonlinear interactions cause turbulence to grow and evolve in unpredictable ways, making it difficult to model or control compared to the more straightforward collisional processes in neoclassical transport. Turbulence occurs across a wide range of spatial and temporal scales, from the microscopic scales of ion and electron gyro-orbits to mesoscopic self-organized flows. These nonlinear interactions result in a cascade of energy across scales, complicating the prediction of transport. Full turbulence simulations over transport time scales are computationally very costly. They are feasible for source-driven cases, often excluding kinetic electrons, and for durations limited to a single confinement time [75]. However, such simulations are not suitable for exploring the impact of various parameters or for studying time scales relevant to current profile diffusion. Gyrokinetic simulations [76] have emerged as a powerful tool for understanding the underlying mechanisms of turbulence by resolving the small-scale motions that contribute to transport. Turbulence modeling is a key area of research in plasma physics, where both computational and theoretical advances are crucial to understanding and controlling plasma behavior in fusion devices.

1.2.3. Integrated Modeling Frameworks for Tokamak Simulations

In order to understand and predict plasma behavior in tokamaks, it is essential to model the wide range of physical processes occurring over different spatial and temporal scales. Transport phenomena, including turbulent and neoclassical transport, interact with magnetohydrodynamic (MHD) instabilities, wave propagation, and other complex plasma dynamics. These processes, each with their own timescales, from microseconds for turbulence to seconds for macroscopic equilibrium, pose a significant challenge for accurate simulations of plasma discharges.

One of the key approaches to addressing this complexity is **integrated modeling frameworks** [77], which allow different physical phenomena, modeled through distinct codes or solvers, to be combined into a unified simulation. In such frameworks, individual models, each optimized to describe specific physics, are coupled to simu-

late the overall plasma dynamics. This coupling is necessary because no single model can capture the full range of scales involved, from the microscale fluctuations driving turbulent transport to the global evolution of plasma profiles. At the heart of these frameworks lies the scale separation assumption: small-scale fast-evolving phenomena (like turbulence) are decoupled from large-scale slowly-evolving phenomena (like plasma equilibrium and confinement). For example, while turbulence acts on the order of microseconds and millimeters, the global transport of energy and particles, which determines the plasma's overall confinement, spans seconds and meters. A typical integrated modeling framework consists of transport solvers that calculate the evolution of plasma density and temperature profiles, turbulence models that estimate the fluxes of particles and heat, and sources models.
The transport equation governing the evolution of plasma density n can be represented as a diffusion-convection problem expressed in the following form:

$$\frac{\partial n}{\partial t} + \nabla \cdot \Gamma = S, \tag{1.6}$$

with:

$$\Gamma = -D\nabla n + V n,$$

where Γ is the particle flux, S the sources, and where D and V are the diffusion and convection coefficients. In integrated modeling frameworks, these two last quantities are decomposed into contributions from neoclassical, and turbulent transport mechanisms. These frameworks allow for workflow-based integration where outputs from one model, such as the turbulence-driven fluxes, are used to evolve the profiles, which themselves serve as inputs for another model, such as the source model. The framework iterates between models, ensuring that the solution accounts for both small-scale physics and large-scale behavior. Such integrated modeling frameworks provide a powerful tool for predicting density and temperature profiles, which are routinely measured in tokamak experiments. These models enable the comparison of predicted turbulent fluxes with experimental measurements. While integrated modeling frameworks provide valuable tools for addressing the complex, multi-scale nature of plasma behavior, the accuracy of these simulations heavily relies on the models used to describe the underlying physical phenomena. In particular, the transport of particles and energy in tokamaks is predominantly governed by turbulence, which is often the most challenging aspect to model and predict accurately.

The next section explores the modeling of turbulent transport in more detail, focusing on the development and application of gyrokinetic quasilinear models, which have become essential tools for simulating turbulence in integrated modeling frameworks.

1.3. Turbulent transport modelling

1.3.1. Gyrokinetic Theory

Gyrokinetic theory provides the essential framework for studying plasma turbulence in magnetically confined fusion plasmas, such as those found in tokamaks or stellerators. The theory focuses on describing the dynamics of microinstabilities that drive turbulent transport, leading to the radial transport of particles, momentum, and energy. These microinstabilities, such as drift waves and interchange modes, are destabilized by steep gradients in density and temperature, even in plasmas that are stable against magnetohydrodynamic (MHD) instabilities.

The material presented here summarizes some of the fundamental aspects of gyrokinetic theory, but for a more comprehensive exploration, including a detailed mathematical formalism, refer to Brizard and Hahm's review on nonlinear gyrokinetic theory [78].

One of the main goals of gyrokinetic theory is to predict and understand turbulent transport in fusion plasmas. Given the large number of particles in a fusion plasma (around $10^{20}\,\mathrm{m}^{-3}$ in a volume of $830\,\mathrm{m}^{-3}$ for ITER), it is impractical to track the trajectory of each particle. As a result, a statistical approach using a particle distribution function is adopted. Plasma dynamics is governed by the Vlasov equation, a six-dimensional kinetic equation, which is solved for each species and coupled to Maxwell's equations [79]. However, solving the full Vlasov equation for each plasma species in a high-dimensional system is computationally expensive, especially when considering the complex geometry of a tokamak, the non-linear nature of plasma turbulence, and the wide range of spatial and temporal scales involved in particular between ions and electrons. Gyrokinetic theory simplifies this problem by taking advantage of a natural scale separations in magnetized plasmas. Plasma turbulence occurs on spatial scales comparable to the Larmor radius ρ_L and temporal scales much longer than the cyclotron motion. Gyrokinetic theory makes the following assumptions to simplify the system:

— **Magnetized Plasma Approximation**: The plasma is strongly magnetized, meaning the Larmor radius ρ_L is much smaller than the characteristic length of the profiles variations L ($\rho_L \ll L$).

— **Time Scale Separation**: Turbulence occurs on much longer timescales than those associated with gyromotion, allowing us to focus on phenomena with frequencies ω much smaller than the gyrofrequency ($\omega \ll \Omega_c$). By averaging over the fast gyro-motion of particles, the system's dimensionality is reduced from six to five dimensions: three spatial coordinates, one for the parallel velocity $v_\parallel$, and one for the magnetic moment $\mu = \frac{m v_\perp^2}{2B}$, an adiabatic invariant.

The last reduction is crucial as it simplifies the governing equations by removing fast gyro-motion while retaining essential kinetic effects responsible for microturbulence. The primary objective of gyrokinetic theory is to describe phenomena with frequencies ω much smaller than the gyrofrequency Ω_c, which allows us to restrict the description to slower dynamics. The process of eliminating fast gyro-motion not only reduces

the dimensionality but also enables numerical models to handle the system more efficiently. The final result is a five-dimensional system, which is computationally more feasible than solving the full six-dimensional Vlasov-Maxwell system.

Gyrokinetic Equations

The resulting system of gyrokinetic equations consists of the gyrokinetic Vlasov equation for the gyrocenter distribution function $F_s(\mathbf{x}, v_\parallel, \mu)$, coupled with the gyrokinetic Poisson equation for the electrostatic potential ϕ, and Ampère's law for the parallel and perpendicular component of the vector potential A.

The gyrokinetic Vlasov equation, which describes the evolution of the distribution function of the gyrocenters $F_s(\mathbf{x}, \mathbf{v})$, is given by:

$$\frac{\partial F_s}{\partial t} + \frac{d\mathbf{x}}{dt} \cdot \frac{\partial F_s}{\partial \mathbf{x}} + \frac{d\mathbf{v}}{dt} \cdot \frac{\partial F_s}{\partial \mathbf{v}} = C_s(F_s(\mathbf{x}, \mathbf{v})) \tag{1.7}$$

where $C_s(F_s)$ is the collision operator. The gyrokinetic Poisson equation for the electrostatic potential ϕ is:

$$\nabla^2 \phi = -\frac{\rho}{\epsilon_0},$$

where ρ is the charge density, and ϵ_0 is the permittivity of free space. Similarly, Ampère's law for the vector potential A is:

$$\nabla^2 A = \mu_0 J,$$

where J is the current density, and μ_0 the magnetic permeability of free space. These equations govern the interaction between charged particles and electromagnetic fields, filtered to focus on the slower, large-scale dynamics relevant to turbulent transport. The five-dimensional nature of gyrokinetic equations allows for practical numerical simulations of plasma turbulence. Two primary approaches are employed:

— **Lagrangian (Particle-in-Cell, PIC) Methods**: These methods sample particles' initial positions in phase space and follow the trajectories of "markers" representing groups of particles. Codes like GTC [80], GT3D [81], and ORB5 [82] use this approach. While Lagrangian methods have the advantage of being statistically interpretable, they are prone to noise due to finite sampling.

— **Eulerian Methods**: These methods involve a fixed grid in phase space, using techniques such as finite differences or Fourier transforms to solve the equations. Notable codes using this approach include GS2 [83, 84], GENE [85, 86], GYRO [87], GT5D [88, 89] and GKW [3]. GKW, in particular, will be the code used in this work. Although Eulerian methods avoid sampling noise, they face stability constraints, which are often addressed by implicit or semi-implicit time integration methods.

GYSELA [90] employs a semi-Lagrangian approach, which combines advantages from both Eulerian and Lagrangian methods. Further details are available in [76].

The gyrokinetic framework lays the foundation for modeling plasma turbulence in tokamaks. However, in practice, further approximations are often required to make the simulations more tractable. One such approximation is the local δf approximation,

which focuses on small deviations from a known equilibrium distribution function F_0. This approximation reduces the computational load and allows for more efficient exploration of the dynamics of small-scale fluctuations in plasma. In the next section, we will introduce and discuss the local δf approximation in detail, highlighting its advantages and limitations in the context of gyrokinetic simulations.

1.3.1.1. Local and δf Approximations

The δf approximation is a widely used method in gyrokinetic simulations that separates the plasma distribution function f_{tot} into two components: a macroscopic equilibrium distribution, f_0, and a microscopic turbulent perturbation, δf. This decomposition is expressed as:

$$f_{\text{tot}} = f_0 + \delta f$$

Here, f_0 represents the equilibrium distribution, which is assumed stationary, while δf accounts for small turbulent perturbations. This method is valid when the fluctuations are weak, i.e., $\frac{\delta n}{n_0} \ll 1$, where δn is the fluctuating density and n_0 the equilibrium density. By adopting this approximation, the computational complexity is reduced, as only the perturbed part, δf, is solved while the equilibrium distribution remains fixed. This allows for a more efficient analysis of plasma turbulence, capturing the essential physics without the need to resolve the entire distribution.

In addition to the δf approach, the local approximation simplifies the problem further by exploiting spatial scale separations inherent in gyrokinetic theory. In particular, fluctuations are assumed to occur on the scale of the ion gyroradius, ρ_L, which is significantly smaller than the equilibrium gradients of background quantities like temperature and density. In tokamaks, the perpendicular correlation length of turbulent fluctuations scales with the ion gyroradius rather than the equilibrium length scales of the plasma. This is because the strong magnetic field restricts particle motion across magnetic flux surfaces, limiting long-wavelength correlations. This ordering is essential for understanding how turbulence develops at small scales while remaining relatively localized in the perpendicular direction to the magnetic field. It is important to note that, in addition to the local approximation, global gyrokinetic codes also exist. These global models account for fluctuations over a broader radial domain, allowing them to capture non-local effects that may be missed by local flux-tube codes. Recent studies [91, 92, 93] have evaluated the validity of the local approximation by comparing it with global simulations.

Flux-Tube Models

The flux-tube model is commonly employed in local gyrokinetic simulations to take advantage of these spatial orderings. In this model, a narrow, helically twisted region of the plasma, known as a flux tube, is simulated along the magnetic field lines. The simulated domain is centered on a single flux surface at a fixed radial position, allowing for a focused study of local turbulence, taking advantage of the strong parallel magnetic field component ($B_\parallel$) relative to the weaker perpendicular component ($B_\perp$). By assuming that turbulence is homogeneous in the plane perpendicular to the magnetic field (the local approximation), periodic boundary conditions can be applied,

and Fourier decomposition is used to solve the governing equations efficiently. The flux-tube model offers a powerful computational tool to study plasma turbulence at reduced cost, while retaining the critical physics of the turbulent structures. Large-scale numerical simulations based on electromagnetic gyrokinetic models require significant computational resources. Consequently, many simulations are carried out in the flux-tube geometry [83, 85, 87, 94, 95, 3, 96, 97], which balances accuracy with computational efficiency.

The next section will shift focus from the kinetic descriptions used in gyrokinetic theory to a fluid-based perspective, exploring how turbulence and transport phenomena can be modeled using fluid moments in plasma dynamics. Since a key objective of this PhD work involves verifying a fluid model against a gyrokinetic model, we will first introduce the fundamental concepts of the fluid approach, which will later be compared to the more detailed gyrokinetic simulations.

1.3.1.2. Fluid Moments

In plasma physics, the fluid moments approach offers a reduced description of plasma behavior compared to fully kinetic models [98]. Instead of solving the gyrokinetic Vlasov equation to track the detailed evolution of the entire particle distribution function f, the fluid approach calculates key macroscopic quantities such as density, velocity, and pressure by integrating over velocity space. These integrals, known as the moments of the distribution function, reduce the number of degrees of freedom, making the fluid approach computationally much more efficient. However, this reduction comes with limitations, as certain kinetic effects, such as wave-particle resonances, are not fully captured in a fluid description.

Moments of the Distribution Function

The fluid moments are derived from the distribution function f, which describes the number of particles at each position and velocity in phase space. By integrating over the velocity space, we can obtain key macroscopic properties of the plasma. Each moment corresponds to a specific macroscopic quantity:

— **Density:** The zeroth moment of the distribution function gives the plasma density n, which represents the number of particles per unit volume:

$$n = \int f \, d^3\mathbf{v}$$

This is a fundamental quantity that describes how many particles are present at each spatial point in the plasma.

— **Fluid velocity:** The first moment of the distribution function, weighted by the particle velocity $\mathbf{v}$, gives the average velocity of the plasma particles, known as the fluid velocity $\mathbf{u}$:

$$\mathbf{u} = \frac{1}{n} \int \mathbf{v} f \, d^3\mathbf{v}$$

This describes the bulk motion of the plasma and represents the average velocity of all particles at a given point.

— **Pressure tensor:** The second moment, weighted by the velocity difference from the mean flow, gives the pressure tensor $\bar{P}$. This tensor captures not only the isotropic pressure but also any anisotropies in the plasma pressure:

$$\bar{P} = \int m(\mathbf{v}-\mathbf{u}) \otimes (\mathbf{v}-\mathbf{u}) f \, d^3\mathbf{v}$$

The pressure tensor describes how the particles are distributed in velocity space around the mean flow and is critical for capturing the forces acting within the plasma, including both isotropic and directional pressures.

— **Heat flux:** The third moment, weighted by the particle kinetic energy, gives the heat flux $\mathbf{Q}$:

$$\mathbf{Q} = \int \frac{m|\mathbf{v}|^2}{2} \mathbf{v} f_s \, d^3\mathbf{v}$$

The heat flux describes how thermal energy is transported within the plasma, driven by gradients in temperature or density.

Each of these moments provides valuable information about the collective behavior of the plasma, turning the microscopic description provided by the distribution function into a macroscopic, fluid-like description.

Conservation Laws from Fluid Moments

By integrating the Vlasov equation over velocity space, the fluid moments approach can be used to derive fundamental conservation laws governing the plasma.

— **Continuity equation (mass conservation):** The zeroth moment of the Vlasov equation gives the continuity equation:

$$\frac{\partial n}{\partial t} + \nabla \cdot (n\mathbf{u}) = 0$$

— **Momentum conservation:** The first moment of the Vlasov equation, obtained by multiplying the equation by $m\mathbf{v}$, gives the momentum conservation equation.

— **Energy conservation:** The second moment of the Vlasov equation, found by integrating over the particle kinetic energy $\frac{1}{2}m|\mathbf{v}|^2$, gives the energy conservation equation.

The Closure Problem

While the fluid moments method offers a powerful way to describe plasma dynamics, it encounters a significant limitation known as the closure problem. In theory, the full kinetic description of the plasma is equivalent to an infinite hierarchy of fluid moments. Each fluid equation derived from the Vlasov equation depends on higher-order moments, which means that solving the fluid equations requires knowledge of the entire hierarchy. In practice, only the first few moments (density, velocity, pressure, and possibly heat flux) are used in fluid models. To solve the equations, the system must be truncated, but this introduces the need for a closure condition. The closure condition expresses the highest-order moment in terms of the lower-order moments, thereby truncating the hierarchy. The closure problem is challenging because it typically requires assumptions about the behavior of the plasma and no

universal closure exists, making this an open issue in plasma modeling.

The fluid moments approach is used in gyrofluid models which combine elements of fluid and kinetic theories. These models are build by taking moments of the gyrocenter distribution function and of the gyrokinetic equations. While retaining the computational efficiency of fluid models, they incorporate kinetic effects from gyrokinetic theory, such as finite Larmor radius corrections. A key example of this approach is the **TGLF** (Trapped Gyro-Landau Fluid) code [1, 2], which will be discussed in detail later in the thesis. TGLF is a reduced model based on gyrofluid theory used to simulate turbulence in tokamak plasmas, providing a practical balance between accuracy and computational feasibility. For more detailed discussions on fluid models and gyrofluid turbulence modeling, refer to [99].

1.3.2. Derivation of Turbulent Radial Fluxes

Building on the local δf approximation discussed in Section 1.3.1.1, we now derive the expressions for turbulent radial fluxes within the flux-tube geometry. By assuming turbulence is homogeneous in the plane perpendicular to the magnetic field, periodic boundary conditions can be applied. This allows for the use of Fourier decomposition to solve the governing equations. Consequently, fluctuating quantities can be expressed as a Fourier series in the plane orthogonal to the magnetic field (x, y):

$$\delta\phi(\boldsymbol{x}) = \sum_{k_y}\sum_{k_x} \tilde{\phi}_{k_x,k_y} \exp\{ik_x x\}\exp\{ik_y y\} \tag{1.8}$$

$$\delta f(\boldsymbol{x}) = \sum_{k_y}\sum_{k_x} \tilde{f}_{k_x,k_y} \exp\{ik_x x\}\exp\{ik_y y\} \tag{1.9}$$

$$\delta A_\parallel(\boldsymbol{x}) = \sum_{k_y}\sum_{k_x} \tilde{A}_{\parallel k_x,k_y} \exp\{ik_x x\}\exp\{ik_y y\} \tag{1.10}$$

$$\delta B_\perp(\boldsymbol{x}) = \sum_{k_y}\sum_{k_x} \tilde{B}_{\parallel k_x,k_y} \exp\{ik_x x\}\exp\{ik_y y\} \tag{1.11}$$

All theses quantities are real, so if we consider a fluctuating quantity X, we have $X = X^\dagger$ (where † denotes the complex conjugate). So we have:

$$\begin{aligned}\sum_{k_x}\sum_{k_y} \tilde{X}_{k_x,k_y} \exp\{ik_x x\}\exp\{ik_y y\} &= \sum_{k_x}\sum_{k_y} \tilde{X^\dagger}_{k_x,k_y} \exp\{-ik_x x\}\exp\{-ik_y y\} \\ &= \sum_{k_x}\sum_{k_y} \tilde{X^\dagger}_{-k_x,-k_y} \exp\{ik_x x\}\exp\{ik_y y\}\end{aligned} \tag{1.12}$$

By identification we have:

$$\tilde{X}_{k_x,k_y} = \tilde{X}^\dagger_{-k_x,-k_y} \tag{1.13}$$

The energy flux, Q_s, particle flux, Γ_s and toroidal angular momentum flux $\Pi_s^\parallel$, are defined as the radial components of the flux-surface-averaged guiding center energy

and particle fluxes. These fluxes are expressed as:

$$Q_s = \langle \int \frac{1}{2} m_s v^2 f_s [\boldsymbol{v}_E + \boldsymbol{v}_{B_\perp} + \boldsymbol{v}_{\nabla B_\parallel}] \cdot \nabla_r d\boldsymbol{v} \rangle \tag{1.14}$$

$$\Gamma_s = \langle \int f [\boldsymbol{v}_E + \boldsymbol{v}_{B_\perp} + \boldsymbol{v}_{\nabla B_\parallel}] \cdot \nabla_r d\boldsymbol{v} \rangle \tag{1.15}$$

$$\Pi_s^\parallel = \langle \int \frac{s_B R B_t}{B} m_s v_\parallel f [\boldsymbol{v}_E + \boldsymbol{v}_{B_\perp} + \boldsymbol{v}_{\nabla B_\parallel}] \cdot \nabla_r d\boldsymbol{v} \rangle \tag{1.16}$$

Where $\langle \cdot \rangle$ correspond to an average over the corresponding flux-surface. The flux surface average of a quantity A is given by:

$$\langle A \rangle = \frac{\int A(x) \delta(r - r_0) \mathscr{J}_{xy\theta} dx dy d\theta}{\int \delta(r - r_0) \mathscr{J}_{xy\theta} dx dy d\theta} \tag{1.17}$$

Where r_0 is the radial coordinate of the flux surface on which the average is being performed, r is the value of the radial coordinate at position $\boldsymbol{x}$ and the integral is being performed over the whole plasma volume.

In the fluxes expressions, f_s is the perturbed guiding center distribution function of species s, and the three drift velocities:

— Electrostatic drift $\boldsymbol{v}_E$
— Magnetic flutter drift $\boldsymbol{v}_{B_\perp}$
— Magnetic compression drift $\boldsymbol{v}_{\nabla B_\parallel}$

are given by:

$$\boldsymbol{v}_E = \frac{\boldsymbol{b} \times \nabla \langle \delta\phi \rangle_{gy}}{B}, \quad \boldsymbol{v}_{B_\perp} = -v_\parallel \frac{\boldsymbol{b} \times \nabla \langle \delta A_\parallel \rangle_{gy}}{B}, \quad \boldsymbol{v}_{\nabla B_\parallel} = \frac{\mu}{Z_s e} \frac{\boldsymbol{b} \times \nabla \langle \delta B_\parallel \rangle_{gy}}{B} \tag{1.18}$$

where $\langle \delta\phi \rangle_{gy}$, $\langle \delta A_\parallel \rangle_{gy}$, and $\langle \delta B_\parallel \rangle_{gy}$ are the gyro-averaged perturbed electrostatic potential, parallel vector potential, and parallel magnetic field, respectively. In the following, we derive the expression for the heat flux Q_s, starting with the contribution from electrostatic fluctuations and subsequently incorporating the electromagnetic contributions.

The contribution of the perturbed electrostatic potential, $\langle \delta\phi \rangle_{gy}$, to the energy flux Q_s is defined as:

$$Q_{s,\phi} = \left\langle \int \frac{1}{2} m_s v^2 f \, \boldsymbol{v}_E \cdot \nabla_r \, d\boldsymbol{v} \right\rangle \tag{1.19}$$

To evaluate this term, we expand $\boldsymbol{v}_E \cdot \nabla r$ as follows:

$$\boldsymbol{v}_E \cdot \nabla r = \left(\frac{\partial \langle \delta\phi \rangle_{gy}}{\partial x} \frac{\boldsymbol{b} \times \boldsymbol{e_x}}{B} + \frac{\partial \langle \delta\phi \rangle_{gy}}{\partial y} \frac{\boldsymbol{b} \times \boldsymbol{e_y}}{B} + \frac{\partial \langle \delta\phi \rangle_{gy}}{\partial z} \frac{\boldsymbol{b} \times \boldsymbol{e_z}}{B} \right) \cdot \nabla r \tag{1.20}$$

Since $\boldsymbol{b} \times \boldsymbol{e_x}$ and $\boldsymbol{b} \times \boldsymbol{e_z}$ are orthogonal to ∇r, only the y-component contributes, giving:

$$\boldsymbol{v}_E \cdot \nabla r = \frac{\partial \langle \delta\phi \rangle_{gy}}{\partial y} \frac{\boldsymbol{b} \times \boldsymbol{e_y}}{B} \cdot \nabla r = \frac{\partial \langle \delta\phi \rangle_{gy}}{\partial y} \varepsilon^{ry} \tag{1.21}$$

where we define $\varepsilon^{ry} = \frac{\boldsymbol{b}\times\boldsymbol{e_y}}{B}\cdot\nabla r$ as a geometric factor capturing the alignment between the magnetic and radial directions. Substituting into the expression for $Q_{s,\phi}$, we obtain:

$$Q_{s,\phi} = \left\langle \int \frac{m_s v^2}{2} \varepsilon^{ry} f \frac{\partial \langle \delta\phi \rangle_{gy}}{\partial y} \, d\boldsymbol{v} \right\rangle \tag{1.22}$$

The gyro-averaged perturbed electrostatic potential, $\langle \delta\phi \rangle_{gy}$, is defined as:

$$\begin{aligned}
\langle \delta\phi \rangle_{gy}(\boldsymbol{x}) &= \frac{1}{2\pi}\int_0^{2\pi} \delta\phi(\boldsymbol{x}+\boldsymbol{\rho})\, d\xi \\
&= \frac{1}{2\pi}\int_0^{2\pi} \sum_{\boldsymbol{k}} \tilde{\phi}_k \exp\left(i\boldsymbol{k}\cdot\boldsymbol{x}\right)\exp\left(i\boldsymbol{k}\cdot\boldsymbol{\rho}\right) d\xi \\
&= \frac{1}{2\pi}\sum_{\boldsymbol{k}} \tilde{\phi}_k \exp\left(i\boldsymbol{k}\cdot\boldsymbol{x}\right)\int_0^{2\pi} \exp\left(i k_\perp \rho\cos\xi\right) d\xi \\
&= \sum_{\boldsymbol{k}} \tilde{\phi}_k \exp\left(i\boldsymbol{k}\cdot\boldsymbol{x}\right) J_0(k_\perp\rho)
\end{aligned} \tag{1.23}$$

where J_0 is the Bessel function of the first kind, and ρ the particle Larmor radius. Thus, we can write:

$$\langle \delta\phi \rangle_{gy}(\boldsymbol{x}) = \delta\phi(\boldsymbol{x}) J_0(k_\perp\rho) \tag{1.24}$$

Starting from Eq. 1.22, using the Fourier expansion of fluctuating quantities we express the electrostatic contribution $Q_{s,\phi}$ as:

$$\begin{aligned}
Q_{s,\phi} &= \left\langle \int \frac{m_s v^2}{2} \varepsilon^{ry} \sum_{k_y}\sum_{k_x} \tilde{f}_{k_x,k_y} e^{ik_x x} e^{ik_y y} \sum_{k'_y}\sum_{k'_x} ik'_y \tilde{\phi}_{k'_x,k'_y} J_0(k_\perp\rho) e^{ik'_x x} e^{ik'_y y} \, d\boldsymbol{v} \right\rangle \\
&= \left\langle \int \frac{m_s v^2}{2} \varepsilon^{ry} \sum_{k_y}\sum_{k_x}\sum_{k'_y}\sum_{k'_x} ik'_y \tilde{f}_{k_x,k_y} \tilde{\phi}_{k'_x,k'_y} J_0(k_\perp\rho) e^{i(k_x+k'_x)x} e^{i(k_y+k'_y)y} \, d\boldsymbol{v} \right\rangle
\end{aligned} \tag{1.25}$$

As we are applying flux surface averaging over the x- and y-directions, due to the orthogonality of the exponential terms, only terms where $k'_x = -k_x$ and $k'_y = -k_y$ will contribute. This results in:

$$Q_{s,\phi} = \left\langle \int \frac{m_s v^2}{2} \varepsilon^{ry} \sum_{k_y}\sum_{k_x} -ik_y \tilde{f}_{k_x,k_y} \tilde{\phi}_{-k_x,-k_y} J_0(k_\perp\rho)\, d\boldsymbol{v} \right\rangle \tag{1.26}$$

Using the relation of Eq. 1.13, we substitute $\tilde{\phi}_{-k_x,-k_y} = \tilde{\phi}^\dagger_{k_x,k_y}$, giving:

$$Q_{s,\phi} = \left\langle \int \frac{m_s v^2}{2} \varepsilon^{ry} \sum_{k_y}\sum_{k_x} -ik_y \tilde{f}_{k_x,k_y} \tilde{\phi}^\dagger_{k_x,k_y} J_0(k_\perp\rho)\, d\boldsymbol{v} \right\rangle \tag{1.27}$$

Since the term in the sum vanishes when $k_y = 0$, we can split the sum over k_y into

positive and negative components:

$$
\begin{aligned}
Q_{s,\phi} &= \left\langle \int \frac{m_s v^2}{2} \varepsilon^{ry} \sum_{k_x} \left(\sum_{k_y>0} -ik_y \tilde{f}_{k_x,k_y} \tilde{\phi}^{\dagger}_{k_x,k_y} J_0(k_\perp \rho) + \sum_{k_y<0} -ik_y \tilde{f}_{k_x,k_y} \tilde{\phi}^{\dagger}_{k_x,k_y} J_0(k_\perp \rho) \right) d\boldsymbol{v} \right\rangle \\
&= \left\langle \int \frac{m_s v^2}{2} \varepsilon^{ry} \sum_{k_x} \sum_{k_y>0} \left(-ik_y \tilde{f}_{k_x,k_y} \tilde{\phi}^{\dagger}_{k_x,k_y} J_0(k_\perp \rho) + ik_y \tilde{f}_{-k_x,-k_y} \tilde{\phi}^{\dagger}_{-k_x,-k_y} J_0(k_\perp \rho) \right) d\boldsymbol{v} \right\rangle
\end{aligned}
\tag{1.28}
$$

By applying Eq. 1.13 again, we substitute $\tilde{f}_{-k_x,-k_y} = \tilde{f}^{\dagger}_{k_x,k_y}$ and $\tilde{\phi}_{-k_x,-k_y} = \tilde{\phi}^{\dagger}_{k_x,k_y}$, yielding:

$$
\begin{aligned}
Q_{s,\phi} &= \left\langle \int \frac{m_s v^2}{2} \varepsilon^{ry} \sum_{k_x} \sum_{k_y>0} \left(-ik_y \tilde{f}_{k_x,k_y} \tilde{\phi}^{\dagger}_{k_x,k_y} J_0(k_\perp \rho) \right) + \left(ik_y \tilde{f}^{\dagger}_{k_x,k_y} \tilde{\phi}_{k_x,k_y} J_0(k_\perp \rho) \right) d\boldsymbol{v} \right\rangle \\
&= \left\langle \int \frac{m_s v^2}{2} \varepsilon^{ry} \sum_{k_x} \sum_{k_y>0} \left(-ik_y \tilde{f}_{k_x,k_y} \tilde{\phi}^{\dagger}_{k_x,k_y} J_0(k_\perp \rho) \right) + \left(-ik_y \tilde{f}_{k_x,k_y} \tilde{\phi}^{\dagger}_{k_x,k_y} J_0(k_\perp \rho) \right)^{\dagger} d\boldsymbol{v} \right\rangle \\
&= \left\langle \int m_s v^2 \varepsilon^{ry} \sum_{k_x} \sum_{k_y>0} \mathrm{Re}\left\{ \left(-ik_y \tilde{f}_{k_x,k_y} \tilde{\phi}^{\dagger}_{k_x,k_y} J_0(k_\perp \rho) \right) \right\} d\boldsymbol{v} \right\rangle \\
&= \left\langle \int m_s v^2 \varepsilon^{ry} \sum_{k_x} \sum_{k_y>0} \mathrm{Im}\left\{ \left(k_y \tilde{f}_{k_x,k_y} \tilde{\phi}^{\dagger}_{k_x,k_y} J_0(k_\perp \rho) \right) \right\} d\boldsymbol{v} \right\rangle
\end{aligned}
\tag{1.29}
$$

We finally obtain:

$$
Q_{s,\phi} = \sum_{k_x} \sum_{k_y>0} \left\langle k_y \varepsilon^{ry} \, \mathrm{Im}\left(\int m_s v^2 J_0(k_\perp \rho) \tilde{f}_{k_x,k_y} \tilde{\phi}^{\dagger}_{k_x,k_y} \, d\boldsymbol{v} \right) \right\rangle \tag{1.30}
$$

Similarly, the contribution of the gyro-averaged perturbed parallel vector potential, $\langle \delta A_\parallel \rangle_{gy}$, to the energy flux Q_s is defined as:

$$
Q_{s,A_\parallel} = \left\langle \int \frac{1}{2} m_s v^2 f \, \boldsymbol{v}_{B_\perp} \cdot \nabla_r \, d\boldsymbol{v} \right\rangle \tag{1.31}
$$

And the contribution of the gyro-averaged perturbed parallel magnetic field, $\langle \delta B_\parallel \rangle_{gy}$, to the energy flux Q_s is defined as:

$$
Q_{s,B_\parallel} = \left\langle \int \frac{1}{2} m_s v^2 f \, \boldsymbol{v}_{\nabla B_\parallel} \cdot \nabla_r \, d\boldsymbol{v} \right\rangle \tag{1.32}
$$

Following a similar derivation as for the perturbed electrostatic potential contribution,

we obtain:

$$Q_{s,A_\parallel} = \sum_{k_x} \sum_{k_y>0} \left\langle k_y \varepsilon^{ry} \operatorname{Im}\left(\int m_s v^2 J_0(k_\perp \rho)\, \tilde{f}_{k_x,k_y} v_\parallel \tilde{A}_\parallel{}^\dagger_{k_x,k_y}\, d\boldsymbol{v} \right) \right\rangle \tag{1.33}$$

and

$$Q_{s,B_\parallel} = \sum_{k_x} \sum_{k_y>0} \left\langle k_y \varepsilon^{ry} \operatorname{Im}\left(\int m_s v^2 J_0(k_\perp \rho)\, \tilde{f}_{k_x,k_y} \frac{\mu}{Z_s e} \tilde{B}_\parallel{}^\dagger_{k_x,k_y}\, d\boldsymbol{v} \right) \right\rangle \tag{1.34}$$

Total Energy Flux Q_s

Finally, the total flux-surface-averaged radial component of the energy flux, Q_s, is given by the sum of the contributions from the electrostatic potential, parallel vector potential, and parallel magnetic field:

$$Q_s = \sum_{k_x} \sum_{k_y>0} \left\langle k_y \varepsilon^{ry} \operatorname{Im}\left(\int m_s v^2 J_0(k_\perp \rho)\, \tilde{f}_{k_x,k_y} \left[\tilde{\phi}^\dagger_{k_x,k_y} - v_\parallel \tilde{A}_\parallel{}^\dagger_{k_x,k_y} + \frac{\mu}{Z_s e} \tilde{B}_\parallel{}^\dagger_{k_x,k_y} \right] d\boldsymbol{v} \right) \right\rangle \tag{1.35}$$

Particle Flux

The total contribution of $\langle \delta\phi \rangle_{gy}$, $\langle \delta A_\parallel \rangle_{gy}$, and $\langle \delta B_\parallel \rangle_{gy}$ to the particle flux Γ_s is defined as:

$$\Gamma_s = \left\langle \int f \left(\boldsymbol{v}_E + \boldsymbol{v}_{B_\perp} + \boldsymbol{v}_{\nabla B_\parallel} \right) \cdot \nabla_r\, d\boldsymbol{v} \right\rangle \tag{1.36}$$

The derivation of the particle flux follows a similar approach to that of the energy flux Q_s, with the primary difference being the absence of the factor $\frac{m_s v^2}{2}$. This leads to the following expression for the flux-surface-averaged radial component of the particle flux:

$$\Gamma_s = \sum_{k_x} \sum_{k_y>0} \left\langle k_y \varepsilon^{ry} \int 2 \operatorname{Im}\left(J_0(k_\perp \rho) \tilde{f}_{k_x,k_y} \left[\tilde{\phi}^\dagger_{k_x,k_y} - v_\parallel \tilde{A}_\parallel{}^\dagger_{k_x,k_y} + \frac{\mu}{Z_s e} \tilde{B}_\parallel{}^\dagger_{k_x,k_y} \right] \right) d\boldsymbol{v} \right\rangle \tag{1.37}$$

Toroidal Angular Momentum Flux

The total toroidal angular momentum flux $\Pi_s^\parallel$ is defined as:

$$\Pi_s^\parallel = \left\langle \int \frac{s_B R B_t}{B} m_s v_\parallel f \left(\boldsymbol{v}_E + \boldsymbol{v}_{B_\perp} + \boldsymbol{v}_{\nabla B_\parallel} \right) \cdot \nabla_r\, d\boldsymbol{v} \right\rangle \tag{1.38}$$

Similary, the flux-surface-averaged radial component of the toroidal angular momentum flux is given by:

$$\Pi_s^{\parallel} = \sum_{k_x} \sum_{k_y>0} \left\langle k_y \varepsilon^{ry} \int 2 \frac{s_B R B_t}{B} m_s v_{\parallel} \, \mathrm{Im}\left(J_0(k_{\perp}\rho) \tilde{f}_{k_x,k_y} \left[\tilde{\phi}^{\dagger}_{k_x,k_y} - v_{\parallel} \tilde{A}_{\parallel}{}^{\dagger}_{k_x,k_y} + \frac{\mu}{Z_s e} \tilde{B}_{\parallel}{}^{\dagger}_{k_x,k_y} \right] \right) d\boldsymbol{v} \right\rangle \tag{1.39}$$

1.3.3. Quasi-Linear Theory

1.3.3.1. Introduction to the Quasi-Linear Approach

Quasi-linear theory is built on the premise that the time-averaged nonlinear effects in turbulent plasmas can be approximated using the linearly unstable eigenmodes of the gyrokinetic equations, combined with suitable semi-empirical functions called saturation rules. Although they cannot capture the full spectrum of nonlinear interactions, they offer a compromise for many practical applications, especially for turbulent fluxes predictions. A recent comprehensive review [6] provides an in-depth exploration of quasi-linear theory and its application in gyrokinetic quasi-linear models. Their work offers a detailed overview of both the theoretical foundations and the practical implementation of these models in simulating plasma turbulence. For those interested in a deeper dive into the intricacies of quasi-linear theory and its broader applications, this review serves as an essential reference. In the following sections, our goal is to make the reader familiar with the key principles of quasi-linear theory.

The quasi-linear approach has emerged as an essential tool in gyrokinetic turbulence modeling due to its ability to predict radial turbulent fluxes efficiently while reducing computational costs by several orders of magnitude. While fully nonlinear simulations offer the most detailed insight into plasma dynamics, these methods are often computationally prohibitive. For instance, local δf nonlinear simulations using the GKW code can require in excess of 10^5 CPU hours for a single radial position, rendering them impractical for integrated modelling frameworks. Quasi-linear models, such as TGLF [1, 2], circumvent this limitation by simplifying the nonlinear aspects of turbulence, allowing for predictions of turbulent transport on timescales that are orders of magnitude faster than their nonlinear counterparts. TGLF, for example, can perform flux calculations in approximately 10 CPU seconds, making it suitable for integrated modeling frameworks that require multiple iterative runs across the plasma.

1.3.3.2. Linearization of the Gyrokinetic Equations

To obtain the linear unstable eigenmodes of the system, the gyrokinetic system of equations is linearized. The linearization process is conducted in the local δf approximation. This approximation permits the use of a Fourier decomposition to represent the perturbed quantities, such as the distribution function δf and the

electrostatic potential $\delta\phi$:

$$\delta f = \sum_{\mathbf{k}} \delta \hat{f}_k e^{i(\mathbf{k}\cdot\mathbf{x}-\omega t)}, \quad \delta\phi = \sum_{\mathbf{k}} \delta\hat{\phi}_k e^{i(\mathbf{k}\cdot\mathbf{x}-\omega t)},$$

where $\mathbf{k}$ is the wavevector, $\omega = \omega_r + i\gamma$ is the complex frequency, with ω_r as the real frequency and γ as the growth rate. The growth rate γ determines whether a mode will grow exponentially over time ($\gamma > 0$) or decay ($\gamma < 0$). By linearizing the equations, $\delta\hat{f}_{\mathbf{k}}$ responds linearly to $\delta\hat{\phi}_{\mathbf{k}}$ and the complex interactions between different modes are removed. Leading to a decoupling of the equations for each mode $\mathbf{k} = (k_x, k_y)$, where k_x and k_y are the wavevector components in the plane perpendicular to the magnetic field. This decoupling allows the behavior of each mode to be studied independently, greatly simplifying the analysis of turbulent transport.

The advantage of the linear approach is that it identifies all unstable modes. These modes dominate the radial fluxes of particles, momentum, and energy. However, without the nonlinear interactions present in a fully nonlinear system, the growth of these modes would continue indefinitely, leading to unphysical results as the perturbations grow exponentially, $\propto e^{\gamma t}$, without any saturation in the system.
Nonetheless,what is possible in linear simulations is to compute the quasi-linear weights, which are defined as:

$$W^{QL}_{\Gamma,sN}(k_x,k_y) = \frac{\Gamma^L_{s,k_x,k_y}}{\mathscr{A}^L_{k_x,k_y}}, \tag{1.40}$$

$$W^{QL}_{Q,sN}(k_x,k_y) = \frac{Q^L_{s,k_x,k_y}}{\mathscr{A}^L_{k_x,k_y}}. \tag{1.41}$$

Here, Γ^L_{s,k_x,k_y} and Q^L_{s,k_x,k_y} represent the linear fluxes of particles and heat, respectively, computed for each Fourier component (k_x, k_y). The term $\mathscr{A}^L_{k_x,k_y}$ corresponds to the amplitude of the linear mode, which also grows exponentially at the same rate as the linear fluxes. By normalizing the linear fluxes with the mode amplitude, the quasi-linear weights effectively remove the exponential growth inherent to linear simulations. Quasi-linear weights are a critical tool for predicting turbulent fluxes in quasi-linear models. The next section will delve further into the application of quasi-linear weights for flux predictions.

1.3.3.3. Quasi-Linear Flux Calculation and Saturation Models

In nonlinear simulations, the exponential growth of perturbations is naturally limited by the nonlinear interactions between all the $\delta\hat{f}_{\mathbf{k}}$ and $\delta\hat{\phi}_{\mathbf{k}}$, resulting in a steady state where the turbulent fluxes fluctuate around a mean value. Quasi-linear theory aims to capture this saturation process without explicitly solving the full nonlinear system. To achieve this, a **saturation rule** is introduced to approximate the effects of nonlinear interactions. This saturation rule is used to compute a proxy for the non-

linear saturation amplitude, denoted as $A^{QL}_{k_x,k_y}$. The saturation amplitude is typically prescribed using the linear response of the system combined with free parameters calibrated against experimental data or nonlinear simulations. Since saturation is inherently a non-linear process, it cannot be determined using the linear response alone, as is the case with quasi-linear weights.
Once the saturation amplitude is determined, the quasi-linear fluxes can be computed as:

$$\Gamma_s \sim \Gamma_s^{QL} = \sum_{k_y}\sum_{k_x} A^{QL}_{k_x,k_y} W^{QL}_{\Gamma,sN}(k_x,k_y), \tag{1.42}$$

$$Q_s \sim Q_s^{QL} = \sum_{k_y}\sum_{k_x} A^{QL}_{k_x,k_y} W^{QL}_{Q,sN}(k_x,k_y). \tag{1.43}$$

In these expressions the saturation amplitude, $A^{QL}_{k_x,k_y}$, is determined using a saturation rule model, and the quasi-linear weights, $W^{QL}_{\Gamma,sN}$ and $W^{QL}_{Q,sN}$, are derived from the gyrokinetic or gyrofluid linear responses. They represent the "weighting" contribution of each mode (k_x, k_y) to the fluxes. Quasi-linear theory thus provides a computationally efficient way to predict turbulent fluxes, leveraging the linear response to approximate the nonlinear saturation.

In the electrostatic limit, $A^{QL}_{k_x,k_y}$ corresponds to the predicted saturated intensity of the electrostatic potential fluctuations. The quasi-linear flux calculation can be described as a one-dimensional sum over the binormal wavenumber spectrum k_y, combining two key spectra:

1. **Quasi-linear weights** W_{k_y}: These weights are derived from the linearized equations and represent the linear response of the transported quantities. In quasi-linear models they are typically obtained through reduced linear solvers to make thoses models even more computationally efficient.
2. **Saturated potential fluctuations** $\langle|\delta\hat{\phi}_{k_y}|^2\rangle_{x,\theta,t}$: This term describes the intensity of the electrostatic potential perturbations, averaged over space and time. In quasi-linear models that quantity is estimated and predicted using the linear response combined with fitting coefficients obtained through the fitting of a large non-linear gyrokintic local flux-tube simulations.

The two spectra are multiplied and summed across all unstable modes to estimate the total flux for each species s. Using the formalism and notation from [100], the quasi-linear heat flux for species s is expressed in the electrostatic limit as:

$$Q_s = 2\sum_m \sum_{k_y>0} \Lambda_{s,k_y,m} W^{QL}_{s,k_y,m} \left[\frac{\langle|\delta\hat{\phi}_{k_y}|^2\rangle_{x,\theta,t}}{\Delta k_y}\right]_m \Delta k_y,$$

where:

— $\Lambda_{s,k_y,m} = \frac{W^{NL}_{s,k_y,m}}{W^{QL}_{s,k_y,m}}$ is the quasi-linear approximation (QLA) function. This fitted parameter represents the ratio of non-linear to quasi-linear weights and provides

an explicit measure of how well the quasi-linear approximation holds for each mode in case one has access to the corresponding non-linear simulations.
— $W^{QL}_{s,k_y,m}$ represents the quasi-linear weights computed using the linear solver for species s, for each wavenumber k_y, and each unstable mode m.
— $\langle|\delta\hat{\phi}_{k_y}|^2\rangle_{x,\theta,t}$ is the spectrum of the electrostatic potential fluctuations, averaged over space and time. This term is crucial for understanding the intensity of turbulence, as these potential fluctuations drive the transport processes.
— Δk_y is the binormal wavenumber spacing, which allows for the numerical summation across the k_y spectrum.

For numerical modeling purposes, the electrostatic potential fluctuations $\langle|\delta\hat{\phi}_{k_y}|^2\rangle_{x,\theta,t}$ are normalized by the binormal grid spacing Δk_y. This normalization ensures that the results remain consistent across different grid resolutions. The saturated intensity models for the potential fluctuations, discussed extensively in [100], provide critical insight into how these quantities are approximated based on nonlinear simulations and empirical turbulence measurements. By combining the linear response with the saturation models, quasi-linear theory efficiently estimates time-averaged nonlinear fluxes across selected modes.

Key Assumptions: Cross-Phases in the Quasi-Linear Approximation One of the central assumptions underpinning the quasi-linear approximation is that the cross-phases between fluctuating quantities observed in the nonlinear regime closely resemble those in the linear regime. For that reason the linear response is used. Several gyrokinetic simulation studies [101, 102, 103, 104] have verified this assumption by comparing the cross-phases in the non-linear regime to those of the most unstable linear eigenmodes. Despite these limitations, quasi-linear models remain an essential tool in modern plasma physics, particularly in the context of integrated modeling frameworks. In these frameworks, quasi-linear models are used to compute turbulent fluxes as part of larger simulations that track the evolution of the entire plasma. By providing flux predictions that are orders of magnitude faster than nonlinear simulations, quasi-linear models enable real-time predictions, making them invaluable for predictive modeling and control of tokamak plasmas.

1.4. Thesis Motivation and Outline

This thesis investigates the performance of the TGLF model in high-β plasmas, focusing on benchmarking its quasi-linear predictions against nonlinear simulations performed with the high-fidelity gyrokinetic code GKW. High-β regimes, where electromagnetic effects such as Kinetic Ballooning Modes (KBMs) play a dominant role, present significant challenges for turbulence modeling. While quasi-linear models like TGLF offer computational efficiency, their inherent simplifications necessitate rigorous validation to ensure their reliability in these complex scenarios. The aim of this research is to assess the extent to which TGLF can accurately predict turbulent fluxes in high-β plasmas and to refine its capabilities for use in integrated modeling

frameworks. The work presented in this thesis is structured as follows:
In Chapter 2, we provide a comprehensive overview of the TGLF model, detailing its theoretical fondation, the simulation workflow, and its integration into the Integrated Modelling and Analysis Suite (IMAS). This integration facilitates data exchange and benchmarking efforts, enabling automated comparisons between TGLF and other gyrokinetic codes, such as GKW. In Chapter 3, the focus shifts to the linear response analysis of TGLF. Benchmarking efforts are conducted against GKW for the Waltz standard case scenario and the experimental JET discharge #75225. These scenarios provide a foundation for evaluating TGLF's ability to model KBMs under both standard and high-β conditions. The chapter highlights the strengths of TGLF in capturing KBMs but also identifies challenges, particularly at very low magnetic shear. To address these issues, a new filtering mechanism was developed and implemented within TGLF, enhancing its ability to distinguish between physical and spurious modes. In Chapter 4, the study is extended to quasi-linear flux predictions. TGLF's predictions are systematically compared to nonlinear fluxes computed with GKW for the JET discharge #75225. This analysis evaluates the quasi-linear saturation model of TGLF and identifies optimized parameter settings for modeling KBMs. Despite successes in replicating ion heat and particle fluxes, discrepancies in the electron heat flux due to magnetic flutter contributions are discussed, highlighting areas for future improvement in TGLF's electromagnetic treatment. Finally, we concludes the thesis by summarizing the key findings and proposing directions for future research.

This thesis underscores the critical importance of validating reduced turbulence models in high-β regimes where electromagnetic effects dominate. By addressing these challenges, the research contributes to advancing the predictive capabilities of TGLF and supports its integration into integrated modeling frameworks.

2. The TGLF Code and Its Integration in IMAS

The Trapped Gyro-Landau Fluid (TGLF) [1, 2] code is a quasilinear gyrofluid model used to predict turbulent transport in tokamak plasmas. As a quasilinear code, TGLF solves linear gyrokinetic equations over a range of wavenumbers, and predicts the resulting turbulent transport by applying physics based models to describe the saturation of these instabilities. This approach makes TGLF significantly more efficient compared to fully nonlinear gyrokinetic codes while retaining sufficient accuracy for many practical applications. [6] TGLF provides rapid and reasonably accurate estimates of turbulent fluxes, averaging around 10 CPU-seconds per simulation, which are essential for simulating the overall plasma behavior in a tokamak. In contrast, nonlinear codes, such as GKW [7], offer a detailed representation of the nonlinear dynamics of plasma turbulence, but they come at a significantly higher computational cost, requiring over 10^5 CPU hours for a single radial position at one time step. This makes GKW more suitable for detailed studies of specific phenomena, whereas TGLF is ideal for integrated modeling where fast and efficient flux predictions are required. Nevertheless, TGLF's predictions must undergo rigorous validation before they can be reliably used in integrated modeling frameworks, particularly for challenging regimes like high beta plasmas where electromagnetic instabilities, such as Kinetic Ballooning Modes (KBMs), are prevalent. TGLF has not yet been extensively verified for these conditions, and benchmarking it against a fully nonlinear code like GKW is essential to assess its reliability. This benchmarking work forms the core component of this thesis, aiming to evaluate TGLF's performance under high beta conditions.

In this chapter, we present a comprehensive overview of the TGLF model, covering its theoretical framework, detailed simulation workflow, and integration within the Integrated Modelling and Analysis Suite (IMAS). The chapter begins with a foundational overview of TGLF. Section 2 provides a detailed overview of a TGLF simulation, systematically explaining each stage of the process to detail how TGLF operates in practice. In Section 3, we address the challenges inherent to benchmarking due to varying normalization standards across codes and introduce IMAS as a standardized framework designed to ensure consistency in inter-code comparisons. We then describes the tools developed during this PhD for interfacing TGLF with the IMAS framework, including a comprehensive benchmark study to validate them.

2.1. TGLF Model Overview

The Trapped Gyro-Landau Fluid (TGLF) model builds on and significantly advances the GLF23 model, a gyro-Landau fluid transport model that was widely used for plasma transport modeling in tokamaks. Developed to extend the foundational physics of GLF23, TGLF includes key modifications and refinements that make it suitable for modern fusion research, particularly under high-confinement (H-mode) conditions, low aspect ratio spherical tokamaks, and scenarios involving collisional and electromagnetic effects. The GLF23 model was a pioneering theory-based quasilinear transport model that used gyro-Landau fluid equations to predict turbulent transport in the electrostatic regime. It represented turbulence through two primary instability modes: the ion-temperature-gradient (ITG) and trapped-electron modes (TEM), capturing critical aspects of low-wavenumber (low-k_y) turbulence physics. GLF23 relied on a set of simplified gyrofluid moment equations for circulating particles, and it treated trapped particles and high-k_y regimes through reduced equations. However, due to the computational limitations of its time (mid-1990s), GLF23 was designed to be efficient rather than comprehensive, limiting its applicability to regions where the low-k_y physics is dominant [105]. The TGLF model extends the GLF23 framework by incorporating a more comprehensive treatment of trapped and circulating particle effects across a broader spectrum of wavenumbers, using advanced quasilinear approximations to model turbulent transport more accurately. While GLF23 treated low-k_y ion-scale turbulence effectively, TGLF's improved treatment of trapped particles and inclusion of electron-scale instabilities allow it to address multi-scale turbulence. The k_y-spectrum is generated based on predefined models and configurations, controlled by the input parameter `kygrid_model` (see Section 2.2.3.2). TGLF also integrates a more accurate model for the saturation of turbulent fluctuations, leading to improved predictive capability across a wider range of plasma conditions [2, 106]. TGLF also improves upon GLF23 by including electromagnetic effects, allowing it to model electromagnetic instabilities, such as kinetic ballooning modes, making it suitable for the high-β conditions central to this PhD study.

TGLF is a gyrofluid model (see section 1.3.1.2) using the local δf approximation, derived from the velocity moments of the gyroaveraged kinetic equation [107], coupled with Maxwell's equations. The complete derivation and closure of the TGLF equations are detailed in [108]. The dispersion relation in TGLF is constructed using a gyrofluid approach made of 12 fluid moments for circulating particles and 3 moments for trapped particles, for each species. The model computes the linear eigenmodes of trapped ion and electron modes (TIM, TEM), ion and electron temperature gradient (ITG, ETG) modes and kinetic ballooning modes (KBMs) TGLF, as an eigenvalue solver, identifies the most unstable modes by ranking growth rates across a specified number of modes. It can also find the two dominant unstable modes corresponding to different frequency direction: the electron drift direction and the ion drift direction. The linear eigenmodes calculated by TGLF have been extensively benchmarked against gyrokinetic calculations. During its development, TGLF's linear eigenvalues were tuned against a database of 1800 linear stability calculations from the GKS gyrokinetic

code. Eigenfunctions in TGLF are computed using a projection to a basis of Hermite functions. Further explanation of this process is provided in Section 2.1.3. TGLF predicts energy, particle, and momentum fluxes for up to seven particle species, including electrons, enabling an analysis of multi-species plasmas within a tokamak. For shaped finite aspect ratio geometries, TGLF employs the Miller equilibrium model [109]. This model allows TGLF to handle realistic magnetic geometries with elongation and triangularity effects. A detailed description of the Miller equilibrium model is provided in Section 2.3.2.1.

2.1.1. Turbulence Saturation Models

TGLF includes four distinct saturation models to approximate the saturation of turbulence. Theses models are built based on preceding models, incorporating progressively more physics. The baseline model, **SAT0** [11, 1], provides a basic framework for predicting saturated potential fluctuations. Building on this, **SAT1** [106] enhances the model by incorporating additional effects, such as coupling between wavevectors. **SAT2** [110, 111] extended SAT1 by incorporating additional physical insights gained from observations of turbulent spectra. Key refinements include geometric effects due to the Shafranov shift and plasma elongation, which have been shown to be key for L-mode edge modeling [112]. Building on SAT2, **SAT3** [113, 100] introduced further advancements to capture anti-gyroBohm scaling of fluxes and distinguish between ion-temperature-gradient (ITG) and trapped-electron-mode (TEM) saturations.

The saturation models in TGLF are optimized to best fit a database of 160 nonlinear gyrokinetic turbulence simulations from the GYRO code. No fitting parameters were adjusted based on experimental data, all were derived from linear and nonlinear theory. However, TGLF has been validated against experimental data from several tokamaks, including DIII-D [114, 115], NSTX [116], ASDEX [117] and JET [118].

2.1.2. Key Improvements in TGLF Over GLF23

Improved Treatment of Particle Trapping in TGLF

One significant advances in TGLF over GLF23 is its treatment of trapped particles. In fusion plasmas, particles can become “trapped” by magnetic field inhomogeneities, which create a mirror-like effect. These trapped particles are crucial for accurately modeling turbulent transport, especially for modes like TEM which strongly interact with trapped particle dynamics. Unlike GLF23, which used separate simplified treatments for low-k_y and high-k_y regimes, TGLF unifies trapped and passing particles into a single set of gyro-Landau fluid equations. TGLF introduces an effective trapped particles fraction that depends on k_y rather than mode frequency, allowing a single set of equations to cover all frequencies and poloidal wavenumbers, allowing TGLF to handle a broader range of instabilities within the same system. TGLF uses a refined set of moment closures specifically developed to capture the complex effects of particle trapping on transport. Closure coefficients depend on the trapped fraction and adapt

with changes in magnetic geometry, allowing a more nuanced capture of the trapped particle response across diverse plasma conditions [2, 106].

Collision Modeling in TGLF

The TGLF model refines the limited collisional treatment in GLF23 by incorporating a detailed electron-ion and electron-electron collision model using an energy-dependent pitch-angle scatering operator. [2] To achieve this, TGLF uses optimized fluid closure coefficients calculated to closely fit the kinetic response obtained with the more advanced gyrokinetic solver GYRO [87] for density, pressure, parallel flow, and energy flux under pitch-angle scattering conditions. This fitting process, which solves the local gyrokinetic equation for fluid moments, provides a reduced model with high fidelity to kinetic results The model also enhances accuracy in representing trapped-passing electron interactions by introducing new asymptotic limits and simplified coefficients for the trapped-passing boundary. These adjustments capture the damping effects critical to energy and particle transport, especially near the plasma edge and in transport barriers where collisional exchanges strongly impact transport dynamics [2] Unlike GLF23, where collisions were minimally represented, TGLF adapts its collision coefficients based on the collisionality of the plasma region.

2.1.3. Hermite Basis Function Expansion for Eigenmode Calculations

In TGLF, Hermite functions, denoted as Ψ_n , are employed to project the equations along the magnetic field direction and solve for the eigenmodes of the system. They are defined as:

$$\Psi_n = e^{-\hat{\theta}^2/2} h_n \qquad \text{with} \qquad \int_{-\infty}^{\infty} d\hat{\theta} \Psi_n \Psi_m = \delta_{n,m} \tag{2.1}$$

Where $\hat{\theta} = \theta/\theta_w$, θ being the poloidal angle and θ_w the width of the Gaussian envelope. The normalized Hermite polynomials h_n are given by:

$$h_n = \hat{\theta}\sqrt{\frac{2}{n-1}} h_{n-1} - \sqrt{\frac{n-2}{n-1}} h_{n-2} \tag{2.2}$$

With :

$$h_1 = \frac{\sqrt{2}}{\pi^{1/4}}, \qquad h_2 = \hat{\theta}\sqrt{2} h_1$$

The eigenmodes in TGLF are projected in a finite series of Hermite basis functions with complex coefficients. This choice enables TGLF to achieve accurate solutions with relatively few terms, enhancing numerical efficiency, a primary objective of quasi-linear models. If the Gaussian width is chosen appropriately, the eigenvectors $\delta\phi$, $\delta A_\parallel$, and $\delta B_\parallel$ can be represented with a minimal number of Hermite basis functions. However, if the width is not well-suited, more terms will be required to achieve accurate

eigenmodes. For this reason, an accurate estimate of the Gaussian width θ_w is crucial.

2.2. Simulation Workflow of the TGLF Code

This section provides a detailed explanation of the TGLF simulation workflow, breaking down each step of the process. We will explore how TGLF manages input parameters, performs linear stability analysis, and calculates turbulent transport.

2.2.1. TGLF Simulation Setup

The TGLF simulation begins by reading the content of the `input.tglf` file located in the directory where the simulation is run. All output files generated by the simulation will also be saved in this directory. The code then proceeds to configure the simulation setup according to the specified input values. This includes selecting the system units ('GYRO', 'CGYRO', or 'GENE'). Note that 'CGYRO' units are automatically enforced when saturation models 2 or 3 are specified, as is the case in this thesis. The plasma parameters and numerical settings defined in the input file are also initialized at this stage.

The number of Hermite basis functions used in the simulation is controlled by two input parameters, `nbasis_min` and `nbasis_max`. Both values must lie within the range of 2 to 32, with `nbasis_min` being strictly less than `nbasis_max`. Additionally, these values must be even. If an odd number is entered, TGLF will automatically round down to the nearest even integer.

The parameter `nmodes` determines the number of modes per wavevector included in the simulation, constrained to values between 1 and 16 ($1 \leq$ `nmodes` ≤ 16). However, if the `ibranch` parameter is set to 0, the number of modes is automatically enforced at 2. When `ibranch` is set to 0, TGLF identifies the two most unstable modes, one for each sign of frequency, aligning with the electron drift and ion drift directions. Alternatively, setting `ibranch` to -1, which is the default and the setting used in this thesis, allows TGLF to sort and rank all unstable modes by their linear growth rates. The number of points in the k_y spectrum, denoted by `nky`, must be between 2 and 512 ($2 \leq$ `nky` ≤ 512). In TGLF, the grid for the k_x spectrum cannot be directly controlled. Instead, users can specify a single value for the ratio k_x/k_y, with the default being 0. Changing this ratio affects only the calculation of the predicted saturated potential fluctuations.

TGLF allows for different parameterizations of the magnetic equilibrium based on the value of `geometry_flag`. The options available are '$s-\alpha$', 'Miller', and 'Fourier'. The '$s-\alpha$' geometry cannot be used with the saturation model SAT2. For this thesis, we employ the standard Miller parameterization, which is discussed in more detail in Section 2.3.2.1. When using the Miller parameterization, certain constraints apply: if the flux surface centroid minor radius r_0 exceeds or equals the major radius R, then r is limited to $0.999 \times R$; similarly, if the radial derivative of R, $\frac{dR}{dx}$, is less than or equal to -1, it is adjusted to -0.999. Also, ∇r_0 is automatically set to $\nabla r_0 = \frac{1}{1+\frac{dr}{dx}}$.

Additionally, if the input parameter `use_bper`, which activates the inclusion of transverse magnetic fluctuations $\delta A_\parallel$, is set to `True`, then the input parameter `alpha_mach` is automatically enforced to 0. Here, `alpha_mach` represents a scaling factor for the parallel velocity of all species. Setting this parameter to 0 means that when transverse magnetic fluctuations $\delta A_\parallel$ are included, the parallel velocities for all species are effectively turned off.

At the end of the TGLF setup phase, the code checks the value of the input parameter `use_transport_model`, which is set to `True` by default. If `use_transport_model` is set to `False`, TGLF will run for a single wavevector k_y, computing the linear stability of that specific Fourier mode. In this case, TGLF calculates the corresponding linear eigenvalues and eigenfunctions. On the other hand, if `use_transport_model` is set to `True`, TGLF will evaluate the linear response for each wavevector k_y within the defined spectrum. These linear responses are then used to predict turbulent fluxes by combining them with a model for turbulence saturation, by applying the quasilinear theory detailed in Section 1.3.3.

In the next sections, we will first examine how TGLF handles single-k_y linear stability. Following this, we will explore how TGLF utilizes its transport model to calculate turbulent fluxes.

2.2.2. TGLF simulation workflow in single-k_y linear stability

As mentioned in Section 2.1.3, TGLF uses Hermite functions to project the equations and solve for the system's eigenmodes along the magnetic field lines, and an accurate estimate of the Gaussian width θ_w is crucial. TGLF addresses this with a two-stage solution method. Initially, the eigenvalues are computed using a smaller number of Hermite basis functions set by `NBASIS_MIN`, and this computation is performed across various widths (θ_w). The width that yields the maximum linear growth rate is selected for the subsequent stage, where a larger number of Hermite basis functions, `NBASIS_MAX`, is used to obtain the final results. In the initial stage, TGLF searches for the optimal envelope width by exploring values within a range specified by `WIDTH_MIN` and `WIDTH`, aiming to maximize the linear growth rate. During this stage, if saturation models SAT2 or SAT3 are used, any effects from $\delta A_\parallel$ and $B_\parallel$, if included, are temporarily disabled. The search for the optimal width is further controlled by the parameter `nwidth`, which sets the number of points in the width grid wich is computed in logarithmic space to cover a wide range of values. By default, `use_bisection` is enabled, setting an initial grid size of 5 points and employing a bisection algorithm. When `use_bisection` is active, the algorithm iteratively narrows the search range around the previously identified maximum by halving the grid, selecting the midpoint in each iteration to refine the width estimate. The numerical input parameters `NBASIS_MAX` and `WIDTH` are highly sensitive and can significantly impact the linear results from TGLF, potentially leading to unexpected outcomes. A detailed analysis of the influence of these parameters is provided in Section 3.3.3.

Identifying and Filtering Unstable Modes

Once the optimized Gaussian width has been determined, TGLF proceeds to compute the linear stability for a single k_y-mode. This involves solving a complex linear matrix eigenvalue problem to evaluate the eigenmodes and calculate all the quasi-linear weights associated with the given k_y-value.
Following the computation of eigenvalues and eigenvectors, TGLF applies a filtering process to eliminate non-physical numerical instabilities. High-frequency spurious modes can occasionally appear in simulations and must be excluded to ensure accurate results. To address this, TGLF employs the `FILTER` switch, which is enabled by default with a recommended value of `FILTER` = 2. This setting filters out modes with frequencies exceeding twice the drift-wave frequency, effectively removing spurious modes. However, it also excludes certain high-frequency physical instabilities, such as Kinetic Ballooning Modes (KBMs), which are critical for this study. In Chapter 3, a new refined filter developed during this PhD work will be introduced. This filter, now implemented within TGLF, offers an improved approach to retaining essential high-frequency modes while continuing to suppress numerical instabilities.

Quasi-linear Weights Computation

After filtering, TGLF computes the quasi-linear weights for the retained unstable modes. One advantage of TGLF's reduced linear system is its ability to solve directly for eigenvalues, rather than relying on initial value solvers like those used in gyrokinetic codes such as GKW. This approach makes it easier to identify subdominant modes, and to include their contributions in the calculation of turbulent fluxes. The number of retained modes for this analysis is specified by the input parameter `nmodes`.

As explained earlier, linearised fluctuating quantities grow exponentially with time at the growth rate γ. To extract meaningful and physically consistent results, the quasi-linear weights must be normalized using a quantity that also grows exponentially with time at the same growth rate. In TGLF, this normalization is achieved using $\langle |\delta\phi|^2 \rangle$, which represents the intensity of the electric potential fluctuations.
To obtain $\langle |\delta\phi|^2 \rangle$, TGLF first solves the linear eigenvalue problem to obtain $\delta\phi_L$, the linearised fluctuating electrostatic potential, along with the eigenvalues and eigenvectors of the system. The solution for $\delta\phi_L$ is expanded as a finite series of Hermite basis functions:

$$\delta\phi_L(\theta) = \sum_{n=1}^{\text{nbasis}} \delta\phi_L(n)\Psi_n(\theta)$$

where $\delta\phi_L(n)$ represents the coefficients associated with the n-th Hermite function.

Next, TGLF computes $\langle|\delta\phi_L|^2\rangle$ using the following expression:

$$\begin{aligned}\langle|\delta\phi_L|^2\rangle &= \int_{-\infty}^{\infty} \delta\phi_L \delta\phi_L^\dagger d\hat{\theta} \\ &= \int_{-\infty}^{\infty} \sum_{n=1}^{\text{nbasis}} \delta\phi_L(n)\Psi_n \sum_{m=1}^{\text{nbasis}} \delta\phi_L^\dagger(m)\Psi_m \, d\hat{\theta} \\ &= \sum_{n=1}^{\text{nbasis}} \delta\phi_L(n)\,\delta\phi_L^\dagger(n).\end{aligned} \tag{2.3}$$

This result is obtained because the Hermite basis functions are orthogonal, satisfying $\int_{-\infty}^{\infty} \Psi_n \Psi_m \, d\hat{\theta} = \delta_{n,m}$.
As a result, the normalized electrostatic potential given as an output in TGLF is computed as:

$$\delta\phi = \frac{\delta\phi_L}{\sqrt{\langle|\delta\phi_L|^2\rangle}}. \tag{2.4}$$

And the quasi-linear weights are calculated as:

$$W_{Q,sN}(k_y) = \frac{Q^L_{s,k_y}}{\langle|\delta\phi_L|^2\rangle}, \tag{2.5}$$

where $W_{Q,sN}(k_y)$ represents the quasi-linear weight for the heat flux and Q^L_{s,k_y} represent the linear heat flux (see Eq 1.41).

At the conclusion of these calculations, TGLF stores the quasi-linear weights, eigenvalues, and eigenmodes, completing the single-k_y linear stability analysis. These quantities form the basis for subsequent calculations of turbulent fluxes across the k_y-spectrum in TGLF's transport model.

2.2.3. Transport Model in TGLF

The single-k_y linear stability analysis discussed forms the foundation for TGLF's transport model. When using its transport model, TGLF extends this analysis across a spectrum of k_y-values, systematically evaluating linear responses and then computing spectral integrals of fields, intensities, and fluxes. In this subsection, we delve into the transport model workflow, exploring how TGLF synthesizes these spectral responses to calculate energy, particle, and momentum fluxes for a given plasma equilibrium.

2.2.3.1. Spectral shift model in TGLF

TGLF begins by calculating the quasi-linear fluxes spectrums over k_y. If the simulation includes a non-zero $E \times B$ shearing rate ($\gamma_{E\times B}$), controlled by the input parameter `vexb_shear`, and the input `alpha_quench` is set to 0 (its default value), TGLF employs a double-pass spectral shift model to accounts for the impact of the $E \times B$ shearing rate on the turbulent flux spectra. The linear spectrums in TGLF are evaluated twice: once

without $\gamma_{E\times B}$ and once with them. During the first evaluation, only the eigenvalues (γ, ω_r) are computed, ignoring the effects of $\gamma_{E\times B}$. The eigenvectors are not calculated at this stage. In the second evaluation, both the eigenvalues and eigenvectors are computed, now including the effects of $\gamma_{E\times B}$. As a result, the quasi-linear weights $(W_Q, W_\Gamma, W_\Pi, \ldots)$ are calculated incorporating the $\gamma_{E\times B}$ effects, while the eigenvalues (γ, ω_r) given in output remain unaffected by them. If $\gamma_{E\times B} = 0$, the double-pass evaluation is unnecessary, and the bilinear spectrum is computed directly in a single step.

2.2.3.2. Computation of the k_y-Spectrum in TGLF

This section delves into the computation of the k_y-spectrum, which defines the binormal wavenumbers used in TGLF simulations. In TGLF, the reference Larmor radius, ρ_s, is defined as:

$$\rho_s = \frac{m_D\, c_s}{q\, B_{unit}} \tag{2.6}$$

where m_D is the deuterium mass, c_s is the deuterium sound speed, given by:

$$c_s = \sqrt{\frac{T_e}{m_D}}$$

with T_e representing the electron temperature and q the elementary charge. The effective field strength, B_{unit}, is defined as:

$$B_{unit} = \frac{1}{r}\frac{d\chi_t}{dr} \tag{2.7}$$

where χ_t corresponds to the toroidal magnetic flux divided by 2π. This quantity provides an approximation of the equivalent magnetic field strength that would be obtained if the flux surface were deformed into a circle.

The k_y-spectrum generation relies on various predefined models and numerical configurations, controlled by the input parameter `kygrid_model`. Several options are available for configuring the k_y-grid:

`KYGRID_MODEL = 0`, **Linear k_y-Spectrum:** In this configuration, a uniform k_y-grid is generated between 0 (not included) and `ky` (included). The spacing (Δk_y) is constant and calculated as:

$$\Delta k_y = \frac{\texttt{ky}}{\texttt{nky}},$$

where `ky` defines the maximum k_y-value, and `nky` specifies the total number of grid points. The spectrum values are then computed iteratively by incrementing k_y by Δk_y.

`KYGRID_MODEL = 1`: This spectrum is designed to resolve both small and large k_y-values by dividing the grid into two distinct regions:

— **Linear Region:**
The linear region spans the smaller k_y-values and is initialized with nine points. The k_y-values in this region are uniformly spaced, with the maximum and minimum k_y-values set as:

$$k_y \rho_s|_{\text{max}} = 0.9, \qquad k_y \rho_s|_{\text{min}} = 0.1,$$

A constant spacing (Δk_y) is applied throughout the linear region.

— **Logarithmic Region:**
For larger k_y-values, the spectrum transitions to a logarithmic region, starting from the largest k_y-value in the linear region. The logarithmic region accommodates a fixed number of points, as defined by the input parameter `nky`. Unlike the linear region, the spacing in the logarithmic region grows exponentially.
The k_y-values in the logarithmic region are calculated iteratively using the following relations:

$$k_y^{(i+1)} = k_y^{(i)} \cdot e^{\text{log-step size}}, \qquad \Delta k_y^{(i)} = k_y^{(i)} \cdot \text{log-step size},$$

where the *log-step size* determines the proportional growth between successive k_y-values. This method ensures that the spacing increases proportionally to k_y, maintaining logarithmic scaling. The iterative process continues until the specified number of `nky` points are generated, fully populating the logarithmic region.

`KYGRID_MODEL = 2`**:** This spectrum introduces an additional intermediate linear region with larger spacing, ensuring a more comprehensive coverage of the k_y-range. The three regions are defined as follows:

— **First Linear Region:**
Similar to the `KYGRID_MODEL = 1` spectrum, the first region resolves smaller k_y-values using uniform spacing. However, this region contains a fixed number of $n = 8$ points, with the smallest k_y-value starting at:

$$k_y \rho_s|_{\text{min}} = 0.05,$$

The spacing in this region is constant and calculated as:

$$\Delta k_y \, \rho_s = 0.05.$$

This configuration ensures finer resolution of small k_y-modes compared to the `KYGRID_MODEL = 1` spectrum.

— **Second Linear Region:**
The second region introduces a larger, uniform spacing to span intermediate k_y-values. This region starts from the last k_y-value in the first linear region and includes $n = 7$ additional points. The spacing in this region is larger than in the

first, calculated as:

$$\Delta k_y \rho_s = 0.2$$

— **Logarithmic Region:**
The logarithmic region begins from the largest k_y-value in the second linear region and spans the higher k_y-values. This region follows the same approach to the logarithmic region in the `KYGRID_MODEL = 1` spectrum.

`KYGRID_MODEL = 3`, **Custom Spectrum with $k_y^{\text{min}} = \texttt{ky}$:** This spectrum allow the user to specify the minimum binormal wavevector k_y^{min} through the input parameter `ky`. The procedure for constructing the k_y-spectrum consists of distinct regions. The first region spans from $k_y^{\text{min}}\rho_s = \texttt{ky}$ to $k_y^{\text{max}}\rho_s = 1.0$. Each subsequent k_y-value in the linear region is incremented by a constant spacing:

$$\Delta k_y = k_y^{\text{min}}.$$

If the last value in this region does not reach $k_y\rho_s = 1.0$, a single additional point is introduced to bridge the gap. This ensures a smooth transition to the logarithmic region. The logarithmic region construction follows the same approach to the previous spectrums

`KYGRID_MODEL = 4`, **Spectrum with lower $k_y|_{min}$:** This configuration is similar to the `KYGRID_MODEL = 1` spectrum but emphasizes resolving very low-k_y-values with enhanced precision.

— **Low-k_y Linear Region:**
The low-k_y region is initialized with six k_y-values. The smallest k_y-value (k_y^{min}) is explicitly set as:

$$k_y^{\text{min}}\rho_s = 0.05 \cdot \nabla r_0$$

The remaining five k_y-values are generated with uniform spacing (Δk_y) equal to k_y^{min}. The resulting k_y-values in this region are:

$$k_y^{(i)} = i \cdot k_y^{\text{min}}, \quad i = 1, \ldots, 6.$$

— **Intermediate Linear Region:**
After the low-k_y region, an intermediate linear region is defined. The intermediate region is initialized with six additional k_y-values, where:

$$k_y^{\text{max}}\rho_s = 1.0 \cdot \nabla r_0 \qquad \text{and} \qquad \Delta k_y \rho_s = 0.1 \cdot \nabla r_0$$

Each subsequent k_y-value in this region is determined iteratively as:

$$k_y^{(i)} = k_y^{\text{low}} + (i-6) \cdot \Delta k_y, \quad i = 7, \ldots, 12.$$

— **Logarithmic Region:**
Similar to other spectrum types, the logarithmic region begins at the final k_y-

value of the intermediate linear region and extends to higher k_y-values. The number of points in this region is specified by the input parameter `nky_in`. The logarithmic scaling ensures proportional spacing between successive k_y-values. The calculation follows the same iterative process as in the `KYGRID_MODEL = 1` spectrum:

$$k_y^{(i+1)} = k_y^{(i)} \cdot e^{\text{log-step size}}, \qquad \text{log-step size} = \frac{\ln\left(k_y^{\text{final}} / k_y^{\text{intermediate}}\right)}{\texttt{nky} - 1}.$$

The k_y-values and spacings (Δk_y) for this region are computed iteratively until all points are generated.

This configuration is frequently employed with the SAT2 saturation model, as resolving low-k_y modes can be essential for achieving accurate predictions of turbulent fluxes. However, as will be demonstrated later in this thesis, low-k_y modes are particularly susceptible to numerical issues, making the selection of the k_y-grid spectrum a critical consideration.

2.2.3.3. Identifying the Local Maximum of γ / k_y

In TGLF, the local maximum of the γ / k_y spectrum plays a critical role in the application of the saturation models. These models rely on two key values extracted from the γ / k_y curve:

- $k_{y,\max}$: The binormal wavenumber (k_y) at which the ratio γ / k_y reaches its local maximum.
- $\gamma_{\max}$: The linear growth rate at $k_{y,\max}$.

The objective of this section is to detail how TGLF compute thoses values.

TGLF begins by initializing the growth rate spectrum ($\gamma(k_y)$) and the k_y spectrum obtained from the previous steps. Additionally $k_{y,\text{cut}}$ defines the maximum k_y value to consider for the search and is given by $k_{y,\text{cut}}\rho_s = 0.8$.

The minimum $k_{y,\min}$ value considered for the search of the peak is first set to 0. However it may be adjusted based on the input parameter `alpha_zf`. If the value of `alpha_zf` is negative (it's default value is 0), then:

$$k_{y,\min}\rho_s = 0.173\sqrt{2}\nabla r_0 \tag{2.8}$$

Then, TGLF iterates through the k_y spectrum, only k_y-values that fall between $k_{y,\min}$ and $k_{y,\text{cut}}$ are considered. For each valid k_y, TGLF computes the ratio γ / k_y, and tracks the k_y-value where the maximum of that ratio occurs. If no valid maximum is identified within the range, the subroutine defaults to assigning the first k_y in the spectrum as the location of the maximum.

To improve accuracy, when the maximum lies between discrete values of the k_y-grid, the subroutine applies a quadratic interpolation. This involves selecting three consecutive points around the identified maximum: f_0 (the value before the maximum), f_1

(the value at the maximum), and f_2 (the value after the maximum), where $f = \gamma / k_y$. A quadratic function is then fitted through these points to refine the estimates of both $\gamma_{\max}$ and $k_{y,\max}$.
An important detail is that the refined $\gamma_{\max}$ and $k_{y,\max}$ values derived from the interpolation may not correspond to a point in the original k_y spectrum grid. In such cases, while the subroutine accurately computes these maximum values, the turbulent fluxes at these interpolated points will not be evaluated because they lie outside the predefined k_y-grid. This distinction ensures that the interpolation enhances precision for identifying key parameters without modifying the underlying flux computation framework.

2.2.3.4. Flux Calculation

As previously described, in TGLF for each k_y of the sprectrum, the optimized Gaussian width (θ_w) is determined using the two-stage method outlined earlier. Then the linear solver is called for the given k_y value, computing the quasi-linear weights.
Once these steps are completed, TGLF proceeds to compute the spectrum of the saturated intensity of the electric potential fluctuations, $\left\langle |\delta\phi_{k_y}|^2 \right\rangle$, using its built-in saturation models.
In this work, the saturation model SAT2 is employed. A detailed description of this model can be found in the reference [111]. Later in this thesis (Chapter 4), we will show flux predictions obtained by combining the linear responses from GKW (run in its linear mode) with the same SAT2 saturation model, as described in this reference. These predictions demonstrated good agreement with the non-linear fluxes.
At this stage, with the spectra of quasi-linear weights and saturated potentials computed, TGLF calculates the predicted fluxes. The heat flux, for instance, is determined using the following equation:

$$Q_s = \sum_m \sum_{k_y>0} W_{Q,sN}(k_y, m) \left[\frac{\left\langle |\delta\phi_{k_y}|^2 \right\rangle}{\Delta k_y} \right]_m \Delta k_y \tag{2.9}$$

Here, m represents the retained eigenmodes, and the summation is carried out over the initial k_y spectrum. To ensure numerical consistency, $\left\langle |\delta\phi_{k_y}|^2 \right\rangle$ is normalized to the binormal grid spacing Δk_y, as this normalization ensures invariance under changes in the k_y grid resolution.

This marks the completion of the TGLF simulation workflow, providing a systematic framework for the prediction of turbulent fluxes based on the quasi-linear approximation.

2.3. Unified standard for Gyrokinetic simulations

In gyrokinetic simulations, benchmarking different codes is challenging due to differences in how key physical parameters are defined and normalized. Each code has its own way of defining and normalizing the same physical quantities, such as density and temperature gradients or plasma pressure. These differences can cause errors when comparing the results from multiple codes. This lack of standardization complicates the verification process across different codes, which is crucial for ensuring the reliability of reduced models . To facilitate cross-verifications, a common framework is needed that ensures every code operates on the same basis when handling input and output data. Without such a framework, benchmarking remains error-prone and inefficient.

The **Integrated Modelling and Analysis Suite (IMAS)** provides a solution to this problem. IMAS is a comprehensive framework developed to support all aspects of plasma modeling and analysis for ITER, encompassing a wide range of physics models and workflows, from experimental data integration to complex scenario modeling [4]. Furthermore, IMAS is designed with flexibility in mind, its modular structure allows individual components to be developed, extended, and integrated as needed. While IMAS is designed to be a general infrastructure for data management and model integration, in this work, we focus specifically on its application to flux-tube gyrokinetic simulations through the use of the **Gyrokinetic-local Interface Data Structure (IDS)** [8]. A unified set of conventions and normalizations for the inputs and outputs of δf flux-tube gyrokinetic simulations has been developed to facilitate consistent benchmarking and integration of various gyrokinetic codes, such as TGLF and GKW. By using a common format and normalisations for data, the IMAS framework effectively creates a "common language" for these codes, allowing them to communicate seamlessly. The IDS framework not only supports consistency in simulations but also enhances transparency and reproducibility. Each IDS contains detailed metadata that tracks the provenance of the data, including the code version used, specific settings, and the physical effects included in the simulations. This level of details ensures that results are fully traceable and that benchmarking exercises can be repeated accurately. By providing a common platform that every research group can use, IMAS, when integrated with a centralized database of cases, further reduces redundancy, allowing researchers to focus on advancing the physics rather than managing differences in data format. IMAS's data model is machine-independent, meaning that the benchmarking framework is extensible beyond individual machines or models. IMAS's role goes beyond simulation data standardization, it also integrates experimental data into the same data model. This integration enables direct comparisons between simulations and experimental measurements, enhancing the ability to validate theoretical predictions with empirical data [9]. The foundational motivation and design of IMAS, including its data standardization capabilities, are well documented in [4].

2.3.1. Scripts for IMAS-TGLF Integration

The Python scripts developed as part of this work are designed to automate the conversion of Gyrokinetic IDSs into TGLF input files and to convert TGLF output files back into IDS format. This conversion process, which has already been implemented for the GKW code, has now been extended to TGLF. The Python scripts are designed with a high level of automation and user-friendliness. With a single function call, the scripts can:

— Convert an IDS object to a TGLF input file
— Run a TGLF simulation using these inputs.
— Store the TGLF outputs back into a new IDS object

To ensure that these tools are accessible to the broader research community, the scripts have been made available in an open-source Git repository [119]. The repository includes documentation and example files that demonstrate how to use the routines, allowing other researchers to adopt them easily without extensive setup or configuration. This availability reduces the barrier for other fusion researchers to engage in benchmarking activities, thereby promoting more robust cross-validation across different codes in the community. These routines have already been adopted by other researchers for verification studies.

2.3.2. Structure and Functionalities of the Conversion

In this section, we present the key conversion formulas used to facilitate data exchange between IMAS and TGLF. These formulas handle the normalization and transformation of physical quantities, ensuring consistency between the two systems.

2.3.2.1. Magnetic Equilibrium

One of the key aspects of the conversion involves handling the magnetic equilibrium data, which must be translated between the different representations used in IMAS and TGLF. Both IMAS and TGLF use the same cylindrical coordinate system, defined by (R, φ, Z), where R represents the major radius, φ denotes the toroidal angle, and Z is the elevation. The coordinate system is right-handed, with φ increasing in an anti-clockwise direction when viewed from above the tokamak. Figure 2.1 provides a visual comparison of the coordinate conventions used by TGLF and IMAS. The gyrokinetic equations are solved within a localized flux-tube region, which extends along the flux surface identified by the label Ψ_0. The poloidal contour of this surface is determined by the function $\Psi(R, Z)$
The definitions of R_0, Z_0, and r remain consistent between IMAS and TGLF and are given by:

$$R_0^{\texttt{TGLF}} = R_0^{\texttt{IMAS}} = \frac{1}{2}[R_{\min} + R_{\max}] \qquad Z_0^{\texttt{TGLF}} = Z_0^{\texttt{IMAS}} = \frac{1}{2}[Z_{\min} + Z_{\max}] \tag{2.10}$$

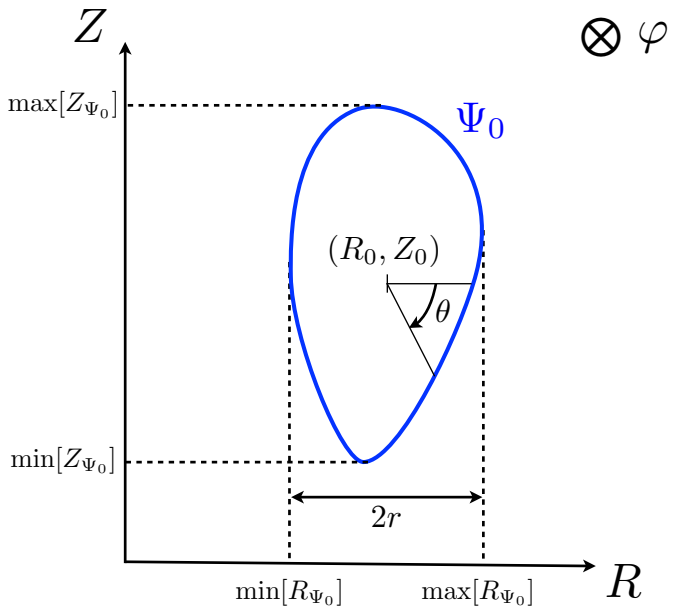


Figure 2.1. – Cylindrical coordinate systems used in TGLF and IMAS. The system is right-handed with R as the major radius, Z as the elevation, and φ as the toroidal angle.

Where R_{min} and R_{max} represent the minimal and maximal values of the major radius for the flux surfaces, and Z_{min} and Z_{max} denote the respective vertical bounds. Similarly, the minor radius (r) is defined as:

$$r^{\texttt{TGLF}} = r^{\texttt{IMAS}} = \frac{1}{2}[R_{\text{max}} - R_{\text{min}}] \tag{2.11}$$

In the flux-tube coordinate system (x, y, θ), each coordinate has a specific physical interpretation related to the structure of the plasma and the magnetic field.

- The radial coordinate x is defined as:

$$x = \frac{r - r_0}{R_0}$$

This coordinate serves as a flux surface label, increasing from the magnetic axis outward toward the plasma edge.

- The binormal coordinate y increases in the direction of the toroidal angle φ.

- The parallel coordinate θ represents the position along the magnetic field lines, often referred to as the extended ballooning angle.

By definition, the equilibrium magnetic field **B** is confined to the flux surfaces, meaning that it has no radial or binormal components. This can be expressed mathe-

matically as:

$$\mathbf{B} \cdot \nabla x = 0 \quad \text{and} \quad \mathbf{B} \cdot \nabla y = 0$$

These conditions ensure that x and y are perpendicular to the equilibrium magnetic field $\mathbf{B}$.

In IMAS, the magnetic equilibrium is parameterized using the Miller eXtended Harmonics (MXH) parameterization [120]. For the purpose of IMAS-TGLF coupling, we employ the standard Miller parameterization available in TGLF. Table 2.1 provides a mapping between key geometric parameters used in the below equations and their corresponding notations in the TGLF input file. The parameter a refers to the radius of the last closed flux surface and x denotes the horizontal position along the mid-plane axis. In TGLF, the Miller parameterization [109] describes the flux surfaces in function

TGLF Input Notation	**Value**
RMIN_LOC	r/a
RMAJ_LOC	R_0/a
ZMAJ_LOC	Z_0/a
DRMINDX_LOC	$\partial r/\partial x$
DRMAJDX_LOC	$\partial R_0/\partial x$
DZMAJDX_LOC	$\partial Z_0/\partial x$
KAPPA_LOC	κ
S_KAPPA_LOC	$\frac{r}{\kappa} \cdot \frac{\partial \kappa}{\partial r}$
DELTA_LOC	δ
S_DELTA_LOC	$r \cdot \frac{\partial \delta}{\partial r}$
ZETA_LOC	ζ
S_ZETA_LOC	$r \cdot \frac{\partial \zeta}{\partial r}$

Table 2.1. – Mapping of magnetic equilibrium parameters from Miller parameterization to TGLF input file notations.

of the poloidal angle θ as:

$$R(r,\theta) = R_0(r) + r\cos(\theta + \arcsin\delta \sin\theta) \tag{2.12}$$

$$Z(r,\theta) = Z_0(r) + \kappa r \sin(\theta + \zeta \sin 2\theta) \tag{2.13}$$

In this formulation, the parameter κ governs the elongation, δ the triangularity, and ζ the squareness of the flux surface shape. The MXH parameterization extends the Miller formulation by including higher-order harmonics to capture more complex flux surface shapes. The flux surfaces are defined with:

$$R(r,\theta) = R_0(r) + r\cos\theta_R \tag{2.14}$$

$$Z(r,\theta) = Z_0(r) + \kappa r \sin\theta \tag{2.15}$$

Where:

$$\theta_R = \theta + c_0(r) + \sum_{n=1}^{N} [c_n(r)\cos n\theta + s_n(r)\sin n\theta] \tag{2.16}$$

To convert between Miller and MXH parameterization, we need to pass through the $(R(r,\theta)\ ,\ Z(r,\theta)\ )$ representation of the flux surface and calculate two adjacent flux surfaces to evaluate the radial derivatives of geometric parameters. The minor radius step, dr, is defined as:

$$dr = 0.01 \cdot r \tag{2.17}$$

allowing us to obtain neighboring surfaces defined at $r_+ = r + dr$ and $r_- = r - dr$. We then obtain:

$$r_\pm = r \pm dr \qquad R_{0\pm} = R_0 \pm \frac{\partial R}{\partial r} \cdot dr$$

$$\kappa_\pm = \kappa \pm s_\kappa \cdot \kappa / r \cdot dr \qquad Z_{0\pm} = Z_0 \pm \frac{\partial Z}{\partial r} \cdot dr$$

$$\delta = \delta \pm s_\delta / r \cdot dr \qquad \zeta = \zeta \pm s_\zeta / r \cdot dr$$

So, in the Miller parametrization, the two adjacent neighbours flux surfaces are obtained as:

$$R(r,\theta)_\pm = R_{0\pm} + r_\pm \cos(\theta + \arcsin\delta_\pm \sin\theta) \tag{2.18}$$

$$Z(r,\theta)_\pm = Z_{0\pm} + \kappa_\pm r \sin(\theta + \zeta_\pm \sin 2\theta) \tag{2.19}$$

So we can obtain the MXH values of θ_R using: $\cos\theta_R = (R - R_0)/r$ and the values of θ using: $\sin\theta = (Z - Z_0)/\kappa r$. The coefficients c_n and s_n are computed by fitting the flux surfaces derived from Miller's description, thereby allowing an accurate representation in the MXH framework.

2.3.2.2. Reference Quantities

In both TGLF and gyrokinetic IDS (GK-IDS), all physical quantities are normalized and made dimensionless through the use of reference quantities. Throughout this section, normalized quantities will be denoted with a subscript "N". For instance, the normalized version of an arbitrary length-like quantity $\mathscr{A}$ is expressed as $\mathscr{A}_N^{\texttt{TGLF}} = \mathscr{A} / L_{\text{ref}}^{\texttt{TGLF}}$ in TGLF, and as $\mathscr{A}_N^{\texttt{IMAS}} = \mathscr{A} / L_{\text{ref}}^{\texttt{IMAS}}$ in GK-IDS.
IMAS normalizations are provided in Table 2.3 and TGLF normalizations are provided in Table 2.2, which lists the reference values for key quantities used in simulations. Notably, the reference magnetic field, B_{unit}, is defined as:

$$B_{unit} = B_{\text{ref}}^{\texttt{TGLF}} = \frac{q}{r}\frac{d\Psi}{dr} \tag{2.20}$$

where Ψ denotes the poloidal magnetic flux.

For the purpose of the conversion between TGLF and GK-IDS, the relationship

Name	Quantity	Notation	Description
$m_{\text{ref}}^{\texttt{TGLF}}$	Mass	m_D	Deuterium mass (3.345×10^{-27} kg)
$n_{\text{ref}}^{\texttt{TGLF}}$	Density	n_e	Electron density
$T_{\text{ref}}^{\texttt{TGLF}}$	Temperature	T_e	Electron temperature
$v_{thref}^{\texttt{TGLF}}$	Velocity	$c_s = \sqrt{T_e/m_D}$	Deuterium sound speed
$L_{\text{ref}}^{\texttt{TGLF}}$	Macro-length	a	Minor radius at the last closed flux surface
$\rho_{\text{ref}}^{\texttt{TGLF}}$	Micro-length	$\rho_s = c_s/\Omega_i$	Reference Larmor radius ($\Omega_i = eB_{unit}/m_D$)
$t_{\text{ref}}^{\texttt{TGLF}}$	Time	a/c_s	Minor radius over sound speed

Table 2.2. – TGLF Normalizations

Name	Quantity	Notation	Description
$m_{\text{ref}}^{\text{IMAS}}$	Mass	m_D	Deuterium mass
$n_{\text{ref}}^{\text{IMAS}}$	Density	n_e	Electron density at $\theta = 0$
$T_{\text{ref}}^{\text{IMAS}}$	Temperature	T_e	Electron temperature at $\theta = 0$
$v_{\text{th,ref}}^{\text{IMAS}}$	Velocity	$v_{\text{th}} = \sqrt{2T_e/m_D}$	Reference thermal velocity
$L_{\text{ref}}^{\text{IMAS}}$	Macro-length	R_0	Major radius of the flux surface centre
$\rho_{\text{ref}}^{\text{IMAS}}$	Micro-length	$\rho_s = v_{\text{th}}/\Omega_i$	Reference Larmor radius ($\Omega_i = eB_{\text{ref}}/m_D$)
$B_{\text{ref}}^{\text{IMAS}}$	Magnetic Field	$B_{\text{ref}} = \lvert B_t(R_0)\rvert > 0$	Toroidal magnetic field at R_0

Table 2.3. – IMAS Normalizations

between normalized quantities involves the ratio of reference quantities. For example:

$$\mathscr{A}_N^{\texttt{IMAS}} = \frac{L_{\text{ref}}^{\texttt{TGLF}}}{L_{\text{ref}}^{\texttt{IMAS}}} \mathscr{A}_N^{\texttt{TGLF}} = L_{\text{rat}} \mathscr{A}_N^{\texttt{TGLF}} \tag{2.21}$$

The ratios of the key reference quantities between TGLF and GK-IDS are:

$$q_{\text{rat}} = \frac{q_{\text{ref}}^{\texttt{TGLF}}}{q_{\text{ref}}^{\texttt{IMAS}}} = \frac{e^{\texttt{TGLF}}}{e^{\texttt{IMAS}}} = 1 \qquad L_{\text{rat}} = \frac{L_{\text{ref}}^{\texttt{TGLF}}}{L_{\text{ref}}^{\texttt{IMAS}}} = \frac{a}{R_0^{\texttt{IMAS}}} = \frac{1}{\texttt{RMAJ_LOC}^{\texttt{TGLF}}}$$

$$m_{\text{rat}} = \frac{m_{\text{ref}}^{\texttt{TGLF}}}{m_{\text{ref}}^{\texttt{IMAS}}} = \frac{m_D^{\texttt{TGLF}}}{m_D^{\texttt{IMAS}}} = 1 \qquad B_{\text{rat}} = \frac{B_{\text{ref}}^{\texttt{TGLF}}}{B_{\text{ref}}^{\texttt{IMAS}}} = \frac{B_{\text{unit}}^{\texttt{TGLF}}}{B_t^{\texttt{IMAS}}(R_0)}$$

$$T_{\text{rat}} = \frac{T_{\text{ref}}^{\texttt{TGLF}}}{T_{\text{ref}}^{\texttt{IMAS}}} = \frac{T_e}{T_e(\theta = 0)} = 1 \qquad n_{\text{rat}} = \frac{n_{\text{ref}}^{\texttt{TGLF}}}{n_{\text{ref}}^{\texttt{IMAS}}} = \frac{n_e}{n_e(\theta = 0)} = 1$$

Here, the subscript "e" refers to the electron species. Using the expression for the

thermal velocity in GK-IDS, $v_{\text{th,ref}}^{\texttt{IMAS}} = \sqrt{\frac{2T_{\text{ref}}^{\texttt{IMAS}}}{m_{\text{ref}}^{\texttt{IMAS}}}}$, the reference velocity ratio is derived as:

$$v_{\text{thrat}} = \frac{c_s^{\texttt{TGLF}}}{v_{\text{th,ref}}^{\texttt{IMAS}}} = \frac{1}{\sqrt{2}}\sqrt{\frac{T_{\text{rat}}}{m_{\text{rat}}}} \tag{2.22}$$

Similarly, using the expression for the reference Larmor radius in GK-IDS, $\rho_{\text{ref}}^{\texttt{IMAS}} = \frac{m_{\text{ref}}^{\texttt{IMAS}} v_{\text{ref}}^{\texttt{IMAS}}}{q_{\text{ref}}^{\texttt{IMAS}} B_{\text{ref}}^{\texttt{IMAS}}}$, the reference Larmor radius ratio is given by:

$$\rho_{\text{rat}} = \frac{m_{\text{rat}} v_{\text{th,rat}}}{q_{\text{rat}} B_{\text{rat}}} \tag{2.23}$$

To compute the value of B_{rat}, we must first calculate the radial and poloidal derivatives ($\frac{\partial}{\partial\theta}$ and $\frac{\partial}{\partial r}$) of the Miller parameters defining the flux surfaces, $R(r,\theta)$ and $Z(r,\theta)$ Starting from equations 2.12 and 2.13 we have:

$$\frac{\partial R(r,\theta)}{\partial\theta} = -r\sin(\theta + \arcsin\delta\sin\theta)(1 + \arcsin\delta\cos\theta) \tag{2.24}$$

$$\frac{\partial Z(r,\theta)}{\partial\theta} = \kappa r\cos(\theta + \zeta\sin 2\theta)(1 + 2\zeta\cos 2\theta) \tag{2.25}$$

and for the radial derivatives:

$$\frac{\partial R(r,\theta)}{\partial r} = \frac{\partial R_0}{\partial x}\frac{\partial x}{\partial r} + \cos(\theta + \arcsin\delta\sin\theta) - \sin(\theta + \arcsin\delta\sin\theta) r\frac{\partial\delta}{\partial r}\sin\theta\frac{1}{\sqrt{1-\delta^2}} \tag{2.26}$$

$$\frac{\partial Z(r,\theta)}{\partial r} = \frac{\partial Z_0}{\partial x}\frac{\partial x}{\partial r} + \kappa\sin(\theta + \zeta\sin 2\theta)\left(1 + \frac{r}{\kappa}\frac{\partial\kappa}{\partial r}\right) + \kappa\cos(\theta + \zeta\sin 2\theta) r\frac{\partial\zeta}{\partial r}\sin 2\theta \tag{2.27}$$

Then, we calculate the Jacobian J_r which relates the radial and poloidal coordinates in the flux-tube geometry:

$$J_r = -R\cdot\left(\frac{\partial R}{\partial x}\frac{\partial Z}{\partial\theta} - \frac{\partial R}{\partial\theta}\frac{\partial Z}{\partial x}\right) \tag{2.28}$$

Additionally, we calculate the differential arc length along the poloidal contour, $\frac{\partial l}{\partial\theta}$, which is used in subsequent computations:

$$\frac{\partial l}{\partial\theta} = \sqrt{\left(\frac{\partial R}{\partial\theta}\right)^2 + \left(\frac{\partial Z}{\partial\theta}\right)^2} \tag{2.29}$$

With these expressions, the radial gradient of the minor radius can be computed as:

$$\nabla r = \frac{R}{J_r}\frac{\partial l}{\partial\theta} \tag{2.30}$$

To proceed with calculating the reference magnetic field ratio, B_{rat}, we need to integrate along the poloidal contour. According to the formalism developed in [121] , the relationship between the TGLF reference magnetic field B_{unit} and the toroidal magnetic field B_t at the magnetic axis is given by:

$$\frac{R_0(r)B_t}{B_{unit}} = 2\pi r \left(\int_0^L \frac{dl'}{R|\nabla r|} \right)^{-1} \tag{2.31}$$

This integral is evaluated along the length L of the poloidal contour. Using this result, we can express the magnetic field ratio as:

$$B_{\text{rat}} = \frac{B_{\text{ref}}^{\texttt{TGLF}}}{B_{\text{ref}}^{\texttt{IMAS}}} = \frac{B_{unit}}{B_t(R_0)} = \frac{B_{unit}}{|R_0 B_t|} R_0 = \frac{R_0}{2\pi r} \int_0^L \frac{dl'}{R|\nabla r|} \tag{2.32}$$

This expression ensures the proper normalization of the magnetic field between the two systems, accounting for the geometry of the flux surface.

In the following subsections, we will provide a detailed explanation of how key physical quantities are mapped between GK-IDS and TGLF. These mappings are essential for ensuring consistency when preparing TGLF inputs from GK-IDS data and, similarly, when converting TGLF simulation outputs back into a GK-IDS. For each physical quantity, whether it pertains to species parameters, magnetic equilibrium, wave vector data, or fluxes, both the IMAS and TGLF definitions will be presented, highlighting the different conventions and normalizations used by each framework. This will be followed by an equation that explicitly relates the IMAS version of the quantity to its corresponding TGLF representation. This structured mapping will cover the inputs needed for TGLF simulations as well as the outputs generated by TGLF that need to be translated back into IMAS's standardized format. Each parameter will be grouped by its physical category (e.g., species parameters, magnetic equilibrium, etc.).

2.3.2.3. Species Parameters

The species parameters include mass, charge, density, temperature, and velocity, all of which need to be consistently normalized when converting between IMAS and TGLF. Below, we break down each parameter and show the relationship between its IMAS and TGLF representations. In this section, the subscript `x` is the number labeling the different species in the TGLF input namelist.

Mass (m_s)

$$m_{sN}^{\texttt{IMAS}} = m_{sN}^{\texttt{TGLF}} \cdot m_{\text{rat}} = \texttt{MASS_x} \cdot m_{\text{rat}} \tag{2.33}$$

Charge (Z_s)

$$Z_s^{\texttt{IMAS}} = Z_s^{\texttt{TGLF}} \cdot q_{\text{rat}} = \texttt{ZS_x} \cdot q_{\text{rat}} \tag{2.34}$$

Density (n_s)

$$n_{sN}^{\texttt{IMAS}} = n_{sN}^{\texttt{TGLF}} \cdot n_{\text{rat}} = \texttt{AS_x} \cdot n_{\text{rat}} \tag{2.35}$$

Temperature (T_s)

$$T_{sN}^{\texttt{IMAS}} = T_{sN}^{\texttt{TGLF}} \cdot T_{\text{rat}} = \texttt{TAUS_x} \cdot T_{\text{rat}} \tag{2.36}$$

Toroidal Velocity (u) In TGLF, the toroidal velocity for each species can be individually specified. However, when exporting TGLF simulation results to the IMAS format, it is important to note that the current IMAS format assumes the same toroidal velocity for all species. As a result, any differences in toroidal velocity between species in the original TGLF simulation will be lost in the conversion. It should be noted, however, that the IDS framework is designed to be adaptable, and future modifications to the IDS structure may allow for more detailed representation of species-specific parameters.

— **IMAS and TGLF Definition:**

$$u_N^{\texttt{IMAS}} = \frac{L_{\text{ref}}^{\texttt{IMAS}}}{v_{\text{thref}}^{\texttt{IMAS}}}\omega_\Phi, \quad u_N^{\texttt{TGLF}} = \text{SIGN}(I_{\text{tor}})\frac{R_{\text{maj}}}{c_s}\frac{V_{\text{tor}}}{R} \tag{2.37}$$

where $\text{SIGN}(I_{\text{tor}})$ indicates the sign of the toroidal current relative to the counterclockwise toroidal direction when the tokamak is viewed from above, taking the value $+1$ for counterclockwise and -1 for clockwise.

— **Conversion Equation**:

$$u_N^{\texttt{IMAS}} = s_j^{\texttt{TGLF}} \cdot u_N^{\texttt{TGLF}} \cdot \frac{v_{\text{thrat}}}{L_{\text{rat}}} = \texttt{SIGN_IT} \cdot \texttt{VPAR_1} \cdot \frac{v_{\text{thrat}}}{L_{\text{rat}}} \tag{2.38}$$

Logarithmic Density Gradient R/L_{n_s}

— **IMAS Definition**:

$$R/L_{n_s}{}^{\texttt{IMAS}} = -\frac{L_{\text{ref}}^{\texttt{IMAS}}}{n_s}\frac{\partial n_s}{\partial r} \tag{2.39}$$

— **TGLF Definition**:

$$R/L_{n_s}{}^{\texttt{TGLF}} = -\frac{L_{\text{ref}}^{\texttt{TGLF}}}{n_s}\frac{\partial n_s}{\partial r} \tag{2.40}$$

— **Conversion Equation**:

$$R/L_{n_s}{}^{\texttt{IMAS}} = R/L_{n_s}{}^{\texttt{TGLF}} \cdot \frac{1}{L_{\text{rat}}} = \texttt{RLNS_x} \cdot \frac{1}{L_{\text{rat}}} \tag{2.41}$$

— The values are positive for peaked profiles.

Logarithmic Temperature Gradient R/L_{T_s}

— **IMAS Definition**:

$$R/L_{T_s}{}^{\texttt{IMAS}} = -\frac{L_{\text{ref}}^{\texttt{IMAS}}}{T_s}\frac{\partial T_s}{\partial r} \tag{2.42}$$

— **TGLF Definition**:

$$R/L_{T_s}{}^{\texttt{TGLF}} = -\frac{L_{\text{ref}}^{\texttt{TGLF}}}{T_s}\frac{\partial T_s}{\partial r} \tag{2.43}$$

— **Conversion Equation**:

$$R/L_{T_s}{}^{\texttt{IMAS}} = R/L_{T_s}{}^{\texttt{TGLF}} \cdot \frac{1}{L_{\text{rat}}} = \texttt{RLTS_x} \cdot \frac{1}{L_{\text{rat}}} \tag{2.44}$$

— The values are positive for peaked profiles.

Plasma Beta

— **IMAS Definition**:

$$\beta_{eN}^{\texttt{IMAS}} = 2\mu_0 \frac{n_{\text{ref}}^{\texttt{IMAS}} T_{\text{ref}}^{\texttt{IMAS}}}{(B_{\text{ref}}^{\texttt{IMAS}})^2} \tag{2.45}$$

— **TGLF Definition**:

$$\beta_{N}^{\texttt{TGLF}} = 3\mu_0 \frac{n_{\text{ref}}^{\texttt{TGLF}} T_{\text{ref}}^{\texttt{TGLF}}}{(B_{\text{ref}}^{\texttt{TGLF}})^2} \tag{2.46}$$

— **Conversion Equation**:

$$\beta_{eN}^{\texttt{IMAS}} = \beta_{N}^{\texttt{TGLF}} \cdot \frac{2B_{\text{rat}}^2}{3n_{\text{rat}}T_{\text{rat}}} = \frac{B_{\text{rat}}^2}{\frac{3}{2}n_{\text{rat}}T_{\text{rat}}} \cdot \texttt{BETAE} \tag{2.47}$$

Debye Length

— **IMAS Definition**:

$$\lambda_{DN}^{\texttt{IMAS}} = \frac{1}{\rho_{\text{ref}}^{\texttt{IMAS}}}\sqrt{\frac{\epsilon_0 T_{\text{ref}}^{\texttt{IMAS}}}{n_{\text{ref}}^{\texttt{IMAS}} q_{\text{ref}}^{\texttt{IMAS}^2}}} \tag{2.48}$$

— **TGLF Definition**:

$$\lambda_{DN}^{\texttt{TGLF}} = \frac{1}{\rho_{ref}^{\texttt{TGLF}}}\sqrt{\frac{\epsilon_0 T_{\text{ref}}^{\texttt{TGLF}}}{n_{\text{ref}}^{\texttt{TGLF}} q_{\text{ref}}^{\texttt{TGLF}^2}}} \tag{2.49}$$

— **Conversion Equation**:

$$\lambda_{DN}^{\texttt{IMAS}} = \lambda_{DN}^{\texttt{TGLF}} \cdot \rho_{\text{rat}} \cdot \sqrt{\frac{n_{\text{rat}}q_{\text{rat}}^2}{T_{\text{rat}}}} = \texttt{DEBYE} \cdot \rho_{\text{rat}} \cdot \sqrt{\frac{n_{\text{rat}}q_{\text{rat}}^2}{T_{\text{rat}}}} \tag{2.50}$$

Toroidal Velocity Gradient

— **IMAS Definition**:

$$u'_{sN}{}^{\texttt{IMAS}} = -\frac{(L_{\text{ref}}^{\texttt{IMAS}})^2}{v_{\text{thref}}^{\texttt{IMAS}}}\frac{\partial \omega_{\varphi,s}}{\partial r} \tag{2.51}$$

— **TGLF Definition**:

$$u'^{\texttt{TGLF}}_{sN} = -\text{SIGN}(I_{\text{tor}}) R_{\text{maj}} \frac{\partial}{\partial r}\left(\frac{V_{tor}}{R}\right)\frac{a}{c_s} \tag{2.52}$$

— **Conversion Equation**:

$$u'^{\texttt{IMAS}}_{sN} = s_j^{\texttt{TGLF}} \cdot u'^{\texttt{TGLF}}_{sN} \cdot \frac{v_{\text{thrat}}}{L_{\text{rat}}} = \texttt{SIGN_IT} \cdot \texttt{VPAR_SHEAR_x} \cdot \frac{v_{\text{thrat}}}{L_{\text{rat}}} \tag{2.53}$$

Shearing Rate Norm

— **IMAS Definition**:

$$\gamma_{E_N}^{\texttt{IMAS}} = -\frac{L_{\text{ref}}^{\texttt{IMAS}}}{v_{\text{thref}}^{\texttt{IMAS}}} \frac{1}{B_{\text{ref}}^{\texttt{IMAS}}} \left(\frac{\partial \Psi}{\partial r}\right)^2 \frac{\partial^2 \Phi}{\partial \Psi^2} \tag{2.54}$$

— **TGLF Definition**:

$$\gamma_{E_N}^{\texttt{TGLF}} = -\text{SIGN}(I_{\text{tor}}) \frac{r}{|q|} \frac{\partial}{\partial r}\left(\frac{V_{E\times B}}{R}\right)\frac{a}{c_s} \tag{2.55}$$

— **Conversion Equation**:

$$\gamma_{E_N}^{\texttt{IMAS}} = s_j^{\texttt{TGLF}} \cdot \gamma_{E_N}^{\texttt{TGLF}} \cdot \frac{v_{\text{thrat}}}{L_{\text{rat}}} B_{\text{rat}} = \texttt{SIGN_IT} \cdot \texttt{VEXB_SHEAR} \cdot \frac{v_{\text{thrat}}}{L_{\text{rat}}} B_{\text{rat}} \tag{2.56}$$

Collisionality In IMAS, the collisionality for each species couple a/b is defined as:

$$\nu_N^{a/b\,\texttt{IMAS}} = \frac{L_{\text{ref}}^{\texttt{IMAS}}}{v_{\text{thref}}^{\texttt{IMAS}}} \nu^{a/b} \tag{2.57}$$

Where $\nu^{a/b}$ is the collision frequency of species a against species b defined as:

$$\nu^{a/b} = \frac{n_b Z_a^2 Z_b^2 e^4 \ln \Lambda^{a/b}}{4\pi\epsilon_0^2 m_a^2 v_{\text{tha}}^3} \tag{2.58}$$

where n_b is the density of species b, m_a and v_{tha} the mass and thermal velocity of species a, and $\ln \Lambda^{a/b}$ the Coulomb logarithm.

In TGLF, only electron-ion collision frequency is included:

$$\nu_N^{e/i\,\texttt{TGLF}} = \frac{a}{c_s} \nu_{e/i} \tag{2.59}$$

We can then define the **Conversion Equation**:

$$\nu_N^{e/i\,\texttt{IMAS}} = \nu_N^{e/i\,\texttt{TGLF}} \cdot \frac{v_{\text{thrat}}}{L_{\text{rat}}} = \texttt{XNUE} \cdot \frac{v_{\text{thrat}}}{L_{\text{rat}}} \tag{2.60}$$

And all the other collision terms are set to zero.

2.3.2.4. Wave Vectors

The radial and binormal wave vectors in the Fourier expansions are represented in this section. In the local approximation, where turbulence is considered homogeneous in the plane perpendicular to the magnetic field, the perturbed distribution function and the associated fields are expressed as a sum of Fourier modes.

For a given function $h(x,y,\theta)$, its Fourier components, denoted as $\hat{h}(k_x,k_y,\theta)$, represent the spatial structure of the turbulence in terms of wavenumbers in the radial (k_x) and binormal (k_y) directions. This Fourier expansion can be written as:

$$h(x,y,\theta) = \sum_{k_x,k_y} \hat{h}(k_x,k_y,\theta)\exp\left(ik_x x + ik_y y\right) \tag{2.61}$$

In a flux-tube geometry, the perpendicular wave vector $k_\perp$, which describes the scale of turbulent eddies, depends on the parallel coordinate θ and can be expressed as:

$$k_\perp^2(\theta) = g^{xx}(\theta)k_x^2 + 2g^{xy}(\theta)k_x k_y + g^{yy}(\theta)k_y^2 \tag{2.62}$$

Here, $g^{xx}(\theta)$, $g^{xy}(\theta)$, and $g^{yy}(\theta)$ represent the metric tensors that describe the geometry of the flux surface. These are defined as follows:

— $g^{xx}(\theta) = \nabla x \cdot \nabla x$, the radial metric component,
— $g^{xy}(\theta) = \nabla x \cdot \nabla y$, the cross term between radial and binormal directions,
— $g^{yy}(\theta) = \nabla y \cdot \nabla y$, the binormal metric component.

Additionally, it is important to note that by convention, only positive values of the binormal wave vector k_y are stored in the IDS. This convention is sufficient because any real field can be reconstructed using the property of Hermitian symmetry in the Fourier components.

Binormal Wave Vector ($k_\theta\rho$)

— **IMAS Definition**:

$$k_{\theta*}\rho_{\text{ref}}{}^{\texttt{IMAS}} = k_y\sqrt{g^{yy}(\theta=0)}\rho_{\text{ref}}^{\texttt{IMAS}} \tag{2.63}$$

— **TGLF Definition**:

$$\texttt{KY} = k_y\rho_{\text{ref}}{}^{\texttt{TGLF}} = \frac{nq}{r}\rho_{s,\text{unit}}^{\texttt{TGLF}} \tag{2.64}$$

Using the catalogue of shape functions defined in [Candy:PPCF2009] we can relate the two definitions as:

$$k_{\theta*}\rho_{\text{ref}}{}^{\texttt{IMAS}} = \texttt{KY}\cdot G_q(\theta=0)\cdot\frac{1}{\rho_{\text{rat}}} \tag{2.65}$$

with

$$G_q = \frac{1}{q}\frac{rB}{RB_p} \tag{2.66}$$

Radial Wave Vector ($k_r\rho$)

— **IMAS Definition**:

$$k_{r*}\rho_{\text{ref}}{}^{\texttt{IMAS}} = k_x\sqrt{g^{xx}(\theta=0)}\rho_{\text{ref}}^{\texttt{IMAS}} \tag{2.67}$$

— **TGLF Definition**:

$$\texttt{KX0_LOC} = \frac{k_x}{k_y} \tag{2.68}$$

— **Conversion Equation**:

$$k_{r*}\rho_{\text{ref}}{}^{\texttt{IMAS}} = \texttt{KX0_LOC}\cdot\texttt{KY}\cdot\frac{1}{\rho_{\texttt{rat}}}\sqrt{g^{xx}(\theta=0)} = \texttt{KX0_LOC}\cdot\texttt{KY}\cdot\frac{1}{\rho_{\texttt{rat}}}\cdot|\nabla r|_{\theta=0} \tag{2.69}$$

2.3.2.5. Fields

The fields in IMAS are normalised as follows:

$$\phi_N^{\texttt{IMAS}} = \frac{q_{\text{ref}}^{\texttt{IMAS}}L^{\texttt{IMAS}}}{T_{\text{ref}}^{\texttt{IMAS}}\rho_{\text{ref}}^{\texttt{IMAS}}}\cdot\phi, \qquad A_{\parallel N}^{\texttt{IMAS}} = \frac{L_{\text{ref}}^{\texttt{IMAS}}}{B_{\text{ref}}^{\texttt{IMAS}}\rho_{\text{ref}}^{\texttt{IMAS}2}}\cdot A_\parallel, \qquad B_{\parallel N}^{\texttt{IMAS}} = \frac{L^{\texttt{IMAS}}}{B_{\text{ref}}^{\texttt{IMAS}}\rho_{\text{ref}}^{\texttt{IMAS}}}\cdot B_\parallel \tag{2.70}$$

Similarly, in TGLF, the Gyro-Bohm normalisation is used for the fields so we have:

$$\phi_N^{\texttt{TGLF}} = \frac{q_{\text{ref}}^{\texttt{TGLF}}L^{\texttt{TGLF}}}{T_{\text{ref}}^{\texttt{TGLF}}\rho_{\text{ref}}^{\texttt{TGLF}}}\cdot\phi, \qquad A_{\parallel N}^{\texttt{TGLF}} = \frac{L_{\text{ref}}^{\texttt{TGLF}}}{B_{\text{ref}}^{\texttt{TGLF}}\rho_{\text{ref}}^{\texttt{TGLF}2}}\cdot A_\parallel, \qquad B_{\parallel N}^{\texttt{TGLF}} = \frac{L^{\texttt{TGLF}}}{B_{\text{ref}}^{\texttt{TGLF}}\rho_{\text{ref}}^{\texttt{TGLF}}}\cdot B_\parallel \tag{2.71}$$

It then comes for the "units" normalization :

$$\phi_N^{\texttt{IMAS}} = \frac{T_{\text{rat}}\rho_{\text{rat}}}{q_{\text{rat}}L_{\text{rat}}}\cdot\phi_N^{\texttt{TGLF}}, \qquad A_{\parallel N}^{\texttt{IMAS}} = \frac{B_{\text{rat}}\rho_{\text{rat}}{}^2}{L_{\text{rat}}}\cdot A_{\parallel N}^{\texttt{TGLF}}, \qquad B_{\parallel N}^{\texttt{IMAS}} = \frac{B_{\text{rat}}\rho_{\text{rat}}}{L_{\text{rat}}}\cdot B_{\parallel N}^{\texttt{TGLF}} \tag{2.72}$$

For linear runs, the IMAS mode amplitude used to normalise the exponentially growing fields is:

$$\mathscr{A}_f^{\texttt{IMAS}} = \sqrt{\frac{1}{2\pi}\int\left[|\phi_N^{\texttt{IMAS}}|^2 + |A_{\parallel N}^{\texttt{IMAS}}|^2 + |B_{\parallel N}^{\texttt{IMAS}}|^2\right]\mathrm{d}\theta} \tag{2.73}$$

We call $\phi_{N,out}^{\texttt{TGLF}}$, $A_{\parallel N,out}^{\texttt{TGLF}}$ and $B_{\parallel N,out}^{\texttt{TGLF}}$ the TGLF outputs from the file `out.tglf.wavefunction`. The TGLF mode amplitude $\mathscr{A}_f^{\texttt{TGLF}}$ is defined as:

$$\phi_{N,out}^{\texttt{TGLF}} = \frac{\phi_N^{\texttt{TGLF}}}{\mathscr{A}_f^{\texttt{TGLF}}}, \qquad A_{\parallel N,out}^{\texttt{TGLF}} = \frac{A_{\parallel N}^{\texttt{TGLF}}}{\mathscr{A}_f^{\texttt{TGLF}}}, \qquad B_{\parallel N,out}^{\texttt{TGLF}} = \frac{B_{\parallel N}^{\texttt{TGLF}}}{\mathscr{A}_f^{\texttt{TGLF}}} \tag{2.74}$$

Where $\mathscr{A}_f^{\texttt{TGLF}} = \sqrt{\int|\phi_N^{\texttt{TGLF}}|^2}$ (see section 2.2.2).
So the ratio of the IMAS to TGLF mode amplitudes is therefore given by:

$$\mathscr{A}_{\text{rat}} = \frac{\sqrt{2\pi}}{\sqrt{\int\left[|\frac{T_{\text{rat}}\rho_{\text{rat}}}{q_{\text{rat}}L_{\text{rat}}}\phi_{N,out}^{\texttt{TGLF}}|^2 + |\frac{B_{\text{rat}}\rho_{\text{rat}}{}^2}{L_{\text{rat}}}A_{\parallel N,out}^{\texttt{TGLF}}|^2 + |\frac{B_{\text{rat}}\rho_{\text{rat}}}{L_{\text{rat}}}B_{\parallel N,out}^{\texttt{TGLF}}|^2\right]\mathrm{d}\theta}} \tag{2.75}$$

where the integral is performed over the full simulation domain. In IMAS, an arbitrary phase factor α is chosen so that the real part of $\phi_N^{\texttt{IMAS}}$ is positive and its imaginary part is zero at $\theta = \theta_*$ where θ_* is the θ value at which $|\phi_N^{\texttt{IMAS}}|$ is maximum. So we have:

$$e^{i\alpha} = \frac{|\phi_N^{\texttt{IMAS}}(\theta_*)|}{\phi_N^{\texttt{IMAS}}(\theta_*)} \tag{2.76}$$

Finally we obtain:

$$\phi_{Nf}^{\texttt{IMAS}} = \phi_{N,out}^{\texttt{TGLF}} \cdot \frac{T_{\text{rat}}\rho_{\text{rat}}}{q_{\text{rat}}L_{\text{rat}}} \cdot \mathscr{A}_{\text{rat}} e^{i\alpha}, \qquad A_{\|Nf}^{\texttt{IMAS}} = -A_{\|Nout}^{\texttt{TGLF}} \cdot \frac{B_{\text{rat}}\rho_{\text{rat}}^2}{L_{\text{rat}}} \cdot \mathscr{A}_{\text{rat}} e^{i\alpha} \qquad B_{\|N}^{\texttt{IMAS}} = -B_{\|N,out}^{\texttt{TGLF}} \cdot \frac{B_{\text{rat}}\rho_{\text{rat}}}{L_{\text{rat}}} \cdot \mathscr{A}_{\text{rat}} \tag{2.77}$$

Where $\phi_{N,out}^{\texttt{TGLF}}$, $A_{\|N,out}^{\texttt{TGLF}}$, $B_{\|N,out}^{\texttt{TGLF}}$ are found in the file `out.tglf.wavefunction`

2.3.2.6. Mode growth rate and frequency

In IMAS, the normalised mode growth rate $\gamma^{\texttt{IMAS}}$ and frequency $\omega_r^{\texttt{IMAS}}$ are defined as:

$$\gamma_N^{\texttt{IMAS}} = \gamma \cdot \frac{L_{\text{ref}}^{\texttt{IMAS}}}{v_{\text{thref}}^{\texttt{IMAS}}} \qquad \text{and} \qquad \omega_{rN}^{\texttt{IMAS}} = \omega_r \cdot \frac{L_{\text{ref}}^{\texttt{IMAS}}}{v_{\text{thref}}^{\texttt{IMAS}}} \tag{2.78}$$

And in TGLF:

$$\gamma_N^{\texttt{TGLF}} = \gamma \cdot \frac{L_{\text{ref}}^{\texttt{TGLF}}}{v_{\text{thref}}^{\texttt{TGLF}}} \qquad \text{and} \qquad \omega_{rN}^{\texttt{TGLF}} = \omega_r \cdot \frac{L_{\text{ref}}^{\texttt{TGLF}}}{v_{\text{thref}}^{\texttt{TGLF}}} \tag{2.79}$$

We note that in TGLF, the frequency convention is set to opposite direction (electron diamagnetic direction modes positive, ion diamagnetic direction negative). So finally we have:

$$\gamma_N^{\texttt{IMAS}} = \gamma_{N,out}^{\texttt{TGLF}} \cdot \frac{v_{\text{thrat}}}{L_{\text{rat}}} \qquad \text{and} \qquad \omega_{rN}^{\texttt{IMAS}} = -\omega_{rN,out}^{\texttt{TGLF}} \cdot \frac{v_{\text{thrat}}}{L_{\text{rat}}} \tag{2.80}$$

Where $\gamma_{N,out}^{\texttt{TGLF}}$ and $\omega_{rN,out}^{\texttt{TGLF}}$ are found in the file `out.tglf.eigenvalue_spectrum`

2.3.2.7. Linear mode weights

The particle, energy and toroidal angular momentum linear mode weights are defined as:

For IMAS :

$$\Gamma_{sN}^{\texttt{IMAS}}(k_x,k_y) = \frac{1}{\mathscr{A}_f^{\texttt{IMAS}^2}} \frac{L_{\text{ref}}^{\texttt{IMAS}^2}}{n_s v_{\text{thref}}^{\texttt{IMAS}} \rho_{\text{ref}}^{\texttt{IMAS}^2}} \cdot \Gamma_s \tag{2.81}$$

$$Q_{sN}^{\texttt{IMAS}}(k_x,k_y) = \frac{1}{\mathscr{A}_f^{\texttt{IMAS}^2}} \frac{L_{\text{ref}}^{\texttt{IMAS}^2}}{n_s T_{\text{ref}}^{\texttt{IMAS}} v_{\text{thref}}^{\texttt{IMAS}} \rho_{\text{ref}}^{\texttt{IMAS}^2}} \cdot Q_s \tag{2.82}$$

$$\Pi_{sN\parallel}^{\texttt{IMAS}}(k_x,k_y) = \frac{1}{\mathscr{A}_f^{\texttt{IMAS}^2}} \frac{L_{\text{ref}}^{\texttt{IMAS}^2}}{n_s m_{\text{ref}}^{\texttt{IMAS}} v_{\text{thref}}^{\texttt{IMAS}^2} \rho_{\text{ref}}^{\texttt{IMAS}^2} L_{\text{ref}}^{\texttt{IMAS}}} \cdot \Pi_{s\parallel} \tag{2.83}$$

$$\Pi_{sN\perp}^{\texttt{IMAS}}(k_x,k_y) = \frac{1}{\mathscr{A}_f^{\texttt{IMAS}^2}} \frac{L_{\text{ref}}^{\texttt{IMAS}^2}}{n_s m_{\text{ref}}^{\texttt{IMAS}} v_{\text{thref}}^{\texttt{IMAS}^2} \rho_{\text{ref}}^{\texttt{IMAS}^2} L_{\text{ref}}^{\texttt{IMAS}}} \cdot \Pi_{s\perp} \tag{2.84}$$

For TGLF :

$$\Gamma_{sN}^{\texttt{TGLF}}(k_x,k_y) = \frac{1}{2} \frac{1}{\mathscr{A}_f^{\texttt{TGLF}^2}} \frac{L_{\text{ref}}^{\texttt{TGLF}^2}}{n_e v_{\text{thref}}^{\texttt{TGLF}} \rho_{\text{ref}}^{\texttt{TGLF}^2}} \cdot \Gamma_s \tag{2.85}$$

$$Q_{sN}^{\texttt{TGLF}}(k_x,k_y) = \frac{1}{2} \frac{1}{\mathscr{A}_f^{\texttt{TGLF}^2}} \frac{L_{\text{ref}}^{\texttt{TGLF}^2}}{n_e T_{\text{ref}}^{\texttt{TGLF}} v_{\text{thref}}^{\texttt{TGLF}} \rho_{\text{ref}}^{\texttt{TGLF}^2}} \cdot Q_s \tag{2.86}$$

$$\Pi_{sN\parallel}^{\texttt{TGLF}}(k_x,k_y) = \frac{1}{2} \frac{1}{\mathscr{A}_f^{\texttt{TGLF}^2}} \frac{L_{\text{ref}}^{\texttt{TGLF}^2}}{n_e m_{\text{ref}}^{\texttt{TGLF}} v_{\text{thref}}^{\texttt{TGLF}^2} \rho_{\text{ref}}^{\texttt{TGLF}^2} R_0^{\texttt{TGLF}}} \cdot \Pi_{s\parallel} \tag{2.87}$$

$$\Pi_{sN\perp}^{\texttt{TGLF}}(k_x,k_y) = \frac{1}{2} \frac{1}{\mathscr{A}_f^{\texttt{TGLF}^2}} \frac{L_{\text{ref}}^{\texttt{TGLF}^2}}{n_e m_{\text{ref}}^{\texttt{TGLF}} v_{\text{thref}}^{\texttt{TGLF}^2} \rho_{\text{ref}}^{\texttt{TGLF}^2} R_0^{\texttt{TGLF}}} \cdot \Pi_{s\perp} \tag{2.88}$$

In TGLF, the quantities $\Gamma_{sN}^{\texttt{TGLF}}(k_x,k_y)$, $\Pi_{sN\parallel}^{\texttt{TGLF}}(k_x,k_y)$ and $Q_{sN}^{\texttt{TGLF}}(k_x,k_y)$ are found in the file `out.tglf.QL_flux_spectrum`. We note that the perpendicular toroidal angular momentum is not directly given by TGLF. However, it can be obtained by subtracting the parallel toroidal angular momentum to the total toroidal angular momentum given by TGLF. We also note the factor $\frac{1}{2}$ in the TGLF expression of the flux cross-phases due to historical convention.
Comparing the TGLF and IMAS definitions, we finally obtain:

$$\Gamma_{sN}^{\texttt{IMAS}} = 2\Gamma_{sN,out}^{\texttt{TGLF}} \cdot \mathscr{A}_{\text{rat}}^2 \cdot \frac{n_{\text{rat}} v_{\text{thrat}} \rho_{\text{rat}}^2}{L_{\text{rat}}^2} \cdot \frac{1}{\texttt{AS_X}} \tag{2.89}$$

$$Q_{sN}^{\texttt{IMAS}} = 2Q_{sN,out}^{\texttt{TGLF}} \cdot \mathscr{A}_{\text{rat}}^2 \cdot \frac{n_{\text{rat}} T_{\text{rat}} v_{\text{thrat}} \rho_{\text{rat}}^2}{L_{\text{rat}}^2} \cdot \frac{1}{\texttt{AS_X}} \tag{2.90}$$

$$\Pi_{sN\parallel}^{\texttt{IMAS}} = 2\Pi_{sN\parallel,out}^{\texttt{TGLF}} \cdot \mathscr{A}_{\text{rat}}^2 \cdot \frac{m_{\text{rat}} n_{\text{rat}} v_{\text{thrat}}^2 \rho_{\text{rat}}^2}{L_{\text{rat}}^2} \cdot \frac{1}{\texttt{AS_X}} \tag{2.91}$$

Where $\Gamma^{\texttt{TGLF}}_{sN,out}$, $\Pi^{\texttt{TGLF}}_{sN\parallel,out}$ and $Q^{\texttt{TGLF}}_{sN,out}$ are found in the file `out.tglf.QL_flux_spectrum`

2.3.2.8. Total Fluxes

This section discusses the total fluxes. These fluxes can be categorized as either non-linear fluxes or, in the context of TGLF, quasi-linear fluxes.
Comparing the TGLF and IMAS definitions, we finally obtain:

$$\Gamma^{\texttt{IMAS}}_{s} = \Gamma^{\texttt{TGLF}}_{s,out} \cdot \frac{n_{\text{rat}} v_{\text{thrat}} \rho^2_{\text{rat}}}{L^2_{\text{rat}}} \tag{2.92}$$

$$Q^{\texttt{IMAS}}_{s} = Q^{\texttt{TGLF}}_{s,out} \cdot \frac{n_{\text{rat}} T_{\text{rat}} v_{\text{thrat}} \rho^2_{\text{rat}}}{L^2_{\text{rat}}} \tag{2.93}$$

$$\Pi^{\texttt{IMAS}}_{s\parallel} = \Pi^{\texttt{TGLF}}_{s\parallel,out} \cdot \frac{m_{\text{rat}} n_{\text{rat}} v^2_{\text{thrat}} \rho^2_{\text{rat}}}{L^2_{\text{rat}}} \tag{2.94}$$

Where $\Gamma^{\texttt{TGLF}}_{s,out}$, $\Pi^{\texttt{TGLF}}_{s\parallel,out}$ and $Q^{\texttt{TGLF}}_{s,out}$ are found in the file `out.tglf.gbflux`

2.3.3. Parameter Enforcement and Technical Choices for TGLF Input Conversion

The process of converting an gyrokinetic IDS into an input file suitable for the TGLF model presented several technical constraints. These constraints stemmed primarily from the limitations in the information available within the IDS structure, as well as certain constraints inherent to the TGLF code itself. The following points outline key parameters that are enforced during the conversion process, with detailed explanations for each decision:

— **Miller Parametrization for Flux Surfaces**: The flux surface geometry used by TGLF is constrained to the Miller parameterization. This is specified in the TGLF input by setting the flag:

$$\texttt{GEOMETRY_FLAG} = 1$$

— **Exclusion of Compressional Magnetic Fluctuations** ($\delta B_\parallel$):
Compressional magnetic fluctuations are excluded in TGLF due to its limited ability to accurately resolve these effects. This approach, discussed in consultation with TGLF developer Gary Staebler, is implemented by setting:

$$\texttt{USE_BPAR} = \texttt{False}$$

To further refine the treatment of magnetic fluctuations, we apply the setting:

$$\texttt{USE_MHD_RULE} = \texttt{True}$$

which forces the drifts due to ∇B and curvature to cancel each other out, leveraging an approximation valid at the MHD level [Waltz1999, JoinerPoP2010]. Al-

though retaining $\delta B_{\parallel}$ and setting `USE_MHD_RULE` to `False` would be ideal, TGLF's limited number of moments can be insufficient to properly resolve compressional magnetic fluctuations effects.
Depending on whether the simulation is specified as electrostatic or electromagnetic, the perpendicular magnetic field fluctuations ($B_{\perp}$) are included or excluded and is enabled with `USE_BPER` = `True`.

— **Normalization of the Major Radius**:
The normalized major radius is fixed at the default value:

$$\texttt{RMAJ_LOC} = 1.0$$

This value is critical, as it is directly tied to the ratio L_{rat} used in the conversions outlined in the previous section. However, altering the value of `RMAJ_LOC` does not impact the results when expressed in IMAS normalizations, since all quantities involving length are correctly normalized during the conversion process. We conducted several tests by varying this value and observing the TGLF outputs in IMAS normalizations. These tests confirmed the validity of the conversion routine: the normalized output values in IMAS remained unchanged, regardless of the value of `RMAJ_LOC` in the TGLF input file.

— **Minor Radius Derivative**:
The derivative of the minor radius with respect to the midplane radial coordinate x is set to:

$$\texttt{DRMINDX_LOC} = 1.0$$

This assumption enforces $x = r$, since no substantial reason exists to differentiate between these coordinates in the current context.

— **Saturation Rule**:
The default saturation rule for turbulent transport in TGLF is applied by setting:

$$\texttt{SAT_RULE} = 2$$

— **Units for the Saturation Rule**:
TGLF's input is configured to use the CGYRO units system, ensuring consistency with the conventions used by setting:

$$\texttt{UNITS} = \texttt{CGYRO}$$

— **Parallel Basis Functions**:
The number of parallel basis functions used in TGLF simulations is constrained between a minimum of 2 and a maximum of 6 by setting:

$$\texttt{NBASIS_MIN} = 2, \quad \texttt{NBASIS_MAX} = 6$$

This range provides a balance between computational efficiency and accuracy in resolving parallel dynamics. Further discussion on the rationale for these settings will follow in the next section.

— **Handling of Centrifugal Effects and Collisions in TGLF**:
TGLF, as a quasilinear code, does not support the inclusion of certain advanced physics effects, such as centrifugal effects or detailed collision mechanisms, which are sometimes included in the gyrokinetic IDS. The following checks are enforced during the conversion process:
Centrifugal Effects: TGLF does not support centrifugal effects. If centrifugal effects are included in the IDS, a warning is issued, and the user is notified that TGLF cannot simulate these effects.
Collisionality Assumptions: TGLF uses simplified collisional models Only pitch-angle scattering is considered and TGLF does not account for momentum conservation, energy conservation, or finite Larmor radius effects in the collision operator.
If any of these parameters are not set correctly in the IDS, a warning is issued to inform the user that TGLF is incompatible with the selected collisionality settings. These restrictions ensure that the converted input file remains within the physical and computational capabilities of the TGLF model, avoiding misinterpretations of results. The user is just warned and the scripts continues.

— **Handling the Binormal Wavevector Grid in TGLF**:
The number of points in the binormal wavevector grid is enforced to 19, consistent with the default settings used for TGLF in the integrated modelling code JETTO (v060619). This is achieved by setting:

$$\texttt{NKY} = 19$$

The `KYGRID_MODEL` input parameter in TGLF controls the configuration of the binormal wavevector grid k_y (see section 2.2.3.2). In the conversion routine, the following logic is applied to configure the binormal wavevector grid accordingly: The script first checks if the non-linear then linear part of the IDS contains information about the binormal wavevector. If such information is available, the script iterates through the list of wavevectors to find the maximum value of k_y. If no explicit wavevector information is provided, a default TGLF spectrum grid is used . Based on the magnitude of $k_{y,\max}$, the appropriate binormal wavevector grid model is chosen. If $k_{y,\max} > 19$ in TGLF units, the grid model (`KYGRID_MODEL`) is set to either 1 or 4, depending on the chosen saturation rule (`SAT_RULE`). If $k_{y,\max} \leq 19$, the ajusted grid model is selected, with `KYGRID_MODEL` = 0. Also, if the IDS was originally generated from a TGLF simulation, the script retrieves the previously used spectral grid parameters from the IDS (`KY`, `NKY`, `KX0_LOC`, `KYGRID_MODEL`). This ensures consistency when converting or re-running TGLF simulations.

To ensure the reliability and robustness of the conversion routines developed for the IMAS-TGLF interface, an extensive validation process was conducted. This process involved the iterative cycling of data between IMAS and TGLF: starting with an initial IDS, converting it to a TGLF input file, running the TGLF simulation, converting the output back to an IDS, and repeating this process in a loop, each time passing

the results of the previous run as input to the next. Importantly, after each loop, the outputs were carefully compared to verify that no discrepancies had arisen due to normalization or data conversion. The results demonstrated that the outputs remained consistent and identical to the original after each iteration, thus validating the robustness and stability of the conversion routines.

The conversion scripts where written to be easily extensible for future updates in IMAS data structures or new versions of TGLF with a modular structure allowing for the integration of new parameters or changes in existing ones with minimal effort.

2.3.4. Tests Overview

The primary objective of this section is to validate the conversion routines developed for interfacing gyrokinetic IMAS data structures with TGLF. The approach involves a comparison of the linear growth rates and frequencies of the most unstable mode obtained with TGLF and GKW. Quasi-linear weights were also evaluated as part of the validation process. These comparisons are essential for confirming that the normalization and transformation processes embedded in the scripts correctly handle the input and output conversions between TGLF and IMAS.

The goal is to observe whether discrepancies arise between the results from GKW and TGLF as certain plasma parameters are varied. Specifically, we aim to detect any emerging normalization factor or trend that suggests a mismatch in how quantities are transformed between IMAS, TGLF, and GKW. This methodology has proven effective in highlighting potential errors in the conversion routines, allowing us to make necessary corrections.

2.3.4.1. Description Process

For each plasma parameter being scanned (mass, charge, safety factor, etc.), we start from the same reference simulation case. The reference used in this study is the Waltz standard case (see table 3.1), due to TGLF's demonstrated accuracy in modeling this case in the ion temperature gradient (ITG) regime, making it an ideal starting point for validation. By using a case where TGLF is expected to perform well, we can better isolate discrepancies due to conversion errors rather than inherent differences in the linear response of the two codes.

The verification process is structured as follows:

— First, a linear simulation is performed with GKW, varying one plasma parameter at a time from the reference Waltz standard case.
— After each GKW simulation, an IDS object is created from the GKW run.
— Using the developed scripts, this IDS is then converted into a TGLF input file.
— TGLF is run using the generated input file, and the resulting output is converted back into an IDS object.
— Finally, the linear growth rate and frequency of the most unstable mode are compared between the GKW and TGLF IDS outputs, ensuring that all results are consistently expressed in IMAS units.

The plasma parameters for the Waltz standard case are outlined in Table 3.1. Two species (deuterium and electrons) are included and treated kinetically, with the magnetic equilibrium described by circular flux surfaces using the Miller parameterization in both GKW and TGLF. Collisions and rotation are neglected.

Table 2.4. – IMAS normalized plasma parameters of the Waltz Standard case

q	$\hat{s}$	p'_N	r_N	R/L_n	$R/L_{Ti} = R/L_{Te}$	T_i/T_e
2	1	0	0.16	3	9	1.0

2.3.4.2. Effect of Binormal Wavevector $k_\theta \rho_s$

This section explores the impact of the binormal wavevector $k_\theta \rho_s$. By examining a wide range of $k_\theta \rho_s$ values, we can capture both ion-scale and electron-scale drift wave turbulence regimes. The comparison is made between TGLF and GKW simulations, with both x- and y-axes presented in logarithmic scale for clarity.

Figure 2.2 shows the linear growth rate and frequency as a function of $k_\theta \rho_s$, with values expressed in IMAS normalizations. The results for both TGLF and GKW are plotted on a logarithmic scale for $k_\theta \rho_s$, revealing the response across a wide range of wavevector values. For the frequency plot, note that the y-axis is also logarithmic, except for the range from -0.1 to 0.1, where a linear scale is used to handle values close to zero.

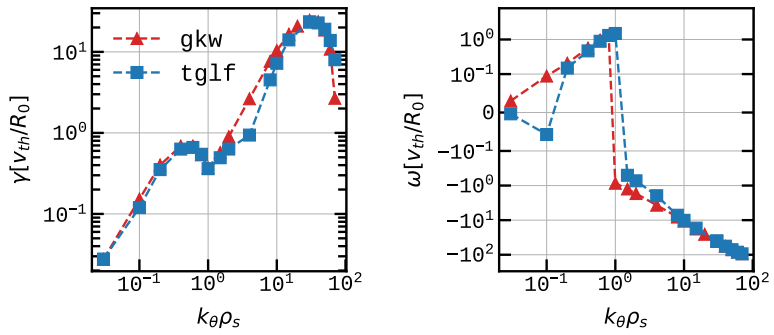


Figure 2.2. – Linear growth rate and frequency as a function of $k_\theta \rho_s$, comparing TGLF and GKW results. Both axes use logarithmic scales, except for the frequency plot near zero.

The plot shows good agreement between TGLF and GKW across most of the $k_\theta \rho_s$ spectrum, confirming the validity of the binormal wavevector conversion.

A discrepancy in the frequency is observed at $k_\theta \rho_s = 0.1$, where TGLF predicts a different linear frequency compared to GKW. This difference is likely related to the challenges that arise when modeling very low $k_\theta \rho_s$ values in quasi-linear models like TGLF, which use reduced linear solvers. Despite this discrepancy, the overall trend remains consistent.

Mode Structure Comparison To further investigate the observed discrepancy, we compare the mode structures for this value and the next point at $k_\theta \rho_s = 0.2$. Figure 2.3 shows the real part of the electrostatic potential as a function of the parallel coordinate θ for both values of $k_\theta \rho_s$.

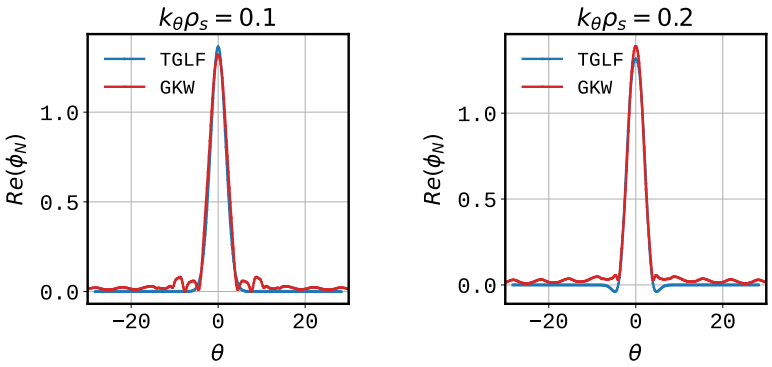


Figure 2.3. – Real part of the electrostatic potential as a function of θ for $k_\theta \rho_s = 0.1$ and $k_\theta \rho_s = 0.2$, comparing TGLF and GKW.

For $k_\theta \rho_s = 0.1$, despite the discrepancy in frequency, the mode structures from both TGLF and GKW are in reasonable agreement, suggesting that the observed frequency difference is not due to a fundamental mismatch in the mode structures but likely arises from limitations in the TGLF model at very low $k_\theta \rho_s$. The mode structure at $k_\theta \rho_s = 0.2$, however, shows close alignment between TGLF and GKW in both frequency and mode structure.

Overall, the strong agreement observed throughout the $k_\theta \rho_s$ scan validates the accuracy of the binormal wavevector conversion applied in the TGLF-IMAS conversion routines. For the next cases, we will fix the binormal wavevector at $k_\theta \rho_s = 0.4$.

2.3.4.3. Effect of Ion Charge, Mass, and Temperature

This section presents the scans for ion charge (Z), ion mass (m_i), and ion temperature (T_i) and their effect on the linear growth rate and frequency of the most unstable mode, as predicted by TGLF and GKW. The aim is to validate the conversion routines developed for each of these quantities in IMAS and TGLF normalizations.

In Figure 2.4, we observe the effect of ion charge (Z) on the linear growth rate and frequency, where quasi-neutrality is maintained by adjusting the normalized ion density accordingly. Figure 2.5 shows the response of both codes to changes in ion mass (m_i), and in Figure 2.6, the effect of varying the ion temperature (T_i) is presented. Across all three parameters, TGLF and GKW demonstrate consistent trends, validating the conversion routines.

2.3.4.4. Effect of Density and Temperature Gradients (R/L_N and R/L_T)

This section presents the validation of the conversion routines for the ion and electron density and temperature gradients, R/L_N and R/L_T. The scan was performed

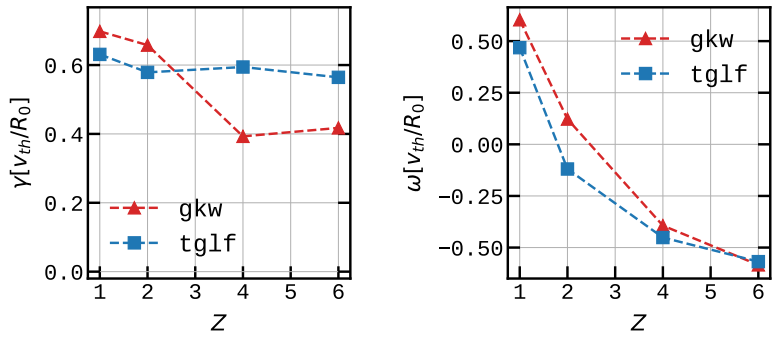


Figure 2.4. – Linear growth rate and frequency as a function of ion charge (Z), comparing TGLF and GKW results.

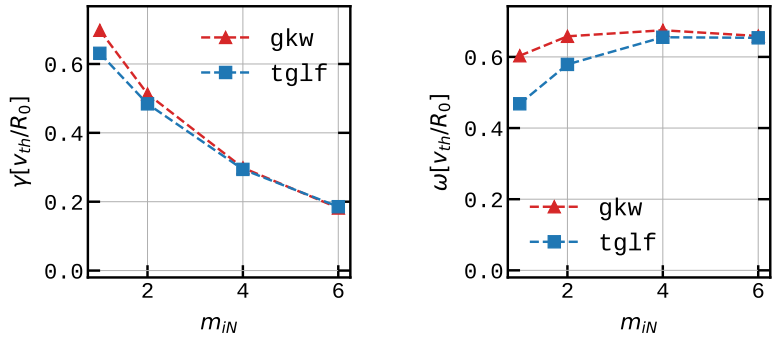


Figure 2.5. – Linear growth rate and frequency as a function of ion mass (m_i), comparing TGLF and GKW results.

by simultaneously varying the density gradient for both ions and electrons for R/L_N, and similarly for the temperature gradient, R/L_T, ensuring that $R/L_{N,i} = R/L_{N,e} = R/L_N$ and $R/L_{T,i} = R/L_{T,e} = R/L_T$. The impact of varying the density and temperature gradient on the linear growth rate and frequency is displayed in Figures 2.7 and 2.8, respectively. Both GKW and TGLF results are plotted in IMAS normalizations, showing the same trend across the entire scan range for each gradient, and validating the conversion scripts for the density and temperature gradients.

2.3.4.5. Effect of Magnetic Shear ($\hat{s}$) and Pressure Gradient (p'_N)

This section presents the validation of the conversion routines for the magnetic shear, $\hat{s}$, and the pressure gradient, p'_N (often denoted as β'), by comparing the linear growth rate and frequency from TGLF and GKW simulations. The simulations follow the Waltz standard case with these quantities systematically varied.

Figures 2.9 and 2.10 display the linear growth rate and frequency as functions of the magnetic shear and pressure gradient, respectively. The TGLF input files were generated using the conversion routines based on the GKW output IDS. The results for both codes are expressed in IMAS normalizations.

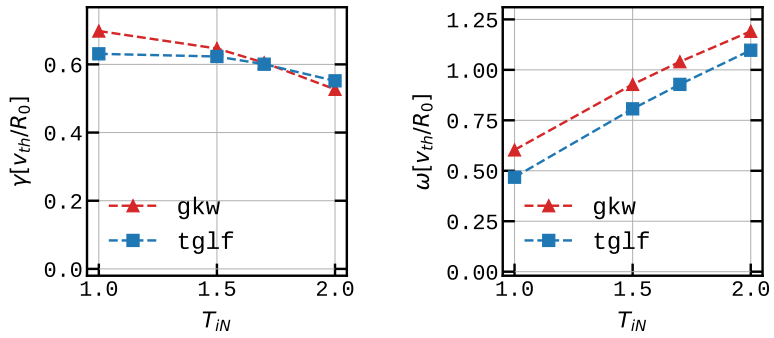


Figure 2.6. – Linear growth rate and frequency as a function of ion to electron temperature ratio $T_{iN} = T_i/T_e$, comparing TGLF and GKW results.

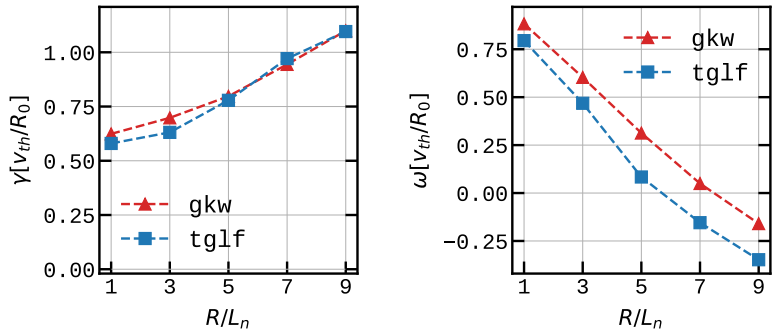


Figure 2.7. – Linear growth rate and frequency as a function of R/L_N, comparing GKW and TGLF results.

The strong consistency observed between TGLF and GKW for both $\hat{s}$ and p'_N provides robust validation of the conversion routines developed for these quantities. Minor differences can be attributed to intrinsic model differences, but the overall trends confirm the reliability of the conversions.

2.3.4.6. Effect of plasma shaping parameters

This section explores the radial derivative of the major radius ($\frac{\partial R}{\partial r}$), the plasma elongation (κ) and its radial derivative ($\partial\kappa/\partial r$), the inverse aspect ratio (r_N), and the safety factor (q). Figures 2.11, 2.12, 2.13, 2.14, and 2.15 illustrate the linear growth rate and frequency of the most unstable mode as predicted by TGLF and GKW, with each parameter varied individually while keeping all others fixed. The Waltz standard case serves as the reference for these comparisons. Parameter values are expressed using IMAS normalizations, and TGLF input files were generated via conversion routines based on the GKW output IDS.

As shown in the figures, TGLF and GKW shows consistent trends. This consistency verifies the accuracy of the conversion routines for these quantities.

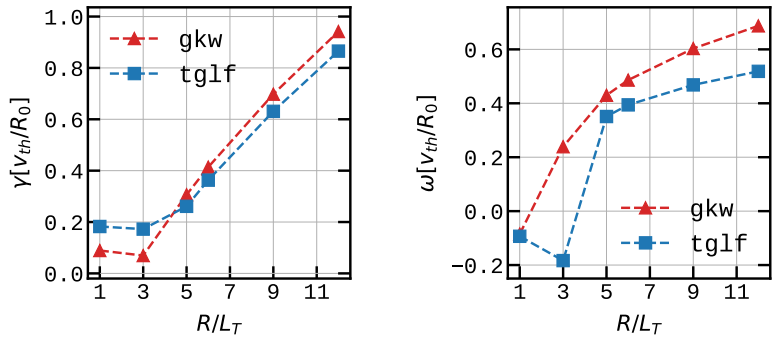


Figure 2.8. – Linear growth rate and frequency as a function of R/L_T, comparing GKW and TGLF results.

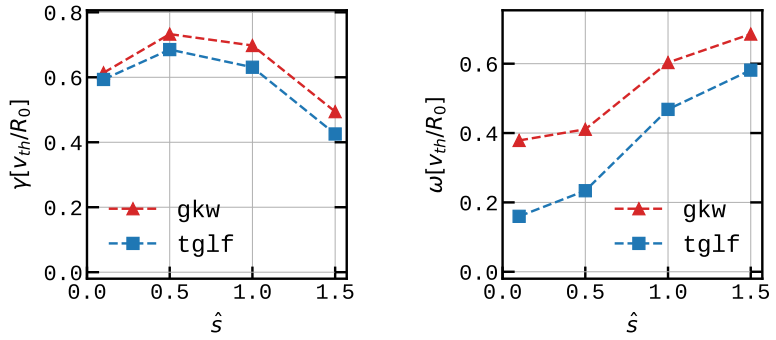


Figure 2.9. – Comparison of TGLF and GKW linear growth rate and frequency as a function of magnetic shear ($\hat{s}$) in IMAS units.

2.3.4.7. Effect of Electron-Ion Collision Frequency

This section examines the impact of varying the electron-ion collision frequency on the linear growth rate and frequency of the most unstable mode, as predicted by TGLF and GKW. Since TGLF allows only the electron-ion collision frequency to be provided as input, the scans performed here in both GKW and TGLF are restricted to variations in the electron-ion collision frequency.

To better highlight collisional effects, we have slightly deviated from the original Waltz standard case, which is dominated by the Ion Temperature Gradient (ITG) instability, and shifted towards a regime more sensitive to collisions. Specifically, we reduced the ion temperature gradient to zero ($R/LT_i = 0$), moving the plasma closer to a regime where collisional effects are more prominent, such as Trapped Electron Modes (TEM).

Impact on Linear Growth Rate and Frequency Figure 2.16 shows the linear growth rate and frequency of the most unstable mode as a function of the electron-ion collision frequency, plotted on a logarithmic scale. The results are presented in IMAS normalizations, with two curves: one representing TGLF and the other representing

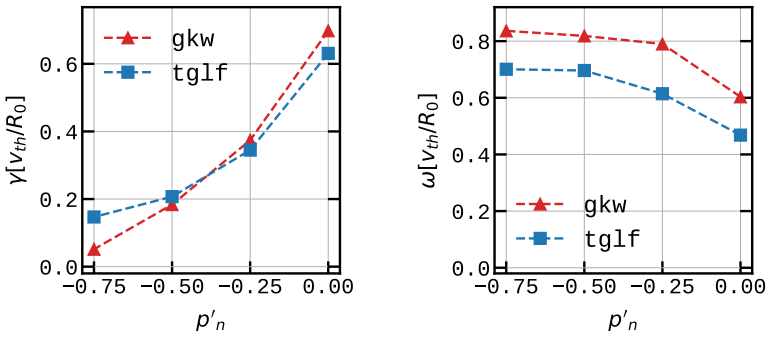


Figure 2.10. – Comparison of TGLF and GKW linear growth rate and frequency as a function of pressure gradient (p'_N) in IMAS units.

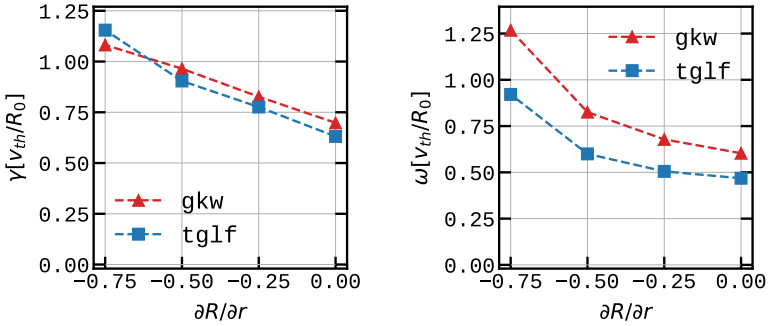


Figure 2.11. – Comparison of TGLF and GKW linear growth rate and frequency as a function of $\frac{\partial R}{\partial r}$, in IMAS units.

GKW. For the collision settings in GKW, only pitch-angle scattering is included to replicate the same limitations of TGLF.

As shown in Figure 2.16, similar trends are observed. The TEM stabilisation [122] by electron-ion pitch angle scattering is observed in both codes with some quantitative differences in the growth rate values and the critical collisionality at which one transition to ITG instability.

2.3.4.8. Effect of Plasma Beta

This section explores the impact of varying plasma β on the linear growth rate and frequency of the most unstable mode, as predicted by TGLF and GKW. The simulations are based on the Waltz standard case outlined in Table 3.1, with plasma β being systematically varied while keeping all other parameters fixed.

Impact on Linear Growth Rate and Frequency The plot in Figure 2.17 shows the linear growth rate and frequency of the most unstable mode as a function of plasma β. The values are plotted in IMAS normalizations, with two curves: one representing the results from TGLF and the other from GKW. Each point on the TGLF curve corresponds

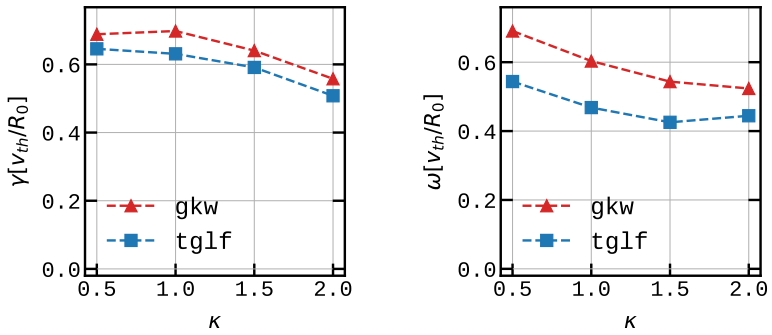


Figure 2.12. – Comparison of linear growth rate and frequency as a function of elongation (κ) between GKW and TGLF in IMAS units.

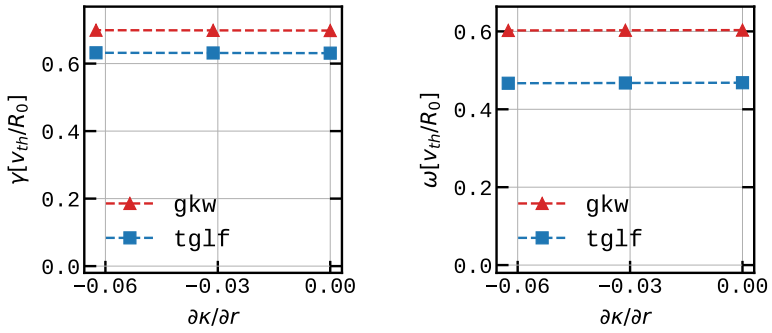


Figure 2.13. – Comparison of TGLF and GKW linear growth rate and frequency as a function of $\partial\kappa/\partial r$, expressed in IMAS units.

to a simulation where the TGLF input file was generated from the corresponding GKW output IDS using the developed conversion routines.

As shown in the plot, the growth rate and frequency exhibit a transition from the Ion Temperature Gradient (ITG) instability regime to a regime dominated by Kinetic Ballooning Modes (KBM) as plasma β increases. This transition is noticeable by the sharp jump in the frequency of the most unstable mode, which can be seen around $\beta = 0.5\%$. Additionally, the sudden rise in the linear growth rate further indicates the onset of KBM instabilities, marking a shift from the ITG-driven regime to one where electromagnetic effects play a more dominant role. These distinct changes in behavior with increasing β are consistent with theoretical expectations for tokamak plasmas, and the detailed mechanisms behind this transition will be explored further in the next chapters.

The consistency between TGLF and GKW results across the whole range of β values confirms the reliability of the conversion routine. However, as β increases, some discrepancies start to appear in the growth rates, which may be attributed to the different models used by the codes in treating KBM instabilities.

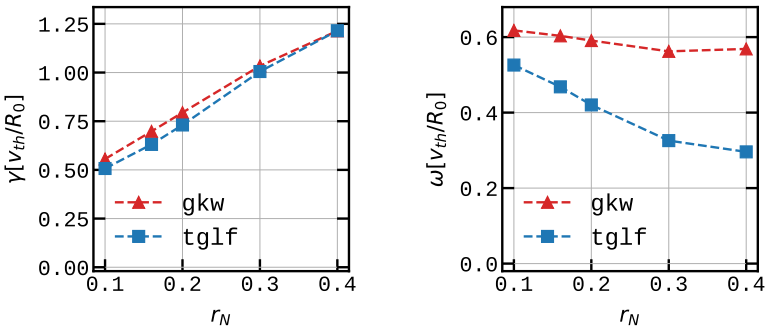


Figure 2.14. – Linear growth rate and frequency as a function of inverse aspect ratio (r_N), comparing GKW and TGLF results.

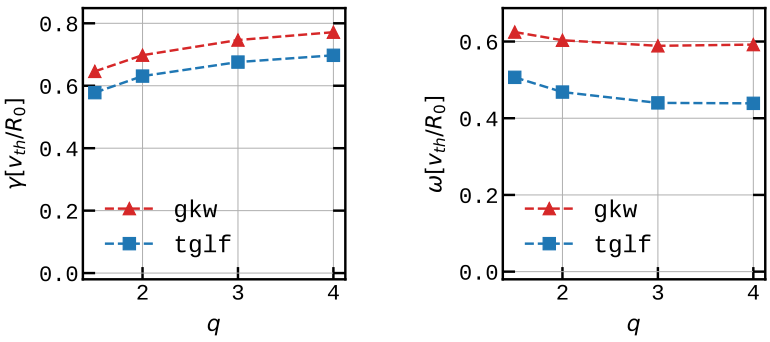


Figure 2.15. – Linear growth rate and frequency as a function of safety factor (q), comparing GKW and TGLF results.

Mode Structure Comparison To further validate the conversion routines, we compare the mode structures by examining the real part of the electrostatic potential as a function of the parallel coordinate, θ, in IMAS units for both TGLF and GKW.

Figure 2.18 shows the mode structure for a plasma β value of 0.2% (ITG regime) and 1% (KBM regime).

The mode structures are well-matched for both ITG and KBM instabilities.

2.3.5. Conclusions

The comprehensive scans and comparisons conducted have confirmed the validity of the conversion routines developed to bridge the normalizations used in TGLF and the IMAS gyrokinetic IDS. The routines have been made available in an open-source Git repository [119], with documentation and example files for ease of use. This resource enables researchers to quickly perform gyrokinetic flux checks with TGLF and facilitates benchmarking and cross-validation across the fusion research community. Moving forward, this validation allows us to have confidence in the conversion process itself. Thus, when discrepancies between TGLF and GKW arise, we can confidently attribute them to differences in the physical models and approximations used by the

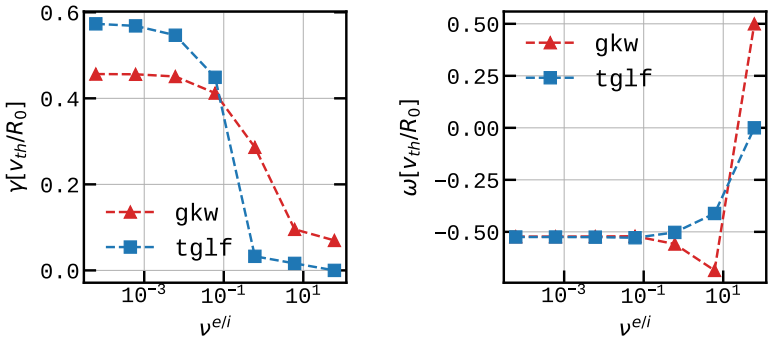


Figure 2.16. – Linear growth rate and frequency as a function of electron-ion collision frequency. Results from GKW and TGLF are compared, with both curves expressed in IMAS units.

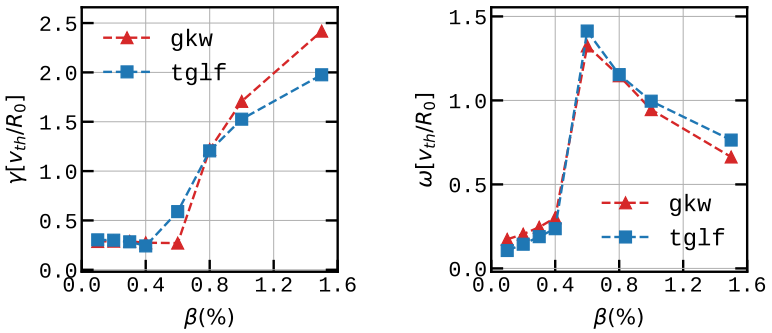


Figure 2.17. – Linear growth rate and frequency as a function of plasma β. The results from GKW and TGLF are plotted for comparison, with both curves expressed in IMAS units.

two codes rather than to inaccuracies in the normalization process. This provides a solid foundation for the in-depth analysis of the codes behavior, which will be explored in the next chapters.

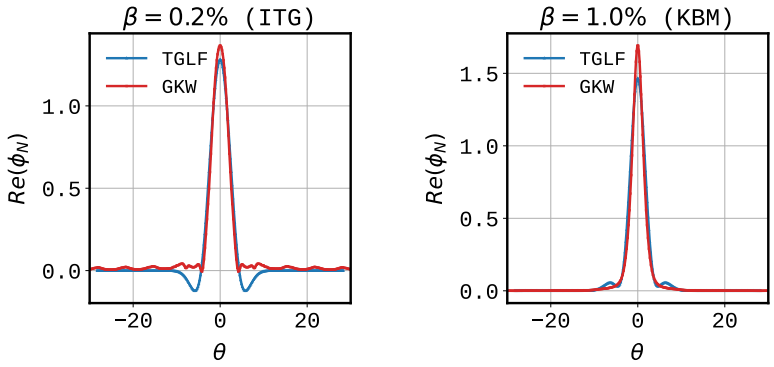


Figure 2.18. – Real part of the electrostatic potential as a function of the parallel coordinate, θ, for $\beta = 0.2\%$ (ITG regime) and , for $\beta = 1\%$ (KBM regime).

3. Verification of TGLF Linear Response in High-Beta Plasmas

In this chapter, we investigate the linear stability of two dominant instabilities that are crutial to determine turbulent transport in tokamak plasmas: the ion-temperature-gradient (**ITG**) modes [123, 124] and the kinetic ballooning modes (**KBM**s). ITG modes are generally the dominant instability in low plasma β conditions, where the ratio of plasma pressure to magnetic pressure is small. These modes are driven by steep ion temperature gradients, and their destabilization leads to significant radial transport of energy. We begin by presenting a derivation of simplified analytical dispersion relations for ITG modes, showing both kinetic and fluid approaches to characterize the linear growth rate of this instability. In high-β regimes, where the ratio of plasma pressure to magnetic pressure is large, electromagnetic modes such as KBMs become unstable. KBMs are primarily driven by the interaction between steep plasma pressure gradients and regions of unfavorable magnetic curvature. These modes impose a limit on the maximum plasma pressure sustainable in high-confinement mode (H-mode) tokamak plasmas. KBMs are particularly prevalent in regions of strong pressure gradients, including the pedestal in tokamaks [125], the core plasmas with low magnetic shear [12], and spherical tokamaks [126].

In this chapter, we will show gyrokinetic simulations using TGLF and GKW to study two plasma scenarios. The first scenario is the **Waltz Standard Case**, where beta scans are used to assess TGLF's ability to capture the ITG-KBM transition. In the second scenario, we analyze the **JET hybrid H-mode discharge 75225** at the two radial positions $\rho = 0.15$ and $\rho = 0.33$, where ρ represents the normalized toroidal flux coordinate, where we assess TGLF's linear response accuracy under conditions of high beta and low magnetic shear, with KBMs predicted to be unstable in the plasma core.

3.1. Simplified Linear Fluid and Kinetic Models for the Toroidal ITG Instability

In this section, we derive two simplified analytical linear dispersion relations for the ITG mode, using both kinetic and fluid models. ITG modes exhibit two primary branches: the slab branch, where the instability is driven by the resonance with the parallel ion motion, and the toroidal branch, where the instability arises from the resonance with the perpendicular magnetic drift. Here, we focus on the toroidal ITG instability.

3.1.1. The reference delta-f gyrokinetic equation

We begin with the gyrokinetic equation in the local δf approximation, as implemented in GKW [1]. Here, δf represents the perturbed gyro-center distribution function, while the total gyro-center distribution function F is expressed as:

$$F = F_M + \delta f,$$

where F_M corresponds to the equilibrium Maxwellian background gyro-center distribution function, defined as:

$$F_M = \frac{n_0}{\sqrt{\pi}^3 v_{th}^3} e^{-\frac{v^2}{v_{th}^2}}. \tag{3.1}$$

where $v_{th} = \sqrt{2T/m}$ is the thermal velocity and n_0 the density. To simplify this model, we neglect the vector potential fluctuations to make the model electrostatic. Additional simplifications include omitting Coriolis and centrifugal force terms in the co-moving frame, the parallel rotation gradient in the source term, and the β' correction to the curvature drift. With these assumptions, the gyrokinetic equation reduces to:

$$\frac{\partial \delta f}{\partial t} + (\boldsymbol{v}_D + v_\parallel \boldsymbol{b} + \boldsymbol{v}_E) \cdot \nabla \delta f - \frac{\boldsymbol{b}}{m} \cdot (\mu \nabla B) \frac{\partial \delta f}{\partial v_\parallel} = S, \tag{3.2}$$

where $v_\parallel$ correspond to the parallel velocity along the magnetic field, $\boldsymbol{b}$ in the unit vector in the direction of the unperturbed magnetic field, and S stands for the source terms given by:

$$S = -(\boldsymbol{v}_E + \boldsymbol{v}_D) \cdot \left[\frac{\nabla n_0}{n_0} + \left(\frac{v_\parallel^2}{v_{th}^2} + \frac{\mu B}{T} - \frac{3}{2} \right) \frac{\nabla T}{T} \right] F_M - \frac{Ze}{T} (v_\parallel \boldsymbol{b} + \boldsymbol{v}_D) \cdot \nabla \langle \phi \rangle F_M, \tag{3.3}$$

And where, $\boldsymbol{v}_D$ and $\boldsymbol{v}_E$ are drift velocities, expressed as:

$$\boldsymbol{v}_D = \frac{1}{Ze} \left(\frac{m v_\parallel^2}{B} + \mu \right) \frac{\boldsymbol{b} \times \nabla B}{B}, \qquad \text{and} \qquad \boldsymbol{v}_E = \frac{\boldsymbol{b} \times \nabla \langle \hat{\phi} \rangle}{B}, \tag{3.4}$$

with $\mu = \frac{m v_\perp^2}{2B}$ being the magnetic moment and m the mass of the considered species. From this set of equations, we build a reduced one-point model by assuming a purely toroidal magnetic field and evaluating all quantities at the low-field-side mid-plane of a given flux surface.
To simplify the notation in the following discussion, we define $\hat{f} \equiv \delta f$ and $\hat{\phi} \equiv \delta \phi$.

1. Refer to Eq. (1.28) in the GKW manual [127]

3.1.2. Coordinate System

To describe the geometry, we use an orthogonal coordinate system (x, y, z) related to the toroidal coordinates (R, Z, φ) showed in Figure (ref chap 2) with:

— $x = R$
— $y = Z$
— $z = R_0\varphi$

where R_0 is the reference major radius, taken to be the major radius at the low-field-side mid-plane of the selected flux surface.

3.1.3. Magnetic Geometry

We assume a purely toroidal magnetic field given by:

$$\boldsymbol{B} = RB\nabla\varphi = B\boldsymbol{e}_z, \quad \text{with} \quad B = \frac{R_0 B_0}{R},$$

where B_0 is the corresponding reference magnetic field at R_0. Under this assumption, the magnetic field magnitude at $R = R_0$ is $B = B_0$, and the gradient of B is therefore given by:

$$\nabla B = \begin{bmatrix} -\frac{B_0}{R_0} \\ 0 \\ 0 \end{bmatrix}. \tag{3.5}$$

The drift velocity $\boldsymbol{v}_D$ at $R = R_0$ then becomes:

$$\begin{aligned} \boldsymbol{v}_D(R = R_0) &= \frac{1}{Ze}\left(\frac{mv_\parallel^2}{B} + \mu\right)\frac{\boldsymbol{B}\times\nabla B}{B^2} \\ &= -\frac{1}{ZeR_0}\left(\frac{mv_\parallel^2}{B_0} + \mu\right)\boldsymbol{e}_y. \end{aligned} \tag{3.6}$$

3.1.4. Perturbed Quantities and Gyro-Average

We assume a homogeneous simulation domain in the x, y, and z directions, seeking solutions of the form:

$$\hat{f} = f_1 e^{i[\boldsymbol{k}\cdot\boldsymbol{x} - \omega t]}, \tag{3.7}$$

$$\hat{\phi} = \phi_1 e^{i[\boldsymbol{k}\cdot\boldsymbol{x} - \omega t]}, \tag{3.8}$$

where $\omega = \omega_r + i\gamma$ represents the complex frequency. Under these assumptions, we find:

$$\nabla\hat{f} = i\boldsymbol{k}\hat{f} \tag{3.9}$$

$$\nabla\hat{\phi} = i\boldsymbol{k}\hat{\phi} \tag{3.10}$$

The gyro-average of the electrostatic potential ϕ is defined as:

$$\langle\phi\rangle(\boldsymbol{X}) = \int_0^{2\pi} \frac{d\zeta}{2\pi}\phi(\boldsymbol{X}+\boldsymbol{\rho}), \tag{3.11}$$

where $\boldsymbol{X}$ is the gyro-center position and $\boldsymbol{\rho}$ is the particle Larmor radius, dependent on the gyro-angle ζ. We compute the gyro-average of $\hat{\phi}$:

$$\begin{aligned}\langle\hat{\phi}\rangle(\boldsymbol{X}) &= \int_0^{2\pi} \frac{d\zeta}{2\pi}\hat{\phi}(\boldsymbol{X}+\boldsymbol{\rho}) \\ &= \frac{1}{2\pi}\int_0^{2\pi} \phi_1 e^{i[\boldsymbol{k}\cdot\boldsymbol{X}+\boldsymbol{k}\cdot\boldsymbol{\rho}-\omega t]} d\zeta \\ &= \frac{\phi_1}{2\pi} e^{i[\boldsymbol{k}\cdot\boldsymbol{X}-\omega t]}\int_0^{2\pi} e^{i(\boldsymbol{k}\cdot\boldsymbol{\rho})} d\zeta \\ &= \frac{\phi_1}{2\pi} e^{i[\boldsymbol{k}\cdot\boldsymbol{X}-\omega t]}\int_0^{2\pi} e^{ik_x\rho\cos(\zeta)} e^{ik_y\rho\sin(\zeta)} d\zeta.\end{aligned} \tag{3.12}$$

From here, since the integral is over a gyro-period, we can write it as:

$$\langle\hat{\phi}\rangle(\boldsymbol{X}) = \frac{\phi_1}{2\pi} e^{i[\boldsymbol{k}\cdot\boldsymbol{X}-\omega t]}\int_0^{2\pi} e^{ik_\perp\rho\cos(\zeta)} d\zeta \tag{3.13}$$

where $k_\perp^2 = k_x^2 + k_y^2$. Noticing that the function inside the integral is even, and by defining the Bessel function of the first kind as:

$$J_0(a) = \frac{1}{\pi}\int_0^{\pi} e^{ia\cos(\theta)} d\theta,$$

We can finally express the gyro-average as:

$$\langle\hat{\phi}\rangle(\boldsymbol{X}) = \phi_1(\boldsymbol{X}) J_0(k_\perp\rho). \tag{3.14}$$

The expression for the $E\times B$ velocity $\boldsymbol{v}_E$ is then given by:

$$\begin{aligned}\boldsymbol{v}_E &= \frac{\boldsymbol{b}\times\nabla\langle\hat{\phi}(\boldsymbol{X})\rangle}{B} \\ &= \frac{i}{B}\boldsymbol{b}\times\boldsymbol{k}\langle\hat{\phi}\rangle(\boldsymbol{X}) \\ &= \frac{i}{B}(k_x\boldsymbol{e}_y - k_y\boldsymbol{e}_x)\langle\hat{\phi}\rangle(\boldsymbol{X}).\end{aligned} \tag{3.15}$$

3.1.5. Linearized One-Point Gyrokinetic Equation

With the expressions derived above, we can rewrite the reference gyrokinetic equation (Eq.3.2) in a simplified form and linearize it by neglecting terms that are quadratic

in the perturbed quantities:

$$-i\omega\hat{f} + iv_\parallel \hat{f} k_z - i\hat{f}k_y\left(\frac{mv_\parallel^2}{BZeR_0} + \frac{mv_\perp^2}{2BZeR_0}\right) = \frac{i\hat{\phi}}{B}\frac{\partial n}{\partial x}\frac{k_y}{n}F_M +$$
$$\frac{i\hat{\phi}}{B}\left(\frac{v_\parallel^2}{v_{th}^2} - \frac{3}{2} + \frac{\mu B}{T}\right)\frac{\partial T}{\partial x}\frac{k_y}{T}F_M - \frac{iZe}{T}\hat{\phi}F_M v_\parallel k_z + \frac{iZe}{T}\hat{\phi}F_M k_y \frac{1}{BZe}\left(\frac{mv_\parallel^2}{B} + \mu\right)\frac{B}{R_0}$$

To make the gyrokinetic equation more compact, we introduce the following definitions:

$$\omega_D = -\frac{mv_{th}^2}{ZeBR_0}k_y, \qquad R/L_n = -\frac{R_0}{n}\frac{\partial n}{\partial x}, \qquad \epsilon_D = \frac{v_\parallel^2}{v_{th}^2} + \frac{1}{2}\frac{v_\perp^2}{v_{th}^2}, \tag{3.16}$$

$$\omega_E = \frac{T_e}{eBR_0}k_y, \qquad R/L_T = -\frac{R_0}{T}\frac{\partial T}{\partial x}, \qquad \epsilon_T = \frac{v^2}{v_{th}^2} - \frac{3}{2}. \tag{3.17}$$

where:

— ω_D denotes the characteristic frequency of the curvature and ∇B drift, at the thermal velocity over a wavelength of the perturbed quantities.

— ω_E represents the characteristic frequency of the radial $E \times B$ drift over the reference length R_0 for an electrostatic potential perturbation of wavevector k_y and amplitude T_e/e, where gyro-averaging is neglected.

Applying these definitions, the gyrokinetic equation reduces to:

$$\omega\hat{f} - v_\parallel \hat{f} k_z - \hat{f}\omega_D\epsilon_D = \frac{\omega_E}{T}\hat{\phi}F_M e\left[\frac{R}{L_n} + \frac{R}{L_T}\epsilon_T\right] + \frac{\hat{\phi}ZeF_M}{T}\left[v_\parallel k_z + \omega_D\epsilon_D\right]. \tag{3.18}$$

3.1.6. Quasi-Neutrality and Adiabatic Electron Approximation

The previously derived equation expresses the perturbed distribution function $\hat{f}$ in terms of the perturbed electrostatic potential $\hat{\phi}$. To close this system, we need an additional relationship linking $\hat{f}$ and $\hat{\phi}$. This is provided by the quasi-neutrality equation, which states that the charge density in real space must be zero, i.e., the sum of the gyro-center density and the polarization density of all species (sp) must be zero:

$$\sum_{sp} Z\int J_0(k_\perp\rho)\hat{f}\,d\boldsymbol{v} + Z^2 n\left[\Gamma(b) - 1\right]\frac{e\hat{\phi}}{T} = 0, \tag{3.19}$$

where the sum is taken over all plasma species and the integral over velocity space. Here, $J_0(k_\perp\rho)$ is the zeroth-order Bessel function, which accounts for the gyro-average of $\hat{\phi}$, and $\Gamma(b)$ is given by:

$$\Gamma(b) = I_0(b)e^{-b} = \int_0^\infty J_0^2(\sqrt{2bx})e^{-x}\,dx \qquad \text{with} \qquad b = \frac{1}{2}\frac{k_\perp^2 m^2 v_{th}^2}{e^2B^2} \tag{3.20}$$

In this formulation, I_0 is the modified Bessel function of the first kind. We will only assume two species, main ion and electrons, and neglect the gyro-average for the electrons, setting $\rho_e = 0$, $J_e(0) = 1$, and $\Gamma_e(b) = 1$. This simplification is justified because the electron Larmor radius ρ_e is much smaller than the ion Larmor radius ρ_i, due to the electron's significantly lower mass. Consequently, the condition $k_\perp \rho_e \ll 1$ holds, allowing us to approximate the electron gyro-average as negligible.
Using the adiabatic approximation $\left(\frac{\delta n_e}{n_e} = \frac{e\hat{\phi}}{T_e}\right)$, the quasi-neutrality equation (3.19) reduces to:

$$Z_i \int J_0(k_\perp \rho_i)\hat{f}_i \, d\boldsymbol{v} + Z_i^2 n_i \left[\Gamma(b) - 1\right] \frac{e\hat{\phi}}{T_i} - \frac{e\hat{\phi}}{T_e} n_e = 0. \tag{3.21}$$

To simplify further, we assume an ion charge of unity ($Z = 1$), equal electron and ion temperatures ($T_e = T_i = T$), and we neglect the gyro-average for ions ($k_\perp \rho_i \ll 1$). Under these assumptions, the quasi-neutrality equation (3.21) reduces to:

$$\int \hat{f}_i \, d\boldsymbol{v} = \frac{e\hat{\phi}}{T} n_e. \tag{3.22}$$

Thus, we have:

$$\delta n_i = \frac{e\hat{\phi}}{T} n_e = \delta n_e \tag{3.23}$$

3.1.7. Kinetic Model

By combining the linearized gyrokinetic equation (3.18) and the linearized quasi-neutrality equation (3.23), we obtain the following dispersion relation:

$$\omega \hat{f} - v_\parallel \hat{f} k_z - \hat{f} \omega_D \epsilon_D = \omega_E \frac{\delta n}{n} F_M \left(\frac{R}{L_n} + \frac{R}{L_T} \epsilon_T \right) + Z F_M \frac{\delta n}{n} \left(v_\parallel k_z + \omega_D \epsilon_D \right) \tag{3.24}$$

The perturbed distribution function can then be expressed as:

$$\hat{f} = \left(F_M \frac{\delta n}{n} \right) \frac{\omega_E \left(\frac{R}{L_n} + \frac{R}{L_T} \epsilon_T \right) + \left(v_\parallel k_z + \omega_D \epsilon_D \right)}{\omega - v_\parallel k_z - \omega_D \epsilon_D} \tag{3.25}$$

To simplify, we normalize all quantities using v_{th} for velocities, R_0 for lengths, and v_{th}/R_0 for frequencies. Normalized quantities are denoted by a hat $\hat{()}$. The normalized background distribution function is given by $\hat{F}_M = F_M v_{th}^3 / n$. We also note that $\hat{\omega}_D = -\rho_0 k_y$ and $\hat{\omega}_E = \frac{1}{2}\rho_0 k_y$. The distribution function $\hat{f}$ then becomes:

$$\hat{f} = F_M \hat{n} \frac{\hat{\omega}_E \left(\frac{R}{L_n} + \frac{R}{L_T} \epsilon_T \right) + \hat{v}_\parallel \hat{k}_z + \hat{\omega}_D \epsilon_D}{\hat{\omega} - \hat{v}_\parallel \hat{k}_z - \hat{\omega}_D \epsilon_D}, \tag{3.26}$$

where δn is by definition:

$$\delta n = \int \hat{f} \, d\boldsymbol{v}. \tag{3.27}$$

we then have:

$$\delta n = \int \hat{n} \frac{\hat{\omega}_E \left(\frac{R}{L_n} + \frac{R}{L_T} \epsilon_T \right) + \hat{v}_\parallel \hat{k}_z + \hat{\omega}_D \epsilon_D}{\hat{\omega} - \hat{v}_\parallel \hat{k}_z - \hat{\omega}_D \epsilon_D} F_M \, d\boldsymbol{v}.$$

The resulting expression for the dispersion relation, after normalizing becomes:

$$1 = \frac{1}{v_{th}^3} \int \frac{\hat{\omega}_E \left(\frac{R}{L_n} + \frac{R}{L_T} \epsilon_T \right) + \hat{v}_\parallel \hat{k}_z + \hat{\omega}_D \epsilon_D}{\hat{\omega} - \hat{v}_\parallel \hat{k}_z - \hat{\omega}_D \epsilon_D} \hat{F}_M \, d\boldsymbol{v}. \tag{3.28}$$

Expanding further, we have:

$$1 = 2\pi \int \frac{\frac{1}{2}\rho_0 k_y \left(\frac{R}{L_n} + \frac{R}{L_T} \left[\hat{v}_\parallel^2 + \hat{v}_\perp^2 - \frac{3}{2} \right] \right) + \hat{v}_\parallel \hat{k}_z - \rho_0 k_y \left[\hat{v}_\parallel^2 + \frac{1}{2} \hat{v}_\perp^2 \right]}{\hat{\omega} - \hat{v}_\parallel \hat{k}_z + \rho_0 k_y \left[\hat{v}_\parallel^2 + \frac{1}{2} \hat{v}_\perp^2 \right]} \hat{F}_M \, v_\perp \, d\hat{v}_\parallel \, d\hat{v}_\perp. \tag{3.29}$$

The dispersion relation for our kinetic model, in terms of $k_y\rho$, $\hat{k}_z$, R/L_n, and R/L_T, is given by:

$$\left| 1 - 2\pi \int \frac{\frac{1}{2}\rho_0 k_y \left(\frac{R}{L_n} + \frac{R}{L_T} \left[\hat{v}_\parallel^2 + \hat{v}_\perp^2 - \frac{3}{2} \right] \right) + \hat{v}_\parallel \hat{k}_z - \rho_0 k_y \left[\hat{v}_\parallel^2 + \frac{1}{2} \hat{v}_\perp^2 \right]}{\hat{\omega} - \hat{v}_\parallel \hat{k}_z + \rho_0 k_y \left[\hat{v}_\parallel^2 + \frac{1}{2} \hat{v}_\perp^2 \right]} \hat{F}_M \, v_\perp \, d\hat{v}_\parallel \, d\hat{v}_\perp \right| = 0. \tag{3.30}$$

The eigenvalues in this dispersion relation can be obtained numerically by finding the values of ω that satisfy this equation. For this purpose, a minimizing function algorithm in Python was employed, managing the resonance effects introduced by the denominator. The next section transitions to a fluid model, which inherently avoids these resonances.

3.1.8. Fluid Model

For closure, we assume that the perturbed distribution function $\hat{f}$ is given by:

$$\hat{f} = \left[\frac{\delta n}{n} + 2 \frac{\delta V_\parallel}{v_{th}} \frac{v_\parallel}{v_{th}} + \frac{\delta T}{T} \left(\frac{v^2}{v_{th}^2} - \frac{3}{2} \right) \right] F_M, \tag{3.31}$$

where

$$F_M = \frac{n}{\sqrt{\pi}^3 v_{th}^3} e^{-\frac{v^2}{v_{th}^2}}. \tag{3.32}$$

To obtain the zeroth moment, which corresponds to the continuity equation, we integrate the linearized gyrokinetic equation (3.18) over velocity space. The detailed calculations for the integrals of that section are presented in Appendix A. The zeroth

moment of the distribution function, after integrating over velocity space, yields:

$$\omega\delta n - k_z n\delta V_\parallel - \omega_D\left(\delta n + n\frac{\delta T}{T}\right) = \frac{\omega_E}{T}\frac{R}{L_n}n\phi e + \frac{Ze}{T}\omega_D n\phi. \tag{3.33}$$

For the first moment, we multiply the linearized equation (3.18) by $v_\parallel$ and then integrate over velocity space. This procedure gives us:

$$\omega n\delta V_\parallel - \frac{1}{2}k_z v_{th}^2\left(\delta n + n\frac{\delta T}{T}\right) - 2\omega_D n\delta V_\parallel = \frac{1}{2}\frac{Ze}{T}k_z v_{th}^2\phi n. \tag{3.34}$$

To obtain the second moment of the distribution function, corresponding to the energy balance equation, we multiply equation (3.18) by v^2 and integrate over velocity space. This yields:

$$\begin{aligned}&3\omega v_{th}^2\left(\delta n + n\frac{\delta T}{T}\right) - 5nv_{th}^2\left(k_z\delta V_\parallel + \omega_D\left(\delta n + 2n\frac{\delta T}{T}\right)\right)\\ &= 3\frac{\omega_E\phi e n v_{th}^2}{T}\left(\frac{R}{L_N}+\frac{R}{L_T}\right) + \frac{5Ze\phi}{T}nv_{th}^2\omega_D.\end{aligned}$$

To simplify further, we introduce thoses normalized quantities:

$$\hat{n} = \frac{\delta n}{n}, \qquad \hat{T} = \frac{\delta T}{T}, \qquad \hat{V}_\parallel = \frac{\delta V_\parallel}{v_{th}}, \tag{3.35}$$

$$\hat{\phi} = \frac{e\phi}{T_e}, \qquad \hat{n_e} = \hat{\phi} = \hat{n_i}, \qquad \hat{k_z} = k_z R_0, \tag{3.36}$$

$$\hat{\omega} = \frac{\omega R_0}{v_{th}}, \qquad \hat{\omega}_D = \frac{\omega_D R_0}{v_{th}}, \qquad \hat{\omega}_E = \frac{\omega_E R_0}{v_{th}}, \tag{3.37}$$

$$\hat{f} = \frac{f v_{th}^3}{n}, \qquad \hat{F}_M = \frac{F_M v_{th}^3}{n}, \qquad \hat{v}_\parallel = \frac{v_\parallel}{v_{th}}. \tag{3.38}$$

Substituting these definitions, we obtain:

$$\hat{\omega}\left(\hat{n}+\hat{T}\right) - \frac{5}{3}\left(\hat{k_z}\hat{V}_\parallel + \hat{\omega}_D\left(\hat{n}+2\hat{T}\right)\right) = \hat{\omega}_E\hat{\phi}\left(\frac{R}{L_N}+\frac{R}{L_T}\right) + \frac{5}{3}\hat{\phi}\hat{\omega}_D. \tag{3.39}$$

Subtracting the continuity equation from this expression gives:

$$\begin{aligned}&\hat{\omega}\hat{n} + \hat{\omega}\hat{T} - \frac{5}{3}\hat{k_z}\hat{V}_\parallel - \frac{5}{3}\hat{\omega}_D\hat{n} - \frac{10}{3}\hat{\omega}_D\hat{T} - \hat{\omega}\hat{n} + \hat{k_z}\hat{V}_\parallel + \hat{\omega}_D\hat{n} + \hat{\omega}_D\hat{T}\\ &= \hat{\omega}_E\hat{\phi}\frac{R}{L_N} + \hat{\omega}_E\hat{\phi}\frac{R}{L_T} + \frac{5}{3}\hat{\phi}\hat{\omega}_D - \hat{\omega}_E\frac{R}{L_n}\hat{\phi} - \hat{\phi}\hat{\omega}_D.\end{aligned}$$

Finally, we obtain:

$$\hat{\omega}\hat{T} - \frac{2}{3}\hat{k_z}\hat{V}_\parallel - \frac{2}{3}\hat{\omega}_D\hat{n} - \frac{7}{3}\hat{\omega}_D\hat{T} = \hat{\omega}_E\hat{\phi}\frac{R}{L_T} + \frac{2}{3}\hat{\phi}\hat{\omega}_D. \tag{3.40}$$

To resume, the first moments of the linearized normalized gyrokinetic equation (Eq. 3.18) are:

$$\hat{\omega}\hat{n} - \hat{k_z}\hat{V_\parallel} - \hat{\omega}_D\left(\hat{n}+\hat{T}\right) = \hat{\omega}_E\frac{R}{L_n}\hat{\phi} + \hat{\phi}\hat{\omega}_D, \tag{3.41}$$

$$\hat{\omega}\hat{V_\parallel} - \frac{\hat{k_z}}{2}\left(\hat{n}+\hat{T}\right) - 2\hat{\omega}_D\hat{V_\parallel} = \frac{\hat{\phi}\hat{k_z}}{2}, \tag{3.42}$$

$$\hat{\omega}\hat{T} - \frac{2}{3}\hat{k_z}\hat{V_\parallel} - \frac{2}{3}\hat{\omega}_D\hat{n} - \frac{7}{3}\hat{\omega}_D\hat{T} = \hat{\omega}_E\hat{\phi}\frac{R}{L_T} + \frac{2}{3}\hat{\phi}\hat{\omega}_D. \tag{3.43}$$

And the normalized quasi-neutrality equation is given by:

$$\hat{n} = \hat{\phi} \tag{3.44}$$

Derivation of toroidal ITG

We will further simplify and neglect perturbations in the parallel direction ($k_z = 0$) and will consider an adiabatic response from electrons ($\hat{n} = \hat{\phi}$), to derive the toroidal ITG fluid model.
Noticing that:

$$\hat{\omega}_D = -\rho_0 k_y \qquad \text{and} \qquad \hat{\omega}_E = \frac{1}{2}\rho_0 k_y \tag{3.45}$$

Where ρ_0 corresponds to the ion larmor radius. And replacing $\hat{n}$ by $\hat{\phi}$, we can rewrite the continuity and energy balance equations as:

$$\begin{cases} \hat{\omega}\hat{\phi} - \hat{\omega}_D\left(\hat{\phi}+\hat{T}\right) & = \hat{\omega}_E\frac{R}{L_n}\hat{\phi} + \hat{\phi}\hat{\omega}_D \\ \hat{\omega}\hat{T} - \frac{2}{3}\hat{\omega}_D\hat{\phi} - \frac{7}{3}\hat{\omega}_D\hat{T} & = \hat{\omega}_E\hat{\phi}\frac{R}{L_T} + \frac{2}{3}\hat{\phi}\hat{\omega}_D \end{cases} \tag{3.46}$$

The first equation gives us:

$$\hat{T} = \frac{\hat{\phi}}{\hat{\omega}_D}\left(\hat{\omega} - 2\hat{\omega}_D - \frac{R}{L_n}\hat{\omega}_E\right) \tag{3.47}$$

And by using this value in the second equation we finally obtain:

$$\hat{\omega}^2 - \left(\frac{R}{L_n}\hat{\omega}_E + \frac{13}{3}\hat{\omega}_D\right)\hat{\omega} + \left(\frac{7}{3}\frac{R}{L_n} - \frac{R}{L_T} + \frac{10}{3}\frac{\hat{\omega}_D}{\hat{\omega}_E}\right)\hat{\omega}_E\hat{\omega}_D = 0 \tag{3.48}$$

The solutions are:

$$\hat{\omega} = \frac{1}{2}\left(\left(\frac{R}{L_n}\hat{\omega}_E + \frac{13}{3}\hat{\omega}_D\right) \pm \sqrt{\underbrace{\left(\frac{R}{L_n}\hat{\omega}_E + \frac{13}{3}\hat{\omega}_D\right)^2 - 4\hat{\omega}_E\hat{\omega}_D\left(\frac{7}{3}\frac{R}{L_n} - \frac{R}{L_T} + \frac{10}{3}\frac{\hat{\omega}_D}{\hat{\omega}_E}\right)}_{\Delta}}\right) \tag{3.49}$$

Where $\omega = \omega_r + i\gamma$ represents the complex frequency. So when $\Delta < 0$ we have for the imaginary part:

$$\gamma = \pm\frac{1}{2}\sqrt{\left(\frac{R}{L_n}\hat{\omega}_E + \frac{13}{3}\hat{\omega}_D\right)^2 - 4\hat{\omega}_E\hat{\omega}_D\left(\frac{7}{3}\frac{R}{L_n} - \frac{R}{L_T} + \frac{10}{3}\frac{\hat{\omega}_D}{\hat{\omega}_E}\right)} \tag{3.50}$$

Equation 3.48 represents the simplified dispersion relation for toroidal ITG modes derived from our fluid model. Solving this equation provides the linear growth rate γ, which determines how rapidly the perturbations of the form $f = f_1 e^{i[\boldsymbol{k}\cdot\boldsymbol{x}-\omega t]}$ will grow over time within the linear approximation. Unlike the kinetic dispersion relation in Equation 3.30, the fluid dispersion relation in Equation 3.31 does not capture resonances. This fluid dispersion relation allows us to observe how the growth rate γ varies with the density gradient R/L_n and the temperature gradient R/L_T for fixed values of ω_D and ω_E. As illustrated in Figure 3.1, R/L_n acts as a stabilizing factor, while R/L_T drives the instability by increasing γ. For a fixed density gradient, there exists a threshold value of R/L_T: if the temperature gradient is below this threshold, the perturbation remains stable. This behavior aligns with the literature, where toroidal ITG modes become unstable when the temperature gradient exceeds a critical value that rises with increasing density gradient.

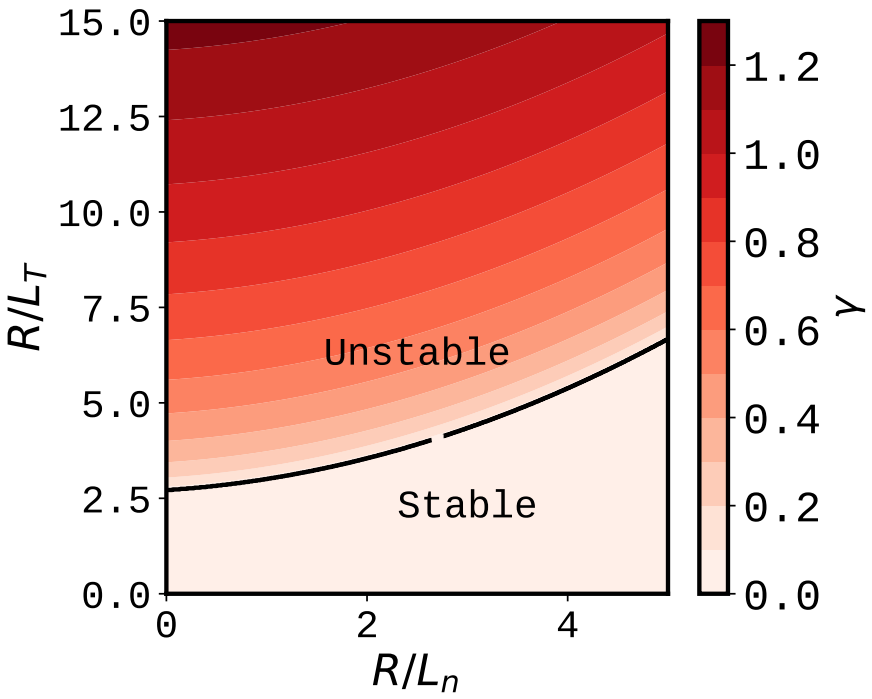


Figure 3.1. – Growth rate γ as a function of the temperature gradient R/L_T and density gradient R/L_n using the fluid model with $\hat{k_z} = 0$ and $\rho_0 k_y = 0.5$

3.1.9. Comparison between the Fluid and Kinetic Models

Figure 3.2 shows the linear growth rate γ as a function of R/L_T for the simplified fluid model and kinetic model derived in this work, along with results from the gyrokinetic code GKW, using parameters $R/L_n = 3$, $k_y\rho_0 = 0.4$, and $\hat{k}_z = 0$. A notable difference appears between the fluid and kinetic models in their predictions of the linear threshold. This is because the kinetic model captures additional dynamics, such as the resonance that is absent in the fluid perturbed distribution function $\hat{f}$, leading to additional destabilisation at low temperature gradients. When we compare these models with results from the more advanced gyrokinetic model GKW, we find that GKW aligns closely with our simplified kinetic model rather than with the fluid model. Both kinetic models predict a threshold for instability, but this threshold is lower than the one observed in the fluid model.

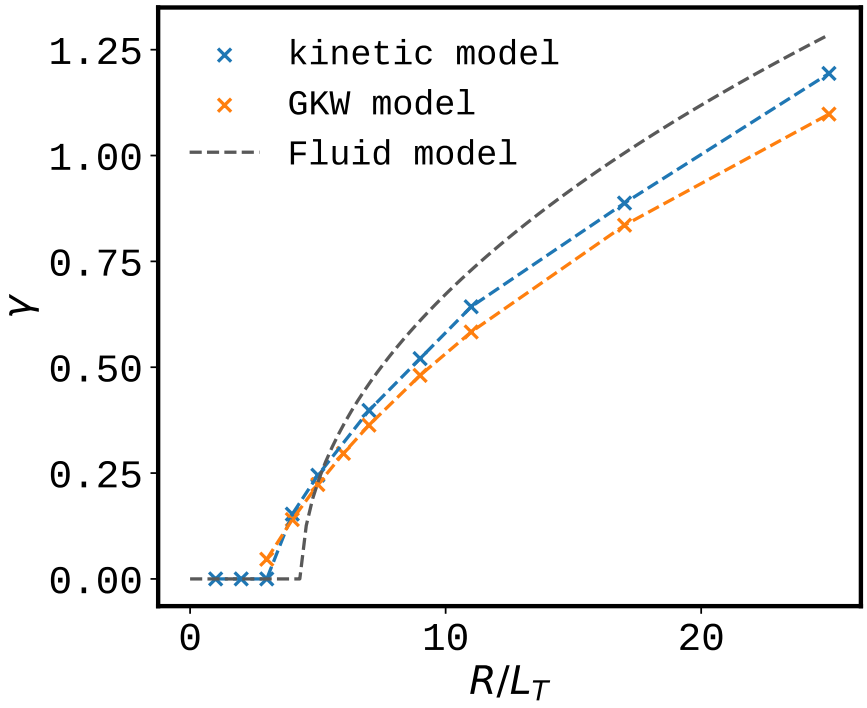


Figure 3.2. – Comparison of growth rate γ as a function of R/L_T for $R/L_n = 3$, $k_y\rho = 0.4$, and $\hat{k}_z = 0$. The results from the simplified fluid model, kinetic model, and GKW are shown. For GKW, linear simulations were performed with a magnetic shear $\hat{s} = 1$ and a safety factor $q = 2$, at $k_y\rho = 0.4$, using adiabatic electrons and evaluating a single point at $\theta = 0$.

The kinetic model derived in this chapter does not account for finite Larmor radius (FLR) effects, as we neglected the gyro-averaging for both electrons and ions. This simplification limits the model's accuracy, especially as the perpendicular wavelength of the perturbation becomes comparable to the Larmor radius. As we increase $k_y\rho$, the size of the perturbation decreases relative to the Larmor radius of the particles.

When $k_y\rho$ is large, particles complete a cyclotron turn over a path length longer than the perturbation scale, meaning that FLR effects become significant and the gyro-averaging cannot be neglected. Consequently, as shown in Figure 3.3, increasing $k_y\rho$ leads to greater discrepancies between the growth rates predicted by our kinetic model and those predicted by the gyrokinetic code GKW, which fully includes FLR effects. Another distinction between our kinetic model and `GKW` lies in the treatment

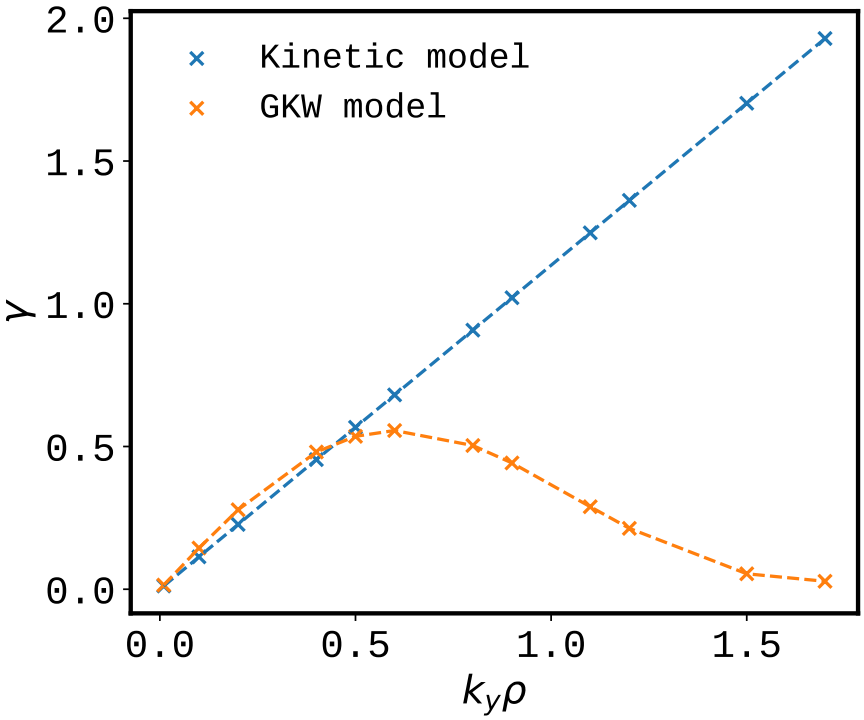


Figure 3.3. – Growth rate γ as a function of $k_y\rho$ for $R/L_n = 3$ and $\hat{k}_z = 0$, comparing the kinetic model with GKW for $R/L_T = 9$.

of magnetic geometry. In the kinetic model derived here, we only consider geometry effects through the curvature drift velocity, whereas GKW incorporates a more complete representation of toroidal geometry. For reference, the study in ref [128] presents a local linear gyrokinetic plasma dispersion relation formulated specifically for toroidal geometry. Their model, although electrostatic and collisionless, considers a non-rotating plasma with adiabatic electrons and excludes parallel dynamics. Unlike our kinetic model, however, it incorporates the full effects of toroidal circular geometry, providing an additional layer of accuracy for stability analyses in more realistic configurations.

In this work, we derived simplified dispersion relations for toroidal ITG-driven turbulence using both kinetic and fluid models. The simplified models reproduce that the density gradient R/L_n acts as a stabilizing factor, while the temperature gradient R/L_T drives the instability, consistent with observations reported in the literature. These derived models provide a simplified framework for understanding the linear

stability properties of ITG turbulence in tokamak plasmas. In the next section, we shift focus to the analytical treatment of Kinetic Ballooning Modes (KBMs), which introduce additional layers of complexity, in high-β plasmas where electromagnetic effects become significant. Using insights from established literature, we will examine the dispersion relation for KBMs, providing a theoretical context that will lead us into numerical simulations of these instabilities. This exploration of KBMs will further refine our understanding of linear stability boundaries and their implications for confinement in advanced plasma regimes.

3.2. Kinetic Ballooning Modes

The study of kinetic ballooning modes (KBMs) has grown critical for understanding transport dynamics in high β plasmas particularly in core regions with low magnetic shear. While KBMs were initially studied in pedestal regions [129, 130, 131], recent research has increasingly focused on their role in core plasma of high β tokamaks plasmas, in particular at low magnetic shear [5, 132, 12, 133, 134].

ITG Stabilization

In the previous section, we rederived a simplified theoretical framework for analyzing ion-temperature-gradient (ITG)-driven modes [123, 124], which are commonly the dominant instabilities at low plasma β. However, as the plasma β increases, electromagnetic effects begin to stabilize ITG-driven turbulence [135, 136, 137, 138, 139]. In this context, the parameter β, defined as the ratio of the plasma pressure to the magnetic pressure, serves as a measure of the importance of electromagnetic effects. A linear stabilization occurs due to the coupling of ITG modes with shear Alfvén waves, which facilitates the transfer of energy away from the ITG mode [136]. In this regime, a strong nonlinear stabilization of ITG turbulence when increasing β is also observed [140, 141]. This strong nonlinear electromagnetic stabilization has been highlighted by including electromagnetic effect to electrostatic cases and comparing the results. Notably, the relative reduction in heat fluxes was significantly greater than the reduction in linear growth rates between these cases [95, 142]. This enhanced stabilization in the nonlinear regime is correlated with an increased drive of zonal flows, which act to suppress turbulent transport further [97]. Fast ions also play a critical role in the nonlinear stabilization of ITG turbulence [134]. The pressure gradients associated with fast ions contribute to electromagnetic effects that suppress ITG-driven turbulence, resonances with fast-ion drifts can have a direct impact on linear stability and fast ion driven modes can couple to and drive zonal flows affecting the non-linear saturation These effects are particularly pronounced in high-β regimes, where auxiliary heating methods, such as Ion Cyclotron Resonance Heating (ICRH) and Neutral Beam Injection (NBI), increase the fraction of fast ions in the plasma. However, in this thesis, we focus on the electromagnetic effects of β without considering the additional influence of fast ions. As β continues to rise and exceeds a critical threshold,

$\beta > \beta_{\text{crit}}$, the stabilizing effects of β are eventually counteracted by the destabilization of Kinetic Ballooning Modes (KBMs). These KBMs represent a key limiting factor for the maximum sustainable β in magnetic confinement devices and will be the focus of the next section.

Kinetic Ballooning Modes

Kinetic Ballooning Modes (KBMs) are critical electromagnetic instabilities that limit the maximum plasma β sustainable in a magnetic fusion device. These instabilities are driven by the interplay of steep plasma pressure gradients and regions of unfavorable magnetic curvature. When the pressure gradient surpasses a critical threshold, KBMs are destabilized, leading to significant turbulent transport.

The study of ballooning modes originated within the ideal magnetohydrodynamic (MHD) framework, where stability analyses were performed using the ballooning transform [143]. In this framework, ballooning modes become unstable when the plasma β exceeds a critical MHD threshold, $\beta_{\text{crit}}^{\text{MHD}}$, defined as [144]:

$$\beta_{\text{crit}}^{\text{MHD}} \approx \frac{0.6\hat{s}}{q^2\left(2R/L_n + R/L_{T_i} + R/L_{T_e}\right)}, \tag{3.51}$$

where $\hat{s}$ correspond to the magnetic shear. Subsequent inclusion of kinetic effects refined the understanding of these instabilities and established KBMs as electromagnetic microinstabilities [107, 145]. KBMs are influenced by kinetic phenomena, such as magnetic drift, finite Larmor radius effects, and the interaction between magnetic shear $\hat{s}$ and the plasma pressure gradient α. These effects can cause the KBM threshold, β_{crit}, to deviate significantly from the MHD prediction [146, 147].

The plasma pressure gradient is quantified by the parameter α, given by:

$$\alpha = q^2 \sum_s \beta_s \left(\frac{R}{L_{T_s}} + \frac{R}{L_{n_s}}\right), \tag{3.52}$$

where the summation is performed over all plasma species s and β_s is the species' β. As β increases, the pressure gradient steepens, driving α higher. KBMs are destabilized when the driving force from α in regions of unfavorable curvature exceeds the stabilizing influence of the magnetic field [145, 148].

Magnetic shear, $\hat{s}$, plays a crucial role in determining the stability of KBMs. Low magnetic shear configurations are particularly susceptible to KBM destabilization due to their reduced β_{crit} [149, 150]. These configurations are also characterized by extended mode structures along magnetic field lines. One proposed explanation for the stabilizing effect of higher magnetic shear is that it restricts the spatial extent of the modes along magnetic field lines, thereby reducing their ability to access free energy from gradients in regions of bad magnetic curvature away from the outboard midplane [151, 150]. KBMs share the same parity characteristics with ion-temperature-gradient (ITG) modes along magnetic field lines. Specifically, the electrostatic potential perturbation, $\delta\phi$, exhibits even parity, while the parallel vector potential perturbation,

$\delta A_\parallel$, has odd parity [152].

Importance of $\delta B_\parallel$

Recent research during the design phase of the Spherical Tokamak for Energy Production (STEP) [153] has emphasized the importance of parallel magnetic-field perturbations ($\delta B_\parallel$) in gyrokinetic simulations of high-β plasmas. The study found that $\delta B_\parallel$ is crucial for accurately modeling Kinetic Ballooning Modes. Neglecting these perturbations causes artificial stabilization of the modes and leads to underestimated transport predictions. The same study examined the MHD approximation, which neglects $\delta B_\parallel$ by adjusting magnetic drift terms to partially compensate for its effects. In TGLF, this approximation is implemented by setting `USE_MHD_RULE = True`, enforcing an approximation on curvature and ∇B drifts. TGLF's treatment of $\delta B_\parallel$ is constrained by the limited number of moments in the model, necessitating the use of the MHD approximation. The study analyzed two implementations of the MHD approximation and found that both underpredicted transport compared to simulations that fully included $\delta B_\parallel$. These results suggest that TGLF's MHD-based simplifications may be inadequate for high-β scenarios, such as those in STEP, where $\delta B_\parallel$ effects are critical. Despite these limitations, this thesis adopts the MHD approximation within TGLF (`USE_MHD_RULE = True`) due to practical constraints, excluding $\delta B_\parallel$ but including $\delta B_\perp$ effects which are resolved more reliably. Further research expanded on these findings with a detailed analysis of nonlinear electromagnetic turbulence and transport mechanisms in STEP's high-β core plasmas [126]. The results underscored the necessity of including $\delta B_\parallel$ for accurate transport modeling. Building on these findings, a quasi-linear model for high-β turbulent transport in STEP's operational conditions was developed using a database of nonlinear gyrokinetic simulations of STEP discharges [154]. The model was validated against local nonlinear gyrokinetic simulations, demonstrating quantitative agreement in turbulent heat transport across a wide parameter space. This validation enables its application within a transport solver for flux-driven simulations of STEP. This study underscores the potential of reduced transport models in modelling high-β plasmas. It aligns directly with the objectives of this thesis, which employs the quasilinear TGLF model to predict transport in high-β conditions.

JET Discharge #75225: A Benchmark Case for High-β KBM-Driven Transport Modeling

Hybrid scenarios, such as the JET discharge #75225, are notable for their improved confinement and flattened safety factor (q) profile, achieved through optimized current density evolution (see Section 1.1.4) [5]. The JET discharge #75225 is a hybrid H-mode plasma at high-β, characterized by low magnetic shear in the core plasma [2]. These features make it an ideal case for investigating high-β turbulence dominated

2. $\rho < 0.3$, where ρ represents the normalized toroidal flux coordinate

by Kinetic Ballooning Modes. Indeed, the inner core of this discharge was shown to exhibit unstable KBMs [5]. Building on these findings, Kumar et al. (2021) [12] conducted an in-depth analysis of KBM-driven transport in JET discharge #75225 using the gyrokinetic code GKW. Linear gyrokinetic simulations confirmed KBMs as the dominant instabilities in the inner core, while nonlinear simulations showed that KBMs significantly drive ion and electron heat flux. A key insight from that study is the limitation of quasi-linear models in accurately capturing magnetic flutter contributions to electron heat flux. This limitation was suggested to arise from low-k_θ microtearing modes (MTMs), which are stable in linear analyses but contribute significantly to electron transport in the nonlinear regime. To address this, the study proposed extending quasi-linear models to better account for magnetic flutter fluxes, thereby improving predictive accuracy in high-β conditions.

This thesis adopts the JET discharge #75225 as a reference case scenario to evaluate the performance of the quasi-linear TGLF model in high-β conditions dominated by KBMs. In Section 3.3.4, we compare linear predictions from TGLF and GKW to assess TGLF's ability to capture linear KBM dynamics. In Chapter 3, this benchmark is extended to a quasi-linear analysis, comparing TGLF flux predictions with nonlinear GKW simulations to evaluate the accuracy of the TGLF model in high-β regimes.

3.3. Comparison of TGLF linear response against gyrokinetic simulations (GKW)

This study aims to benchmark the TGLF reduced model against the higher-fidelity gyrokinetic GKW code to assess TGLF's accuracy in capturing KBMs within high-β regimes, particularly at low magnetic shear near the magnetic axis. By comparing these two models, this work evaluates the limitations and capabilities of TGLF in capturing KBMs, which are critical for accurate turbulent transport predictions in integrated modeling frameworks. Part of the results presented in this chapter have been reported in Ref [155].

In this section, we will compare the linear response of TGLF against GKW. Our initial focus is on the Waltz standard case [10], a reference scenario with plasma parameters detailed in Table 3.1. We choose to start with this case due to TGLF's demonstrated accuracy in modeling the ITG regime, including electromagnetic β scans [11]. Our approach involves beta scans to explore the ITG to KBM transition. These scans are executed for two different values of the magnetic shear, at $\hat{s} = 1.0$ to examine TGLF under standard conditions, and at $\hat{s} = 0.05$, anticipating low shear conditions met closer to the magnetic axis of a tokamak. Afterwards, our focus shifts to the JET hybrid H-mode discharge 75225 to evaluate the accuracy of TGLF linear response in the central region of high beta low magnetic shear plasmas where Kinetic Ballooning Modes are predicted to be unstable [5, 12].

To accurately benchmark TGLF against GKW, we must ensure that any differences in outputs reflect genuine discrepancies in model physics rather than normalization inconsistencies. Therefore, the benchmarking procedure involves a systematic use of

IMAS normalized data structures conversion routines (see Section 2.3). The overall benchmarking workflow is summarized in Figure 3.4

3.3.1. Practical Steps in Benchmarking

Our benchmarking workflow unfolds as follows:

1. **Initial GKW Simulation**: For each benchmark scenario, we begin by running a relevant GKW simulation. The output from this simulation, representing a specific plasma state, serves as our reference data.
2. **IDS GKW**: We then convert the GKW output into a structured IMAS gyrokinetic IDS object, encapsulating all relevant results in a standardized format. This IDS object stores the GKW data, maintaining consistent IMAS normalizations across all parameters.
3. **TGLF Input Generation**: Using the GKW-based IDS object, we apply the routines developed during this thesis to produce a corresponding TGLF input file. This step ensures that TGLF receives inputs directly comparable to those used by GKW.
4. **TGLF Simulation**: We run TGLF with the generated input file, allowing us to obtain outputs for the same plasma conditions that GKW simulated.
5. **IDS TGLF**: Finally, we convert TGLF's output into a new IDS object.

This enables a direct comparison between GKW and TGLF results by analyzing the two IDS objects side-by-side, as both are now consistently normalized. This workflow ensures that observed differences reflect model physics rather than differences in data normalization or format. To help quantifying the differences between TGLF and

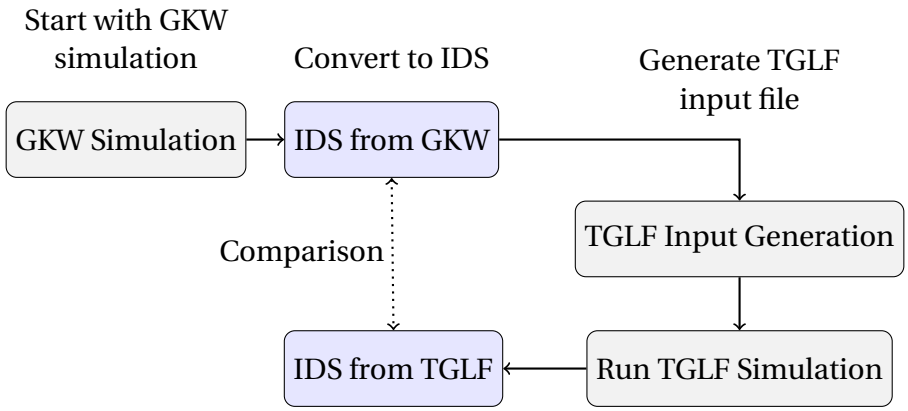


Figure 3.4. – Benchmarking workflow for comparing TGLF against GKW using IMAS IDS for standardized normalization.

GKW, we now introduce a set of metric coefficients. Each coefficient, denoted as $\alpha_{\mathbf{X}}$,

corresponds to a specific quantity $\mathbf{X}$, and is calculated as follows:

$$\alpha_{\mathbf{X}} = \frac{|\mathbf{X}^{GKW} - \mathbf{X}^{TGLF}|}{|\mathbf{X}^{GKW}|} \tag{3.53}$$

3.3.2. Codes setup

All linear GKW simulations used the following numerical grids: $N_s = 32$, $N_{pol} = 29$, $N_\mu = 16$, $N_{v_\parallel} = 64$, with N_s the number of parallel grid points per poloidal turns, N_{pol} the number of poloidal turns (or connected radial modes), N_μ the number of magnetic moment grid points and $N_{v_\parallel}$ the number of parallel velocity grid points. Both $B_\perp$ and $B_\parallel$ fluctuations are included. When present (sec 3.3.4), all inter-species collisions are included using a linearised Fokker-Planck collision operator with enforced momentum and energy conservation. Parallel flow shear and inertial effects due to toroidal rotation are included.

The following settings were used for all linear TGLF simulations performed in this study: `NBASIS_MIN` = 2, `NBASIS_MAX` = 6, `WIDTH` = 3, `FILTER` = 0, `USE_BPER` = True, `USE_BPAR` = False and `USE_MHD_RULE` = True.

The `NBASIS_MIN` and `NBASIS_MAX` parameters determine the minimum and maximum number of Hermite basis functions used to solve the wave functions. The default values are 2 and 4, respectively. We opted for `NBASIS_MAX` = 6 instead of 4 as it provides more accurate results without notably increasing the computational cost of the simulations. A detailed investigation of the impact of `NBASIS_MAX` is presented in section 3.3.3.1.

The `WIDTH` parameter specifies the maximum width of the Gaussian envelope used in the Hermite polynomial projection. In this study, we used a `WIDTH` value of 3 instead of the default 1.65 to better capture the extended wave functions observed at low magnetic shear (see section 3.3.3.2).

The `FILTER` input, when set to 0, prevents TGLF from filtering out high-frequency modes, including KBM modes. High-frequency spurious modes are sometimes observed in TGLF simulations. These modes are non-physical and need to be filtered out. To address this, the `FILTER` switch was implemented and is recommended by default, with a value of `FILTER` = 2. This setting filters out modes with a frequency higher than twice the drift wave frequency, therefore eliminating the spurious modes but also KBMs, which are crucial for our study. To retain KBMs, the `FILTER` is therefore set to 0. Later in this paper, a new refined filter will be introduced.

Additionally, all TGLF simulations include perpendicular magnetic field fluctuations ($B_\perp$) but exclude parallel magnetic field fluctuations ($B_\parallel$). Instead, the setting (`USE_MHD_RULE` = True) is used, which forces the ∇B and curvature drifts to be equal, exploiting a cancellation at the MHD level to approximate the effect of magnetic compression [156, 157]. Ideally, one would prefer to keep fluctuations of $B_\parallel$ and set `USE_MHD_RULE` = False., but this goes beyond TGLF electromagnetic solver capabilities.

3.3.3. Waltz Standard Case linear analysis

The input parameters for the Waltz standard case are listed in Table 3.1. Two species (deuterium and electrons) are included and treated kinetically. The magnetic equilibrium (circular flux surfaces) is specified using the Miller parametrisation in both codes. Collisions and rotation are set to zero.

Table 3.1. – IMAS normalized plasma parameters of the Waltz Standard case

q	$\hat{s}$	p'_N	r_N	R/L_n	$R/L_{Ti} = R/L_{Te}$	T_i/T_e
2	1	0	0.16	3	9	1.0

All parameters in this study adhere to the IMAS gyrokinetic normalizations [8] detailed in Chapter 1.

To evaluate TGLF's ability to capture the ITG to KBM transition, a scan in plasma β is performed. Figure 3.5 shows the variations in the growth rate (γ), frequency (ω_r), and quasi-linear weights as a function of β for the Waltz Standard case at $k_\theta \rho_s = 0.4$, with a fixed pressure gradient $\beta' = 0$, for two magnetic shear values, $\hat{s} = 1.0$ and $\hat{s} = 0.05$.

At low β, corresponding to the ITG regime, an increase in plasma pressure β exerts a stabilizing effect. This stabilizing trend persists until a critical threshold β^{crit} is reached. Beyond this point, KBMs become the dominant instability. Subsequently, KBMs are further destabilized by the increasing β. For $\hat{s} = 1.0$, there is a quantitative agreement between TGLF and GKW linear responses across both the ITG and KBM regions, with discrepancies observed at the transition between these regimes due to a slight differences in the threshold. For $\hat{s} = 0.05$, while the agreement remains good in the KBM region, notable differences emerge around the ITG-KBM transition. Around that transition ($\beta \approx 0.4\%$), reducing the magnetic shear extends the mode structure significantly and TGLF struggles to accurately capture it. To illustrate the eigenfunction differences, Figure 3.6 shows the real part of the normalized perturbed electrostatic potential ϕ_N for different values of $\hat{s}$ and β as a function of the poloidal angle θ.

As shown in Figure 3.6, the wavefunctions obtained with GKW become very extended at low shear values around the ITG-KBM threshold. Far from the threshold, deep in the KBM region ($\beta = 2.0\%$), this extension effect of the mode structure is barely noticeable.

The next two sections explore the effects of two key parameters on TGLF's ability to replicate extended mode structures: the number of Hermite basis functions and the width of the Gaussian envelope used in their projection.

3.3.3.1. Impact of the number of Hermite basis functions in TGLF

To enable TGLF to replicate extended mode structures, we increased the number of Hermite basis functions by adjusting the `NBASIS_MAX` input parameter, while keeping all other settings consistent with those described in Section 3.3.2. Figure 3.7 illustrates the real part of the perturbed electrostatic potential ϕ_N as a function of the parallel

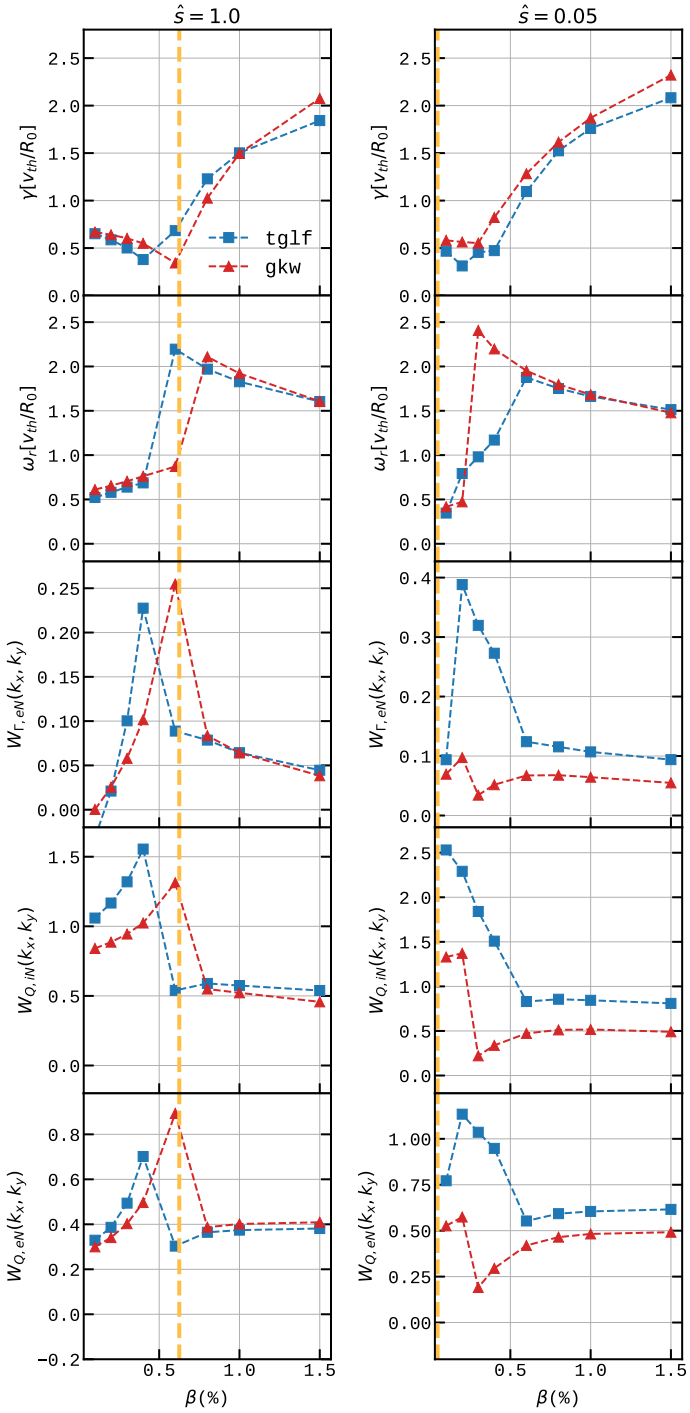


Figure 3.5. – Growth rate (γ), frequency (ω_r), and linear mode weights variations for the Waltz Standard case as a function of plasma β, for the Waltz Standard case at $k_\theta \rho_s = 0.4$, at a fixed pressure gradient $\beta' = 0$, for two different values of the magnetic shear, $\hat{s} = 1.0, 0.05$.

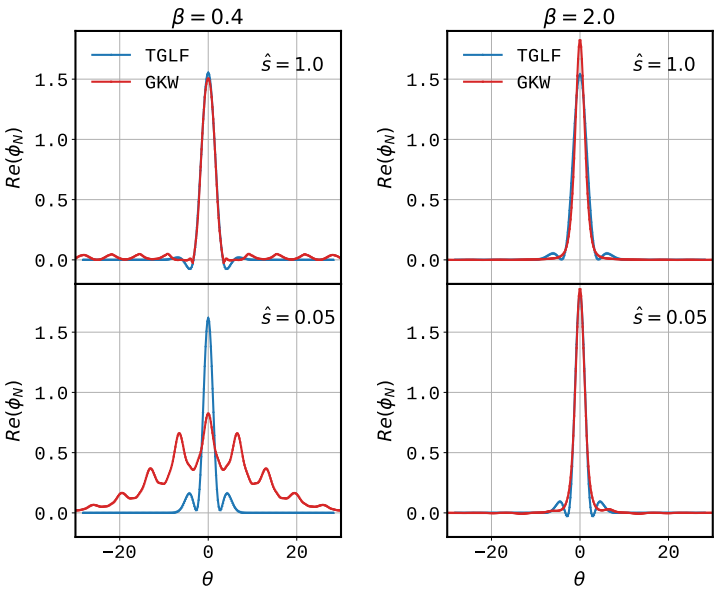


Figure 3.6. – Real part of the normalized perturbed electrostatic potential ϕ_N for different values of $\hat{s}$ and β as a function of the poloidal angle θ.

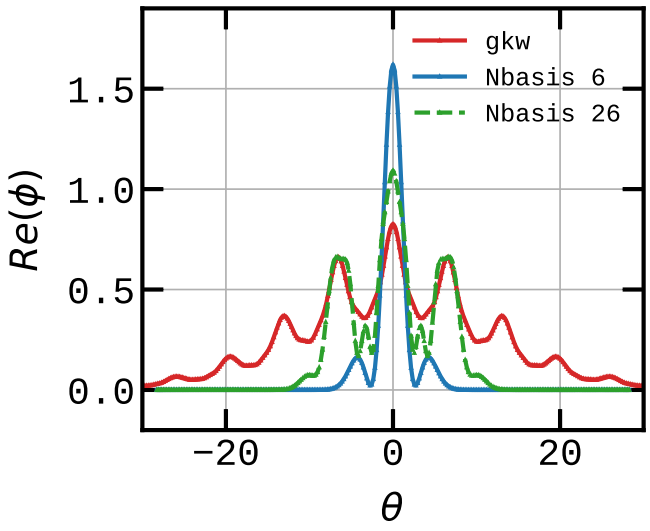


Figure 3.7. – Comparison of the real part of the perturbed electrostatic potential ϕ_N as a function of the parallel direction θ, obtained from GKW and TGLF for NBASIS_MAX values of 6 and 26 in the Waltz STD case at $k_\theta \rho_s = 0.4$, $\beta = 0.4\%$, and $\hat{s} = 0.05$.

direction θ, obtained from GKW and TGLF for NBASIS_MAX values of 6 and 26 in the Waltz STD case at $k_\theta \rho_s = 0.4$, $\beta = 0.4\%$, and $\hat{s} = 0.05$. For TGLF, these simulations involved setting the WIDTH parameter to 3 (default is 1.65). The figure shows that increasing NBASIS_MAX influences the shape of the wave function, making it more

extended and closer to the result obtained with GKW. However, it is important to note that the computational time of TGLF increases exponentially with the value of NBASIS_MAX. Figure 3.8 shows the relative errors in the linear response parameters

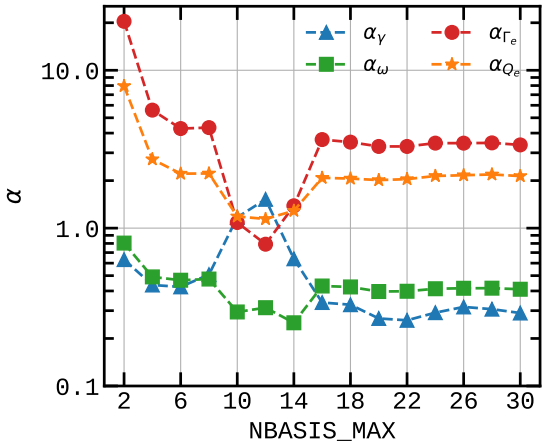


Figure 3.8. – Relative errors in the linear response parameters ($\alpha_{\gamma,\omega,\Gamma,Q}$) between TGLF and GKW as a function of NBASIS_MAX for the Waltz STD case at $k_\theta \rho_s = 0.4$, $\beta = 0.4\%$, and $\hat{s} = 0.05$.

($\alpha_{\gamma,\omega,\Gamma,Q}$ as defined in section 3.3.1) between TGLF and GKW as a function of NBASIS_MAX for the Waltz STD case. Initially, increasing the number of Hermite basis functions up to NBASIS_MAX = 6 improves the linear response. However, further increasing this value does not lead to a significant reduction in the relative errors.

Figure 3.9 presents the relative errors in the linear response parameters between TGLF and GKW for the JET #75225 discharge. This specific case will be the focus of the next section of this linear analysis, where it will be examined in greater detail. This figure serves to anticipate the upcoming analysis by providing an initial comparison of the impact of the number of Hermite basis functions for this discharge. Similar to the Waltz STD case, there is a general trend of improvement with increasing NBASIS_MAX, but the errors do not consistently decrease. This indicates that while increasing the number of Hermite basis functions can improve the representation of the wave function, it is not sufficient on its own to achieve accurate linear response predictions. For our case, this indicates that better replicating the wave function structures is insufficient to address the discrepancies observed at low shear values around the ITG-KBM transition.

3.3.3.2. Effect of the gaussian envelope width in TGLF

The WIDTH parameter in TGLF determines the maximum width of the Gaussian envelope used in the Hermite polynomial projection of wave functions (see Section 2.1.3). Increasing this parameter allows TGLF to capture more extended wave functions. At low magnetic shear, mode structures can become significantly extended and the default WIDTH value of 1.65 may not be sufficient to capture these extended wave

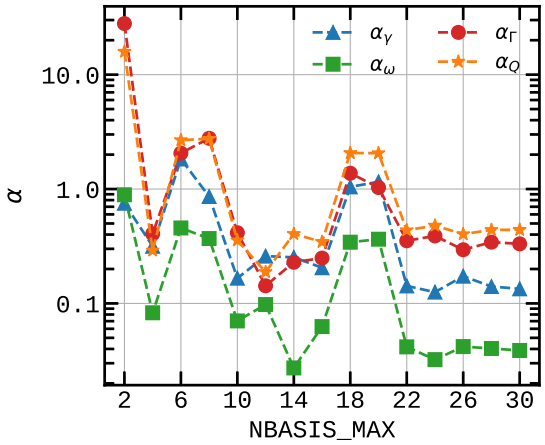


Figure 3.9. – Relative errors in the linear response parameters ($\alpha_{\gamma,\omega,\Gamma,Q}$) between TGLF and GKW for the JET 75225 discharge as a function of `NBASIS_MAX`, at $\rho = 0.15$, $\beta = 3.2\%$, and $\hat{s} = 0.05$.

functions. During our study, we observed that for the reference Waltz standard case, increasing the `WIDTH` value improved the linear response, though the difference was not substantial for most simulations since the wave functions were not particularly extended in the parallel direction. The default value of 1.65 is robust and allows to cover a broad spectrum of simulations. However, for the JET 75225 discharge at $\rho = 0.15$, increasing the `WIDTH` value proved crucial for effectively capturing the more extended and complex wave functions. Figure 3.10 shows the linear growth rate and frequency as a function of β for the JET 75225 discharge at $\rho = 0.15$, comparing GKW and TGLF with `WIDTH` values of 1.65 and 3.0 and `FILTER=-1.5`. The other settings are the same as in Fig. 3.19. The linear response with the default `WIDTH` value of 1.65 is inaccurate, while the `WIDTH` value of 3.0 provides a much better response. Additionally, Figure 3.11 shows the real part of the normalized perturbed electric potential for `WIDTH` values of 1.65 and 3.0 at $\beta = 4.2\%$. This figure illustrates that with a `WIDTH` of 3.0, TGLF better captures the extended wave functions.

3.3.3.3. Effect of β' Stabilization

In figure 3.5 we observe that the ITG-KBM threshold β^{crit} increases with the magnetic shear $\hat{s}$, as expected from the MHD ballooning limit [95]:

$$\beta^{crit}_{MHD} \approx 0.6\hat{s}/\left(q_0^2(2R/L_n + R/L_{T_i} + R/L_{T_e})\right) \tag{3.54}$$

This β^{crit}_{MHD} value is represented as the yellow line in Figures 3.5 and 3.14. In Figure 3.5 we varied the plasma pressure β while maintaining a fixed pressure gradient $\beta' = 0$. Previous studies [158, 159] indicate that β' exerts a stabilizing influence on KBMs and, of course, in a tokamak β and β' are strongly coupled. Here, we will verify that TGLF captures the stabilizing influence of the radial pressure gradient β' on Kinetic

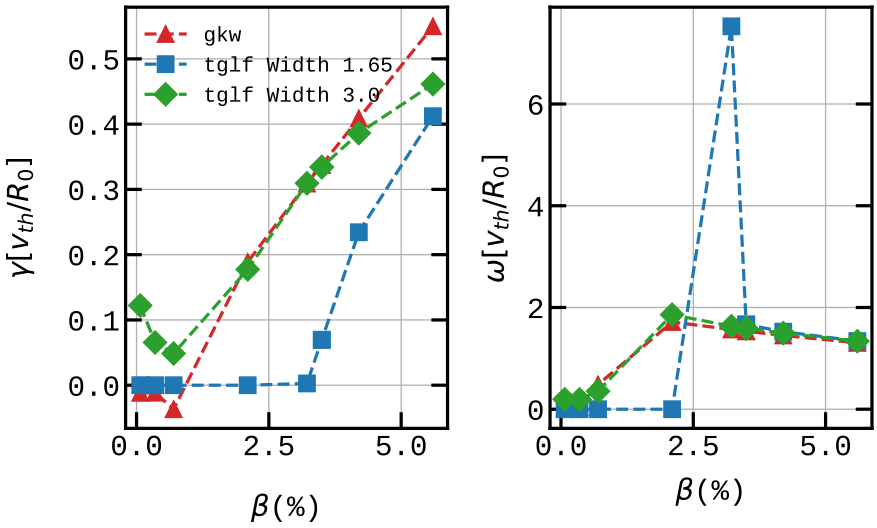


Figure 3.10. – Linear growth rate and frequency as a function of β for the JET 75225 discharge at $\rho = 0.15$. Comparison between GKW and TGLF with `WIDTH` values of 1.65 and 3.0 and `FILTER=-1.5`.

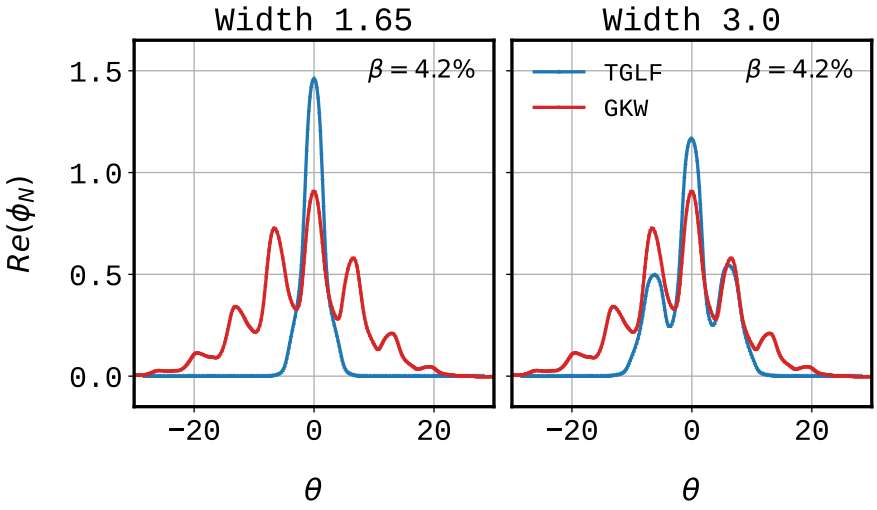
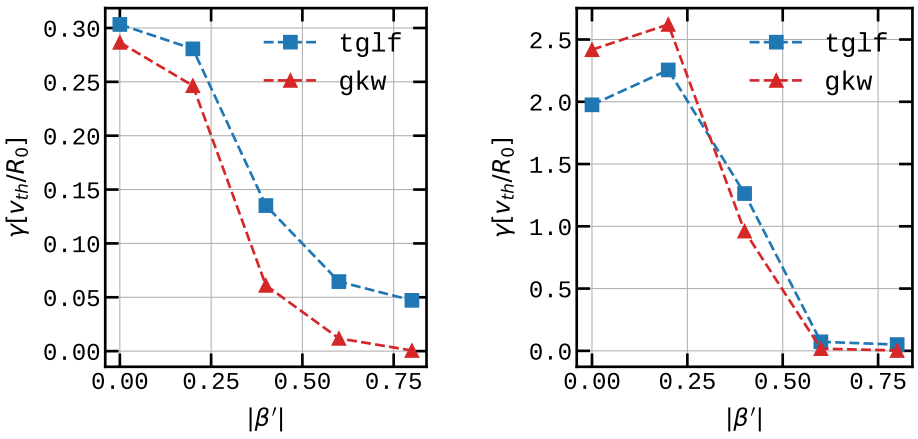


Figure 3.11. – Parallel mode structure of the real part of the normalized electric potential ϕ for the Jet 75225 simulation at $\rho = 0.15$, for $\beta = 4.2\%$ with `WIDTH` values of 1.65 and 3.0

Ballooning Modes [158, 159].

Figure 3.12 shows β' scans using the Waltz Standard case parameters (Table 3.1) at $k_\theta \rho_s = 0.15$ and $\hat{s} = 1.0$. Scenarios at $\beta = 0.1\%$ (a) and $\beta = 1.5\%$ (b) represent the ITG and KBM regimes, respectively, at $\beta' = 0$.

The results show that increasing $|\beta'|$ exerts a pronounced stabilizing effect on both ITG and KBM modes. When β' is varid proportionally to β, (Figure 3.13), the KBM destabilisation due to the β increase is compensated by the β' stabilisation when



(a) ITG Regime **(b) KBM Regime**

Figure 3.12. – Effect of β' on growth rates for (a) ITG regime at $\beta = 0.1\%$ and (b) KBM regime at $\beta = 1.5\%$, for the Waltz Standard case with $k_\theta \rho_s = 0.15$ and $\hat{s} = 1.0$.

β exceeds 1%. This occurs because $|\beta'|$ exerts a strong stabilizing effect, offsetting the destabilizing impact of higher β values and ultimately stabilizing KBMs. TGLF accurately captures this behaviour and yields results close to that of GKW.

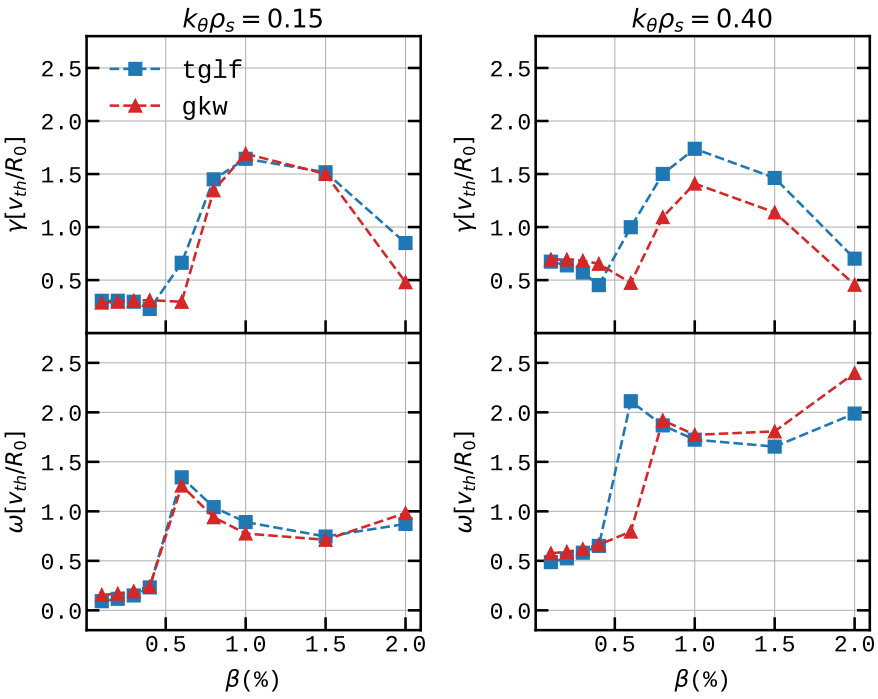


Figure 3.13. – Growth rates and frequencies as a function of β for the Waltz Standard case with β' proportional to β, at $\hat{s} = 1.0$.

3.3.3.4. Metric-Based Evaluation on Waltz STD case

Figure 3.14 uses the metric introduced in Section 3.3.1 to show the relative differences between TGLF and GKW for the growth rate (α_γ), frequency (α_ω), and quasi-linear weights (α_{Γ_e}, α_{Q_i}, α_{Q_e}) in a magnetic shear and plasma beta scan centered around the Waltz standard case. The MHD ballooning limit is indicated by a yellow curve in each subplot.

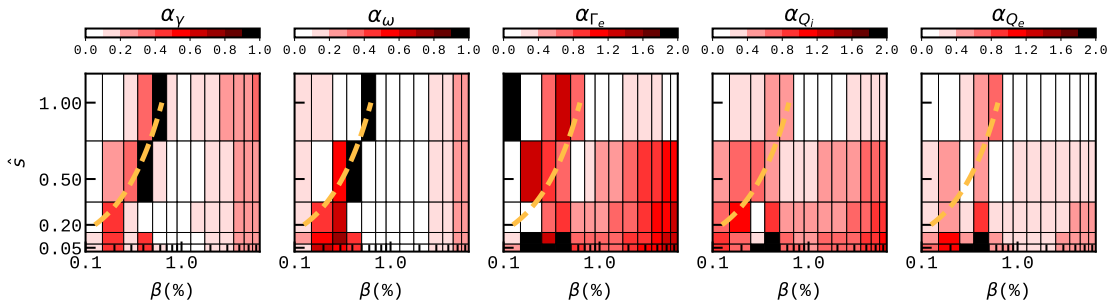


Figure 3.14. – Relative differences between TGLF and GKW for the growth rate (α_γ), frequency (α_ω), and linear mode weights (α_{Γ_e}, α_{Q_i}, α_{Q_e}) in the Waltz Standard case at $k_\theta \rho_s = 0.4$.

Overall, differences below 10% for γ and ω, and below 40% for $W_{\Gamma,sN}(k_x, k_y)$ and $W_{Q,sN}(k_x, k_y)$ are achieved in the KBM region. However, two specific areas exhibit deviations: at very low magnetic shear $\hat{s}$ and around the ITG-KBM transition. These discrepancies arise due to differences in the KBM threshold and the limitations of TGLF at very low shear values.

In conclusion, TGLF effectively models the linear response for KBMs in the Waltz standard case, but challenges remain at very low magnetic shear and close to the ITG-KBM transition where discrepancies persist despite adjustments of TGLF code settings.

3.3.4. Jet hybrid H-mode #75225

After evaluating TGLF's capability to model KBMs in an idealized scenario represented by the Waltz standard case, this section extends the benchmark by comparing results from TGLF and GKW for the JET hybrid H-mode discharge #75225. This hybrid H-mode discharge, performed when the tokamak JET featured carbon walls, underwent a detailed analysis in a previous study [12]. The discharge is characterized by high-quality core profile measurements for electrons and main ions, the absence of sawteeth, and no other significant core MHD activity within the selected time interval, $t = 6.0 - 6.5$ seconds. The simulation input parameters were derived from a Gaussian process regression of experimental measurements. In this section, our investigation centers on modeling this discharge at the two radial positions $\rho = 0.15$ and $\rho = 0.33$, where ρ represents the normalized toroidal flux coordinate. The relevant local plasma input parameters in the IMAS gyrokinetics normalisation [8] are detailed in Table 3.2.

The simulations encompass three species: deuterium ions, electrons and carbon. The linear GKW simulations in this section use section 3.3.2 settings with N_{pol} = 49. This increase from 29 to 49 poloidal turns is necessary for the JET case due to the presence of more extended wavefunctions. TGLF simulations follow the same settings as in section 3.3.2. By default, TGLF sets the `FILTER` parameter to 2, which

Table 3.2. – IMAS normalized plasma parameters of the JET 75225 discharge

ρ	R/L_{Ti}	R/L_{Te}	R/L_{Tc}	R/L_{ni}	R/L_{ne}	R/L_{nc}
0.15	4.2	2	4.2	1.67	1.5	-0.7
0.33	7.6	4.03	7.6	3.08	2.7	-1.49
ρ	T_i/T_e	T_c/T_e	n_i/n_e	n_c/n_e	β(%)	u
0.15	1.43	1.43	0.93	0.01	3.2	0.38
0.33	1.19	1.19	0.92	0.01	2.5	0.34
ρ	u'	ν	q	r_N	p'_N	$\hat{s}$
0.15	0.59	0.015	1.1	0.05	0.37	0.05
0.33	1.31	0.020	1.12	0.12	0.42	0.2

ρ	κ	$R_0\frac{\partial\kappa}{\partial r}$	$\frac{\partial R_c}{\partial r}$	$\frac{\partial Z_c}{\partial r}$	c_n	s_n	$R_0\frac{\partial c_n}{\partial r}$	$R_0\frac{\partial s_n}{\partial r}$
0.15	1.35	-0.13	-0.08	-0.005	[0,0]	[0,0.02]	[0,0]	[0,0.19]
0.33	1.30	-0.002	-0.13	-0.01	[0,0]	[0,0.036]	[0,0]	[0,0.26]

automatically removes any modes with frequencies exceeding twice the drift wave frequency. While this effectively eliminates spurious non-physical modes, it also excludes genuine high-frequency modes such as KBMs. This feature was therefore disabled until now by setting `FILTER` = 0. However, this significantly increases the risk of incorrect spurious modes slipping through, resulting in excessively high and erroneous quasi-linear flux predictions. To address this issue, we developed a new filter that removes high-frequency modes unless they have an even structure in the real part of the electrostatic potential. This adjustment effectively filters out spurious modes (which tend to have odd parity eigenfunctions) while preserving Kinetic Ballooning Modes. This new option is activated by setting the `Filter` parameter to a negative value. In this section, we used `Filter` = -1.5 for the `New Filter` configuration.

Figure 3.15 displays the growth rate and frequency as a functioin of the binormal wavevector $k_\theta \rho_s$ for the JET #75225 discharge at ρ = 0.15. Three TGLF settings are employed in this figure:

— `Default` : Uses the parameter values outlined in section 3.3.2 with `Filter` set to 0 (i.e., keeps all modes)

— `High Nbasis`: Employs the same parameter values as in section 3.3.2, but with 16 Hermite basis functions (see Section 2.1.3).

— `New Filter`: Uses the values from section 3.3.2 but employs the new filtering

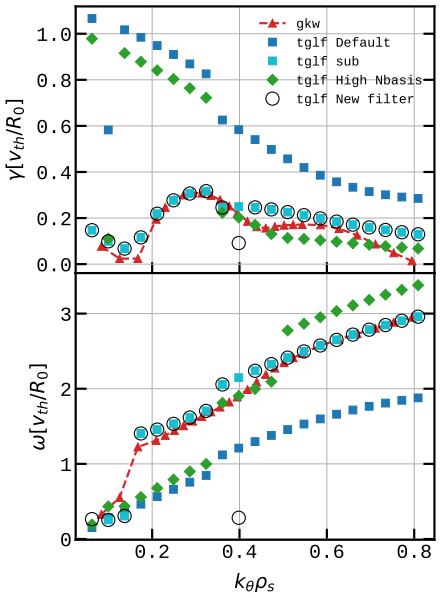


Figure 3.15. – Spectra of linear growth rates and real frequencies as a function of the binormal wavevector $k_\theta\rho_s$ for the JET 75225 discharge at $\rho = 0.15$. The spectra are shown for TGLF configurations with the default filter, high `Nbasis`, and the new filter settings.

method (`Filter` set to -1.5).

In the `High Nbasis` configuration with 16 Hermite basis functions, the computational time increased exponentially (scaling as 2 to the power of this number), making simulations slow and unsuitable for integrated modeling. In contrast, the `New Filter`, retains the original number of basis functions, preserving computational efficiency. This improvement is crucial for enhancing modeling within integrated frameworks without compromising simulation speed.

Figure 3.15 shows that using TGLF with the default values leads to inaccurate linear results. The growth rates obtained with these default settings are excessively high compared to the GKW reference values. Additionally, even with the computationally expensive High Nbasis configuration, these incorrect high growth rate modes persist at low binormal wavevectors ($k_\theta\rho_s < 0.4$). However, the subdominant modes obtained from TGLF with Default settings are close to GKW reference points. This motivated the development of the improved filtering to eliminate the spurious modes.

3.3.4.1. New Filter in TGLF

The newly implemented filter in TGLF addresses the challenge of distinguishing between kinetic ballooning modes and spurious modes. The primary goal is to accurately capture the KBMs while effectively filtering out spurious modes. This section details the methodology and effectiveness of the new filter.

Methodology

The initial filtering methodology in TGLF involves filtering out any mode with a frequency ω_r that exceeds a specified multiple of the drift wave frequency ω_{DW}. This multiple correspond to the value provided in the TGLF input parameter `Filter` and by default its value is set to 2. This approach removes spurious high-frequency modes but also excludes KBMs, which are characterized by high frequencies.

The observation that TGLF spurious high-frequency modes tend to have an odd parity along the field line whereas KBMs have even parity motivated the development of a new filtering mechanism. The steps involved are:

— Frequency Check:
  The filter compares the real part of the mode frequency ω_r with the drift wave frequency ω_{DW}. If $|\omega_r|$ exceeds a specified multiple of $|\omega_{DW}|$, additional checks are performed. Note that this multiple correspond to the value provided in the TGLF input parameter `Filter`.

— Parity Check:
  For high-frequency modes that goes though the frequency check, the real part of the electrostatic potential $\mathrm{Re}(\phi)$ is examined for parity. Modes with high frequencies that are even and propagates in the ion diamagnetic drift direction are identified as KBMs and are not filtered out. All other modes that do not meet these conditions are recognized as spurious and are filtered out.

The mode structure in TGLF are projected on a basis of Hermite functions (see Section 2.1.3). To determine the parity of the mode, we use the properties of the basis Hermite functions, where odd-indexed Hermite polynomials correspond to even functions of the parallel direction θ, and even-indexed Hermite polynomials correspond to odd functions. We construct a function with the same parity as the electrostatic potential ϕ and evaluate its parity by calculating the ratio of the absolute value of its sum to the sum of its absolute values. Modes with a ratio higher than 0.9 are classified as even.

Test on the robustness of the even parity evaluation

To test the robustness of the new filtering technique, we increased the parallel velocity shear to alter the parity of the KBM mode structure. The parity check for the filter was found to remain effective except in rare cases where the mode structure was extremely uneven. In these instances, the ratio between the absolute value of the sum and the sum of the absolute values is around 0.5, making it difficult to adjust the filter threshold reliably. Out of 441 test cases varying $k_\theta \rho_s$ and the parallel velocity shear, 5 cases exhibited this parity check issue and were not recognized as KBMs, resulting in their exclusion.

Test on case with spurious modes and KBMs

Figure 3.16 shows the growth rate and the frequency as a function of ky for the JET #75225 discharge, comparing GKW with TGLF using different `Filter` settings

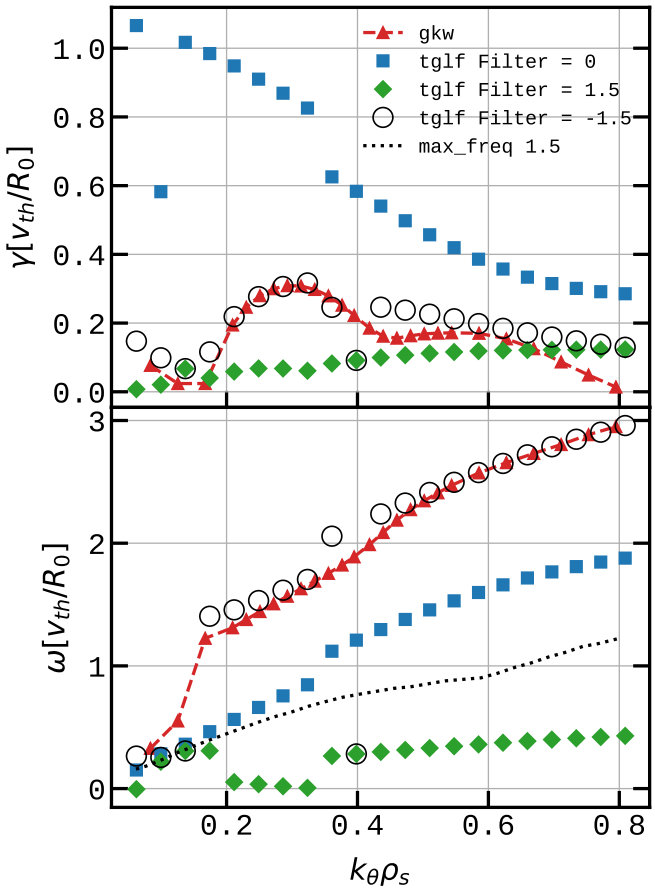


Figure 3.16. – Growth rate and frequency as a function of $k_\theta \rho_s$ for the JET 75225 discharge. Comparison of GKW with TGLF `Filter` = 0, 1.5 and -1.5.

(0, 1.5, and -1.5). With TGLF `Filter` = 0, all modes found by TGLF are displayed, including spurious modes. These spurious modes exhibit high frequencies and are not filtered out because the filter is disabled. When using TGLF `Filter` = 1.5, these modes are filtered out as their frequencies exceed 1.5 times the drift wave frequency (represented by the black dotted line labeled 'max_freq 1.5'). Using TGLF `Filter` = -1.5, the spurious modes are filtered out because they have high frequencies and exhibit an odd mode structure. KBMs, which have an even mode structure, are retained even if their frequencies are higher than 1.5 times the drift wave frequency. This filtering mechanism ensures that spurious modes are excluded while KBMs are accurately captured, improving the reliability of the simulations.

Figure 3.17 shows a decision tree that outlines the steps taken by the new filter to determine whether a mode should be kept or removed.

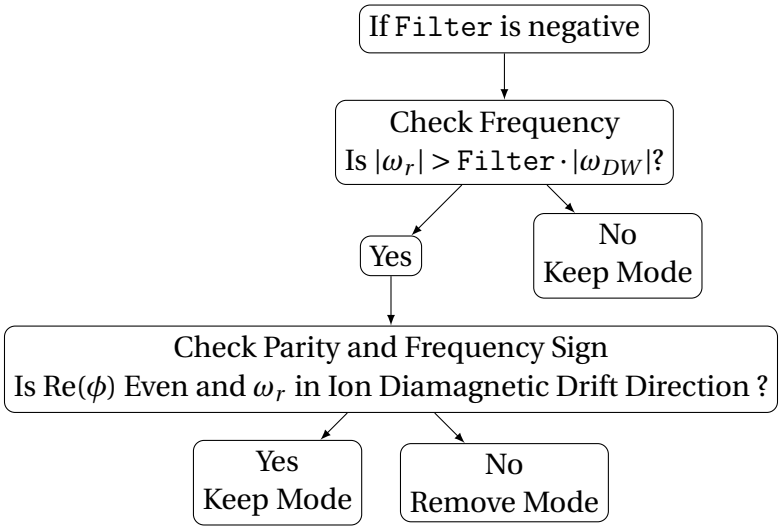


Figure 3.17. – Decision Tree for New Filter

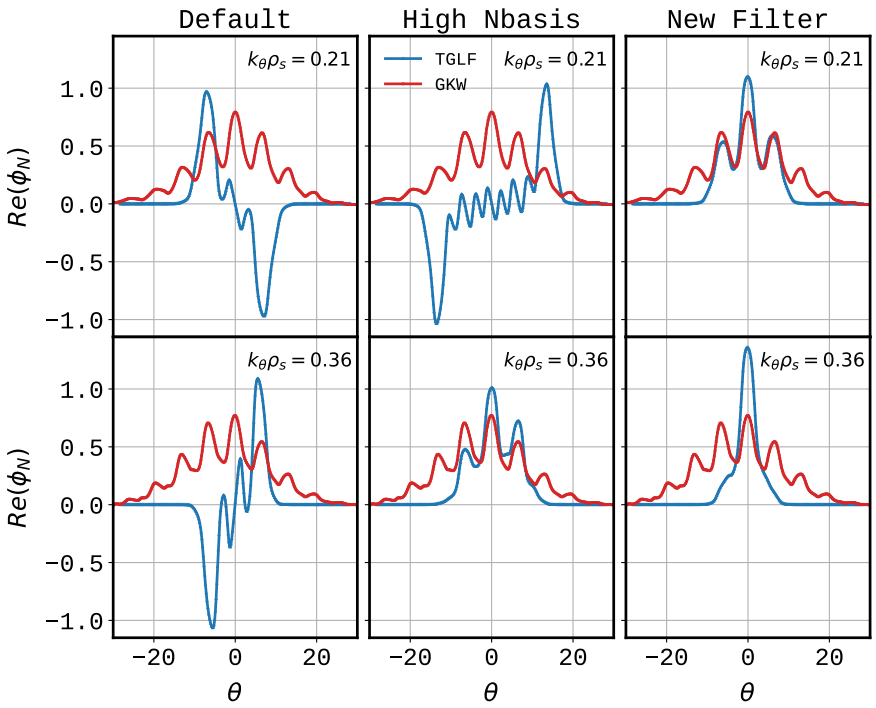


Figure 3.18. – Parallel mode structure of the real part of the normalized electric potential ϕ_N for the JET 75225 simulation at $\rho = 0.15$ for different values of $k_\theta \rho_s$ and TGLF settings.

3.3.4.2. TGLF linear response with the new filter for the Jet hybrid H-mode #75225

As represented in Figure 3.15, the New Filter configuration shows a generally good agreement between TGLF and GKW across all binormal wavevectors, successfully capturing Kinetic Ballooning Modes without including spurious modes. Figure 3.18 illustrates the parallel mode structure of the real part of the normalized electric potential ϕ_N for the JET #75225 simulation at $\rho = 0.15$ for two different values of $k_\theta \rho_s$ (0.21 and 0.36) using the three TGLF settings: Default, High Nbasis, and New Filter. At both $k_\theta \rho_s$ values, the Default setting produces an odd wavefunction indicative of spurious modes. In contrast, the New Filter settings yield an even-shaped wavefunction, corresponding to a valid KBM mode with accurate growth rates and frequencies. For the High Nbasis configuration, increasing the number of Hermite basis functions does not improve the results at $k_\theta \rho_s = 0.21$, but it does provide better results at $k_\theta \rho_s = 0.36$.

The linear response of TGLF and GKW is then compared in a beta scans for the JET #75225 discharge at two distinct radial positions, $\rho = 0.15$ and $\rho = 0.33$. The results are shown in Figure 3.19. At $\rho = 0.33$, TGLF shows strong agreement with GKW across both the ITG and KBM branches. Although TGLF predicts higher values for the linear mode weights compared to GKW, the overall agreement remains robust. At $\rho = 0.15$, significant discrepancies emerge between TGLF with `Default` settings and GKW. TGLF overestimates the linear growth rate, fails to align with the frequency predicted by GKW, and shows considerable deviations in the linear mode weights. These inaccuracies are not due to difficulties in replicating extended wavefunctions in the very low shear regime but stem from the spurious modes previously discussed. The implementation of the New Filter yields a linear response that more closely matches the reference values provided by GKW. This indicates that TGLF can effectively model KBMs even under conditions of very low magnetic shear, provided that spurious modes are effectively filtered out while retaining KBMs.

To investigate the potential mechanism behind the appearance of spurious modes in TGLF simulations, we compared plasma parameters corresponding to the JET case #75225 at the two radial positions $\rho = 0.15$ and $\rho = 0.33$. Initially, we hypothesized that the lower magnetic shear at $\rho = 0.15$ might be the cause of the spurious modes. However, the results demonstrated no significant correlation between magnetic shear variations and the presence of spurious modes. Further investigation revealed a strong correlation between the appearance of spurious modes and the inverse aspect ratio ϵ, with spurious modes more prevalent at low inverse aspect ratio ϵ.

Conclusion

In summary, TGLF's linear response for Kinetic Ballooning Modes (KBMs), using the Waltz standard case and the JET #75225 discharge, is close to the GKW reference, provided spurious modes are filtered out using the newly developed method. In the next chapter, we will compare the quasi-linear flux predictions from TGLF with those obtained from nonlinear simulations conducted using the gyrokinetic code GKW.

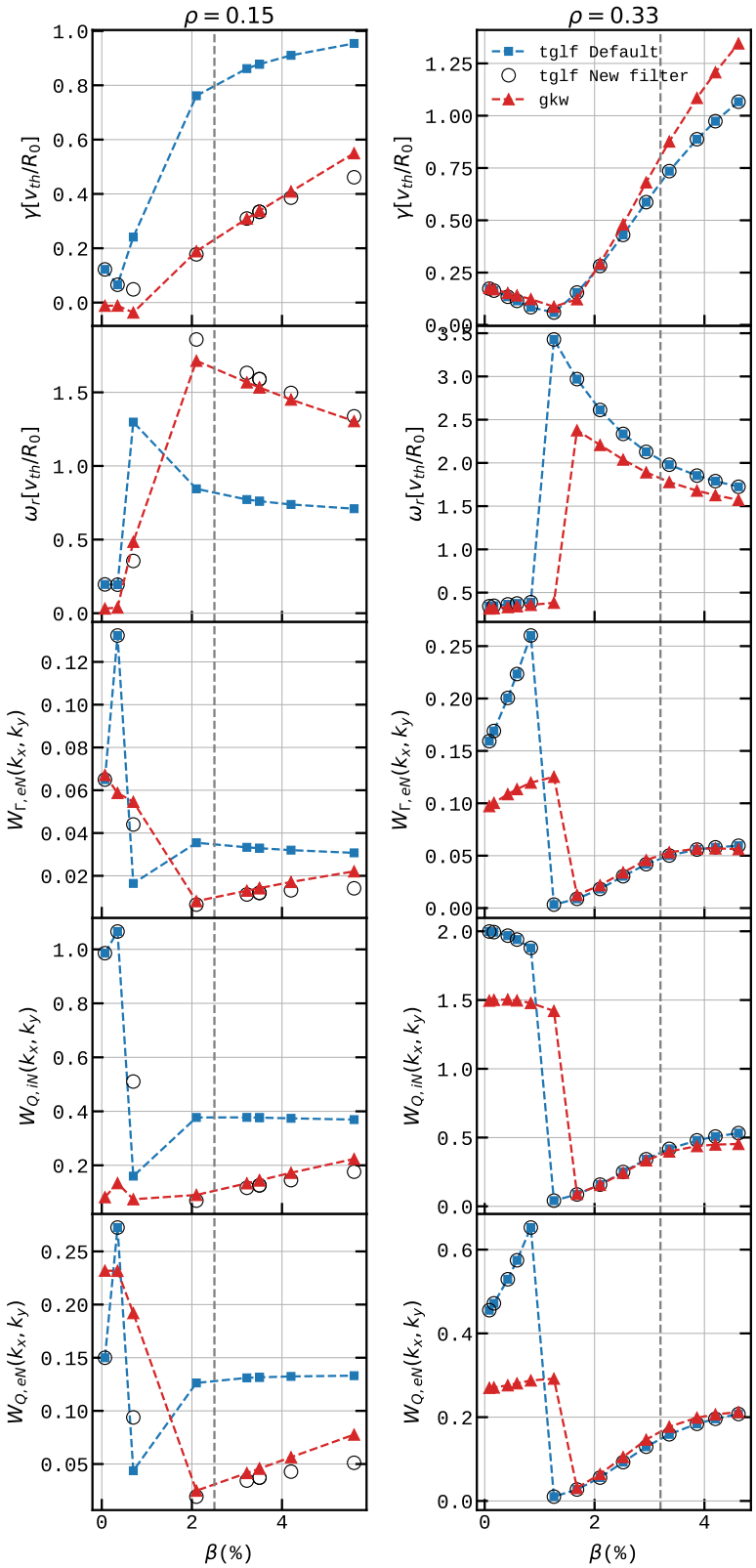


Figure 3.19. – Growth rate (γ), frequency (ω_r), and linear mode weights variations for Jet #75225 case as a function of plasma β, at two different radial positions, $\rho = 0.15$ ($k_\theta \rho_s = 0.29$) and $\rho = 0.33$ ($k_\theta \rho_s = 0.32$).

4. Comparison of TGLF Quasi-linear Fluxes Against Gyrokinetic Nonlinear Simulations for KBM turbulence

Observations from high-performance plasma studies in DIII-D, suggest that KBMs are key in the regulation of internal transport barriers [160]. Furthermore, KBMs have been predicted to be unstable in the core of JET hybrid H-mode discharges, which are relevant to ITER's high β plasmas [5, 12]. The study of KBMs is crucial for understanding transport in these critical regions and for the development of predictive models for future fusion devices [161, 162, 138]. Beyond experimental observations, high-fidelity gyrokinetic simulations have been instrumental to provide insights into the nonlinear evolution of KBMs, emphasizing the critical roles of zonal flows and nonlinear mode coupling in regulating KBM turbulence [163, 164]. A notable study analysed turbulent transport and zonal flow dynamics in mixed KBM and ion temperature gradient (ITG) mode-dominated turbulence using gyrokinetic simulations based on experimental observations from the HL-2A tokamak [165]. That study suggests that KBMs and ITGs are the main contributors to turbulent transport in these scenarios. Nonlinear simulations indicated that at higher β values, the transition from ITG to KBM-dominated turbulence increases transport despite stronger zonal flows. In the stellarator Wendelstein 7-X, a recent study have highlighted the role of subdominant KBMs in enhancing turbulent transport at high β values [166]. These modes which become unstable well below the ideal MHD ballooning threshold, are strongly excited in ITG-dominated turbulence. Their nonlinear interactions contribute to zonal-flow erosion, resulting in an increase in turbulent transport. This phenomenon underscores the intricate interplay between KBMs and ITG modes in driving heat flux increases, even in regimes where KBMs remain subdominant.

While non-linear gyrokinetic simulations are useful to capture and analyse the complex dynamics of KBM turbulence, as explained in the previous chapters they are extremely expensive and cannot be used in integrated modelling frameworks. This has motivated efforts to validate reduced quasi-linear models, such as TGLF [1, 2] which offer significant computational efficiency, operating in approximately 10 CPU-seconds per simulation, thus making them viable for use in integrated modeling frameworks. Recent research has benchmarked quasi-linear models like QuaLiKiz [167] and TGLF against high-fidelity gyrokinetic simulations for a high β JET hybrid discharge [132]. It demonstrated that while both models can reproduce certain linear and nonlinear

characteristics of the turbulence, significant differences remain, especially regarding the isotope effect and the influence of electromagnetic stabilization. This study was performed around mid-radius, in a region close to but before the KBM threshold.

In this chapter, we compare the quasi-linear fluxes predicted by TGLF with those obtained from nonlinear GKW simulations, presenting results in IMAS-standardized normalizations. The JET hybrid H-mode discharge #75225 at the radial position $\rho = 0.15$ serves as the reference case for this benchmark The quasi-linear weights of that case have been verified in the previous chapter, allowing us to now focus on the quasi-linear saturation model. The ultimate goal is to quantify the accuracy and limitations of TGLF's quasi-linear flux predictions in high β regimes, particularly for integrated modeling applications that necessitate both efficiency and precision in turbulence simulations. This analysis is structured as follows: we begin by detailing the setup for both GKW and TGLF simulations. Next, we examine the time evolution and steady-state fluxes from the GKW nonlinear simulations, using these as the benchmark for TGLF's quasi-linear predictions. Finally, we explore TGLF's ability to reproduce GKW results across various parameter scans, showing the impact of specific TGLF configuration parameters (e.g., `WIDTH` and `KYGRID_MODEL`) on flux predictions. This rigorous benchmarking highlights TGLF's strengths and limitations in modeling KBM-driven transport, providing insights into potential areas for model refinement and enhanced applicability in high β integrated modeling frameworks.

4.1. Codes Setup

The plasma parameters for this study, already detailed in Section 3.3.4, are based on the JET hybrid H-mode discharge #75225.

Non-linear GKW Setup Parameters

All nonlinear GKW simulations are conducted with the following grid parameters: $N_y = 16$ binormal modes, $N_x = 261$ radial modes, $N_s = 32$ parallel grid points, $N_\mu = 16$ magnetic moments and $N_{v_\parallel} = 48$ parallel velocity grid points. The $k_r\rho_s$ and $k_\theta\rho_s$ grids are defined by $|k_r\rho_s|_{\min} = 0.044$, $|k_r\rho_s|_{\max} = 5.73$, $k_\theta\rho_s|_{\min} = 0.08$, and $k_\theta\rho_s|_{\max} = 1.25$. The time step size is set to `DTIM` = 0.00015 in normalized GKW units. Numerical dissipation is applied with the following coefficients: `disp_par = 0.9` for parallel derivatives, `disp_x = 3.0` for the radial direction, and `disp_y = 0.1` for the binormal direction. The physics settings are the same as for the linear simulations but the simulations now include four species: deuterium, electrons, carbon and fast ions, whereas the linear simulations focused on three species (deuterium, electrons and carbon). The relevant local plasma input parameters in the IMAS gyrokinetics normalisation [8] are detailed in Table 3.2.

Quasi-linear TGLF Setup Parameters

The TGLF simulations are set-up based on the results from the linear analysis, with FILTER = −1.5 and WIDTH = 3 to better capture KBMs. The quasi-linear saturation model is SAT_RULE = 2. The KYGRID_MODEL parameter is set to 1, which adapts the wavenumber grid so that the minimum $k_\theta \rho_s$ is 0.1 . This is in contrast to the grid with KYGRID_MODEL set to 4, where the minimum $k_\theta \rho_s$ would be 0.05. KYGRID_MODEL = 1 is recommended to avoid issues associated with low $k_\theta \rho_s$ values. Additionally, the parameter ALPHA_ZF is set to -1, and is particularly important in quasi-linear flux predictions. While it does not affect the linear response, it significantly influences the estimation of the non-linear saturation level of the turbulent fluxes. In regions dominated by Kinetic Ballooning Modes, the peak of γ/k_y often occurs at the lowest k_y values due to unstable modes in that region. Setting ALPHA_ZF = -1 excludes the lowest k_y values during the identification of $\gamma/k_y|_{max}$, preventing an incorrect and excessively high predicted saturated potential peaking at the first k_y point.

4.2. Nonlinear Simulations with GKW

To benchmark TGLF's performance in capturing KBM turbulence, we conducted a series of 14 nonlinear simulations using the GKW code. The parameters varied in these simulations include R/L_{Ti}, R/L_{Te}, R/L_n, and the shearing rate γ_{E_N}. Table 4.1 summarizes the characteristics of each simulation. Note that close to the magnetic axis, the toroidal rotation gradient is rather low and the associated shearing rate is modest compared to the maximum linear growth rate, with only a small impact on the saturation level observed in non-linear simulations.

Figure 4.1 shows the time evolution of non-linear gyro-Bohm normalized ion and electron heat fluxes, and electron particle fluxes obtained with GKW for two different values of R/L_{Ti} and R/L_{Te}. The plots indicate that varying R/L_{Ti} has a much stronger impact on the fluxes compared to R/L_{Te}, as R/L_{Ti} is a primary driver for KBMs. Both increases result in higher particle and heat fluxes, with changes in R/L_{Ti} having a more pronounced effect. In the following sections, we will compare the time-averaged heat and particle fluxes obtained from the GKW nonlinear simulations with the quasi-linear flux predictions from TGLF.

4.2.1. Comparing the Saturated Potential: Nonlinear GKW vs. Quasilinear TGLF

To assess TGLF's performance in predicting the saturated potential, we compare the binormal spectra of the electric potential $\langle|\delta\phi|^2\rangle$ from nonlinear GKW simulations to those from quasilinear TGLF simulations across various settings.

$$\langle|\delta\phi|^2\rangle = \frac{\sum_{k_r\rho_s}\langle|\delta\phi(k_r,k_\theta)|^2\rangle_{\text{time, flux-surface}}}{\Delta k_\theta \rho_s} \tag{4.1}$$

Case index	R/L_{Ti}	R/L_{Te}	R/L_{Ne}	γ_{E_N}
1	4.2	2	1.5	0
2	**3.15**	2	1.5	0
3	4.2	**1.5**	1.5	0
4	4.2	**2.5**	1.5	0
5	4.2	2	**1.2**	0
6	4.2	2	**0.9**	0
7	**3.15**	2	**1.2**	0
8	4.2	2	1.5	**0.05**
9	4.2	**1.5**	1.5	**0.05**
10	4.2	2	**0.9**	**0.05**
11	**3.15**	2	1.5	**0.05**
12	4.2	**2.5**	1.5	**0.05**
13	4.2	2	**1.2**	**0.05**
14	**3.15**	2	**1.2**	**0.05**

Table 4.1. – Summary of the plasma parameters varied in the 14 nonlinear GKW simulations. Case 1 corresponds to the reference case. Bold values indicate deviations from the reference case.

Here, $\langle|\delta\phi|^2\rangle$ is the squared saturated potential, time averaged, flux-surface averaged, summed over all $k_r\rho_s$ and normalized by $\Delta k_\theta\rho_s$ to account for the potentially different binormal wavevector grids in TGLF and GKW. The optimized TGLF settings, which provide the closest match to the GKW results for the cases analyzed, are summarized in Table 4.2. These settings serve as the baseline for our comparisons and analysis. From these optimized settings, we explore:

Parameter	Optimized Value
`FILTER`	-1.5
`WIDTH`	3
`KYGRID_MODEL`	1
`ALPHA_ZF`	-1

Table 4.2. – Optimized TGLF parameter settings for modeling KBM turbulence

— `FILTER`: Changing from -1.5 (optimized) to 2 (default).
— `WIDTH`: Changing from 3 (optimized) to 1.65 (default).
— `KYGRID_MODEL`: Changing from 1 (optimized) to 4.
— `ALPHA_ZF`: Changing from -1 (optimized) to 1 (default).

Figure 4.2 illustrates the $\langle|\delta\phi|^2\rangle$ spectra as a function of the binormal wavevector $k_\theta\rho_s$ for six different cases referenced in Table 4.1. The red curves represent the GKW simulation results, serving as the reference. The TGLF simulation results are shown for five different configurations: optimized (blue), `WIDTH` = 1.65 (orange), `ALPHA_ZF` = 1 (green), `KYGRID_MODEL` = 4 (purple, with open circles) and `FILTER` = 2 (brown). These

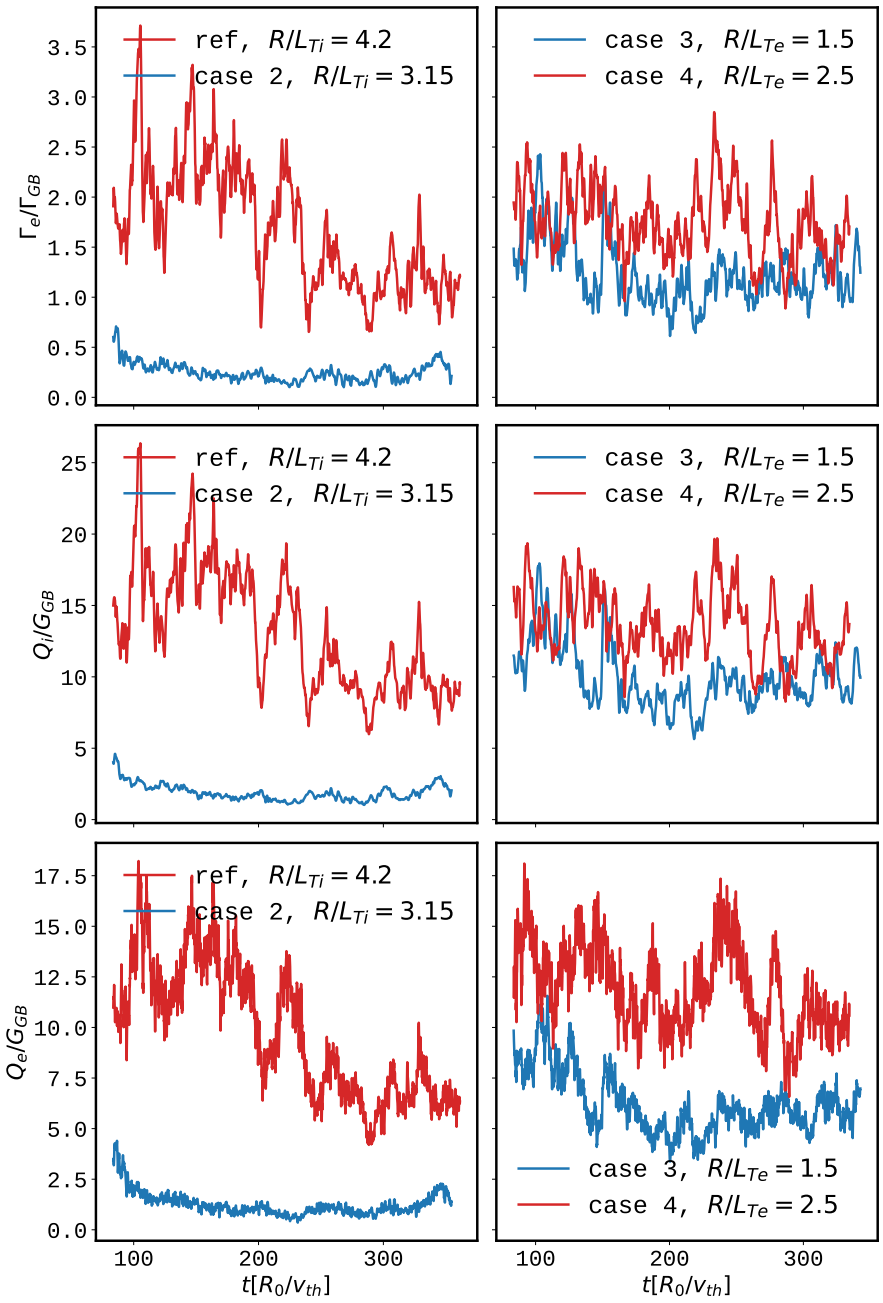


Figure 4.1. – Time evolution of turbulent fluxes for varying ion and electron temperature gradients in nonlinear GKW simulations. Cases 1,2,3 and 4 are shown. The reference case corresponds to $R/L_{Ti} = 4.2$ and $R/L_{Te} = 2$.

six cases were selected as they exhibit distinct behaviors under varying TGLF settings, making them particularly useful for observing the effects analyzed in the subsequent section.

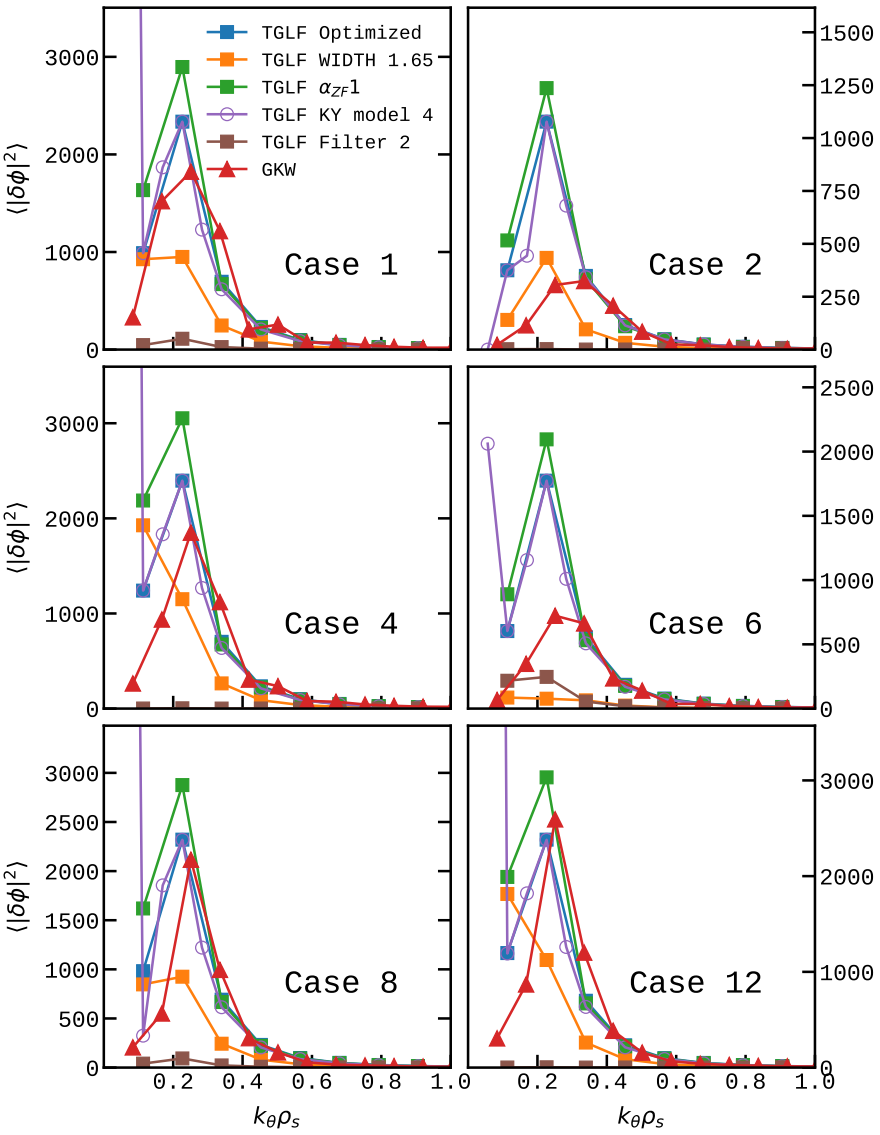


Figure 4.2. – $\langle|\delta\phi|^2\rangle$ profiles from GKW (red) and TGLF simulations for five different settings. Case numbers are indicated referring to Table 4.1.

Impact of `WIDTH`

The `WIDTH` parameter in TGLF specifies the width of the Gaussian envelope used in the Hermite polynomial projection of the wave functions (see section 2.1.3). The default value in TGLF is 1.65, which is optimized for typical turbulence scenarios. However, at low magnetic shear KBMs require a broader envelope due to their extended wavefunctions. Figure 4.2 shows that with the default `WIDTH` of 1.65, the perturbed potential $\langle|\delta\phi^2|\rangle$, is underestimated, missing the peak value. This behaviour can be traced back to an inaccurate linear response (see Section 3.3.3.2). We therefore recommend increasing `WIDTH` to 3 when modeling KBMs at low magnetic shear.

Impact of KYGRID_MODEL

The KYGRID_MODEL parameter in TGLF defines the $k_\theta \rho_s$ grid used in simulations. There are two pre-defined grids: KYGRID_MODEL = 1 and KYGRID_MODEL = 4. Table 4.3 summarizes the $k_\theta \rho_s$ spectra values for both grids in our analysis case with IMAS normalizations. TGLF grid include electron scale modes and extends up to $k_\theta \rho_s$

Table 4.3. – $k_\theta \rho_s$ spectra for KYGRID_MODEL = 1 and 4 (IMAS normalizations)

KYGRID_MODEL	$k_\theta \rho_s$ values
1	{0.11, 0.23, 0.34, 0.45, 0.57, 0.68, 0.79, 0.91, 1.02, 1.13, 1.36, 1.65, 1.98, 2.39, 2.88, 3.48, 4.19, 5.05, 6.09, 7.35, 8.86, 10.68, 12.87, 15.52, 18.71, 22.56, 27.2, 32.79}
4	{**0.06**, 0.11, **0.17**, 0.23, **0.28**, 0.34, 0.45, 0.57, 0.68, 0.79, 0.91, 1.02, 1.13, 1.36, 1.65, 1.98, 2.39, 2.88, 3.48, 4.19, 5.05, 6.09, 7.35, 8.86, 10.68, 12.87, 15.52, 18.71, 22.56, 27.2, 32.79}

values not included in the GKW non-linear simulations. This difference does not matter for the comparison since ETG modes are stable for these parameters and no contribution from the electron-scale modes are observed in TGLF simulations. The standard grid (KYGRID_MODEL = 1) is recommended for modeling KBMs. This recommendation stems from the fact that KYGRID_MODEL = 4 extends further into the lower $k_\theta \rho_s$ spectrum, increasing the risk of not capturing the correct peak of the $\langle|\delta\phi^2|\rangle$ spectrum with the $\frac{\gamma}{k_\theta \rho_s}$ proxy used in TGLF. This divergence at very low $k_\theta \rho_s$ values is observed in Figure 4.2 for cases 1, 4, 6, 8, and 12, where the maximum value of $\langle|\delta\phi^2|\rangle$ occurs at $k_\theta \rho_s = 0.06$.

Impact of ALPHA_ZF

To mitigate situations where the ion-scale peak of $\frac{\gamma}{k_\theta \rho_s}|_{max}$ occurs at the lowest $k_\theta \rho_s$ values, TGLF allows for the exclusion of very low $k_\theta \rho_s$ values (see Section 2.2.3.3) during the identification of $\frac{\gamma}{k_\theta \rho_s}|_{max}$ by setting the ALPHA_ZF parameter to -1. This adjustment prevents the peak from occurring at $k_\theta \rho_s$ values below the threshold. By default, when ALPHA_ZF is set to 1, all $k_\theta \rho_s$ modes are included in the search for the peak of $\frac{\gamma}{k_\theta \rho_s}$, potentially resulting in higher predicted potentials due to the influence of very low $k_\theta \rho_s$ values. This effect is particularly pronounced when ALPHA_ZF = 1 is combined with KYGRID_MODEL = 4, leading to highly inaccurate predictions with excessively high potentials at the first $k_\theta \rho_s$ point. In our analysis of the JET #75225 case, the ALPHA_ZF parameter proved essential for accurate quasi-linear flux predictions in regions dominated by KBMs. By excluding very low $k_\theta \rho_s$ values, it avoids overemphasizing these contributions, which can distort the predicted potential. However, the robustness of this method is not guaranteed since it can lead to the exclusion of

important contributions to the fluxes. Careful consideration and examination of the spectrum of the saturated potential are necessary when using this method.

Impact of `FILTER`

For the `FILTER` parameter, the default value of 2 filters out KBMs, leading to an almost null predicted potential. For accurate KBM modeling, we recommend setting `Filter` to -1.5, retaining relevant KBM modes while excluding spurious ones.

4.3. Comparison of TGLF Quasi-linear Fluxes and GKW Nonlinear Fluxes

We now compare the quasi-linear flux predictions from TGLF, using the optimized settings of table 4.2 with the nonlinear fluxes obtained from GKW simulations. Figure 4.3 presents a comparative analysis of the heat and particle fluxes for both ions and electrons. Each point in the plots represents one of the 14 different simulations listed in Table 4.1. The dashed line indicates where the TGLF predictions would perfectly match the GKW results. Overall, the ion and electron particle fluxes predicted by TGLF align well with those from GKW, although there are some exceptions where TGLF predicts an ion particle flux with the wrong sign. For the ion heat flux, TGLF tends to overestimate the fluxes compared to GKW. However, for the electron heat flux, TGLF underestimates the fluxes, particularly in cases with higher fluxes.

The verification and calibration of TGLF against a large database of gyrokinetic turbulence simulations are detailed in [111]. In that study, the Root Mean Square (RMS) average of the relative error between TGLF's quasi-linear fluxes (Γ^{TGLF}) and the reference nonlinear fluxes (Γ^{NL}) was calculated using the following formula:

$$\alpha_\Gamma = \sqrt{\frac{\sum_{\text{scan}} \left(\Gamma^{NL} - \Gamma^{TGLF}\right)^2}{\sum_{\text{scan}} \Gamma^{NL\,2}}} \tag{4.2}$$

where the summation is performed for each scan in the database. The study reported an RMS average errors over all of the scans of Q_i : 16.2%, Q_e : 16.6%, and Γ_e : 33.5%. In our study, using the results shown in Figure 4.3, we calculate the RMS average error across all simulations listed in Table 4.1. The errors are: Q_i : 75.9%, Q_e : 64.7%, Γ_e : 45.6%, and Γ_i : 67.0%.

In addition to the TGLF and GKW comparisons, we introduce a hybrid "GKW-QL" approach, which combines the linear response from GKW (most unstable mode only) with TGLF's saturation model (TGLFsat2). The green markers in Figure 4.3 represent the results from this hybrid approach. This method assesses the effectiveness of TGLF's saturation model when the linear response is derived from GKW, providing an intermediary validation step. The hybrid GKW-QL approach yields flux predictions that closely align with the nonlinear GKW results, in line with previous assessments of the QL approximation validity in this regime [12] and further demonstrating the

potential of TGLF saturation model when the linear response is accurately captured. However, discrepancies persist for the electron heat flux. To further investigate these discrepancies, we analyze separately the electrostatic (ϕ) and magnetic flutter ($A_\parallel$) contributions to the electron and ion heat fluxes.

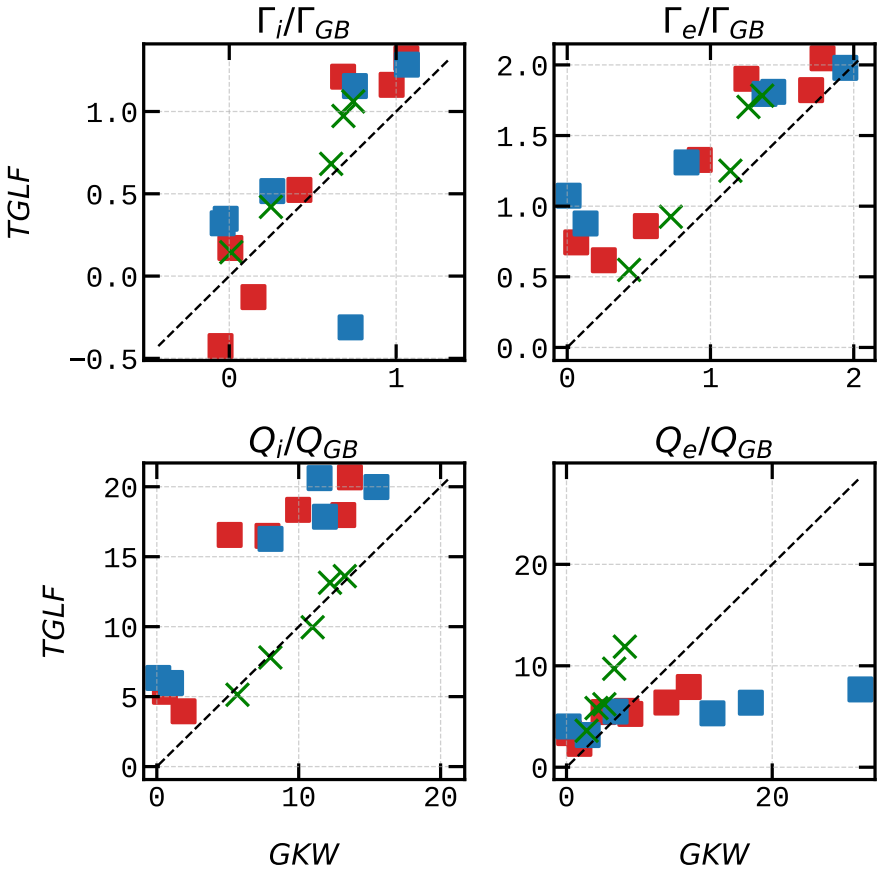


Figure 4.3. – Comparison of ion and electron heat and particle fluxes between TGLF and GKW. Red points represent simulations without shearing rate, blue points include it, and green markers show results from the hybrid GKW-QL approach. The dashed line indicates perfect agreement.

Contributions of ϕ and $A_\parallel$ to Heat Fluxes

Figure 4.4 shows a comparison of the contributions of electrostatic (ϕ) and magnetic flutter ($A_\parallel$) components to the ion and electron heat fluxes for TGLF and GKW. We observe that the electrostatic contribution is better reproduced by TGLF, both for the ion and electron heat fluxes. However, TGLF underestimates the magnetic flutter ($A_\parallel$) contribution to the electron heat flux while overestimating it for ion heat flux. The large electron heat flux driven by magnetic flutter obtained in similar conditions in a previous study was suggested to be driven by the non-linear excitation of subdominant micro-tearing modes [12]. Improvement of existing quasi-linear models would be

needed to take this contribution into account. The underestimation of this component by TGLF leads to the overall lower electron heat flux predictions compared to GKW, as observed in Figure 4.3.

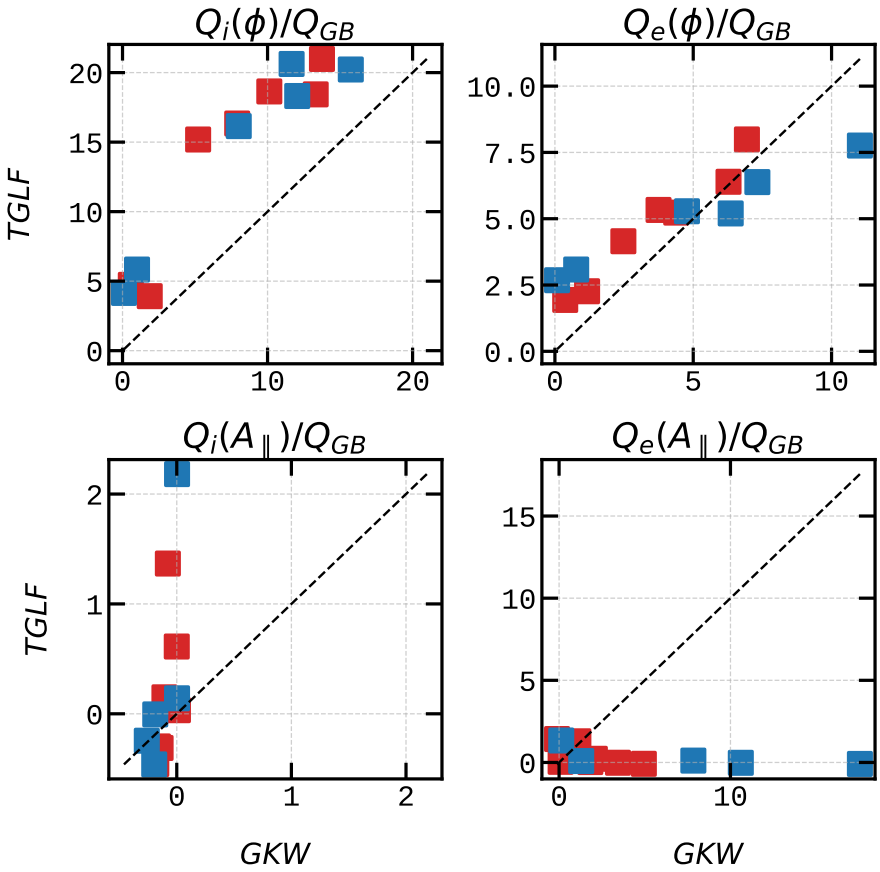


Figure 4.4. – Comparison of electrostatic (ϕ) and magnetic flutter ($A_\parallel$) contributions to ion and electron heat fluxes between TGLF and GKW.

These findings indicate that while TGLF captures the electrostatic component of the heat flux to a reasonable extent, it underestimates the magnetic flutter component for electrons and overestimates it for ions. This discrepancy is particularly impactful for the electron heat flux, where the magnetic flutter contribution is significant. Consequently, the total electron heat flux predicted by TGLF is lower than that observed in GKW simulations.

Spectrum Decomposition of Ion and Electron Heat Fluxes

To gain further insights into the discrepancies between TGLF and GKW predictions, we analyze the spectrum decomposition of ion and electron heat fluxes, highlighting the contributions of ϕ and $A_\parallel$. Figures 4.5 and 4.6 present these decompositions for the cases 1, 3, 4, and 12, defined in Table 4.1. In cases 3, 1, and 4 the electron temperature gradient is progressivelly increased from $R/L_{T_e} = 1.5$ to 2.5 and, in case

12, $E \times B$ shearing is added. Figure 4.5 illustrates the behaviour of the ion heat flux spectrum as a function of the binormal wavevector $k_\theta \rho_s$. For the ion heat flux, TGLF reproduces the electrostatic contribution well, occasionally overestimating the fluxes but showing a correct overall agreement. TGLF underestimates the magnetic flutter ($A_\parallel$) contribution, but the overall impact on the total ion heat flux is minimal due to the dominance of the electrostatic component. Figure 4.6 presents the electron heat flux

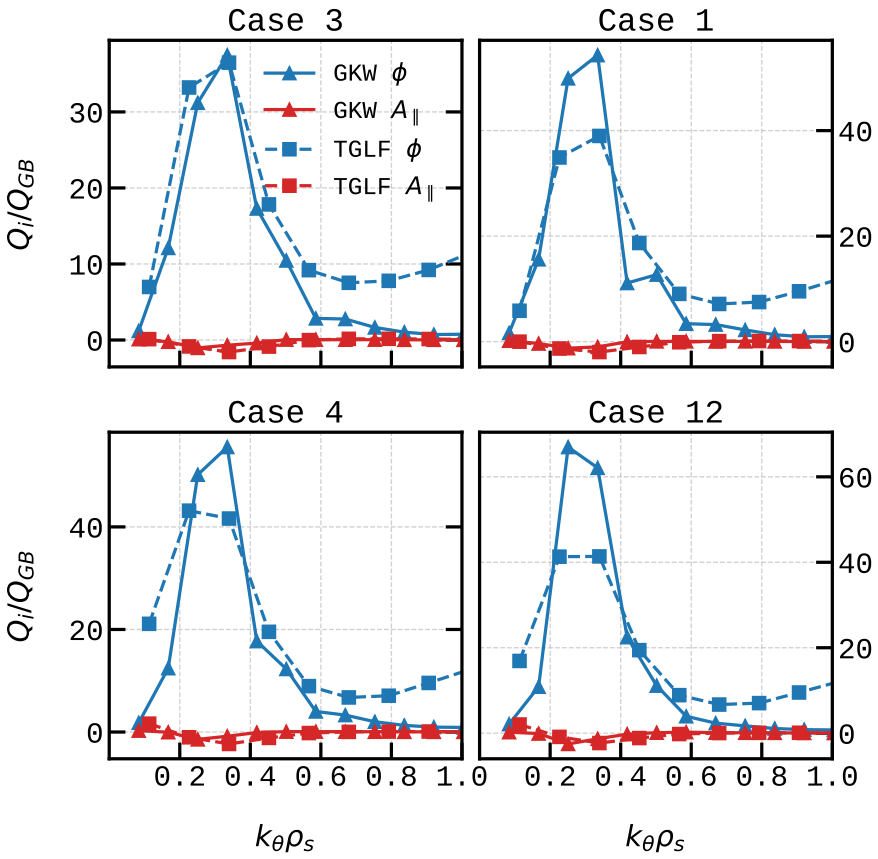


Figure 4.5. – Spectrum decomposition of ion heat flux (Q_i) for TGLF and GKW, showing electrostatic (ϕ) and magnetic flutter ($A_\parallel$) contributions for cases 3 ($R/L_{T_e} = 1.5$), 1 ($R/L_{T_e} = 2$), 4 ($R/L_{T_e} = 2.5$), and 12 ($R/L_{T_e} = 2.5$ and ExB shearing).

spectrum for the same cases. Similarly to the ion heat flux, TGLF accurately captures the electrostatic contribution compared to GKW and tends to slightly overestimate it. However, the magnetic flutter ($A_\parallel$) contribution is significantly underestimated by TGLF. In GKW simulations, the magnetic flutter contribution to the electron heat flux is observed to increase with R/L_{T_e}, consistently with a potential excitation of micro-tearing modes, and displays a rather flat $k_\theta \rho_s$ spectrum. Adding $E \times B$ shearing almost doubles the magnetic flutter contribution while the electrostatic component is left largely unchanged. This strong dependence on the shearing rate level was robustly observed in other cases and would deserve further investigations.

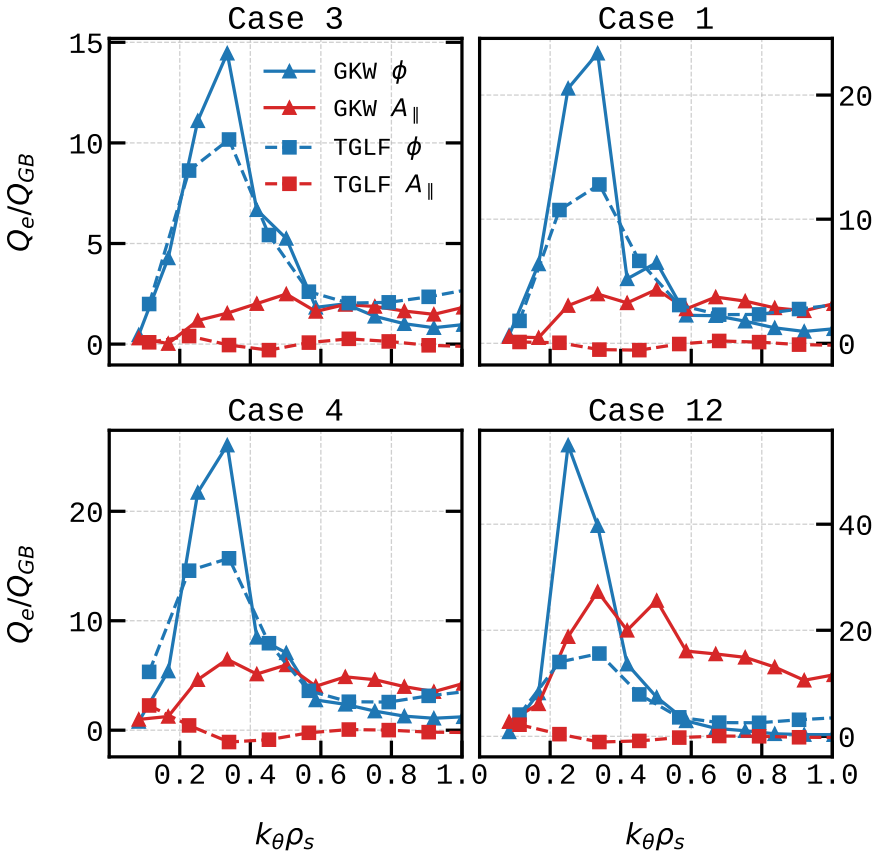


Figure 4.6. – Spectrum decomposition of electron heat flux (Q_e) for TGLF and GKW, showing electrostatic (ϕ) and magnetic flutter ($A_\parallel$) contributions for cases 3 ($R/L_{T_e} = 1.5$), 1 ($R/L_{T_e} = 2$), 4 ($R/L_{T_e} = 2.5$), and 12 ($R/L_{T_e} = 2.5$ and ExB shearing).

Comparison of Flux Responses to R/L_{Te} and R/L_{Ti} Variations

Finally, we present a scan of R/L_{Te} and R/L_{Ti} for ion and electron particle and heat fluxes. This scan evaluates how well TGLF captures the trends observed in GKW nonlinear simulations across different temperature gradient values. Figure 4.7 illustrates the ion and electron heat fluxes as well as electron particle fluxes as functions of R/L_{Te} and R/L_{Ti} for both TGLF and GKW. As in the previous sections, we observe that TGLF tends to overestimate fluxes compared to GKW, with the exception of the electron heat flux. Despite this overestimation, TGLF follows the general trend observed in GKW simulations, indicating its capability to reproduce the overall behavior of fluxes with increasing temperature gradients.

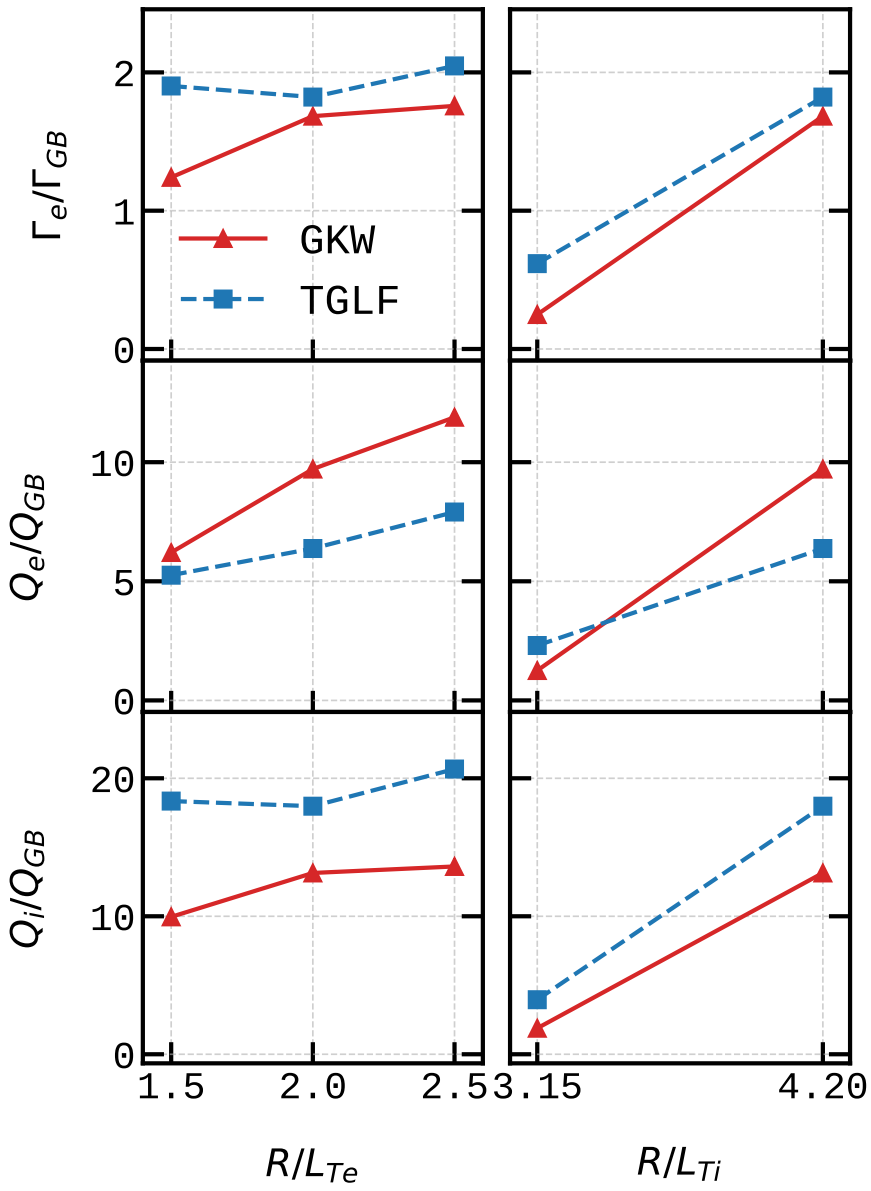


Figure 4.7. – Comparison of TGLF and GKW fluxes as a function of R/L_{Te} and R/L_{Ti}.

5. Conclusions and Future Perspectives

Achieving high β plasma, is a key goal for improving fusion performance, as it enhances the fusion power generated in a fusion reactor. However, as β increases, electromagnetic effects become more pronounced, introducing new challenges in accurately modeling turbulence and its impact on transport. Understanding and predicting turbulent transport in high-β plasmas is crucial for the developpement of recent and future fusion devices such as JT60-SA, ITER and DEMO, where higher β regimes are expected. In such regimes, instabilities like Kinetic Ballooning Modes (KBMs) driven by electromagnetic effects arise, presenting new challenges to turbulent transport modeling. While the inclusion of electromagnetic effects in reduced transport models has gained increasing attention in recent years, a validation effort is still required compared to electrostatic-only modeling approaches.

Modeling the time evolution of plasma profiles is essential for understanding the dynamic behavior of fusion plasmas and for predicting their performance in operational scenarios. This involves solving the transport equations for quantities such as density and temperatures, which evolve under the influence of turbulent transport processes. Nonlinear gyrokinetic simulations offer a comprehensive description of turbulence. However, their computational cost makes them impractical for integrated modeling frameworks, which demand fast evaluations of turbulent fluxes across multiple radial positions and time steps. Quasi-linear turbulence models, such as TGLF, balances computational efficiency with a physics-based foundation. These models bridge the gap between high-fidelity nonlinear gyrokinetic simulations and the demands of integrated modeling frameworks. However, the inherent simplifications in quasi-linear models, particularly in their treatment of the non-linear saturation mechanisms, limit their reliability when applied to less-explored parameter regimes.

For high-β plasmas, where electromagnetic effects dominate, quasi-linear models like TGLF have not been extensively benchmarked, leaving significant uncertainties in their predictive capabilities. Verifying these models in such regimes is essential before they can be confidently applied in integrated modeling studies. This thesis directly addressed these uncertainties by verifying TGLF's quasi-linear predictions against nonlinear fluxes computed with the gyrokinetic code GKW, providing critical insights into its strengths and limitations in modeling turbulence in high-β regimes. This work has contributed to the verification and refinement of turbulence model reductions for high-β tokamak plasmas.

The first objective of this thesis was to facilitate the verification of TGLF quasi-linear predictions against gyrokinetic simulations from higer fidelity gyrokinetic models. To

achieve this, TGLF was integrated into the IMAS-GK framework, a unified computational infrastructure designed to streamline data exchange and comparison among different δf flux-tube gyrokinetic models. The Integrated Modelling and Analysis Suite (IMAS) provides a standardized data structure, the Interface Data Structure (IDS), to unify simulation inputs and outputs across diverse tokamak scenarios. By adopting this framework, benchmarking efforts can be executed consistently, avoiding discrepancies caused by differing normalization conventions or data handling methods. The first step of this integration focused on developing routines to enable TGLF simulations to interface seamlessly with the IMAS framework. These routines, now available in a public open source Git repository [119], convert the inputs and outputs of TGLF into the Gyrokinetic IDS (GK-IDS) format. This ensures compatibility with other codes already integrated within IMAS, such as the non-linear gyrokinetic code GKW. These routines have already been adopted by other researchers for verification studies. This integration effort not only supports the objectives of this thesis but also serves as a tools for future benchmarking and comparative studies involving the TGLF model.

The next step in this thesis was to verify the linear response of TGLF in high-β plasmas. This investigation began by benchmarking TGLF against the high-fidelity gyrokinetic code GKW in the Waltz standard case scenario. This case provided a robust testing ground for assessing TGLF's accuracy in capturing the transition from Ion Temperature Gradient (ITG)-driven turbulence to Kinetic Ballooning Modes (KBMs). In both regimes, TGLF successfully reproduced the linear growth rates and mode structures predicted by GKW under standard magnetic shear conditions, reaffirming its capability to model KBMs under baseline scenarios. However, discrepancies emerged at very low magnetic shear values, particularly near the ITG-KBM transition, where extended mode structures posed significant challenges for TGLF's modeling capabilities. The study then extended this linear verification to an experimental high-β plasma scenario, focusing on the JET hybrid H-mode discharge #75225 at the radial position $\rho = 0.15$. This case, characterized by low magnetic shear and high β in the core plasma, was selected to evaluate TGLF's performance in KBM-dominated regimes. Results showed that TGLF struggled to accurately capture the growth rates and mode structures for low values in the binormal wavevector spectrum, which are critical for predicting quasi-linear fluxes. This highlighted a limitation in TGLF's standard filtering mechanism, which could not effectively distinguish between physical KBMs and high-frequency spurious modes. A new filtering mechanism was therefore developed and integrated into TGLF. The filter uses a dual criterion based on mode frequency and parity to distinguish KBMs from spurious modes. By retaining modes with even parity in the real part of the electrostatic potential and propagating in the ion diamagnetic direction, the filter excluded non-physical modes while preserving KBMs. This innovation significantly enhanced TGLF's ability to model KBMs in high-β plasmas, particularly under conditions of low magnetic shear. Its implementation represents a substantial contribution to the TGLF codebase and offers a pathway for more reliable quasi-linear predictions in these challenging regimes.

The investigation then shifted to the quasi-linear flux predictions from TGLF, ver-

ifying them against nonlinear fluxes obtained from GKW simulations. This phase of the study aimed to assess TGLF's quasi-linear saturation model, building on the linear response analysis conducted in the preceding section. This verifying effort focused on the same JET hybrid H-mode discharge #75225. Nonlinear simulations with GKW were conducted for 14 distinct cases, systematically varying the ion and electron temperature gradients (R/L_{T_i} and R/L_{T_e}), density gradients (R/L_{N_e}), and the $E \times B$ shearing rate ($\gamma_{E\times B}$). By systematically analyzing TGLF settings, we identified an optimized configuration for modeling KBMs. Our findings highlight the sensitivity of TGLF's performance to its parameter settings and underscore the importance of careful parameter selection. The optimized TGLF settings in Table 4.2 offer a baseline for modeling KBMs, but its robustness across other scenarios would deserve further validation and testing. Using the new filter and optimized settings, TGLF's flux predictions were compared to GKW nonlinear simulations for ion and electron heat and particle fluxes. The Root Mean Square (RMS) average errors were 67.0% for the ion particle flux (Γ_i), 45.6% for the electron particle flux (Γ_e), 75.9% for the ion heat flux (Q_i), and 64.7% for the electron heat flux (Q_e). TGLF was found to underestimate the electron heat flux. This discrepancy arises from the strong underestimation of the magnetic flutter contribution to the electron heat flux by TGLF. This contribution, which may arise from the non-linear excitation of sub-dominant micro-tearing modes [12], would require further development of quasi-linear models to be accounted for. For the electrosatic part, as long as the linear response is properly captured, TGLF saturation model provides a correct prediction of the non-linear fluxes in the KBM regime. Finally, a parametric scan of R/L_{T_i} and R/L_{T_e} demonstrated that TGLF successfully reproduces the trends with respect to temperature gradients observed in GKW nonlinear simulations. This verification underscores TGLF's potential for integrated modeling frameworks, provided its saturation models are further refined to address the identified discrepancies. The results of this study, including the development of the new filtering mechanism, are currently under review in the journal *Plasma Physics and Controlled Fusion*.

Several avenues for future research emerge from this work. This thesis has highlighted specific areas where the TGLF model can be refined to improve its performance in high-β plasmas. A key area of focus is the specification of the Gaussian envelope used in TGLF for projecting wave functions. As shown in this study, low magnetic shear conditions often result in extended wavefunctions, making the Gaussian width a critical parameter for accurately modeling eigenmodes. Developing a more adaptive approach to determine this width, potentially based on local magnetic shear, could enhance TGLF's accuracy in KBM-dominated regimes. Additionally, the method for identifying the peak of the γ/k_y spectrum, which is central to the saturation model, faces challenges when the peak occurs at very low k_y values. A more robust refinement process for this peak estimation would mitigate these issues and improve the reliability of the TGLF model. Improving TGLF's treatment of electromagnetic effects, particularly the magnetic flutter contribution to electron heat flux, is another critical direction for future research. Furthermore, the optimized settings identified in this study and the analysis conducted were specifically limited to the JET #75225 discharge.

Extending this verification to additional high-β experimental scenarios is crucial for evaluating the robustness and generalizability of TGLF's performance. Additionally, these settings should be tested within integrated modeling frameworks, as even minor adjustments to numerical parameters can significantly affect the predicted fluxes. Validating these predictions across diverse high-β cases will ensure their reliability and broader applicability. Recent advancements, such as neural network surrogate models, have demonstrated significant reductions in computational costs while preserving accuracy. A french granted project named FASTER, for instance, focuses on creating fast surrogate models for gyrokinetic turbulence simulations, leveraging high-fidelity datasets from linear and nonlinear simulations to train machine learning algorithms. Future work could focus on refining TGLF's linear response and saturation models using similar machine learning tools, trained on high-fidelity gyrokinetic datasets.

The integration of TGLF into the IMAS-GK framework, the development of a new filtering mechanism, and the identification of optimized settings provide a robust foundation for future work. By addressing the challenges outlined in this thesis, future research can further refine TGLF and advance its role in predictive plasma modeling to prepare JT60-SA and ITER operations.

ANNEXES

A. Integrals For Moment of fluid model derivation

To obtain the zeroth moment of the distribution function we need first to calculate the integrals below.

$$\int f\, d\boldsymbol{v} = \delta n \tag{A.1}$$

$$\int f v_{\parallel}\, d\boldsymbol{v} = n\delta V_{\parallel} \tag{A.2}$$

$$\begin{aligned}
\int F_M d\boldsymbol{v} &= \frac{n}{\sqrt{\pi}^3 v_{th}^3} \int e^{-\frac{v^2}{v_{th}^2}} d\boldsymbol{v} \\
&= \frac{n}{\sqrt{\pi}^3 v_{th}^3} (\int e^{-\frac{v^2}{v_{th}^2}} dv)^3 \\
&= \frac{n}{\sqrt{\pi}^3 v_{th}^3} (v_{th} \int e^{-u^2} du)^3 \\
&= \frac{n}{\sqrt{\pi}^3 v_{th}^3} v_{th}^3 \sqrt{\pi}^3 \\
&= n
\end{aligned} \tag{A.3}$$

$$\begin{aligned}
\int F_M v_{\parallel} d\boldsymbol{v} &= \frac{n}{\sqrt{\pi}^3 v_{th}^3} \int v_{\parallel} e^{-\frac{v^2}{v_{th}^2}} d\boldsymbol{v} \\
&= \frac{n}{\sqrt{\pi}^3 v_{th}^3} [\underbrace{\int_{v_{\parallel}>0} v_{\parallel} e^{-\frac{v^2}{v_{th}^2}} d\boldsymbol{v} + \int_{v_{\parallel}<0} v_{\parallel} e^{-\frac{v^2}{v_{th}^2}} d\boldsymbol{v}}_{0}] \\
&= 0
\end{aligned} \tag{A.4}$$

$$
\begin{aligned}
\int F_M v^2 d\boldsymbol{v} &= \frac{n}{\sqrt{\pi}^3 v_{th}^3} \int v^2 e^{-\frac{v^2}{v_{th}^2}} d\boldsymbol{v} \\
&= \frac{n}{\sqrt{\pi}^3 v_{th}^3} \int (v_x^2 + v_y^2 + v_z^2) e^{-\frac{v_x^2+v_y^2+v_z^2}{v_{th}^2}} dv_x dv_y dv_z \\
&= \frac{n}{\sqrt{\pi}^3 v_{th}^3} \iiint [v_x^2 e^{-\frac{v_x^2}{v_{th}^2}} e^{-\frac{v_y^2}{v_{th}^2}} e^{-\frac{v_z^2}{v_{th}^2}} + v_y^2 e^{-\frac{v_x^2}{v_{th}^2}} e^{-\frac{v_y^2}{v_{th}^2}} e^{-\frac{v_z^2}{v_{th}^2}} + v_z^2 e^{-\frac{v_x^2}{v_{th}^2}} e^{-\frac{v_y^2}{v_{th}^2}} e^{-\frac{v_z^2}{v_{th}^2}}] dv_x dv_y dv_z \\
&= \frac{n}{\sqrt{\pi}^3 v_{th}^3} (\iint v_{th}^3 \frac{\sqrt{\pi}}{2} e^{-\frac{v_y^2}{v_{th}^2}} e^{-\frac{v_z^2}{v_{th}^2}} dv_y dv_z + \iint v_{th}^3 \frac{\sqrt{\pi}}{2} e^{-\frac{v_x^2}{v_{th}^2}} e^{-\frac{v_z^2}{v_{th}^2}} dv_x dv_z + \dots \\
&= \frac{n}{\sqrt{\pi}^3 v_{th}^3} (\int v_{th}^4 \frac{\sqrt{\pi}^2}{2} e^{-\frac{v_y^2}{v_{th}^2}} \sqrt{\pi} dv_y + \int v_{th}^4 \frac{\sqrt{\pi}^2}{2} e^{-\frac{v_x^2}{v_{th}^2}} \sqrt{\pi} dv_x + \int v_{th}^4 \frac{\sqrt{\pi}^2}{2} e^{-\frac{v_x^2}{v_{th}^2}} \sqrt{\pi} dv_x) \\
&= 3 \frac{n}{\sqrt{\pi}^3 v_{th}^3} v_{th}^5 \frac{\sqrt{\pi}^3}{2} \\
&= \frac{3}{2} n v_{th}^2
\end{aligned}
\tag{A.5}
$$

$$
\begin{aligned}
\int F_M v_\parallel^2 d\boldsymbol{v} &= \frac{n}{\sqrt{\pi}^3 v_{th}^3} \int v_\parallel^2 e^{-\frac{v^2}{v_{th}^2}} d\boldsymbol{v} \\
&= \frac{n}{\sqrt{\pi}^3 v_{th}^3} \iint v_\parallel^2 e^{-\frac{v_\parallel^2+v_\perp^2}{v_{th}^2}} 2\pi v_\perp dv_\perp dv_\parallel \\
&= \frac{2\pi n}{\sqrt{\pi}^3 v_{th}^3} \int_0^\infty \int v_\parallel^2 e^{-\frac{v_\parallel^2}{v_{th}^2}} e^{-\frac{v_\perp^2}{v_{th}^2}} v_\perp dv_\perp dv_\parallel \\
&= \frac{2\pi n}{\sqrt{\pi}^3 v_{th}^3} \int_0^\infty v_{th}^3 \frac{\sqrt{\pi}}{2} e^{-\frac{v_\perp^2}{v_{th}^2}} v_\perp dv_\perp \\
&= \frac{\pi n}{\sqrt{\pi}^2} \int_0^\infty e^{-\frac{v_\perp^2}{v_{th}^2}} v_\perp dv_\perp \\
&= n v_{th}^2 \int_0^\infty u e^{-u^2} du \\
&= n v_{th}^2 \int_0^\infty u e^{-u^2} du \\
&= \frac{1}{2} n v_{th}^2
\end{aligned}
\tag{A.6}
$$

$$
\begin{aligned}
\int F_M v_\perp^2 d\boldsymbol{v} &= \frac{n}{\sqrt{\pi}^3 v_{th}^3} \int v_\perp^2 e^{-\frac{v^2}{v_{th}^2}} d\boldsymbol{v} \\
&= \frac{n}{\sqrt{\pi}^3 v_{th}^3} \int_0^\infty \int v_\perp^2 e^{-\frac{v_\parallel^2 + v_\perp^2}{v_{th}^2}} 2\pi v_\perp dv_\perp dv_\parallel \\
&= \frac{2\pi n}{\sqrt{\pi}^3 v_{th}^3} \int_0^\infty \int v_\perp^3 e^{-\frac{v_\parallel^2}{v_{th}^2}} e^{-\frac{v_\perp^2}{v_{th}^2}} dv_\perp dv_\parallel \\
&= \frac{2\pi n}{\sqrt{\pi}^3 v_{th}^3} \int_0^\infty v_\perp^3 e^{-\frac{v_\perp^2}{v_{th}^2}} dv_\perp \int e^{-\frac{v_\parallel^2}{v_{th}^2}} dv_\parallel \\
&= \frac{2\pi n}{\sqrt{\pi}^3 v_{th}^3} \int_0^\infty v_\perp^3 e^{-\frac{v_\perp^2}{v_{th}^2}} dv_\perp \int v_{th} e^{-u^2} du \\
&= \frac{2\pi n}{\sqrt{\pi}^2 v_{th}^2} \int_0^\infty v_\perp^3 e^{-\frac{v_\perp^2}{v_{th}^2}} dv_\perp \\
&= \frac{2n}{v_{th}^2} v_{th}^4 \int_0^\infty u^3 e^{-u^2} du \\
&= 2n v_{th}^2 \frac{1}{2} \\
&= n v_{th}^2
\end{aligned}
\tag{A.7}
$$

$$
\begin{aligned}
\int F_M v_\perp^2 v_\parallel d\boldsymbol{v} &= \frac{n}{\sqrt{\pi}^3 v_{th}^3} \int v_\perp^2 v_\parallel e^{-\frac{v^2}{v_{th}^2}} d\boldsymbol{v} \\
&= \frac{n}{\sqrt{\pi}^3 v_{th}^3} \iint v_\perp^3 v_\parallel e^{-\frac{v_\perp^2}{v_{th}^2}} e^{-\frac{v_\parallel^2}{v_{th}^2}} 2\pi dv_\parallel dv_\perp \\
&= \frac{2\pi n}{\sqrt{\pi}^3 v_{th}^3} \underbrace{\int v_\parallel e^{-\frac{v_\parallel^2}{v_{th}^2}} dv_\parallel}_{0} \int_0^\infty v_\perp^3 e^{-\frac{v_\perp^2}{v_{th}^2}} dv_\perp \\
&= 0
\end{aligned}
\tag{A.8}
$$

$$\begin{aligned}
\int F_M v_\perp^2 v^2 d\boldsymbol{v} &= \frac{n}{\sqrt{\pi}^3 v_{th}^3} \int v_\perp^2 v^2 e^{-\frac{v^2}{v_{th}^2}} d\boldsymbol{v} \\
&= \frac{2\pi n}{\sqrt{\pi}^3 v_{th}^3} \iint v_\perp^3 (v_\parallel^2 + v_\perp^2) e^{-\frac{v_\perp^2}{v_{th}^2}} e^{-\frac{v_\parallel^2}{v_{th}^2}} dv_\parallel dv_\perp \\
&= \frac{2\pi n}{\sqrt{\pi}^3 v_{th}^3} \left(\iint v_\perp^3 v_\parallel^2 e^{-\frac{v_\perp^2}{v_{th}^2}} e^{-\frac{v_\parallel^2}{v_{th}^2}} dv_\parallel dv_\perp + \iint v_\perp^5 e^{-\frac{v_\perp^2}{v_{th}^2}} e^{-\frac{v_\parallel^2}{v_{th}^2}} dv_\parallel dv_\perp \right) \\
&= \frac{2\pi n}{\sqrt{\pi}^3 v_{th}^3} \left(v_{th}^3 \frac{\sqrt{\pi}}{2} v_{th}^4 \frac{1}{2} + v_{th} \sqrt{\pi} v_{th}^6 \right) \\
&= \frac{5}{2} n v_{th}^4
\end{aligned} \tag{A.9}$$

$$\begin{aligned}
\int F_M v_\parallel^2 v^2 d\boldsymbol{v} &= \frac{n}{\sqrt{\pi}^3 v_{th}^3} \int v_\parallel^2 v^2 e^{-\frac{v^2}{v_{th}^2}} d\boldsymbol{v} \\
&= \frac{2\pi n}{\sqrt{\pi}^3 v_{th}^3} \iint v_\parallel^2 v_\perp (v_\parallel^2 + v_\perp^2) e^{-\frac{v_\perp^2}{v_{th}^2}} e^{-\frac{v_\parallel^2}{v_{th}^2}} dv_\parallel dv_\perp \\
&= \frac{2\pi n}{\sqrt{\pi}^3 v_{th}^3} \left(\iint v_\perp v_\parallel^4 e^{-\frac{v_\perp^2}{v_{th}^2}} e^{-\frac{v_\parallel^2}{v_{th}^2}} dv_\parallel dv_\perp + \iint v_\perp^3 v_\parallel^2 e^{-\frac{v_\perp^2}{v_{th}^2}} e^{-\frac{v_\parallel^2}{v_{th}^2}} dv_\parallel dv_\perp \right) \\
&= \frac{2\pi n}{\sqrt{\pi}^3 v_{th}^3} \left(v_{th}^7 \frac{5\sqrt{\pi}}{8} \right) \\
&= \frac{5}{4} n v_{th}^4
\end{aligned} \tag{A.10}$$

$$\begin{aligned}
\int f v_\perp^2 d\boldsymbol{v} &= \int v_\perp^2 F_M \left(\frac{\delta n}{n} + 2\frac{\delta V_\parallel}{v_{th}} \frac{v_\parallel}{v_{th}} + \frac{\delta T}{T} (\frac{v^2}{v_{th}^2} - \frac{3}{2}) \right) d\boldsymbol{v} \\
&= \int \frac{\delta n}{n} v_\perp^2 F_M d\boldsymbol{v} + \int 2\frac{\delta V_\parallel}{v_{th}^2} v_\parallel v_\perp^2 F_M d\boldsymbol{v} + \int \frac{\delta T}{T} \frac{v^2}{v_{th}^2} v_\perp^2 F_M d\boldsymbol{v} - \int \frac{\delta T}{T} \frac{3}{2} v_\perp^2 F_M d\boldsymbol{v} \\
&= \frac{\delta n}{n} n v_{th}^2 + 0 + \frac{\delta T}{T} \frac{1}{v_{th}^2} \frac{5}{2} n v_{th}^4 - \frac{3}{2} \frac{\delta T}{T} n v_{th}^2 \\
&= \delta n v_{th}^2 + \frac{\delta T}{T} n v_{th}^2 \left(\frac{5}{2} - \frac{3}{2} \right) \\
&= \delta n v_{th}^2 + \frac{\delta T}{T} n v_{th}^2
\end{aligned} \tag{A.11}$$

$$\begin{aligned}
\int f v_\parallel^2 d\boldsymbol{v} &= \int v_\parallel^2 F_M \left(\frac{\delta n}{n} + 2\frac{\delta V_\parallel}{v_{th}} \frac{v_\parallel}{v_{th}} + \frac{\delta T}{T} (\frac{v^2}{v_{th}^2} - \frac{3}{2}) \right) d\boldsymbol{v} \\
&= \int \frac{\delta n}{n} v_\parallel^2 F_M d\boldsymbol{v} + \int 2\frac{\delta V_\parallel}{v_{th}^2} v_\parallel^3 F_M d\boldsymbol{v} + \int \frac{\delta T}{T} \frac{v^2}{v_{th}^2} v_\parallel^2 F_M d\boldsymbol{v} - \int \frac{\delta T}{T} \frac{3}{2} v_\parallel^2 F_M d\boldsymbol{v} \\
&= \frac{\delta n}{n} \frac{1}{2} n v_{th}^2 + 0 + \frac{\delta T}{T} \frac{1}{v_{th}^2} \frac{5}{4} n v_{th}^4 - \frac{3}{2} \frac{\delta T}{T} \frac{1}{2} n v_{th}^2 \\
&= \frac{1}{2} \delta n v_{th}^2 + \frac{5}{4} \frac{\delta T}{T} n v_{th}^2 - \frac{3}{4} \frac{\delta T}{T} n v_{th}^2 \\
&= \frac{1}{2} \delta n v_{th}^2 + \frac{1}{2} \frac{\delta T}{T} n v_{th}^2
\end{aligned} \tag{A.12}$$

From there, using the definition of f, we can calculate the next three integrals.

$$\begin{aligned}
\int F_M \epsilon_T d\boldsymbol{v} &= \int F_M (\frac{v^2}{v_{th}^2} - \frac{3}{2}) d\boldsymbol{v} \\
&= \int F_M \frac{v^2}{v_{th}^2} d\boldsymbol{v} - \int F_M \frac{3}{2} d\boldsymbol{v} \\
&= \frac{1}{v_{th}^2} \int F_M v^2 d\boldsymbol{v} - \frac{3}{2} \int F_M d\boldsymbol{v} \\
&= \frac{1}{v_{th}^2} \frac{3}{2} n v_{th}^2 - \frac{3}{2} n \\
&= 0
\end{aligned} \tag{A.13}$$

$$\begin{aligned}\int F_M \epsilon_D \omega_D d\boldsymbol{v} &= \omega_D \int F_M (\frac{v_\parallel^2}{v_{th}^2} + \frac{1}{2}\frac{v_\perp^2}{v_{th}^2}) d\boldsymbol{v} \\ &= \frac{\omega_D}{v_{th}^2}\left(\int F_M v_\parallel^2 d\boldsymbol{v} + \int F_M \frac{1}{2} v_\perp^2 d\boldsymbol{v}\right) \\ &= \frac{\omega_D}{v_{th}^2}\left(\frac{1}{2} n v_{th}^2 + \frac{1}{2} n v_{th}^2\right) \\ &= \omega_D n\end{aligned} \tag{A.14}$$

$$\begin{aligned}\int f \epsilon_D \omega_D d\boldsymbol{v} &= \omega_D \int f (\frac{v_\parallel^2}{v_{th}^2} + \frac{1}{2}\frac{v_\perp^2}{v_{th}^2}) d\boldsymbol{v} \\ &= \frac{\omega_D}{v_{th}^2}\left(\int f v_\parallel^2 d\boldsymbol{v} + \int f \frac{1}{2} v_\perp^2 d\boldsymbol{v}\right) \\ &= \frac{\omega_D}{v_{th}^2}\left(\frac{1}{2}\delta n v_{th}^2 + \frac{1}{2}\frac{\delta T}{T} n v_{th}^2 + \frac{1}{2}(\delta n v_{th}^2 + \frac{\delta T}{T} n v_{th}^2)\right) \\ &= \frac{\omega_D}{v_{th}^2}\left(\delta n v_{th}^2 + \frac{\delta T}{T} n v_{th}^2\right) \\ &= \omega_D\left(\delta n + \frac{\delta T}{T} n\right)\end{aligned} \tag{A.15}$$

Using the previous integrals, we obtain:

$$\int f \epsilon_D v_\parallel d\boldsymbol{v} = 2 n \delta V_\parallel \tag{A.16}$$

$$\int F_M \epsilon_T v_\parallel d\boldsymbol{v} = 0 \tag{A.17}$$

$$\int F_M \epsilon_D v_\parallel d\boldsymbol{v} = 0 \tag{A.18}$$

Using the previous integrals, we further obtain:

$$\int f v^2 \, d\boldsymbol{v} = \frac{3}{2} v_{th}^2 \left(\delta n + n \frac{\delta T}{T} \right), \tag{A.19}$$

$$\int f v^2 v_{\parallel} \, d\boldsymbol{v} = \frac{5}{2} \delta V_{\parallel} n v_{th}^2, \tag{A.20}$$

$$\int f \epsilon_D v^2 \, d\boldsymbol{v} = \frac{5}{2} v_{th}^2 \left(\delta n + 2n \frac{\delta T}{T} \right), \tag{A.21}$$

$$\int F_M \epsilon_T v^2 \, d\boldsymbol{v} = \frac{3}{2} n v_{th}^2, \tag{A.22}$$

$$\int F_M \epsilon_D v^2 \, d\boldsymbol{v} = \frac{5}{2} n v_{th}^2. \tag{A.23}$$

Bibliography

[1] G. M. Staebler, J. E. Kinsey, and R. E. Waltz. A theory-based transport model with comprehensive physics. *Physics of Plasmas*, 14:055909, 5 2007.

[2] G. M. Staebler and J. E. Kinsey. Electron collisions in the trapped gyro-landau fluid transport model. *Physics of Plasmas*, 17:122309, 12 2010.

[3] AG Peeters, Yann Camenen, F James Casson, WA Hornsby, AP Snodin, D Strintzi, and Gabor Szepesi. The nonlinear gyro-kinetic flux tube code gkw. *Computer physics communications*, 180(12):2650–2672, 2009.

[4] Frédéric Imbeaux, SD Pinches, JB Lister, Y Buravand, T Casper, Basil Duval, B Guillerminet, Masanari Hosokawa, Wayne Houlberg, Philippe Huynh, et al. Design and first applications of the iter integrated modelling & analysis suite. *Nuclear Fusion*, 55(12):123006, 2015.

[5] S. Moradi, I. Pusztai, I. Voitsekhovitch, L. Garzotti, C. Bourdelle, M.J. Pueschel, I. Lupelli, M. Romanelli, and the JET-EFDA Contributors. Core micro-instability analysis of jet hybrid and baseline discharges with carbon wall. *Nuclear Fusion*, 54(12):123016, nov 2014.

[6] G Staebler, C Bourdelle, J Citrin, and R Waltz. Quasilinear theory and modelling of gyrokinetic turbulent transport in tokamaks. *Nuclear Fusion*, 64(10):103001, 2024.

[7] A.G. Peeters, Y. Camenen, F.J. Casson, W.A. Hornsby, A.P. Snodin, D. Strintzi, and G. Szepesi. The nonlinear gyro-kinetic flux tube code gkw. *Computer Physics Communications*, 180(12):2650–2672, 2009.

[8] Y. Camenen, F. Imbeaux, G. Fuhr, and et al. Design and first applications of the imas interface data structure for flux-tube gyrokinetic simulations. *Submitted to Open Plasma Science*, 2024.

[9] SD Pinches, JF Artaud, FJ Casson, G Corrigan, M De Bock, M Dubrov, D Harting, J Hollocombe, M Hosokawa, F Imbeaux, et al. Progress in the iter integrated modelling programme and the iter scenario database. In *Preprint: 2018 IAEA Fusion Energy Conf.*, pages TH–P6, 2018.

[10] G.M. Staebler et al. R.E. Waltz. A gyro-landau-fluid transport model. *Phys. Plasmas*, 4:2482, 1997.

[11] JE Kinsey, GM Staebler, and RE Waltz. The first transport code simulations using the trapped gyro-landau-fluid model. *Physics of Plasmas*, 15(5), 2008.

[12] N. Kumar, Y. Camenen, S. Benkadda, C. Bourdelle, A. Loarte, A.R. Polevoi, F. Widmer, and JET contributors. Turbulent transport driven by kinetic ballooning modes in the inner core of jet hybrid h-modes. *Nuclear Fusion*, 61(3):036005, jan 2021.

[13] V. Mukhovatov, Y. Shimomura, A. Polevoi, M. Shimada, M. Sugihara, G. Bateman, J.G. Cordey, O. Kardaun, G. Pereverzev, I. Voitsekhovich, J. Weiland, O. Zolotukhin, A. Chudnovskiy, A.H. Kritz, A. Kukushkin, T. Onjun, A. Pankin, and F.W. Perkins. Comparison of iter performance predicted by semi-empirical and theory-based transport models. *Nuclear Fusion*, 43(9):942, aug 2003.

[14] T. Fujita, T. Hatae, T. Oikawa, S. Takeji, H. Shirai, Y. Koide, S. Ishida, S. Ide, Y. Ishii, T. Ozeki, S. Higashijima, R. Yoshino, Y. Kamada, and Y. Neyatani. High performance reversed shear plasmas with a large radius transport barrier in jt-60u. *Nuclear Fusion*, 38(2):207, feb 1998.

[15] H. Kishimoto, S. Ishida, M. Kikuchi, and H. Ninomiya. Advanced tokamak research on jt-60. *Nuclear Fusion*, 45(8):986, aug 2005.

[16] R. J. Hawryluk, S. Batha, W. Blanchard, M. Beer, M. G. Bell, R. E. Bell, H. Berk, S. Bernabei, M. Bitter, B. Breizman, N. L. Bretz, R. Budny, C. E. Bush, J. Callen, R. Camp, S. Cauffman, Z. Chang, C. Z. Cheng, D. S. Darrow, R. O. Dendy, W. Dorland, H. Duong, P. C. Efthimion, D. Ernst, N. J. Fisch, R. Fisher, R. J. Fonck, E. D. Fredrickson, G. Y. Fu, H. P. Furth, N. N. Gorelenkov, B. Grek, L. R. Grisham, G. W. Hammett, G. R. Hanson, H. W. Herrmann, M. C. Herrmann, K. W. Hill, J. Hogan, J. C. Hosea, W. A. Houlberg, M. Hughes, R. A. Hulse, D. L. Jassby, F. C. Jobes, D. W. Johnson, R. Kaita, S. Kaye, J. S. Kim, M. Kissick, A. V. Krasilnikov, H. Kugel, A. Kumar, B. Leblanc, F. M. Levinton, C. Ludescher, R. P. Majeski, J. Manickam, D. K. Mansfield, E. Mazzucato, J. McChesney, D. C. McCune, K. M. McGuire, D. M. Meade, S. S. Medley, R. Mika, D. R. Mikkelsen, S. V. Mirnov, D. Mueller, A. Nagy, G. A. Navratil, R. Nazikian, M. Okabayashi, H. K. Park, W. Park, S. F. Paul, G. Pearson, M. P. Petrov, C. K. Phillips, M. Phillips, A. T. Ramsey, M. H. Redi, G. Rewoldt, S. Reznik, A. L. Roquemore, J. Rogers, E. Ruskov, S. A. Sabbagh, M. Sasao, G. Schilling, J. Schivell, G. L. Schmidt, S. D. Scott, I. Semenov, C. H. Skinner, T. Stevenson, B. C. Stratton, J. D. Strachan, W. Stodiek, E. Synakowski, H. Takahashi, W. Tang, G. Taylor, M. E. Thompson, S. Von Goeler, A. Von Halle, R. T. Walters, R. White, R. M. Wieland, M. Williams, J. R. Wilson, K. L. Wong, G. A. Wurden, M. Yamada, V. Yavorski, K. M. Young, L. Zakharov, M. C. Zarnstorff, and S. J. Zweben. Fusion plasma experiments on tftr: A 20 year retrospective. *Physics of Plasmas*, 5(5):1577–1589, 05 1998.

[17] JET Team. Fusion energy production from a deuterium-tritium plasma in the jet tokamak. *Nuclear Fusion*, 32(2):187, feb 1992.

[18] M. Greenwald, D. Gwinn, S. Milora, J. Parker, R. Parker, S. Wolfe, M. Besen, F. Camacho, S. Fairfax, C. Fiore, M. Foord, R. Gandy, C. Gomez, R. Granetz, B. LaBombard, B. Lipschultz, B. Lloyd, E. Marmar, S. McCool, D. Pappas, R. Petrasso, P. Pribyl, J. Rice, D. Schuresko, Y. Takase, J. Terry, and R. Watterson. Energy confinement of high-density pellet-fueled plasmas in the alcator *c* tokamak. *Phys. Rev. Lett.*, 53:352–355, Jul 1984.

[19] D Grove, V Arunasalam, K Bol, N Bretz, M Brusati, S Cohen, D Dimock, F Dylla, D Eames, and D Boyd. Experimental results of the plt tokamak. *Plasma Physics and Controlled Nuclear Fusion Research 1976, Volume 1*, 1:21–32, 1977.

[20] TFR Group. Tfr, the tokamak of fontenay-aux-roses. *Nuclear Fusion*, 25(9):1025, sep 1985.

[21] W. Stodiek. Experiments on the st tokamak. *Nuclear Fusion*, 25(9):1161, sep 1985.

[22] N. J. PEACOCK, D. C. ROBINSON, M. J. FORREST, P. D. WILCOCK, and V. V. SANNIKOV. Measurement of the electron temperature by thomson scattering in tokamak t3. *Nature*, 224(5218):488–490, 1969.

[23] PC Thonemann, EP Butt, R Carruthers, AN Dellis, DW Fry, A Gibson, GN Harding, DJ Lees, R WP McWhirter, RS Pease, et al. Production of high temperatures and nuclear reactions in a gas discharge. *Nature*, 181, 1958.

[24] EUROFusion, https://www.euro-fusion.org.

[25] EDA ITER et al. Mhd stability, operational limits and disruptions. *Nuclear Fusion*, 39(12 ITER physics basis):2251–2389, 1999.

[26] *BP Energy Outlook*. 2024. Available at: https://www.bp.com/en/global/corporate/energy-economics/energy-outlook.html.

[27] IEA (2023), World Energy Outlook 2023, IEA, Paris https://www.iea.org/reports/world-energy-outlook-2023, Licence: CC BY 4.0 (report); CC BY NC SA 4.0 (Annex A).

[28] IEA (2023), Net Zero Roadmap: A Global Pathway to Keep the 1.5 °C Goal in Reach, IEA, Paris https://www.iea.org/reports/net-zero-roadmap-a-global-pathway-to-keep-the-15-0c-goal-in-reach, Licence: CC BY 4.0.

[29] IEA (2023), Credible pathways to 1.5°C, IEA, Paris https://www.iea.org/reports/credible-pathways-to-150c, Licence: CC BY 4.0.

[30] IEA (2024), CO2 Emissions in 2023, IEA, Paris https://www.iea.org/reports/co2-emissions-in-2023, Licence: CC BY 4.0.

[31] R. d. E. Atkinson and F. G. Houtermans. Zur frage der aufbaumöglichkeit der elemente in sternen. *Zeitschrift für Physik*, 54:656–665, 1929.

[32] Marcus Laurence Elwin Oliphant, P. Harteck, and Ernest Rutherford. Transmutation effects observed with heavy hydrogen. *Proceedings of the Royal Society of London. Series A, Containing Papers of a Mathematical and Physical Character*, 144(853):692–703, 1934.

[33] H. A. Bethe. Energy production in stars. *Phys. Rev.*, 55:434–456, Mar 1939.

[34] Matteo Barbarino. A brief history of nuclear fusion. *Nature Physics*, 16(9):890–893, 2020.

[35] ITER https://www.iter.org/fr.

[36] M. Kovari, M. Coleman, I. Cristescu, and R. Smith. Tritium resources available for fusion reactors. *Nuclear Fusion*, 58(2):026010, dec 2017.

[37] Santacruz Banacloche, Ana R. Gamarra, Yolanda Lechon, and Chiara Bustreo. Socioeconomic and environmental impacts of bringing the sun to earth: A sustainability analysis of a fusion power plant deployment. *Energy*, 209:118460, 2020.

[38] H.-S. Bosch and G.M. Hale. Improved formulas for fusion cross-sections and thermal reactivities. *Nuclear Fusion*, 32(4):611, apr 1992.

[39] D.A. Brown, M.B. Chadwick, R. Capote, A.C. Kahler, A. Trkov, M.W. Herman, A.A. Sonzogni, Y. Danon, A.D. Carlson, M. Dunn, D.L. Smith, G.M. Hale, G. Arbanas, R. Arcilla, C.R. Bates, B. Beck, B. Becker, F. Brown, R.J. Casperson, J. Conlin, D.E. Cullen, M.-A. Descalle, R. Firestone, T. Gaines, K.H. Guber, A.I. Hawari, J. Holmes, T.D. Johnson, T. Kawano, B.C. Kiedrowski, A.J. Koning, S. Kopecky, L. Leal, J.P. Lestone, C. Lubitz, J.I. Márquez Damián, C.M. Mattoon, E.A. McCutchan, S. Mughabghab, P. Navratil, D. Neudecker, G.P.A. Nobre, G. Noguere, M. Paris, M.T. Pigni, A.J. Plompen, B. Pritychenko, V.G. Pronyaev, D. Roubtsov, D. Rochman, P. Romano, P. Schillebeeckx, S. Simakov, M. Sin, I. Sirakov, B. Sleaford, V. Sobes, E.S. Soukhovitskii, I. Stetcu, P. Talou, I. Thompson, S. van der Marck, L. Welser-Sherrill, D. Wiarda, M. White, J.L. Wormald, R.Q. Wright, M. Zerkle, G. Žerovnik, and Y. Zhu. Endf/b-viii.0: The 8th major release of the nuclear reaction data library with cielo-project cross sections, new standards and thermal scattering data. *Nuclear Data Sheets*, 148:1–142, 2018. Special Issue on Nuclear Reaction Data.

[40] Jeffrey P Freidberg. *Plasma physics and fusion energy*. Cambridge university press, 2008.

[41] John Wesson and David J Campbell. *Tokamaks*, volume 149. Oxford university press, 2011.

[42] M. Shimada, V. Mukhovatov, G. Federici, Y. Gribov, A. Kukushkin, Y. Murakami, A. Polevoi, V. Pustovitov, S. Sengoku, and M. Sugihara. Performance of iter as a burning plasma experiment. *Nuclear Fusion*, 44(2):350, jan 2004.

[43] Breanna Bishop. National ignition facility achieves fusion ignition. *Lawrence Livermore National Laboratory, December*, 14, 2022.

[44] A. B. Zylstra, A. L. Kritcher, O. A. Hurricane, D. A. Callahan, J. E. Ralph, D. T. Casey, A. Pak, O. L. Landen, B. Bachmann, K. L. Baker, L. Berzak Hopkins, S. D. Bhandarkar, J. Biener, R. M. Bionta, N. W. Birge, T. Braun, T. M. Briggs, P. M. Celliers, H. Chen, C. Choate, D. S. Clark, L. Divol, T. Döppner, D. Fittinghoff, M. J. Edwards, M. Gatu Johnson, N. Gharibyan, S. Haan, K. D. Hahn, E. Hartouni, D. E. Hinkel, D. D. Ho, M. Hohenberger, J. P. Holder, H. Huang, N. Izumi, J. Jeet, O. Jones, S. M. Kerr, S. F. Khan, H. Geppert Kleinrath, V. Geppert Kleinrath, C. Kong, K. M. Lamb, S. Le Pape, N. C. Lemos, J. D. Lindl, B. J. MacGowan, A. J. Mackinnon, A. G. MacPhee, E. V. Marley, K. Meaney, M. Millot, A. S. Moore, K. Newman, J.-M. G. Di Nicola, A. Nikroo, R. Nora, P. K. Patel, N. G. Rice, M. S. Rubery, J. Sater, D. J. Schlossberg, S. M. Sepke, K. Sequoia, S. J. Shin, M. Stadermann, S. Stoupin, D. J. Strozzi, C. A. Thomas, R. Tommasini, C. Trosseille, E. R. Tubman, P. L. Volegov, C. R. Weber, C. Wild, D. T. Woods, S. T. Yang, and C. V. Young. Experimental achievement and signatures of ignition at the national ignition facility. *Phys. Rev. E*, 106:025202, Aug 2022.

[45] R.L. McCrory, R.E. Bahr, R. Betti, T.R. Boehly, T.J.B. Collins, R.S. Craxton, J.A. Delettrez, W.R. Donaldson, R. Epstein, J. Frenje, V.Yu. Glebov, V.N. Goncharov, O.V. Gotchev, R.Q. Gram, D.R. Harding, D.G. Hicks, P.A. Jaanimagi, R.L. Keck, J.H. Kelly, J.P. Knauer, C.K. Li, S.J. Loucks, L.D. Lund, F.J. Marshall, P.W. McKenty, D.D. Meyerhofer, S.F.B. Morse, R.D. Petrasso, P.B. Radha, S.P. Regan, S. Roberts, F. Séguin, W. Seka, S. Skupsky, V.A. Smalyuk, C. Sorce, J.M. Soures, C. Stoeckl, R.P.J. Town, M.D. Wittman, B. Yaakobi, and J.D. Zuegel. Omega icf experiments and preparation for direct drive ignition on nif. *Nuclear Fusion*, 41(10):1413, oct 2001.

[46] H Shiraga, S Fujioka, M Nakai, T Watari, H Nakamura, Y Arikawa, H Hosoda, T Nagai, M Koga, H Kikuchi, Y Ishii, T Sogo, K Shigemori, H Nishimura, Z Zhang, M Tanabe, S Ohira, Y Fujii, T Namimoto, Y Sakawa, O Maegawa, T Ozaki, K Tanaka, H Habara, T Iwawaki, K Shimada, H Nagatomo, T Johzaki, A Sunahara, M Murakami, H Sakagami, T Taguchi, T Norimatsu, H Homma, Y Fujimoto, A Iwamoto, N Miyanaga, J Kawanaka, T Jitsuno, Y Nakata, K Tsubakimoto, N Morio, T Kawasaki, K Sawai, K Tsuji, H Murakami, T Kanabe, K Kondo, N Sarukura, T Shimizu, K Mima, and H Azechi. Fast ignition integrated experiments with gekko and lfex lasers. *Plasma Physics and Controlled Fusion*, 53(12):124029, nov 2011.

[47] Michel Laberge. Magnetized target fusion with a spherical tokamak. *Journal of Fusion Energy*, 38(1):199–203, 2019.

[48] Egbert Westerhof. Non-inductive current drive. *Fusion Science and Technology*, 61(2T):312–319, 2012.

[49] Rameswar Singh, P. K. Kaw, R. Singh, and Ö. D. Gürcan. Intrinsic non-inductive current driven by etg turbulence in tokamaks. *Physics of Plasmas*, 24(10):102303, 09 2017.

[50] V.S. Mukhovatov and V.D. Shafranov. Plasma equilibrium in a tokamak. *Nuclear Fusion*, 11(6):605, dec 1971.

[51] JF Clarke and DJ Sigmar. High-pressure flux-conserving tokamak equilibria. *Physical Review Letters*, 38(2):70, 1977.

[52] MW Kissick, J-N Leboeuf, and SE Kruger. On the poloidal beta evolution of fixed-q heating in tokamaks. *Physics of Plasmas*, 10(4):1060–1065, 2003.

[53] A Sykes, JA Wesson, and SJ Cox. High-β tokamaks. *Physical Review Letters*, 39(12):757, 1977.

[54] A.E. Costley. On the fusion triple product and fusion power gain of tokamak pilot plants and reactors. *Nuclear Fusion*, 56(6):066003, apr 2016.

[55] Y. Sarazin, J. Hillairet, J.-L. Duchateau, K. Gaudimont, R. Varennes, X. Garbet, Ph. Ghendrih, R. Guirlet, B. Pégourié, and A. Torre. Impact of scaling laws on tokamak reactor dimensioning. *Nuclear Fusion*, 60(1):016010, oct 2019.

[56] E Joffrin, ACC Sips, JF Artaud, A Becoulet, L Bertalot, R Budny, P Buratti, P Belo, CD Challis, F Crisanti, et al. The 'hybrid'scenario in jet: towards its validation for iter. *Nuclear fusion*, 45(7):626, 2005.

[57] C Gormezano, CD Challis, E Joffrin, X Litaudon, and ACC Sips. Chapter 4: Advanced tokamak scenario development at jet. *Fusion science and technology*, 53(4):958–988, 2008.

[58] JET Team et al. Jet results with the new pumped divertor and implications for iter. *Plasma Physics and Controlled Fusion*, 37(11A):A3, 1995.

[59] TC Luce, MR Wade, PA Politzer, SL Allen, ME Austin, DR Baker, B Bray, DP Brennan, KH Burrell, TA Casper, et al. Long pulse high performance discharges in the diii-d tokamak. *Nuclear fusion*, 41(11):1585, 2001.

[60] ACC Sips, GD Conway, R Dux, A Herrmann, J Hobirk, O Gruber, S Günter, C Maggi, M Manso, M Maraschek, et al. Progress towards steady-state advanced scenarios in asdex upgrade. *Plasma physics and controlled fusion*, 44(5A):A151, 2002.

[61] J Hobirk, F Imbeaux, F Crisanti, P Buratti, CD Challis, E Joffrin, B Alper, Y Andrew, P Beaumont, M Beurskens, et al. Improved confinement in jet hybrid discharges. *Plasma Physics and Controlled Fusion*, 54(9):095001, 2012.

[62] YK M Peng and Dennis J Strickler. Features of spherical torus plasmas. *Nuclear fusion*, 26(6):769, 1986.

[63] Alan Sykes, START Team, NBI Team, MAST Team, et al. The spherical tokamak programme at culham. *Nuclear Fusion*, 39(9Y):1271, 1999.

[64] Franco Paoletti, SA Sabbagh, J Manickam, J Menard, RJ Akers, D Gates, SM Kaye, and L Lao. Impact of mhd equilibrium input variations on the high beta stability boundaries of nstx. *Nuclear fusion*, 42(4):418, 2002.

[65] JE Menard, MG Bell, RE Bell, ED Fredrickson, DA Gates, SM Kaye, CE Bush, DW Johnson, R Kaita, HW Kugel, et al. Beta-limiting mhd instabilities in improved performance nstx spherical torus plasmas. *in Fusion Energy*, 2002.

[66] Martin Greenwald, JL Terry, SM Wolfe, S Ejima, MG Bell, SM Kaye, and GH Neilson. A new look at density limits in tokamaks. *Nuclear Fusion*, 28(12):2199, 1988.

[67] Francis Troyon and R Gruber. A semi-empirical scaling law for the β-limit in tokamaks. *Physics Letters A*, 110(1):29–34, 1985.

[68] F Troyon, A Roy, W A Cooper, F Yasseen, and A Turnbull. Beta limit in tokamaks. experimental and computational status. *Plasma Physics and Controlled Fusion*, 30(11):1597, oct 1988.

[69] M. Giacomin, A. Pau, P. Ricci, O. Sauter, T. Eich, the ASDEX Upgrade team, JET Contributors, and the TCV team. First-principles density limit scaling in tokamaks based on edge turbulent transport and implications for iter. *Physical Review Letters*, 128:185003, 5 2022.

[70] E. J. Strait. Stability of high beta tokamak plasmas*. *Physics of Plasmas*, 1(5):1415–1431, 05 1994.

[71] SI Braginskii and MA Leontovich. Reviews of plasma physics, 1965.

[72] Clemente Angioni. Impurity transport in tokamak plasmas, theory, modelling and comparison with experiments. *Plasma Physics and Controlled Fusion*, 63(7):073001, 2021.

[73] P Helander. Classical and neoclassical transport in tokamaks. *Fusion Science and Technology*, 61(2T):133–141, 2012.

[74] FL Hinton and Richard D Hazeltine. Theory of plasma transport in toroidal confinement systems. *Reviews of Modern Physics*, 48(2):239, 1976.

[75] C Gillot, G Dif-Pradalier, Y Sarazin, C Bourdelle, A Bañón Navarro, Y Camenen, J Citrin, A Di Siena, X Garbet, Ph Ghendrih, V Grandgirard, P Manas, and F Widmer. The problem of capturing marginality in model reductions of turbulence. *Plasma Physics and Controlled Fusion*, 65(5):055012, mar 2023.

[76] Xavier Garbet, Yasuhiro Idomura, Laurent Villard, and TH Watanabe. Gyrokinetic simulations of turbulent transport. *Nuclear Fusion*, 50(4):043002, 2010.

[77] Francesca Maria Poli. Integrated tokamak modeling: when physics informs engineering and research planning. *Physics of Plasmas*, 25(5), 2018.

[78] Alain J Brizard and Taik Soo Hahm. Foundations of nonlinear gyrokinetic theory. *Reviews of modern physics*, 79(2):421–468, 2007.

[79] Setsuo Ichimaru. *Statistical plasma physics, volume I: basic principles*. CRC Press, 2018.

[80] Zhihong Lin, Taik Soo Hahm, WW Lee, William M Tang, and Roscoe B White. Turbulent transport reduction by zonal flows: Massively parallel simulations. *Science*, 281(5384):1835–1837, 1998.

[81] Y Idomura, S Tokuda, and Y Kishimoto. Global gyrokinetic simulation of ion temperature gradient driven turbulence in plasmas using a canonical maxwellian distribution. *Nuclear Fusion*, 43(4):234, 2003.

[82] S Jolliet, Alberto Bottino, P Angelino, Roman Hatzky, Trach-Minh Tran, BF Mcmillan, O Sauter, K Appert, Yasuhiro Idomura, and Laurent Villard. A global collisionless pic code in magnetic coordinates. *Computer Physics Communications*, 177(5):409–425, 2007.

[83] Mike Kotschenreuther, G Rewoldt, and WM Tang. Comparison of initial value and eigenvalue codes for kinetic toroidal plasma instabilities. *Computer Physics Communications*, 88(2-3):128–140, 1995.

[84] W Dorland, F Jenko, Mike Kotschenreuther, and BN Rogers. Electron temperature gradient turbulence. *Physical review letters*, 85(26):5579, 2000.

[85] Frank Jenko. Massively parallel vlasov simulation of electromagnetic drift-wave turbulence. *Computer physics communications*, 125(1-3):196–209, 2000.

[86] Florian Merz. *Gyrokinetic simulation of multimode plasma turbulence*. PhD thesis, Universität Münster Münster, 2008.

[87] Jeff Candy and RE Waltz. An eulerian gyrokinetic-maxwell solver. *Journal of Computational Physics*, 186(2):545–581, 2003.

[88] Yasuhiro Idomura, H Urano, Nobuyuki Aiba, and S Tokuda. Study of ion turbulent transport and profile formations using global gyrokinetic full-f vlasov simulation. *Nuclear Fusion*, 49(6):065029, 2009.

[89] Yasuhiro Idomura, Masato Ida, Takuma Kano, Nobuyuki Aiba, and Shinji Tokuda. Conservative global gyrokinetic toroidal full-f five-dimensional vlasov simulation. *Computer Physics Communications*, 179(6):391–403, 2008.

[90] Virginie Grandgirard, Jérémie Abiteboul, Julien Bigot, Thomas Cartier-Michaud, Nicolas Crouseilles, Guilhem Dif-Pradalier, Ch Ehrlacher, Damien Esteve, Xavier Garbet, Ph Ghendrih, et al. A 5d gyrokinetic full-f global semi-lagrangian code for flux-driven ion turbulence simulations. *Computer physics communications*, 207:35–68, 2016.

[91] Ben F McMillan, X Lapillonne, S Brunner, L Villard, S Jolliet, A Bottino, T Görler, and F Jenko. System size effects on gyrokinetic turbulence. *Physical Review Letters*, 105(15):155001, 2010.

[92] Alejandro Bañón Navarro, Daniel Told, Frank Jenko, Tobias Görler, Tim Happel, ASDEX Upgrade Team, et al. Comparisons between global and local gyrokinetic simulations of an asdex upgrade h-mode plasma. *Physics of Plasmas*, 23(4), 2016.

[93] A Di Siena, T Hayward-Schneider, P Mantica, J Citrin, F Vannini, A Bottino, T Görler, E Poli, R Bilato, O Sauter, et al. How accurate are flux-tube (local) gyrokinetic codes in modeling energetic particle effects on core turbulence? *Nuclear Fusion*, 63(10):106012, 2023.

[94] J Candy. Beta scaling of transport in microturbulence simulations. *Physics of Plasmas*, 12(7), 2005.

[95] Moritz J Pueschel, M Kammerer, and F Jenko. Gyrokinetic turbulence simulations at high plasma beta. *Physics of Plasmas*, 15(10), 2008.

[96] DR Hatch, MJ Pueschel, F Jenko, WM Nevins, PW Terry, and H Doerk. Origin of magnetic stochasticity and transport in plasma microturbulence. *Physical review letters*, 108(23):235002, 2012.

[97] MJ Pueschel, PW Terry, F Jenko, DR Hatch, WM Nevins, T Görler, and D Told. Extreme heat fluxes in gyrokinetic simulations: a new critical β. *Physical Review Letters*, 110(15):155005, 2013.

[98] Michael Alan Beer. *Gyrofluid models of turbulent transport in tokamaks*. Princeton University, 1995.

[99] William Douglass Dorland. *Gyrofluid models of plasma turbulence*. Princeton University, 1993.

[100] Harry George Dudding. A new quasilinear saturation rule for tokamak turbulence. October 2022.

[101] A. Casati, C. Bourdelle, X. Garbet, F. Imbeaux, J. Candy, F. Clairet, G. Dif-Pradalier, G. Falchetto, T. Gerbaud, V. Grandgirard, Ö.D. Gürcan, P. Hennequin, J. Kinsey, M. Ottaviani, R. Sabot, Y. Sarazin, L. Vermare, and R.E. Waltz. Validating a quasi-linear transport model versus nonlinear simulations. *Nuclear Fusion*, 49(8):085012, jul 2009.

[102] Tilman Dannert and Frank Jenko. Gyrokinetic simulation of collisionless trapped-electron mode turbulence. *Physics of Plasmas*, 12(7):072309, 07 2005.

[103] D. Told, F. Jenko, T. Görler, F. J. Casson, E. Fable, and ASDEX Upgrade Team. Characterizing turbulent transport in asdex upgrade l-mode plasmas via nonlinear gyrokinetic simulations. *Physics of Plasmas*, 20(12):122312, 12 2013.

[104] N. Bonanomi, C. Angioni, U. Plank, P. A. Schneider, C. F. Maggi, ASDEX Upgrade Team, EUROFusion MST1 Team, and JET Contributors. Edge turbulent transport toward the l–h transition in asdex upgrade and jet-ilw. *Physics of Plasmas*, 28(5):052504, 05 2021.

[105] JE Kinsey, RE Waltz, and JC DeBoo. Perturbative tests of theoretical transport models using cold pulse and modulated electron cyclotron heating experiments. *Physics of Plasmas*, 6(5):1865–1871, 1999.

[106] G. M. Staebler, J. Candy, N. T. Howard, and C. Holland. The role of zonal flows in the saturation of multi-scale gyrokinetic turbulence. *Physics of Plasmas*, 23:062518, 6 2016.

[107] Thomas M Antonsen Jr and Barton Lane. Kinetic equations for low frequency instabilities in inhomogeneous plasmas. *The Physics of Fluids*, 23(6):1205–1214, 1980.

[108] G. M. Staebler, J. E. Kinsey, and R. E. Waltz. Gyro-landau fluid equations for trapped and passing particles. *Physics of Plasmas*, 12:102508, 10 2005.

[109] RL Miller, Ming-Sheng Chu, JM Greene, YR Lin-Liu, and RE Waltz. Noncircular, finite aspect ratio, local equilibrium model. *Physics of Plasmas*, 5(4):973–978, 1998.

[110] Gary M Staebler, Jeffrey Candy, Emily A Belli, Jon E Kinsey, N Bonanomi, and Bhavin Patel. Geometry dependence of the fluctuation intensity in gyrokinetic turbulence. *Plasma Physics and Controlled Fusion*, 63(1):015013, 2020.

[111] G.M. Staebler, E. A. Belli, J. Candy, J.E. Kinsey, H. Dudding, and B. Patel. Verification of a quasi-linear model for gyrokinetic turbulent transport. *Nuclear Fusion*, 61:116007, 11 2021.

[112] C. Angioni, J. Citrin, A. Loarte, A. Polevoi, S. Kim, E. Fable, and G. Tardini. Determining the access to h-mode in the iter pre-fusion and fusion power operation phases at low plasma current with full-radius tglf-sat2 simulations of l-mode plasmas. *Nuclear Fusion*, 63, 1 2023.

[113] H.G. Dudding, F.J. Casson, D. Dickinson, B.S. Patel, C.M. Roach, E.A. Belli, and G.M. Staebler. A new quasilinear saturation rule for tokamak turbulence with application to the isotope scaling of transport. *Nuclear Fusion*, 62:096005, 9 2022.

[114] BA Grierson, GM Staebler, WM Solomon, GR McKee, C Holland, M Austin, A Marinoni, L Schmitz, RI Pinsker, DIII-D Team, et al. Multi-scale transport in the diii-d iter baseline scenario with direct electron heating and projection to iter. *Physics of Plasmas*, 25(2), 2018.

[115] KE Thome, XD Du, BA Grierson, GJ Kramer, CC Petty, C Holland, M Knolker, GR McKee, J McClenaghan, DC Pace, et al. Response of thermal and fast-ion transport to beam ion population, rotation and t e/t i in the diii-d steady state hybrid scenario. *Nuclear Fusion*, 61(3):036036, 2021.

[116] Stanley M Kaye, DJ Battaglia, D Baver, Elena Belova, JW Berkery, Vinicius N Duarte, N Ferraro, E Fredrickson, N Gorelenkov, Walter Guttenfelder, et al. Nstx/nstx-u theory, modeling and analysis results. *Nuclear Fusion*, 59(11):112007, 2019.

[117] C Angioni, T Gamot, G Tardini, E Fable, T Luda, N Bonanomi, CK Kiefer, GM Staebler, ASDEX Upgrade Team, EUROfusion MST1 Team, et al. Confinement properties of l-mode plasmas in asdex upgrade and full-radius predictions of the tglf transport model. *Nuclear Fusion*, 62(6):066015, 2022.

[118] Hyun-Tae Kim, Fulvio Auriemma, Jorge Ferreira, Stefano Gabriellini, Aaron Ho, Philippe Huynh, Krassimir Kirov, Rita Lorenzini, Michele Marin, Michal Poradzinski, et al. Validation of d–t fusion power prediction capability against 2021 jet d–t experiments. *Nuclear Fusion*, 63(11):112004, 2023.

[119] IMAS Gyrokinetics https://gitlab.com/gkdb/imas-gk/-/tree/main/tools/tglf.

[120] R Arbon, J Candy, and E A Belli. Rapidly-convergent flux-surface shape parameterization. *Plasma Physics and Controlled Fusion*, 63:012001, 1 2021.

[121] J Candy. A unified method for operator evaluation in local grad-shafranov plasma equilibria. *Plasma Physics and Controlled Fusion*, 51:105009, 10 2009.

[122] F Ryter, C Angioni, AG Peeters, F Leuterer, H-U Fahrbach, W Suttrop, and (ASDEX Upgrade Team). Experimental study of trapped-electron-mode properties in tokamaks: Threshold and stabilization by collisions. *Physical review letters*, 95(8):085001, 2005.

[123] Ft Romanelli. Ion temperature-gradient-driven modes and anomalous ion transport in tokamaks. *Physics of Fluids B: Plasma Physics*, 1(5):1018–1025, 1989.

[124] SC Guo and F Romanelli. The linear threshold of the ion-temperature-gradient-driven mode. *Physics of Fluids B: Plasma Physics*, 5(2):520–533, 1993.

[125] Shanni Huang, Weixin Guo, and Lu Wang. Impurity transport driven by kinetic ballooning mode in the strong gradient pedestal of tokamak plasmas. *Nuclear Fusion*, 2024.

[126] Maurizio Giacomin, Daniel Kennedy, FJ Casson, CJ Ajay, David Dickinson, BS Patel, and CM Roach. On electromagnetic turbulence and transport in step. *Plasma Physics and Controlled Fusion*, 66(5):055010, 2024.

[127] *GKW manual*. Available at: http://www.gkw.org.uk/tikiwiki/Manual.

[128] P Migliano, David Zarzoso, FJ Artola, Y Camenen, and X Garbet. An improved approximation for the analytical treatment of the local linear gyro-kinetic plasma dispersion relation in toroidal geometry. *Plasma Physics and Controlled Fusion*, 59(9):095004, 2017.

[129] R.J. Groebner, P.B. Snyder, T.H. Osborne, A.W. Leonard, T.L. Rhodes, L. Zeng, E.A. Unterberg, Z. Yan, G.R. McKee, C.J. Lasnier, J.A. Boedo, and J.G. Watkins. Limits to the h-mode pedestal pressure gradient in diii-d. *Nuclear Fusion*, 50(6):064002, may 2010.

[130] Weigang Wan, Scott E. Parker, Yang Chen, Zheng Yan, Richard J. Groebner, and Philip B. Snyder. Global gyrokinetic simulation of tokamak edge pedestal instabilities. *Phys. Rev. Lett.*, 109:185004, Nov 2012.

[131] D.R. Hatch, D. Told, F. Jenko, H. Doerk, M.G. Dunne, E. Wolfrum, E. Viezzer, The ASDEX Upgrade Team, and M.J. Pueschel. Gyrokinetic study of asdex upgrade inter-elm pedestal profile evolution. *Nuclear Fusion*, 55(6):063028, may 2015.

[132] A. Mariani, P. Mantica, I. Casiraghi, J. Citrin, T. Görler, G.M. Staebler, and EUROfusion JET1 contributors. Benchmark of quasi-linear models against gyrokinetic single scale simulations in deuterium and tritium plasmas for a jet high beta hybrid discharge. *Nuclear Fusion*, 61(6):066032, may 2021.

[133] S Y Zheng, D B Zhang, L M Yu, X M Zhang, E B Xue, L J Ma, R Z Tang, J Huang, Y Xiao, M Q Wu, L Ye, X Z Gong, and EAST Team. Gyrokinetic simulation of electromagnetic instabilities in the high betap scenario on east. *Plasma Physics and Controlled Fusion*, 65(7):075012, jun 2023.

[134] J Citrin and P Mantica. Overview of tokamak turbulence stabilization by fast ions. *Plasma Physics and Controlled Fusion*, 65(3):033001, jan 2023.

[135] Jan Weiland and Akira Hirose. Electromagnetic and kinetic effects on the ion temperature gradient mode. *Nuclear Fusion*, 32(1):151, 1992.

[136] JY Kim, W Horton, and JQ Dong. Electromagnetic effect on the toroidal ion temperature gradient mode. *Physics of Fluids B: Plasma Physics*, 5(11):4030–4039, 1993.

[137] A Hirose. On finite β stabilization of the toroidal ion temperature gradient mode. *Physics of Plasmas*, 7(2):433–436, 2000.

[138] J. Citrin, P. Trochim, T. Goerler, D. Pfau, K. L. van de Plassche, and F. Jenko. Fast transport simulations with higher-fidelity surrogate models for iter. *Physics of Plasmas*, 30, 6 2023.

[139] G.G. Whelan, M.J. Pueschel, and P.W. Terry. Nonlinear electromagnetic stabilization of plasma microturbulence. *Physical Review Letters*, 120:175002, 4 2018.

[140] Jonathan Citrin, F Jenko, P Mantica, D Told, C Bourdelle, J Garcia, JW Haverkort, GMD Hogeweij, Thomas Johnson, and MJ Pueschel. Nonlinear stabilization of tokamak microturbulence by fast ions. *Physical review letters*, 111(15):155001, 2013.

[141] J Citrin, F Jenko, P Mantica, D Told, C Bourdelle, R Dumont, J Garcia, JW Haverkort, GMD Hogeweij, Thomas Johnson, et al. Ion temperature profile stiffness: non-linear gyrokinetic simulations and comparison with experiment. *Nuclear Fusion*, 54(2):023008, 2014.

[142] MJ Pueschel and F Jenko. Transport properties of finite-β microturbulence. *Physics of Plasmas*, 17(6), 2010.

[143] JW Connor, RJ Hastie, and JB Taylor. Shear, periodicity, and plasma ballooning modes. *Physical Review Letters*, 40(6):396, 1978.

[144] PW Terry, D Carmody, H Doerk, W Guttenfelder, DR Hatch, CC Hegna, A Ishizawa, F Jenko, WM Nevins, I Predebon, et al. Overview of gyrokinetic studies of finite-β microturbulence. *Nuclear Fusion*, 55(10):104011, 2015.

[145] W.M. Tang, J.W. Connor, and R.J. Hastie. Kinetic-ballooning-mode theory in general geometry. *Nuclear Fusion*, 20(11):1439, nov 1980.

[146] Fulvio Zonca, Liu Chen, JQ Dong, and Robert A Santoro. Existence of ion temperature gradient driven shear alfvén instabilities in tokamaks. *Physics of Plasmas*, 6(5):1917–1924, 1999.

[147] Jiaqi Dong, L Chen, and F Zonca. Study of kinetic shear alfvén modes driven by ion temperature gradient in tokamak plasmas. *Nuclear Fusion*, 39(8):1041, 1999.

[148] CZ Cheng. Kinetic theory of collisionless ballooning modes. Technical report, Princeton Plasma Physics Lab.(PPPL), Princeton, NJ (United States), 1981.

[149] A Hirose and M Elia. Kinetic ballooning mode with negative shear. *Physical review letters*, 76(4):628, 1996.

[150] IJ McKinney, MJ Pueschel, BJ Faber, CC Hegna, Akihiro Ishizawa, and PW Terry. Kinetic-ballooning-mode turbulence in low-average-magnetic-shear equilibria. *Journal of Plasma Physics*, 87(3):905870311, 2021.

[151] GG Plunk, P Helander, P Xanthopoulos, and JW Connor. Collisionless microinstabilities in stellarators. iii. the ion-temperature-gradient mode. *Physics of Plasmas*, 21(3), 2014.

[152] DR Hatch, MJ Pueschel, F Jenko, WM Nevins, PW Terry, and H Doerk. Magnetic stochasticity and transport due to nonlinearly excited subdominant microtearing modes. *Physics of Plasmas*, 20(1), 2013.

[153] Daniel Kennedy, Colin M Roach, Maurizio Giacomin, Plamen Ivanov, Toby Adkins, Facundo Sheffield, Tobias Görler, Arka Bokshi, David Dickinson, Harry George Dudding, et al. On the importance of parallel magnetic-field fluctuations for electromagnetic instabilities in step. *Nuclear Fusion*, 2024.

[154] M Giacomin, D Dickinson, W Dorland, NR Mandell, A Bokshi, FJ Casson, HG Dudding, D Kennedy, BS Patel, and CM Roach. A quasi-linear model of electromagnetic turbulent transport and its application to flux-driven transport predictions for step. *arXiv preprint arXiv:2404.17453*, 2024.

[155] A Najlaoui, Y Camenen, C Bourdelle, and A Loarte. Verifying turbulence model reduction in high beta tokamak plasmas. *Plasma Physics and Controlled Fusion*, 67(4):045016, mar 2025.

[156] R. E. Waltz and R. L. Miller. Ion temperature gradient turbulence simulations and plasma flux surface shape. *Physics of Plasmas*, 6:4265–4271, 11 1999.

[157] N. Joiner, A. Hirose, and W. Dorland. Parallel magnetic field perturbations in gyrokinetic simulations. *Physics of Plasmas*, 17(7):072104, 07 2010.

[158] A. Hirose and M. Elia. Kinetic ballooning stability of internal transport barriers in tokamaks. *Physics of Plasmas*, 10(5):1195–1198, 05 2003.

[159] N. Joiner and A. Hirose. Gyrokinetic verification of the persistence of kinetic ballooning modes in the magnetohydrodynamic second stability regime. *Physics of Plasmas*, 15(8):082107, 08 2008.

[160] X. Jian, J. Chen, S. Ding, A. Garofalo, X. Gong, C. Holland, J. Huang, V. S. Chan, X. Qin, G. Yu, R. R. Ma, X. Du, R. Hong, G. Staebler, H. Wang, Z. Yan, E. Bass, D. Brower, W. Ding, and D. Orlov. Experimental validation of a kinetic ballooning mode in high-performance high-bootstrap current fraction fusion plasmas. *Phys. Rev. Lett.*, 131:145101, Oct 2023.

[161] B Baiocchi, J Garcia, M Beurskens, C Bourdelle, F Crisanti, C Giroud, J Hobirk, F Imbeaux, I Nunes, JET Contributors, and EU-ITM ITER Scenario Modelling group. Turbulent transport analysis of jet h-mode and hybrid plasmas using qualikiz and trapped gyro landau fluid. *Plasma Physics and Controlled Fusion*, 57(3):035003, feb 2015.

[162] M. Giacomin and P. Ricci. Turbulent transport regimes in the tokamak boundary and operational limits. *Physics of Plasmas*, 29, 6 2022.

[163] A. Ishizawa, K. Imadera, Y. Nakamura, and Y. Kishimoto. Global gyrokinetic simulation of turbulence driven by kinetic ballooning mode. *Physics of Plasmas*, 26(8):082301, 08 2019.

[164] Y. Ishida, A. Ishizawa, K. Imadera, Y. Kishimoto, and Y. Nakamura. Global gyrokinetic nonlinear simulations of kinetic infernal modes in reversed shear tokamaks. *Physics of Plasmas*, 27(9):092302, 09 2020.

[165] J.Q. Xu, W. Chen, X.D. Peng, G.Z. Hao, J.Q. Li, H.P. Qu, P.W. Shi, X.X. He, M. Jiang, Y.G. Li, and the HL-2A Team. Gyrokinetic analysis of turbulent transport by electromagnetic turbulence in finite beta plasmas with weak magnetic shear on hl-2a. *Nuclear Fusion*, 63(12):126031, oct 2023.

[166] P Mulholland, K Aleynikova, BJ Faber, MJ Pueschel, JHE Proll, CC Hegna, PW Terry, and C Nührenberg. Enhanced transport at high plasma pressure and subthreshold kinetic ballooning modes in wendelstein 7-x. *Physical Review Letters*, 131(18):185101, 2023.

[167] C. Bourdelle, X. Garbet, F. Imbeaux, A. Casati, N. Dubuit, R. Guirlet, and T. Parisot. A new gyrokinetic quasilinear transport model applied to particle transport in tokamak plasmas. *Physics of Plasmas*, 14:112501, 11 2007.